OCEAN FRONTS FORMED AT SEA ICE BOUNDARIES

by

Siobhan Patricia O'Farrell

A dissertation submitted for the degree of
Doctor of Philosophy
in the University of Cambridge
Sidney Sussex College,
Cambridge.
April 1989

For Jonathan and Daniel

abstract

Meltwater input from sea ice forms a buoyancy source for the upper ocean which creates a strong density gradient in both horizontal and vertical directions. If, in particular, the ocean density front is formed in the Bering sea during winter, the frontal dynamics are influenced by local shelf/slope processes. Further, ice is advected across the front by the wind, thereby altering the heat flux to the ice and leading to an increase in the freshwater buoyancy flux to the ocean. Hence, the surface manifestation of the front is governed by ice position.

In this thesis a detailed study of ice and ocean parameters in such a system is presented using data from the 1982-3 winter Season in the Bering sea. Particular attention is given to the results from MIZEX-West (1983), an intensive mid-winter study. Modelling of the physical processes involved in the development of the meltwater front follows two directions; firstly the buoyancy input to small scale fronts formed in the summer marginal ice zone is considered and secondly, an hierarchy of numerical models of ice and ocean dynamics are employed.

Results are also reported of fieldwork carried out in the East Greenland current (MIZEX-84, LANCE cruise) using a novel, medium resolution, portable CTD system to measure upper ocean density gradients from floe edges and small boats. However, during these experiments conditions were not ideal for the development of meltwater fronts analogous to those found in the Bering Sea. Additionally, one-dimensional and two-layer quasi-steady ocean models coupled to an ice cover are discussed. These models proved useful tools in our understanding of the air-ice-ocean exchanges and frontal adjustment processes within the more complex system.

More detailed modelling studies were undertaken using a two-dimensional, coupled ice-ocean model focusing on the interactive thermodynamic forcing during ice ablation and ice accretion. The thermal and salinity fluxes in the coupling were related to the ice growth calculated by a thermodynamic ice model similar to those is employed by larger scale climate studies. Hence, over short time scales the ice growth in leads and open water that may occur after a change in external forcing conditions is not well represented.

The functional form of the internal stress in the ice momentum equation is investigated with the model. When the amplitude of the internal stress decreases by several orders of magnitude in a few grid points the model was unable to sustain such a gradient and was liable to generate numerical instabilities. If however, the near discontinuity in the internal stress at the ice edge is treated like a moving shock wave (after Røed and O'Brien, 1983) then the ice compactness maintains a coherent ice edge under conditions simulating the passage of a storm.

Acknowledgements

My greatest thanks go to my supervisor, Prof. Vernon Squire, who has given endless advice throughout my thesis work and provided much moral support, besides. This has been particularly true since he relocated to the other side of the globe where contact has been maintained with electronic mail. To Stuart Moore who developed the portable CTD instrumentation, along with Tim Owen, and put many hours in both laboratory and field in turning the original idea into a successful device. My thanks also go to Dr. Peter Wadhams who contributed by many useful discussions on ice-ocean physics, and through his involvement with MIZEX enabled me to partake in two field experiments in the Arctic.

From outside the group I have been able to call (by electronic mail when necessary) on the expertise of Dr. Robin Muench who provide much of the Bering Sea data set used within the thesis, and on Dr. Peter Killworth for help with the techniques used in the numerical modelling schemes.

Further data in the thesis has been culled from a variety of MIZEX sources but I would particularly like to thank Jim Schumacher, Carol Pease, the Bergen Group and Norsk Polarinstitutt. I am grateful for access to the cross-calibration data to E. Svendson, Bergen Group and B. Rudels, Norsk Polarinstitutt.

I am grateful to the computer services at the University of Cambridge for help and in particular for arranging unattended running of the machine during off peak periods. Photography was carried out by Robert Massom who also aided with some of the diagrams.

I wish to thank Dr. David Drewry and the staff of the Institute for their support and the stimulating atmosphere throughout my three and a half year stay, which converted me from an 'Oceanographer' to a 'Polar Scientist'.

During my time at the Scott Polar Research Institute I was supported by NERC on a research studentship. Additional support for equipment and funds to enable me to take part in field programmes was provided by the Office of Naval Research. The work on resubmission was completed partly at the Department of Oceanography at the Univerisity of Southampton, and more recently at the Department of Mathematics, University of Otago, New Zealand where I was given financial support as a Beverley Research Fellow.

Ultimately, I would like to thank my parents for 29 years of support particularly during my extended years of study.

I have dedicated the thesis to two babies: Jonathan Langhorne Squire and Daniel Farrell Leith who have given much pleasure to me in the last 6 months. I hope they will grow up to appreciate New Zealand as much as I have enjoyed my austral summer here.

PREFACE

This dissertation is an account of my work carried out while a research student at the Scott Polar Research institute in the period November 1982 to November 1986 under the direction of my supervisor, Prof. Vernon Squire. The dissertation does not exceed the regulations in length. It is a resubmission with corrections made as requested by the examiners to my thesis presented in November 1986. It is the result of my own work and includes nothing which is the outcome of work done in collaboration.

Siobhan Patricia O'Farrell

April 1989

Contents

List of Figures

List of Tables

Glossary of symbols

a, b, c, n	conductivity calibration coefficients
a_1, a_2, a_3	CTD calibration coefficients
A	ice compactness
B_o	buoyancy input
c	speed of wave propagation in ice
c_o	speed of wave propagation in 100 % ice cover
c_p	specific heat capacity of water
cld	cloud cover
C	conductivity
C_s	coefficient of sensible heat transfer
C_D	air-water drag coefficient
C_E	coefficient of latent heat transfer
C_W	ice-water drag coefficient
C_ϕ	speed of propagation of ϕ
D	depth in ocean
f	Coriolis frequency
$f(x)$	ice growth function
f_m	measured instrument frequency
f_o	frequency at 273.15 K
f_s	surface reference frequency
f^o	diffusive fluxes
f^1	anti-diffusive fluxes
f^c	flux limited diffusive values
F	internal stress
F	internal stress vector
F_A	advective flux
F_L	longwave radiation
F_R	incoming shortwave radiation
F_S	shortwave radiation
F_x	turbulent flux
g	acceleration due to gravity
k	vertical unit vector
h	depth of mixed layer
h_i	thickness of ice
H_r	maximum depth of dissipation
K_L	ice viscosity
L	Monin-Obukhov length
L_m	latent heat coefficient for ice melt/growth
m	mass
m_1, m_2, m_3	dissipation coefficients for KE
n	dissipation coefficient for convective energy
P	ice pressure term
P_*	amplitude of ice pressure term
q^2	local turbulence
Q	total heat budget

Symbol	Definition
Q_a, Q_{sfc}	specific humidities of air and snow/ice surface
R	melt rate
RM, M, MJ	parameters used to define ice concentration distribution
Ri	Richardson number
S	salinity
S_A, S_h	total thermodynamic changes for ice compactness/thickness
S_i	salinity of ice
S_o	salinity of surface ocean layer
T	temperature
T_B	basal temperature of ice
T_i	ice temperature
T_{sfc}	ice/snow surface temperature
T_o	temperature of surface ocean layer
u	ice velocity vector
u', v'	current fluctuations from the mean $\bar{u}, \bar{v}$
u_*	friction velocity
U_g	geostrophic wind velocity
U_w	velocity of upper ocean
w	vertical velocity
w_e	entrainment rate
α	ice albedo
γ	e-folding depth for dissipation
δ_{ij}	delta function
Δ	least count resolution
$\Delta b, \Delta S, \Delta T$	discontinuous steps in buoyancy, salinity and temperature
ϵ	dissipation
ϵ_o	background dissipation
ϵ_i	emissivity of ice
$\dot{\epsilon}_{ij}$	strain rate tensor
κ	ice dispervity
κ_i	thermal conductivity of ice
μ, η	bulk and shear ice viscosity
∇H	sea surface slope
η_1	normalized diffusion coefficient
ϕ	variable for open boundary condition
ρ_a	density of air
ρ_w	density of water
σ	Stefan-Boltzman constant
σ_{ij}	stress tensor
τ_s	sample interval
τ_R	resultant stress
τ_a	air stress vector
τ_w	water stress vector

Symbol	Definition
	2-layer model
U_1, V_1	velocities for upper layer
U_2, V_2	velocities for lower layer
ρ_1, ρ_2	densities of two layers
h_1, h_2	depth of respective layers
f	coriolis frequency
u, v	velocities of ice
A	compactness of ice
ρ_i	density of ice
τ_x, τ_y	stresses on the ocean
τ_{xi}, τ_{yi}	stresses on the ice
α, α_i	coefficients for relative ice/water velocities
β, β_i	coefficients for relative ice/water velocities
	multi-level model
x, y, z	co-ordinate system
u, v, w	velocities for x, y, z directions
f	coriolis frequency
ρ	density of sea water
p	pressure
S	salinity
T	temperature
τ_x, τ_y	stresses on the ocean
A_H, A_z	horizontal/vertical eddy viscosities
K_H, K_z	horizontal/vertical eddy diffusivities
U_g^x, U_g^y	geostrophic wind velocities
C_D, C_w	air-ice/water-ice drag coefficients
u_i, v_i	ice velocities
A	ice compactness
h_i	ice thickness
τ_i^x, τ_i^y	stresses on the ice
F_x, F_y	internal stress

✸

In chapter 1 we review the role of sea ice in the global climate and examine the three major approaches to studying the polar environment; field measurements, remote sensing and numerical modelling. We next examine the large scale heat, salt and momentum budgets of the Arctic and Antarctic regions which encompass our study of the marginal ice zone where the these exchanges are at their most intense. Chapter 2 focuses on the specific processes that occur at the marginal ice zone, examining in turn ocean fronts, upwelling at the ice edge, ice bands and ice edge eddies. In chapter 3 we consider the current meter and CTD data from the MIZEX-WEST field programme, the most extensive study of an ice edge frontal system. Chapter 4 develops three models of the coupling between the ice cover and the ocean. The first is a one-dimensional model of the mixed layer under ice, the second, a two layer geostrophic front under ice and the third a two-dimensional multi-level ocean model coupled to a full ice model including rheology. This last model is developed extensively, and we discuss the various numerical techniques we invoke. In Chapter 5 we give details of the final model runs forced by realistic Bering Sea conditions. Finally, in the Appendix we describe the design and deployment of a portable mini-CTD instrument in the Greenland Sea marginal ice zone.

1

INTRODUCTION

The ocean and atmosphere dominate the Earth's climate system at all latitudes. Numerous interactions between the two fluids occur on time scales ranging from seconds to decades. At high latitudes, the presence of sea ice on the ocean surface inhibits direct transfer of heat and momentum; its insulating properties play a major role in modifying existing circulations in both the polar atmosphere and oceans; and its seasonal cycle of ablation and accretion alters the underlying ocean density structure.

In this thesis, we examine upper ocean dynamics resulting from the input of buoyant meltwater at the ice edge.

✸

1.1 The role of the polar ice cover within the global climate

Although only 10% of the earth's surface is ice-covered, the extent and volume of the sea ice cover and terrestrial ice act as strong climatic indicators; due to the reflectance properties of the ice surface. From our knowledge of preceding ice ages, we can envisage dramatic changes in sea level if substantial melting of the polar ice sheets (which trap 90% of the world's freshwater) were to occur. On a more immediate time scale, variation of sea ice from its seasonal norm, indicates changes in weather patterns over continental landmasses.

In the Arctic basin and peripheral seas (Figure 1.1) the time series of sea ice extent is more correlated to the preceding meteorological forcing than to changes in oceanic forcing (Walsh, 1987). Strong oceanic currents dominate the trajectory of the ice pack (e.g., East Greenland Current, Weddell Sea Gyre), but if the oceanic forcing is weak then atmospheric forcing determines the direction

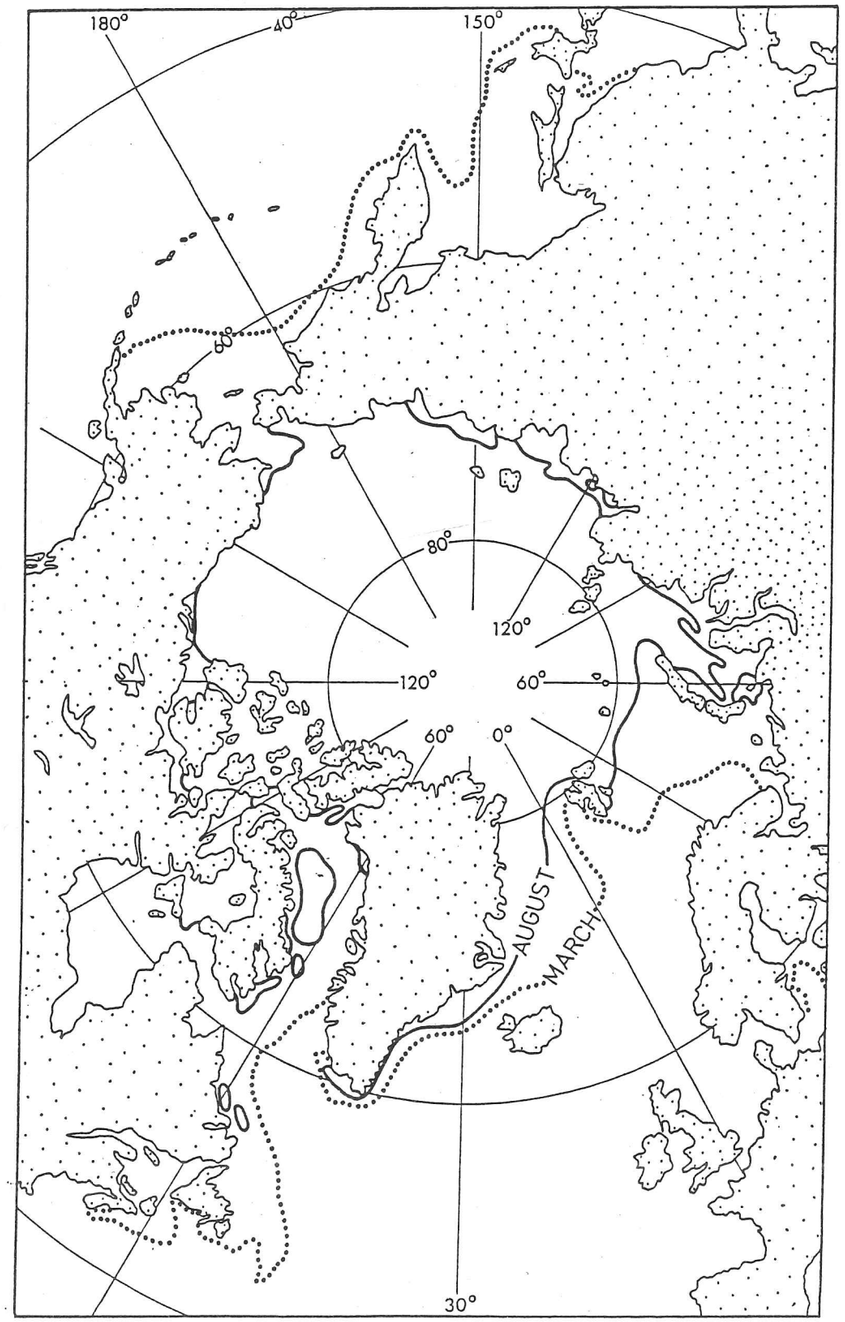

FIGURE 1.1: Map of Arctic ocean basin indicating average sea ice extents, derived from satellite data, for the winter maximum (March) and summer minimum (August)

of ice drift (Overland and Pease, 1982). However, a full understanding of the relationship between the sea ice dynamics, air/water temperatures, and pressure anomalies is complex and has not yet been achieved (Herman, 1984). In particular, interannual comparisons of ice anomalies are hampered as the resolution and quality of the original data sources have altered over the last 30 years (Walsh and Johnson, 1979).

The global climate budget of heat is of considerable interest in the context of the polar regions (Figure 1.1 and Figure 1.2), which act as major heat sinks. Gyre scale atmospheric and oceanic circulations are driven by a poleward heat flux, modifying the imbalance in stored heat created by insolation input (Hastenrath, 1982). In the tropics (30°N – 30°S), 50% of the heat transported poleward is carried by ocean currents. In mid-latitudes 30% of the heat is transported by the ocean, whilst at very high latitudes the atmosphere plays the dominant role in heat transfer (Hastenrath, 1982). The high latitude heat balance, and hence the present day climate, is also sensitive to alterations in the radiation input received in the tropical and temperate oceans (Schneider, 1975).

The sea ice volume is sensitive to changes in the heat balance. This is ably demonstrated by the extensive annual variability of the ice edge in the marginal seas. In particular, changes in the albedo of the ice/snow cover during the melt season may amplify melting processes by allowing ice to absorb more radiation (Kellogg, 1975). If a substantial atmospheric warming was initiated by the increasing global atmospheric CO_2 levels, it is in polar regions that the most critical changes would occur (Herman, 1984). In particular, CO_2 increases are amplified by high latitude cloud cover, thereby altering the radiation transfer through the atmospheric column. The feedback involved in the changing albedo of the ice surface also amplifies any warming trend (Herman, 1984). The response of perturbations of CO_2 within the polar system has been simulated using numerical models which couple atmosphere, ocean and ice momentum equations (Parkinson and Kellogg, 1979; Herman, 1984; Hibler, 1984a). In some early CO_2 climate models, violent changes to the equilibrium of the polar system were forecast (Budyko, 1969). More recent simulations have used a greater understanding of the physics to parameterize the feedback within the system (Kellogg, 1975), and instead a new equilibrium state of reduced ice extent and thickness is reached.

The high latitude oceans are also of particular importance on the global climate timescale because they form the principal source of oceanic deep water, the most dense water to be found in the world ocean basins. Major deep water formation areas are situated in the Greenland sea and Southwest Weddell sea (Killworth, 1983). Prototype deep water is created by the convection of brine

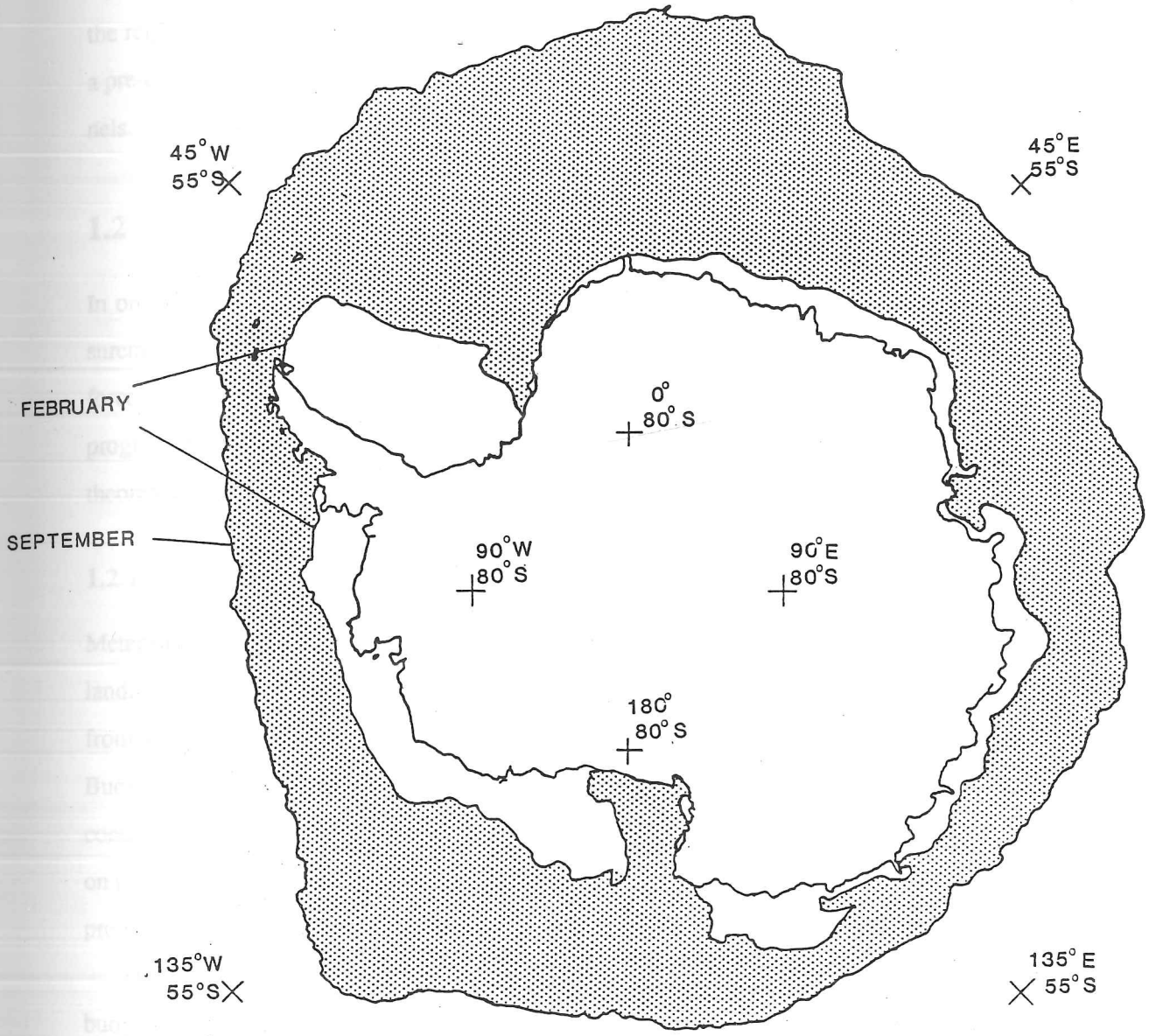

FIGURE 1.2: Map of Southern Ocean about Antarctic continent showing February (summer) and September(winter) sea ice extents derived from passive microwave (ESMR) data. The shaded region represents the seasonal sea ice zone.

rejected from newly formed sea ice. This dense water is then trapped on the continental shelves of the region. Subsequently, this water is mixed to the ocean depths, particularly at locations where a pre-existing dynamic circulation drives the water down slope through suitable topographic channels. (WCP-108).

1.2 Programmes to study the ice-ocean-atmosphere system

In order to fully understand the coupling between the ice, ocean and atmosphere, detailed measurements of each of the dynamic components of the system must be made *in situ* and the external forces acting on each medium must be determined. In the past decade or so data gathered from field programmes have been supplemented by airborne and satellite remote sensing surveys. Also, many theoretical/numerical studies of processes in the polar environment have been undertaken.

1.2.1 Field measurements

Meteorological data in the Arctic are routinely obtained from weather stations on the peripheral landmasses. Data on surface pressure, temperature and ice velocity are also transmitted via satellite from a series of buoys drifting on the ice. These buoys, deployed since 1979 as part of the Arctic Buoy Program (Untersteiner and Thorndike, 1982), have proved a valuable data source and will continue within the World Climate Programme. In a more limited way, land meteorological stations on the Antarctic continent and a recent extension of the Arctic Buoy Program to the Ross Sea have provided useful data records for climatological purposes.

Data sets from the Southern Ocean area are sparse, though increasing numbers of meteorological buoys are being released both on the sea ice and in open water. Isolated data points such as these in the vast expanse of the polar regions will improve our understanding of high-latitude weather systems, as the data provided in near real time can be assimilated into operational meteorological models and act as ground truth for the next generation of satellite sensors. Whilst coverage of large-scale synoptic meteorological fields can now be obtained relatively easily from data buoys and land stations, localized problems in meteorology, including atmospheric boundary layer studies and micro-meteorology over ice, still have to be studied from manned ice stations and ships.

In the ocean, the time and length correlation scales of both mean and turbulent flow fields are somewhat smaller than in the atmosphere; thus adequate definition of the dynamics requires

intensive hydrographic sampling to supplement data from long-term moored arrays.

Several year-long oceanographic experiments were carried out at a series of manned camps in the Beaufort sea under the auspices of the Arctic Ice Dynamics Joint Experiment (AIDJEX). Baroclinic eddies were tracked passing through the array (Hunkins, 1980), but most features on a smaller scale than the nodal spacing (100 km) were poorly defined. Furthermore, the advection of camps over different water masses has to be considered when interpreting the data profiles (Lemke and Manley, 1984). More intensive hydrographic surveys have been done in limited regions, taking advantage of a helicopter borne Conductivity-Temperature-Depth (CTD) profiler (Manley *et al*, 1980) to provide near synoptic sampling.

More recently, field programmes have concentrated on the study of regional dynamics, because of financial and logistical constraints (e.g., the MIZPAC experiment on the Alaskan shelf, Paquette and Bourke, 1981). These programmes have enabled studies of particular processes (upwelling, shore lead development, marginal ice zone dynamics) to be examined in detail, thereby furthering our understanding of the complete system. Some recent programmes have involved placing moorings across Fram Strait to examine the seasonal and annual variations in heat and mass exchange. The MIZEX 1983-1987 (marginal ice zone experiment) programme has concentrated on interactions between atmosphere, ice and ocean within a swathe 200 km either side of the ice edge. This campaign has focussed particularly on the ice formed on the Bering sea shelf and the North-eastern Greenland sea. The study of Antarctic sea ice has increased in recent years (Ackley and Smith, 1983) with a field programme recently undertaken in the Winter Weddell Sea (Augstein, 1987).

1.2.2 Remote sensing data

In the fields of operational planning and climatological statistics the increased data coverage (both spatial and temporal) of ice edge position provided by airborne and satellite remote sensing devices has been invaluable. Moreover, despite the initial outlay, remote sensing techniques prove more economical for surveying the remote polar regions than land/sea expeditions. Visual and infra-red remote sensing respectively, require illumination and cloud-free conditions to operate successfully (Figure 1.3). As neither condition is realistic for high latitude work, we must use passive (e.g., scanning radiometers) or active (e.g., radar) microwave sensors if we require a regular time series of sea ice extent and conditions. These sensors avoid the degradation of images caused by cloud

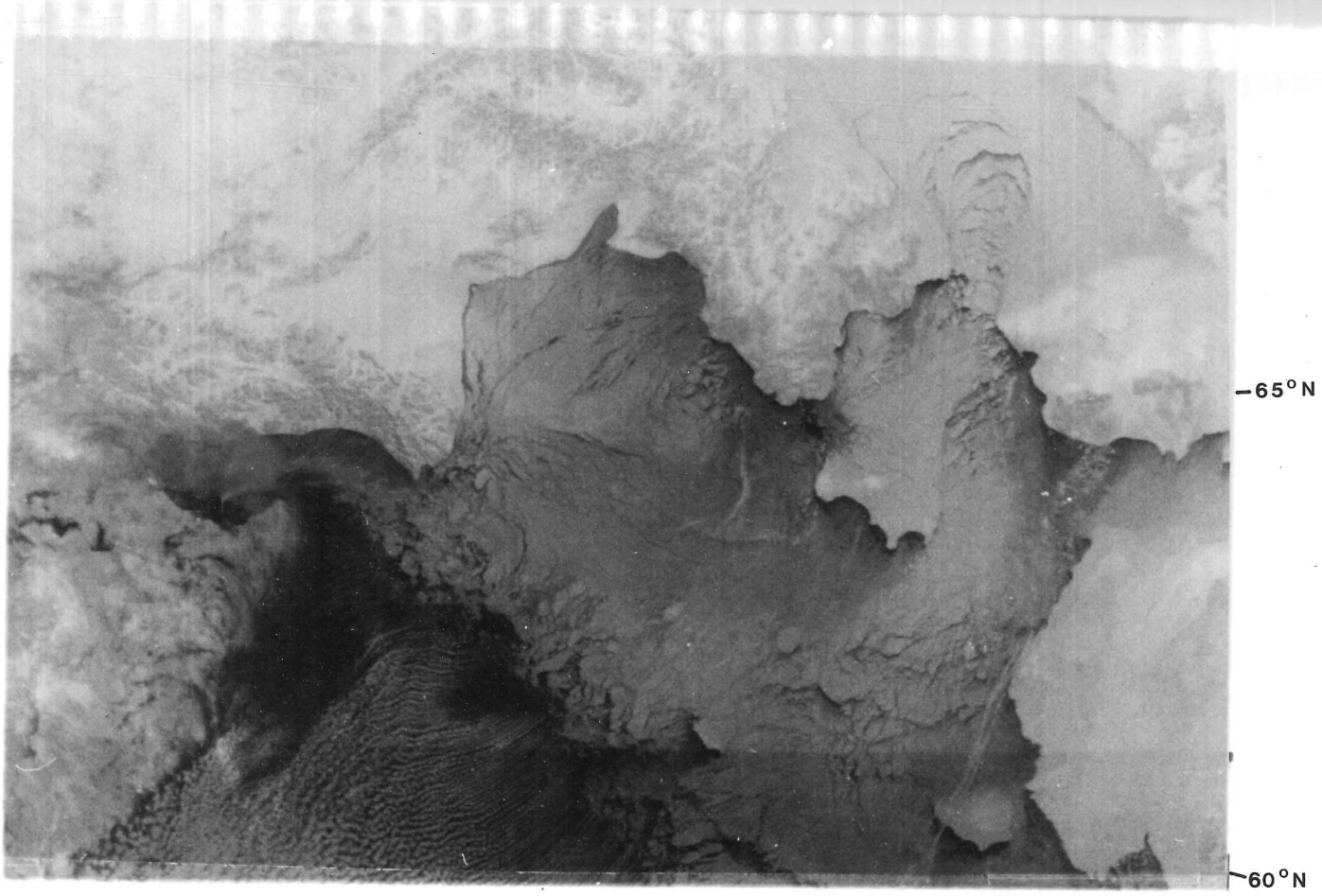

FIGURE 1.3: Satellite photograph of Bering Sea ice edge region on 21st February 1983 midway through MIZEX-West (provided by C. H. Pease, NOAA PMEL).

cover (Zwally and Gloersen, 1977). Passive microwave instruments (e.g., the Electrically scanning microwave radiometer ESMR and the Scanning multichannel microwave radiometer, SMMR) utilize emmissivity differences between open water, grease ice, first-year ice and multi-year ice. Data on measured brightness temperature, collected using multi-channel sensors, are combined via algorithms to provide information on ice concentration and type. Because radiated energy levels in the microwave band are small and antenna size is limited, radiometers have limited resolution ($\approx$ 20 km or so). The active microwave devices, especially synthetic aperture radar (SAR) offer significantly improved resolution over the passive instruments, and may distinguish particular features of interest. This can be especially important near the ice margin where confusing signatures are often produced in passive microwave data. Finally, with respect to remote sensing instruments, we note that an airborne radar altimeter was operated during MIZEX to explore its use for defining the ice margin, ice characteristics and waves in open water regions.

1.2.3 Numerical modelling

To be effective, numerical models developed for the polar regions must either include or parameterize every air-ocean interaction on all time and space scales. Many of these interactive processes occur at scales smaller than the grids used by the global and basinwide models. Then they must be parameterized in terms of gross physical variables (Parkinson and Washington, 1979). Due to the complexity of the fully interactive air-ice-ocean system, all the numerical models developed so far have used a subset of these processes, normally concentrating on the dynamics of one of the three media (air, ice, ocean) and parameterizing the effect of the others.

An ocean model of the Arctic basin topography was developed by Semtner (1976a) using the Bryan and Cox (1968) general circulation (GCM) form. This model did not include an ice cover and was driven by a prescribed averaged wind stress field. Boundary conditions were defined at both the Bering and Fram Straits or at the edge of the Greenland Sea.

An alternative approach to modelling the coupled air-ice-ocean system has been proposed by Hasselman (1979) and co-workers (Lemke *et al*, 1980) who used stochastic models to elucidate the mechanisms behind the sea ice anomalies. A detailed survey of the numerical ocean models which are relevant to our study of ice edge ocean fronts will be given in the appropriate chapter.

Numerical models focussing on both dynamic and thermodynamic processes of the sea ice cover

cover (Zwally and Gloerson, 1977). Passive microwave instruments (e.g., the Electrically scanning microwave radiometer ESMR and the Scanning multichannel microwave radiometer, SMMR) utilize emmissivity differences between open water, grease ice, first-year ice and multi-year ice. Data on measured brightness temperature, collected using multi-channel sensors, are combined via algorithms to provide information on ice concentration and type. Because radiated energy levels in the microwave band are small and antenna size is limited, radiometers have limited resolution ($\approx$ 20 km or so). The active microwave devices, especially synthetic aperture radar (SAR) offer significantly improved resolution over the passive instruments, and may distinguish particular features of interest. This can be especially important near the ice margin where confusing signatures are often produced in passive microwave data. Finally, with respect to remote sensing instruments, we note that an airborne radar altimeter was operated during MIZEX to explore its use for defining the ice margin, ice characteristics and waves in open water regions.

1.2.3 Numerical modelling

To be effective, numerical models developed for the polar regions must either include or parameterize every air-ocean interaction on all time and space scales. Many of these interactive processes occur at scales smaller than the grids used by the global and basinwide models. Then they must be parameterized in terms of gross physical variables (Parkinson and Washington, 1979). Due to the complexity of the fully interactive air-ice-ocean system, all the numerical models developed so far have used a subset of these processes, normally concentrating on the dynamics of one of the three media (air, ice, ocean) and parameterizing the effect of the others.

An ocean model of the Arctic basin topography was developed by Semtner (1976a) using the Bryan and Cox (1968) general circulation (GCM) form. This model did not include an ice cover and was driven by a prescribed averaged wind stress field. Boundary conditions were defined at both the Bering and Fram Straits or at the edge of the Greenland Sea.

An alternative approach to modelling the coupled air-ice-ocean system has been proposed by Hasselman (1979) and co-workers (Lemke *et al*, 1980) who used stochastic models to elucidate the mechanisms behind the sea ice anomalies. A detailed survey of the numerical ocean models which are relevant to our study of ice edge ocean fronts will be given in the appropriate chapter.

Numerical models focussing on both dynamic and thermodynamic processes of the sea ice cover

have been developed over a number of years with the ice treated as a continuum. Such models calculate the ice concentration, ice thickness and floe size distribution (Hibler, 1979,1980; Bratchie, 1984). Ice-ice interaction is represented by a non-Newtonian plastic ice rheology. Including a complex rheology in the ice models increases the computational expense of the coupled model compared to similar scale atmospheric and oceanic models.

In the remainder of this chapter, we discuss in turn the heat, freshwater and momentum budgets which determine the position and characteristics of the polar sea ice cover.

1.3 Thermodynamic features of the sea ice cover

The heat influx from the ocean plays a significant role in the thermodynamic control of the sea ice cover, particularly as it acts as a major influence on whether an ice cover will be present at any position in a given season. A schematic of the dynamic processes associated with an ice covered ocean are given in Figure 1.4.

1.3.1 Heat Exchange in the deep ocean

The net poleward transport in the global heat budget means that considerable heat loss occurs in the Arctic and Antarctic ocean regions, particularly during sensible and latent heat transfer on freezing. The major inflow of warm water to the Arctic basin is provided by the West Spitzbergen current which transports 90% of the incoming ocean heat flux (Aagaard and Griesman, 1975). The West Spitzbergen Current enters the main basin through Fram strait, a 500 km wide passage between Greenland and the Svalbard archipelago (Aagaard and Griesman, 1975). The East Greenland Current and its associated ice cover exits the Arctic basin through the same narrow strait. Consequently, this is an active region of oceanic heat exchange, resulting from direct contact between entering, (warm) and exiting, (cold) currents.

Some of this incoming water cools immediately north of Svalbard and recirculates to contribute to the East Greenland Current. The remainder sinks and can be traced by its temperature maximum as a distinctive Atlantic layer throughout the Arctic basin (Coachman and Barnes, 1963). With time, the temperature and salinity characteristics of this water mass are gradually eroded by entrainment

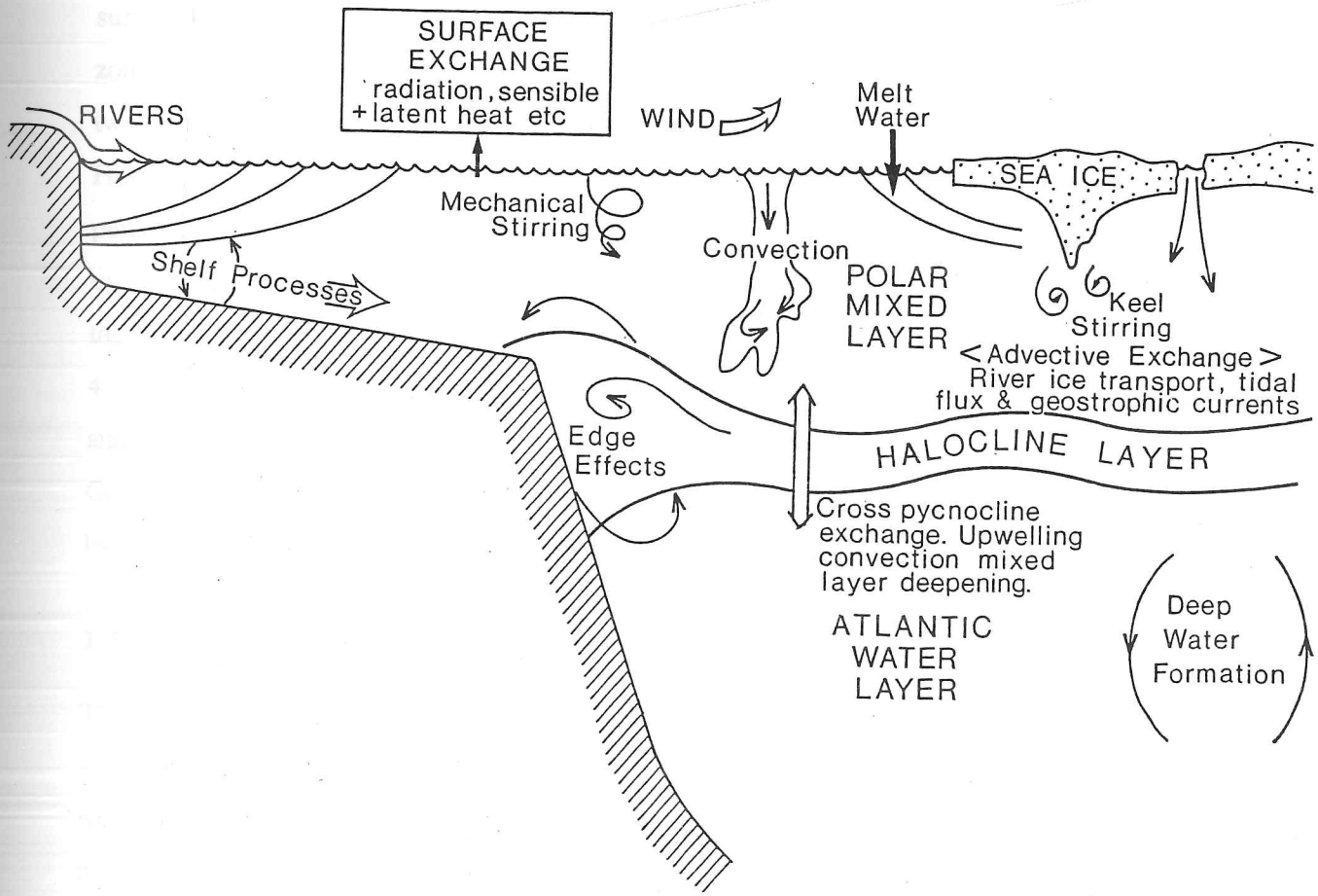

FIGURE 1.4: Schematic of the major dynamic processes involved in the creation of Arctic Ocean water masses (source E. Carmack from SCOR-58 report).

and double diffusive processes, whereas the deep water beneath maintains near uniform salinity and temperature (Coachman and Aagaard, 1974). During summer the northward flow through the Bering Strait is discernible as a warm layer of low salinity water in the Beaufort and Chukchi Seas. This heat source speeds up the ice break-up in this region during the summer months (Paquette and Bourke, 1981).

In contrast to the land locked Arctic Ocean basin in the north, the Southern Ocean surrounding the Antarctic continent forms a major link between the Atlantic, Pacific, and Indian Oceans. Hence, the area is important for heat exchange. The mass transport is driven within the Antarctic Circumpolar Current, a strong wind-driven cyclonic zonal flow. The highest meridional heat flux values in the Southern Ocean are associated with three well-defined frontal regimes which entirely surround the continent. The largest temperature gradients are found in the Sub-tropical convergence zone where a surface temperature decrease of $> 8°$ C is observed within 2° of latitude. The other two fronts positioned within cores of the the Antarctic Circumpolar Current, are the Sub-Antarctic Front and the Antarctic Polar Front, respectively. These fronts are less sharply delineated if the temperature signature gathered by XBT's (expendable bathythermographs) only is considered. Using expendable probes the temperature field on a transect south can easily be measured without slowing the ship's progress. Estimates of the poleward-directed heat flux across the Antarctic polar front of 4.5×10^{14} W have been made (WCP-108). Detailed studies of both the Antarctic polar and sub-antarctic fronts have been undertaken in Drake Passage during the ISOS (International Southern Ocean Studies) programme (Joyce *et al*, 1978). The transfer of heat at this location is dominated by eddy processes (Bryden, 1979) which act to mix the waters of polar and sub-antarctic origin.

1.3.2 Oceanography of the upper 200 meters of the Arctic basin

The surface waters of the Arctic basin are separated from the warmer distinctive Atlantic layer by a strong pycnocline. The density gradient is strongly dependent on the low salinity of the surface waters in the polar temperature range. The surface mixed layer is at, or close to, its freezing point throughout most of the year, and turbulent mixing is maintained over its 50 m depth by momentum transferred through the drifting ice cover. The salinity distribution is governed by the annual freeze/melt cycle and by the introduction of fresh water from river runoff. The strong pycnocline maintained by the freshwater input inhibits mixing, and hence heat loss from the lower water masses to the atmosphere is minimal. The upper part of the pycnocline is also at the ambient freezing point,

which suggests that this water mass is formed by the release of brine during the freezing process over the continental shelves (Aagaard *et al*, 1981) and becomes so dense that it sinks and flows into the main basin.

1.3.3 Impact of heat transfer on ice

The thickness of a multi-year ice cover is very sensitive to changes in the sensible heat flux, both at the ice surface and internally (Maykut and Untersteiner, 1971). Surface melting would be doubled if sensible heat was not lost to the atmosphere from melt pools. Loss of sensible heat through a newly formed or young sea ice cover is also an order of magnitude greater than through the adjacent multi-year cover, although the loss through open water may be an order of magnitude greater again (Maykut, 1978). Hence, the distribution of the ice thickness is crucial in parameterizing regional thermal balance, as well as limiting deformation dynamics (Hibler, 1979; Bratchie, 1984).

Heat from various sources contributes to ice decay during the melt season. Some heat may be entrained through the pycnocline by excess turbulent energy, supplementing short wave radiation trapped in the open water. However, with a strong pycnocline gradient the entrainment process is inhibited, reducing the oceanic heat flux to the ice in the Arctic basin to $3\,W\,m^{-2}$. Whilst small in magnitude, this heat flux can be a significant factor in divergent pack ice regions (Hibler and Bryan, 1984). In the Southern ocean where the vertical density gradient is not as strong and vertical mixing is enhanced at large scale ocean fronts, the oceanic heat flux to the ice is estimated to be $10\,W\,m^{-2}$ (WCP-108).

The position of the ice edge and the thermodynamic state of the ice cover may also be affected by heat which is advected under the ice cover by eddies (Wadhams and Squire, 1983), or by ocean currents (Hendricks *et al*, 1985). Moreover, in marginal ice zones the incoming wave field breaks up the floes and increases the perimeter available for ice decay to occur by lateral melting (Wadhams, 1981). This initiates a positive feedback, increasing the ice melt rate as more water opens up to absorb solar radiation. In calm conditions, a very sharp, warm and shallow layer is created which acts to undercut the ice floe side walls with differential melt rates (Perovich, 1983). If a wind is present, waves are generated in the open water, re-instigating a very shallow mixed layer which increases the transfer of heat to the ice wall. Induced circulations set up by the wind within leads can also transfer heat beneath the ice, thereby increasing bottom ablation.

Studies of lead thermodynamics have been made, both in the AIDJEX programme and in the

Canadian Arctic (Perovich, 1983). Numerical studies of lead dynamics (Schaus and Galt, 1973; Kozo, 1983) have increased our understanding of the circulation and indicated the part such processes play in the large scale field. Also of interest at small scale is the heat transfer across the boundary layers which develop adjacent to the ice wall. This latter problem can perhaps best be examined by scaled, laboratory studies or theoretical models of the ice-ocean interface (Josberger and Martin, 1981; Huppert and Josberger, 1980).

Throughout most of the year, heat is conducted upwards through the ice from the warm ocean to the cold air, with the result that considerable gradients are imposed across the ice. When modelling the annual accretion/ablation cycle, it is necessary to consider the heat transfer processes through multi-year ice, a complex material involving layers of different crystal fabric. A comprehensive, one dimensional model of ice thermodynamics, which includes such physics was proposed by Maykut and Untersteiner (1971). Their multi-layered model has individual conductivities and diffusion terms formulated for each snow/ice layer. When coupling such an ice model to either a realistic atmosphere or ocean, however, the multi-layered model is computationally time consuming and a simplification to three levels is normally followed (Semtner, 1976b). This latter model provides reasonable amplitude and phase estimates for the seasonal cycle, and simulates the ice physics more realistically than a single ice layer by allowing simulation of internal heat sources within the ice lattice and brine pockets (Semtner, 1984a).

1.3.4 The Heat Budget Equation

If we are to describe the heat exchange in ice-covered waters, we require detailed field measurements over the complete range of atmospheric conditions at a variety of ice locations. Unfortunately, most of our knowledge of the heat budget for sea ice is based on data collected in the central Arctic, from drifting scientific camps set up during AIDJEX. Extrapolating these earlier results to other regions presents some problems. This is particularly true when discussing active regions, such as the ice edge zone, where direct coupling between the components of the ice-ocean-atmosphere system is more intense. A review of parameterizations of all heat flux terms may be found in Maykut (1987).

In summer, short wave radiation reaching high latitudes is diffuse due to the relatively low solar angle. Even then, a large proportion is still reflected from the snow surface due to the high albedo (> 0.8). Later in the season as the snow melts and ponds develop on the ice, the albedo decreases to a value of 0.6 on the bare ice and can be as low as 0.3 in melt pools (Maykut, 1987). An

increase in the shortwave radiation absorbed by the ice follows. Most of this short wave radiation is absorbed in the upper 10 cm of the ice where it is directly utilized in melting; the remaining percentage, a function of the incident wavelength and surface scattering, remains stored within the ice (Maykut, 1987). Short wave radiation falling on leads and polynyas normally goes into heating the surface water, with a percentage directed into lateral melting of the floes (Perovich, 1983). AIDJEX data indicated that the excess solar radiation is partly stored in leads, partly in a temporary layer under the ice, with a portion stored within the ice lattice only at the height of summer (Maykut, 1982). This under-ice layer provides most of the oceanic heat flux which causes bottom melting as upwelling and thermocline entrainment processes are negligible in the central Arctic. Consequently, the simplification of allowing the ocean surface layer to remain near freezing as the ice cover decays, which is often used in numerical models (Hibler, 1980) is unrealistic.

The incoming long wave, black-body radiation dominates the radiation balance throughout much of the year and often has an amplitude twice as large as short wave radiation. Nevertheless, the net effect of the long wave radiation budget is a heat loss from the ice surface to the atmosphere. When considering the heat budget integrated over the entire polar basin, the sensible and latent heat terms are often ignored on the grounds that they are small in comparison to the radiation terms, and are thus of local rather than regional significance. However, the turbulent fluxes are important, and represent a considerable fraction of the net radiation budget ($\approx 20\%$). The most rapid sensible heat exchange occurs within open water areas formed during the random deformation of the pack (Hibler, 1979). This large sensible heat loss is often accompanied by a loss of latent heat, as the sea-water in contact with the cold air rapidly refreezes. These turbulent fluxes are parameterized in terms of surface wind speed, surface roughness, stability of the atmospheric boundary layer, and the magnitude of the temperature and water vapour differences across the ice/water interface.

In the present thesis, in common with many modellers (e.g. Parkinson and Washington, 1979), heat budget terms will be calculated with a parameter subset defined as follows:

Shortwave Radiation (F_S)

$$F_S = (1-\alpha)(1-0.6\times \mathrm{cld}^3)F_R, \tag{1.1}$$

where F_R is the incoming radiation, α is the surface albedo of the ice and cld is the cloud cover. The term F_R is a function of latitude, time of year and hour of day.

Longwave Radiation (F_L)

$$F_L = \sigma T_a^4(1 + 0.275\text{cld})(1 - 0.261\exp(-7.77 \times 10^{-4}(T_a - 273)^2). \quad (1.2)$$

In these expressions F_L represents incoming radiation, σ is the Stephan-Boltzman constant, T_a is surface air temperature (absolute). The emissivity (ϵ_I) of bare ice is taken as 0.97, and for snow-covered ice as 0.99.

The net longwave radiation budget is given by

$$\epsilon_I(F_L - \sigma T_{sfc}^4) \quad (1.3)$$

where T_{sfc} is the temperature of the snow/ice surface.

The turbulent heat flux terms are given by

Sensible Heat (F_s)

$$F_s = \rho_a c_p C_s U_g(T_a - T_{sfc}), \quad (1.4)$$

Latent heat (F_E)

$$F_E = \rho_a L C_E U_g(Q_a - Q_{sfc}), \quad (1.5)$$

where ρ_a is density of air, c_p is the specific heat capacity, L is latent heat of evaporation and the 'Q's are specific humidities. The bulk parameters C_E, C_s, are normally of similar magnitude (1×10^{-3}). In unstable conditions, such as might occur above a refreezing lead, however, values up to 3.0×10^{-3} have been measured (Lindsay, 1976). The bulk transfer coefficients C_s and C_E have also been tabulated as functions of the wind speed and temperature difference (Smith, 1981).

Figure 1.5 is a summary diagram representing the thermodynamic balance of an ice floe. Besides the atmospheric exchanges listed above, the figure includes effects due to the transmission of short-wave radiation, the conduction of heat through the ice (F_c) and an oceanic heat flux term (F_o). The first term is normally expressed as a fraction of the shortwave radiation (I_o), whilst the latter two fluxes are expressed as temperature differences across the medium, multiplied by appropriate transfer coefficients.

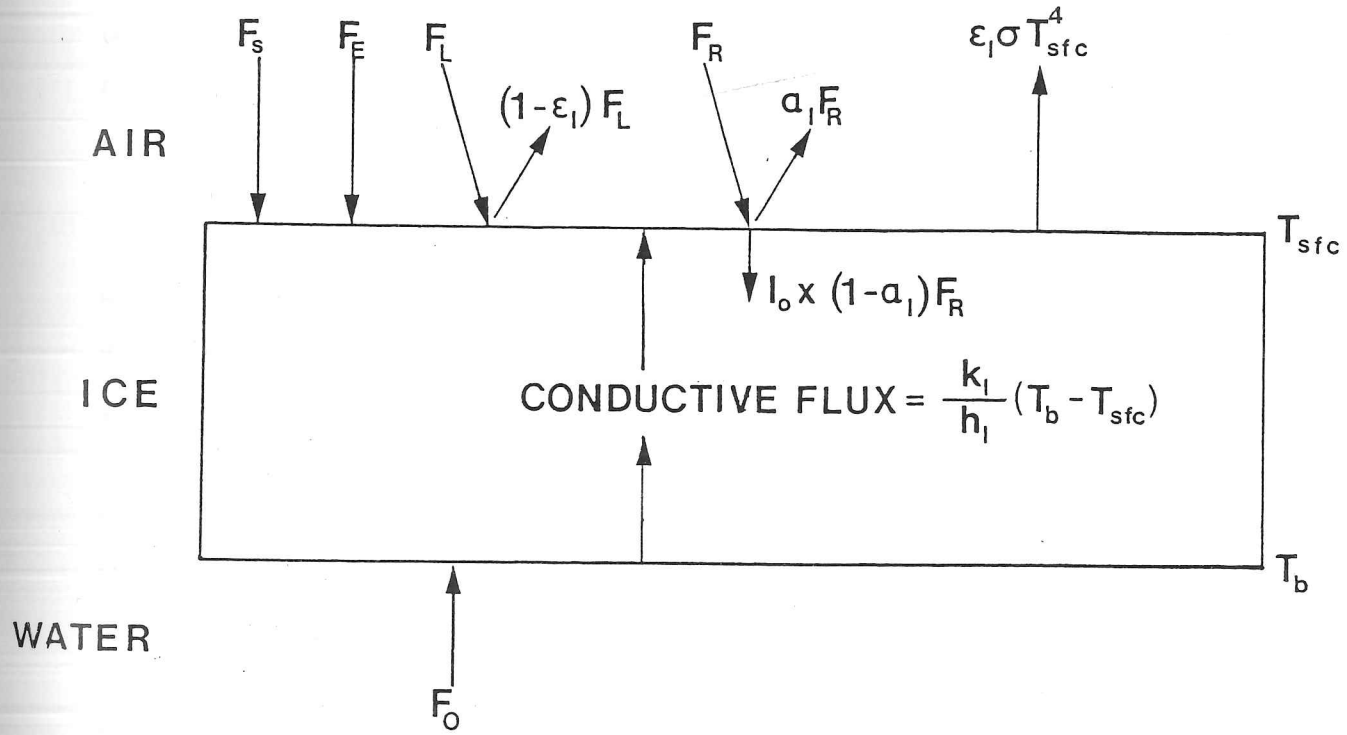

FIGURE 1.5: Summary of the thermodynamic fluxes operating on an ice floe in the ocean introduced in section 1.3.

1.4 Salinity characteristics and freshwater budget

1.4.1 Arctic Ocean Basin

A characteristic which is particular to the Arctic ocean basin is the low salinity of the surface waters, which are more typical of salinities in regions influenced by coastal runoff. Since at low temperatures the density is governed by salinity (Defant, 1961), the salinity of sea water is responsible for the stability of the water column down to 250 m. Principal contributors to the total freshwater inflow are the Ob, Yenisei, Lena, and the Mackenzie rivers (Semtner, 1973). The combined freshwater flux from the 12 principal gauged rivers (Figure 1.6) is normally taken to equal 0.1 Sv (10^6 m^3 s^{-1}) (Ivanov, 1975). Although the ice cover reduces the energy transferred to the upper ocean, momentum is still transmitted to the mixed layer indirectly through mechanical stirring by ice keels. However, this mechanism does not explain the deep remnant mixed layer which is observed in density profiles. This layer is generated by convection of highly saline water formed when brine is expelled from the ice lattice during the freezing process. Lemke and Manley (1984) incorporated both effects in a numerical model using least squares fits to AIDJEX density profiles. In the model, the convective overturning provided twice the energy generated from keel stirring during the winter season. The loss of salt from the sea ice reduces the ice salinity to 8-10 ‰ during the early stages of growth. Multi-year ice floes which have undergone several melting and refreezing cycles have a salinity of less than 4 ‰. During the summer season, the upper mixed layer traps most of the incoming shortwave radiation, accelerating the ice-melt process. The lowest surface salinities are found on shelves and coastal regions where considerable ice melt-back can occur (Coachman and Aagaard, 1974). To calculate a mass and salt budget for the Arctic basin we require details of the transports through both Fram and Bering Straits. A value of 7.1 Sv, calculated from current meter records, (Aagaard and Griesman, 1975) is considered representative of the flow for both the East Greenland and West Spitzbergen currents, with about equal parts in the barotropic and baroclinic flow fields. As no change in sea-level is occurring at the present time, it is assumed that the remaining exchanges through the Bering Strait, the Canadian archipelago, the river inflow and the excess precipitation, must be in rough balance. Also, when we consider the salt/freshwater budget we find that the effects of river-runoff and precipitation are counterbalanced by low salinity water exiting the basin in the form of pack ice in the East Greenland Current.

It has been suggested that any longterm reduction in the Soviet river input to the Arctic basin

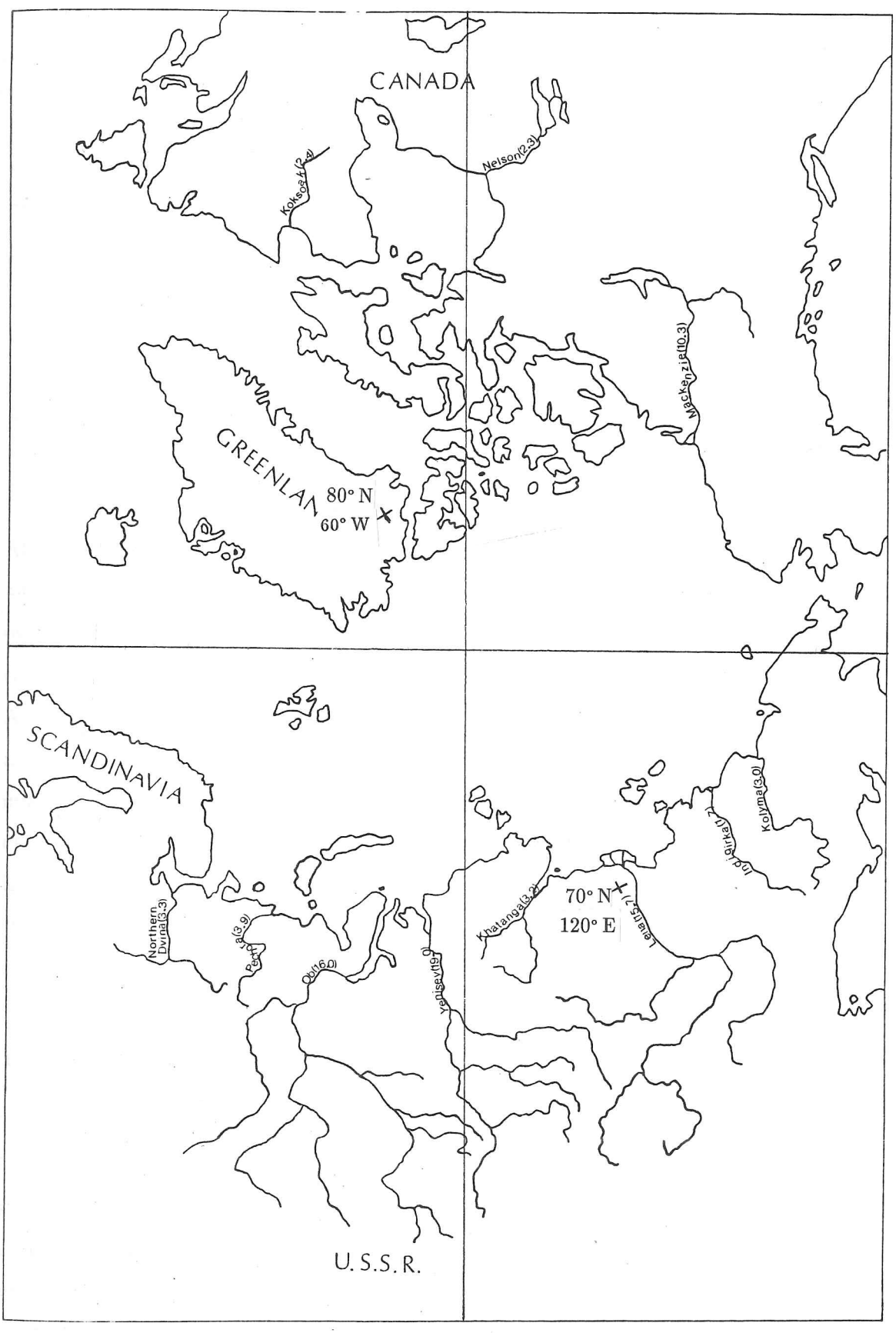

FIGURE 1.6: Positions of the 12 major river sources which provide 77 % of the total riverine flux to Arctic ocean basin. Fluxes shown are in units of 10^4 m^3 s^{-1}.

could alter the ice-freshwater balance and ultimately lead to a decrease in Arctic ice cover (Aagaard and Coachman, 1975). Note, however, that the current sharpness of the pycnocline does owe some of its strength to the lower salinity inflow through the Bering strait (Steigbrant, 1981). In a sensitivity test of Semtner's (1976a) Arctic Ocean model (including the ice cover's effect on the ocean) to proposed USSR river diversions (Micklin, 1981), little change was predicted in ice edge position (Semtner, 1984b). The principal alteration in the model results caused by the change in freshwater influx, was a reduction of salinity gradients at river mouths along with appropriate compensation by the localized ocean velocity field.

1.4.2 Southern Ocean

Although the salt/freshwater budget of Antarctic waters is of equal importance to that in the Arctic, much less is known about the sources and sinks of freshwater. The existence of a sea ice cover over the Southern Ocean further complicates matters as it transports a salt deficit away from the coasts. Loss of glacial ice is not well documented at many locations along the Antarctic coastline. An estimate of yearly mass loss from the glaciers and ice-shelves on Antarctica has been given as $1 - 3 \times 10^{15}$ kg (Orheim, 1984). Also, freshwater stored within the calved icebergs does not usually melt and introduce its salt deficit to the ocean close to the coastal source. A detailed survey of the oceanographic conditions adjacent to and under the Ross ice shelf have estimated the glacial ice loss, using the O^{18} fraction, to be equivalent to 6.3×10^4 m^3 s^{-1} of freshwater inflow (Jacobs, 1984). 35% of this inflow is in the form of basal melting, the remaining percentage from iceberg calving.

1.5 Ice Dynamics

The wind stress is the major external forcing term in the momentum equation governing ice dynamics and its direct effect on the ice pack is visible in several ways. A change in wind direction and strength can alter the location of the ice margin. This occurs if the outward transport of ice from the central pack is not in balance with the decay processes in the edge zone (Pease, 1980). Within the pack, deformation processes allow leads to increase ice decay during spring, and enhance ice growth during winter. There is also considerable deformation of ice close to coasts which has implications for both navigation and exploitation of resources in the polar regions. The transport of ice increases

the ice thickness to more than its normal equilibrium value for certain regions, whilst in counter-balance thinner ice remains in adjacent areas. This transport thereby instigates a redistribution of stored heat within the ice pack.

The dynamics of the ice pack are described using the momentum equation:

$$m\frac{\partial u}{\partial t} = -m\boldsymbol{u}.\nabla\boldsymbol{u} + \boldsymbol{\tau}_a + \boldsymbol{\tau}_w + m\boldsymbol{k} \times f\boldsymbol{u} + \boldsymbol{F} - mg\nabla H \tag{1.6}$$

As in other branches of fluid dynamics, the contribution to the balance from the acceleration and advection terms is considered negligible alongside the external forcing terms. Therefore, in central pack ice regions the resulting force balance which determines the ice velocity vector $\boldsymbol{u}$ is between the air and water stresses ($\boldsymbol{\tau}_a, \boldsymbol{\tau}_w$), Coriolis force, (f is the Coriolis parameter) sea surface slope (∇H) and an additional feature, peculiar to ice-covered areas, known as the internal deformation stress (**F**), (Figure 1.7).

The air and water stresses can be expressed in quadratic form by :-

$$\begin{aligned} \boldsymbol{\tau}_a &= \rho_a C_D \mid \mathbf{U}_g \mid \mathbf{U}_g \\ \boldsymbol{\tau}_w &= \rho_w C_w \mid (\mathbf{u} - \mathbf{U}_w) \mid (\mathbf{u} - \mathbf{U}_w) \end{aligned} \tag{1.7}$$

The air and water stresses are functions of the geostrophic winds ($\mathbf{U}_g$) and the relative ice-water velocity, ($\mathbf{u} - \mathbf{U}_w$) respectively. We also specify drag coefficients (C_D, C_w) which in turn can be a function of the velocity term. Other forms may be used to parameterize the stress terms, most commonly a relationship derived using the complete velocity profile in the appropriate boundary layer (Gaskill *et al*, 1980). In numerical models a linear form for the water stress will minimize non-linearities in the ice momentum equation.

A well-defined oceanic boundary layer beneath the ice was present during the AIDJEX pilot study measurements made in 1972 (McPhee and Smith, 1976), and a detailed data set of velocity and density measurements was collected. This data set has since been used extensively for comparative analysis with boundary layer theory. McPhee (1982) examined a hierarchy of boundary layer models ranging from Ekman constant stress type, through two-layer models with the length scale governed by the surface roughness z_o, to Rossby similarity models with length scale given by u_*/f where u_* is the friction velocity. McPhee then sought the best theoretical match for the AIDJEX observations.

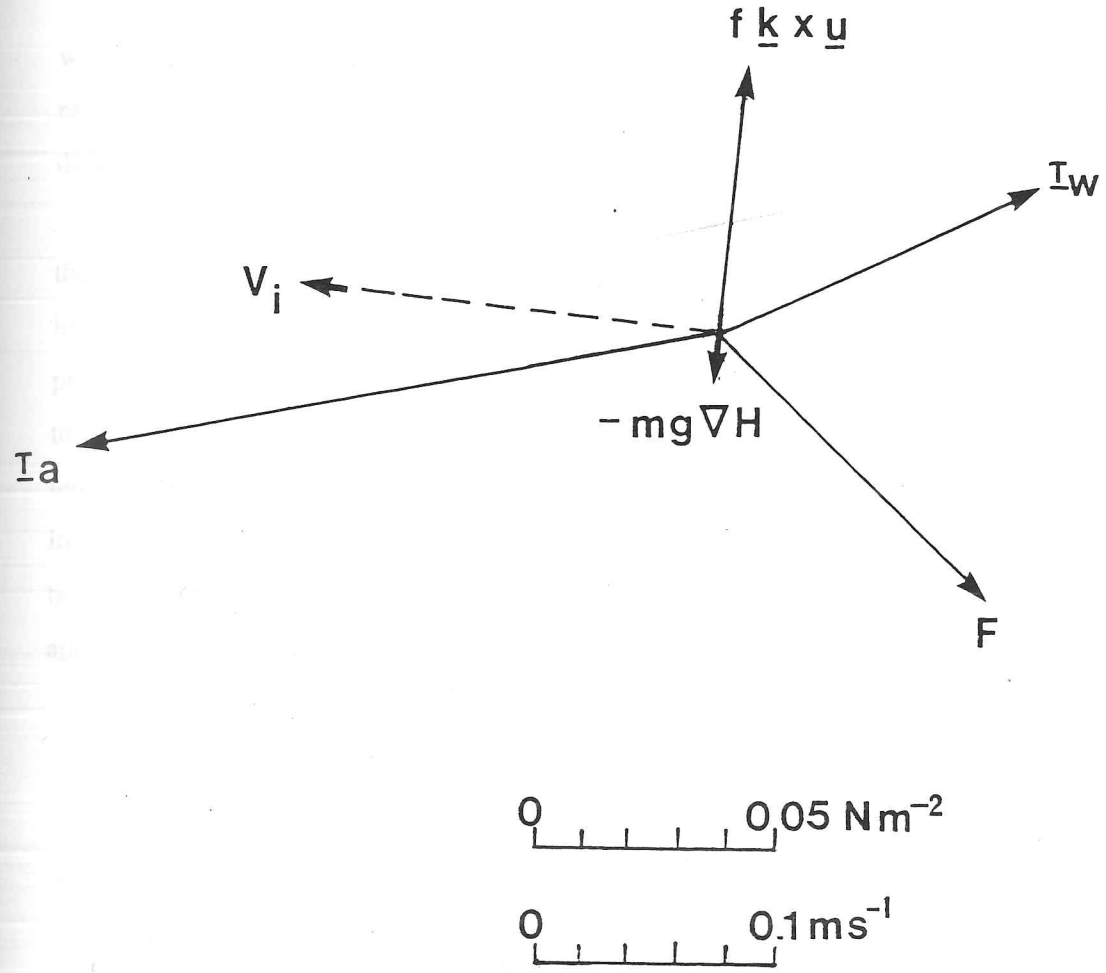

FIGURE 1.7: Diagram of terms in the momentum equation 1.6 showing the relative magnitudes and directions of each of the stresses acting on a typical interior ice floe.

The internal ice stress is modelled using an ice rheology whose ice properties are described in terms of a two dimensional continuum. This rheology varies as a function of the ice strength (tensile and compressive) and thickness. The two-dimensional stress tensor used in recent modelling projects (Hibler, 1979; Bratchie, 1984) is normally described in terms of the strain rate tensor. It is given by

$$\sigma_{ij} = 2\eta\dot{\epsilon}_{ij} + [(\mu - \eta)\dot{\epsilon}_{kk} - P]\delta_{ij} \tag{1.8}$$

where the non-linear bulk (μ) and shear (η) viscosities are functions of the invariants of the strain rate tensor $\dot{\epsilon}_{ij}$, and P is a pressure term (Hibler, 1979). The internal stress vector is obtained by differentiating the stress tensor σ_{ij} with respect to space co-ordinates.

The need to invoke such a complex form for the stress/strain relationship has arisen because the simpler Newtonian viscous constitutive law is unable to resist convergence. This is particularly important when considering ice pack close to coasts and in other highly deformed areas. These problems can be overcome by adopting viscous-plastic rheologies, where the stress state is defined to be within a fixed yield curve which allows the ice to resist compressive loads but to be of low tensile strength. In choosing a representation of the internal stress which will be suitable for use in the marginal ice zone, we have to consider that the ice-ice interaction is dominated here by the bumping of floes which rectifies the predicted ice motion. However, plastic type rheologies still appear to be relevant to Marginal zone conditions particularly during on-ice winds.

2

OCEAN PROCESSES IN MARGINAL ICE ZONE REGIONS

2.1 Definition and location of Marginal Ice Zones

The Marginal Ice Zone (MIZ) is defined in this thesis as the region on either side of the ice edge where ice cover and open ocean interact. Throughout the ice growth/decay period marginal ice zones trace out an area designated as the seasonal sea ice zone (SSIZ); the ice in the region between the winter maximum and summer minimum ice extents (shown in Figure 1.1 and Figure 1.2 for the Arctic and Antarctic, respectively). As a result of this concurrence some authors use the terms MIZ and SSIZ interchangably.

In some sub-Arctic regions a winter sea ice cover is generated within one season. For example, in the Baltic and Bering seas, new ice grows in the north and is advected south by the wind. In other regions such as the East Greenland Current the ice is predominantly of multi-year type (Wadhams, 1981), and is advected from the Arctic basin through Fram Strait. During summer, ice melts within the central basin thereby creating open water areas, especially on the Siberian shelf and in the Chukchi and Beaufort seas. These melt back regimes also conform to marginal ice zone conditions (Paquette and Bourke, 1981). Most of the ice around the Antarctic continent is first year ice though some perennial ice is found in the Bellinghausen, Ross and Weddell seas as well as close to the coast. In the austral summer, only a fifth of the ocean area that is ice covered in mid-winter still contains sea ice with concentrations rarely greater than 85%. Consequently, the greatest variability

of sea ice, areal coverage is found in the Southern Ocean.

As noted in Chapter 1, sea ice extent is an indicator of climate change. Hence, the monitoring of marginal ice zone processes and their interannual variability is an important aspect of the global climate problem. Physical features related to the oceanography of the marginal ice zone will be examined in detail in this chapter.

2.2 Oceanographic conditions associated with ice growth in the SSIZ

During autumn, in the shelf sea areas (less than 100m in depth) of the Arctic basin and its peripheral seas, the summer stratification breaks down due to mixing of the water column by storms, and the water becomes homogeneous in both temperature and salinity. Surface cooling is caused by a net negative radiation budget alongside an increase in heat loss due to sensible and latent heat transfer to the atmosphere. As the surface waters cool, they become more dense as the maximum density of saline water (>24.7 ‰) is below the freezing point (cf. fresh water), thence convective overturning will occur. In shallow regions, the water column is already homogeneous from the mixing induced by wind/tidal effects, and in this case the whole water column cools simultaneously so that it is at or close to freezing when new ice grows.

However, stratification is maintained beneath new ice in the deeper ocean (Greenland Sea, Antarctica) for the convection process is halted at a level where neutral stability is attained. For example, the mixed layer beneath the winter Antarctic pack ice in the Scotia Sea has a depth of 75 m. The surface salinity is reduced to 33.8 ‰ and the temperature is at ambient freezing point for these conditions (Georgi and Piola, 1981). In the Bering Sea, all but 3% of the ice cover is formed around northern sheltered coasts (Niebauer, 1981) and is advected southwest at approximately 25 cm s^{-1} by the wind (Pease, 1980). An ice cover of thickness > 0.5 m over a 600 km wide shelf may be replaced several times during the ice season (Pease, 1980). This transport of the ice opens up polynyas 20 – 40 km in width adjacent to the coast (McNutt, 1981; Pease *et al*, 1985).

The advance of new ice growth in the Southern Ocean lags the position where atmospheric conditions would suggest that it was sufficiently cool to initiate freezing. This is due to the magnitude of the upwelling heat flux from the deep ocean. Rapid rates of ice advance and slower ice retreat are closely linked to the position of intense low pressure systems such as those found in the Weddell sea (Zwally *et al*, 1983). Transport of ice away from the Antarctic coasts often occurs, opening up

polynyas where the considerable temperature contrast and the katabatic winds from the Antarctic continent initiates rapid refreezing.

Pease (1985) examined the thermodynamic balance and wind-driven advection occurring in a coastal polynya area for a range of air temperatures and wind speeds. Brine released during freezing has a significant effect on the density of the ocean underlying polynya regions, with salinity increases of 2.5 ‰ recorded (Schumacher *et al*, 1983). Also, the horizontal density gradients set up by this rejection of brine are considerable, creating close to the St Lawrence Island polynya in the Bering Sea, for example, an off-shore pressure term which is balanced by a geostrophic flow (Schumacher *et al*, 1983).

2.3 Frontal regions in polar waters

An ocean front is a sharp transition zone between water masses with different densities. In cross-section the considerable isopycnal gradients indicate that the lighter water mass flows over the denser fluid. The along front flow is normally in geostrophic balance with the across-front pressure gradient.

A front conforming to the above definition is found at the ice edge, separating buoyant cool meltwater from local ambient ocean conditions. The position of oceanic fronts governs the local heat fluxes into the polar oceans. For example, in the Greenland Sea, the ice-covered region is normally coincident with the region of cold water outflow from the Arctic basin. This cool water mass is separated at all depths from the warmer Atlantic water mass (section 1.3.1) by the Polar front (Carmack and Aagaard, 1973).

During the summer season the surface signature of the Greenland Sea sector of the Polar front is represented by a boundary separating the low salinity, shallow (< 5 m) meltwater layer from the Atlantic surface waters. Highly stable stratified oceanic conditions exist on one side of the front suppressing vertical mixing, and preventing turbulent transfer of heat from lower ocean layers to the ice. When ice crosses the front and melts, an even lighter water mass is introduced cutting off the supply of heat which originally caused the ice to decay. When the ice cover is in motion, the interfacial stress between the ice and the ocean may be sufficient to mix this very shallow upper layer and to re-introduce vertical heat transfer to the ice.

Parts of the Bering and Barents Seas, where meltwater fronts are formed in spring, often evolve

into summer frontal regions (Figure 2.1), as the mixing dynamics of both frontal structures are closely related to the local bottom topography (Kinder and Schumacher, 1981a; Johannessen and Foster, 1978; Niebauer and Alexander, 1985). The initial stratification introduced by meltwater buoyancy is increased by insolation. Indeed, by the time mid-summer is reached the thermal properties of the front dominate the density field, while the direction of the vertical and horizontal salinity gradients have changed sign.

2.3.1 The ocean front associated with an advancing ice edge above shelf seas

The homogeneous water column formed during autumn on the Bering sea shelf is stratified into two distinct layers by the input of buoyant meltwater as the pack ice traverses the shelf. An inner front in the lower part of the water column separates the two-layer system from the homogeneous water column of the shallower shelf. This front represents the dividing mark between the tidally and wind-mixed homogeneous area, and the stratified area where the available turbulent energy is insufficient to mix the complete water column. From energy arguments this frontal location is determined from bottom topography and the amplitude of the local tidal currents (Kinder and Schumacher, 1981b; Simpson *et al*, 1978). After winter storms, sufficient energy may be introduced into the ocean to break down the stratification, thereby increasing heat flow to the ice.

The advancing ice edge cools the water ahead by the introduction of fresh, but cold, meltwater which mixes vertically with the ambient water mass. The ice advances across the front, introducing fresh water which sharpens the horizontal density gradient. Eventually, the upper layer has sufficiently cooled to prevent further melting (McPhee, 1983). Although, the frontal advance lags the ice edge advance, there is a close feedback relationship between the two locations. However, buoyancy input to the upper stratified layer generally occurs at the ice edge as discrete amounts of ice melt, rather than through regular cyclical input (cf. diurnal and seasonal insolation). Both northerly and southerly winds act to increase ice decay. Northerly winds advect ice across the ocean fronts into warm water for melting, whilst the southern winds introduce warmer air to the atmospheric boundary layer above the ice. Frequent storms slow the advance of the ice across the shelf as the accompanying change in atmospheric frontal patterns allows warmer air into the region.

An increase in bottom slope close to the equilibrium position of summer fronts was noted by Kinder and Coachman (1978), and examination of the winter data shows the lower front also occurs close to gradients in bottom topography (Muench and Schumacher, 1985). The tidally-induced

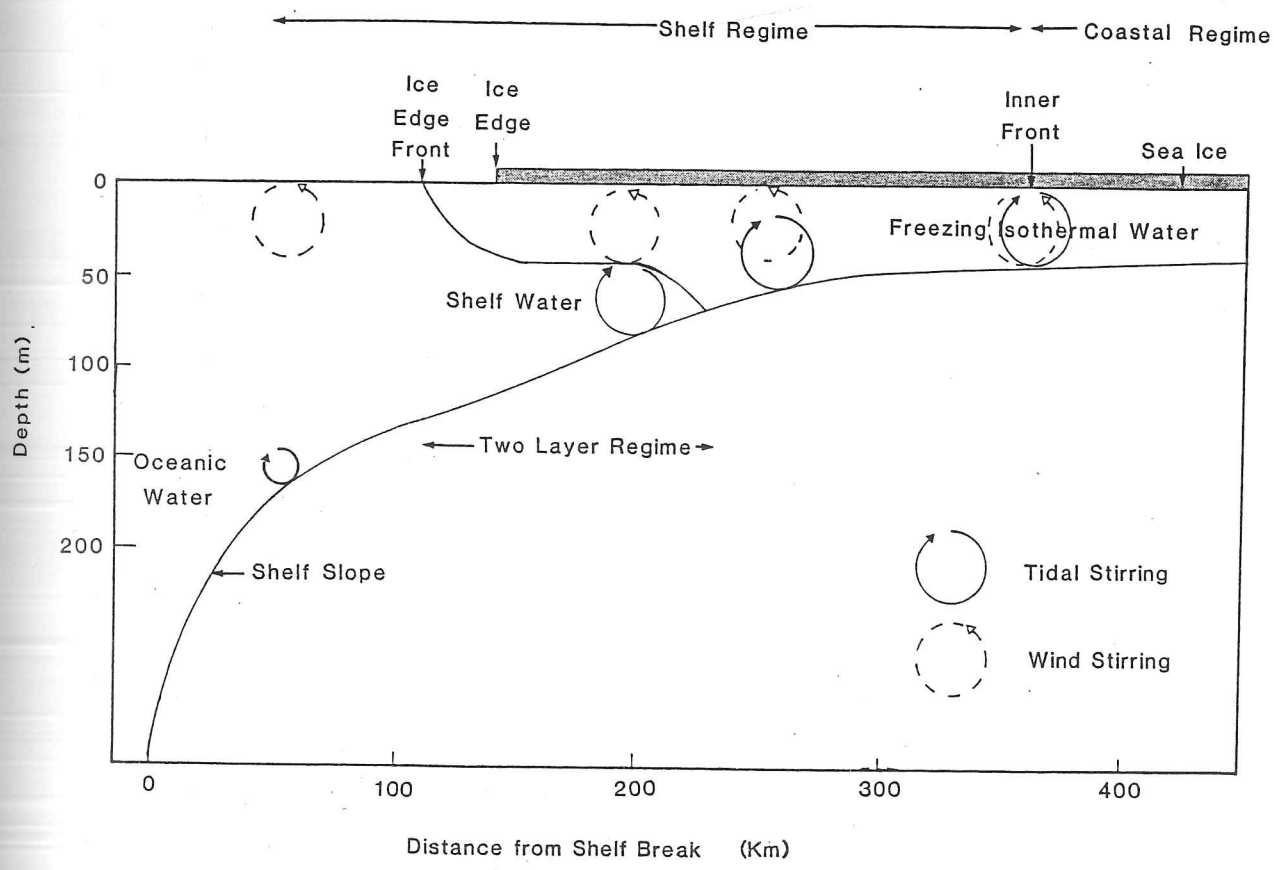

FIGURE 2.1: Schematic of processes involved in formation of ice edge, shelf sea front (adapted from Coachman and Walsh, 1981).

inner front is normally found close to the 50 m isobath (Kinder and Schumacher, 1981a). The outer surface front, however, is entirely independent of topography, and its position is governed only by the ice cover which provides the buoyancy source. Due to its greater inertia the ocean reacts more slowly to changes in the wind forcing. Hence CTD observations of the frontal structure can be made after heavy pack ice has advected 100 km north by southern winds (Muench, 1983).

The density difference between the upper and lower layers of such a frontal region is of the order of 0.4 σ_t units, with a maximum density difference of 0.8 σ_t units occurring at the head of the flow where the interface breaks the surface. The horizontal gradients ($10^{-4}\,^{\circ}\mathrm{C\,m^{-1}}$ and $2\times10^{-5}\,‰\,\mathrm{m^{-1}}$) associated with the ice edge front produces a baroclinic flow of $5-6\,\mathrm{cm\,s^{-1}}$, parallel to the ice edge. No similar baroclinic flow is generated by the summer fronts within the Bering Sea middle shelf regime, which has been characterized by Kinder and Schumacher (1981b) as a region of low ($2\,\mathrm{cm\,s^{-1}}$) mean currents.

Ice advection southward is normally limited to the Bering Sea shelf region and halts at the shelf break. The deeper, warmer slope waters would have to cool significantly for an ice cover to persist for any duration at this location. An along-shelf baroclinic slope current (Kinder and Coachman, 1978) plays a significant role in controlling the ice edge position as it governs the on-shelf heat flux (Hendricks *et al*, 1985). This current tranports a warm core of $3-4^{\circ}$ C water which enters the Bering sea through the Aleutian passes, and travels north-westward aligned with the shelf break. The timing of maximum ice extent is also limited by the increase in shortwave radiation which occurs after the spring equinox.

2.3.2 Ocean fronts formed during ice retreat

In the spring, the north/north-easterly flow which has dominated the advection of the winter Bering Sea ice cover reverses due to a repositioning of the Aleutian low pressure system. The impact of this change to more variable wind conditions is to introduce warmer air above the ice cover which initiates rapid ice decay. Mean May temperatures range from -2° C to $+2^{\circ}$ C for the central part of the Bering shelf (Brower *et al*, 1977). Satellite observations show that the thinnest ice, recently advected from the ice production areas, is the first to melt, opening up the pack adjacent to the coast (McNutt, 1981) and also re-opening recently frozen leads.

An ice retreat of 200 km during an 11 day period was recorded in Spring 1982 with ice velocities ranging from $8-38\,\mathrm{cm\,s^{-1}}$ (Niebauer and Alexander, 1985). This period of ice retreat was

confirmed by data from Argos buoys and was encountered over an extensive part of the Bering Sea region (Reynolds and Pease, 1984).

Examination of profiles obtained during the melt season (Niebauer and Alexander, 1985) shows that the lower front is associated with the 80 m isobath during ice retreat. However, the form of the stratified region during melt-back is inverted, with the intersection of the density interface with the bed being positioned well seaward of the point where the interface breaks the surface (Paquette and Bourke, 1981; Niebauer and Alexander, 1985). During ice retreat, pools of low salinity water are frequently separated from the main meltwater section, probably during upwelling of the pycnocline. The upwelling may be generated either by an ice edge mechanism (section 2.4) or when bottom tidal mixing is of insufficient magnitude to mix the stratified column (Niebauer and Alexander, 1985).

The ice retreat phase on the broad Arctic basin shelves occurs some months later than in the peripheral seas with minimum ice extent being reached by September. Similar ocean frontal regions develop here, however, with a particular case being the ice edge region in the Chuckhi sea, where the now warm inflow from the Bering Strait interacts with the ice cover. The earliest signature of this warm core of water is the creation of shore leads along the Alaskan coasts (Garrison and Pence, 1973). Along the Chuckhi ice edge the retreat phase occurs at different rates. The coincident positions of the ice embayments so formed each year (MIZPAC 1971-8) suggested that the warm core current splits, and is preferentially steered by the local bathymetry to these locations (Graham, 1978; Paquette and Bourke, 1981)

At this ice edge, ocean fronts are located in both the upper and lower layers, separating the inflowing water mass (6 – 10° C) from the local near freezing waters. The upper front is adjacent to the ice edge, though not necessarily coincident as ice advection by the wind occurs on rapid time scales. The lower front where the density interface intersects the bottom has a more complex form. If it is close to an ice peninsula then the water column is normally stagnant and the minimal vertical shear creates a front which is almost vertical (Paquette and Bourke, 1981). Such conditions reduce the rate of retreat of the ice edge. Other frontal configurations have been recorded where the inner and outer fronts are spaced more than 40 km apart, with the lower front being some distance in advance of the ice edge. These frontal zones are normally close to stronger current shears, where rapid ice melting and retreat occur (Paquette and Bourke, 1981).

2.3.3 Interaction of ice cover with fronts in Southern ocean

In section 1.3.1 we outlined the three main frontal features found in the Southern ocean surrounding the Antarctic continent. Very few meridional sections have been carried out during the winter season here due to the difficulties of operating in heavy pack ice. Also, the normal operating schedule for ships is to resupply Antarctic bases in the spring when the ice breaks up. Winter oceanographic conditions are receiving increasing interest and several expeditions, particularly to the Weddell sea area, have recently been undertaken (Augstein, 1987). The analysis of these data is in progress. Besides the major frontal features which delineate significant water mass changes, other frontal features have been identified; in particular, those associated with topographic structures and features where two flow regimes meet, e.g., the Weddell-Scotia confluence. In winter, the ice cover extends to between $55 - 60°$ S, overlying the Antarctic polar front. Hence, interactions will occur between the ice cover and the polar frontal zone which separates waters of Antarctic and sub-Antarctic origin.

The waters to the south of the polar front are observed in spring to be characterized by a temperature minimum layer ($-1°$ C) at $100 - 200$ m. This water is overlain by surface waters where insolation has increased the temperature to $0 - 2°$ C. Beneath the temperature minimum layer at depths of $250 - 300$ m is a warmer water mass ($> 1°$ C). A similar vertical temperature profile exists in most of the South Atlantic sector XBT data, until the continental slope is reached (Bersch *et al*, 1984). At the slope other fronts may exist, either due to the presence of trapped prototype bottom water (section 1.1), to the existance of fresh glacial meltwater (MacAyeal, 1984), or to shelf slope dynamics.

There is a change between winter and summer seasons in the frontal structure in all the major oceanic features (Sub-tropical convergence, sub-Antarctic front, Antarctic polar front), with the near vertical front found in winter changing to a layered summer structure in the space of two months (Lutjeharms and Foldvik, 1986; Lutjeharms and McQuaid, 1986). In summer, the surface manifestations of the front are normally located to the south of the sub-surface feature. Examination of the Sub-tropical convergence shows that the warm surface water also carries a distinctive salinity signal. This suggests that the formation of this water mass is not the result of local insolation processes, which might have been suggested from the temperature records alone. It is more likely to have arisen from transport across the front possibly caused by eddies generated within the Antarctic Circumpolar Current.

2.4 Upwelling at ice edges

A stationary ice edge will act like a coast. Thus, under certain wind conditions upwelling or downwelling can occur, forced by a discontinuity in the curl of the wind stress across an idealized ice margin. Upwelled water transports nutrients to the surface with the result that primary productivity is enhanced. This increased productivity attracts commercial fisheries to ice edge regions. The generation of an upwelling signature in the pycnocline close to an ice edge was first modelled by Gammelsrød *et al* (1975) who assumed the ice cover was fixed in the horizontal plane.

The Bering sea ice edge is a site where one would theoretically expect upwelling to occur, as consistent winds are generated along the ice edge by the passage of low pressure systems (Overland and Pease, 1982). As the ice retreats in spring, upwelling of the density surfaces has been recorded in the hydrographic data collected in the exposed area (Alexander and Niebauer, 1981; Niebauer and Alexander, 1985). The period of ice retreat is coincident with the biological spring bloom, and the freshwater introduced by the melting ice increases the stratification and hence, the intensity of the spring bloom in surface waters. A core or pool of water with high nutrient content is often observed (Iverson *et al*, 1979; Niebauer and Alexander, 1985), and in general the nutrient and chlorophyll sections across the shelf are concurrent with the density sections.

The upwelling is caused by a sharp change in the wind stress, generated by the presence of a compact ice edge. This wind stress drives an off-ice transport in the water column leading to divergence. Unlike the coastal analogy, the divergent ocean circulation occurs on both sides of the ice edge within the baroclinic radius of deformation. However, the same volume of upwelled water is generated in both coastal and ice edge situations for a given wind stress, as only half the pycnocline deviation occurs in the two sided case (Clarke 1978). The horizontal scale of the vertical pycnocline displacement may be altered if the ice concentration distribution plays an active role in the upwelling process. If the ice-covered area gradually merges into open water, the width of the upwelled zone is determined by the gradient of ice concentration. If the ice is in motion whilst upwelling conditions are favoured, a weakened deviation of the pycnocline is experienced on a scale governed by the distance the ice has been advected. This movement of the ice cover changes the way in which the wind stress is transmitted to the ocean. How this alters the upwelling response will be described later in this section.

During the geostrophic adjustment necessitated by changes introduced by the upwelling process,

a strong ice edge jet may develop in the ocean ($10 - 20\,\mathrm{cm\,s^{-1}}$ in amplitude); an associated jet is driven in the ice. This ice jet is of greater magnitude than the upper ocean currents (Johannessen *et al*, 1983), and accelerates the floes in the edge zone relative to the interior pack. The ice jet may interact with the ocean to increase upwelling after the wind forcing has relaxed (Røed and O'Brien, 1983). The jet creates a shear zone at the ice edge which may be baroclinically unstable (Hakkinen 1984).

Although from theoretical considerations, one would expect to find clear and frequent signatures of ice edge upwelling in field data, this is not the case in practice. We find that an along-ice wind ($> 5\,\mathrm{m\,s^{-1}}$) blowing for 36 hours is insufficient to cause an upwelling event (Alexander and Niebauer, 1981). Other observations of pycnocline deviation are not linked to coincident wind events, and may have been caused by storms occurring before the hydrographic survey was undertaken (Buckley *et al*, 1979). The Rossby radius of deformation for the Bering Sea density structure (Alexander and Niebauer, 1981) is $3 - 4\,\mathrm{km}$, and is smaller than the region where there is evidence of pycnocline changes. This is probably caused by ice advection across the water column which is already deformed by the wind stress. The lack of synoptic measurements within the hydrographic section hampers the precise definition of the upwelled region.

Niebauer (1982) addressed the problem of the upwelling signature generated on the Bering Sea shelf using a two-dimensional ocean model. The ice cover was included as a stationary rigid lid, and the wind stress was confined to the open ocean with no variation considered along the ice edge. The linearly stratified ocean was forced by a wind stress of $0.1\,\mathrm{N\,m^{-2}}$ and then relaxed. An on-ice wind produced least vertical displacement, as the circulation was confined to the upper layer. This is because the flow induced by the wind field is opposed by off-ice Ekman transport. An attempt was made to simulate melting conditions by superimposing a shallow front on the oceanic density field. This caused intensification of the along edge jet, though the lighter water overwhelms the density anomaly introduced by the upwelling event.

A second location frequently cited for ice edge upwelling is the ice edge north of Svalbard during the summer months when ice extent is at a minimum. Field investigations in this area have revealed deviations of the pycnocline in hydrographic sections (Buckley *et al*, 1979; Johannessen *et al*, 1983). A north-south section across the edge (Figure 2.2) showed water upwelled from a source at 150 m depth, bounded by two density fronts, one located at the ice edge, the other 12 km further south (Buckley *et al*, 1979). The width of the upwelling feature again suggested ice edge

movement.

An upwelling of the pycnocline of 3 – 6 m was also observed at an ice edge location close to the Buckley *et al* site during the NORSEX study (Johannessen *et al*, 1983). This latter upwelling event was weaker than theory (Gammelsrød *et al*, 1975; and Clarke, 1978) has suggested, and the wind was in the opposite direction relative to the ice. The relative ice-water velocity was monitored during the experiment. Since this proved to be non-zero, one of the basic model assumptions used by Gammelsrød *et al*, and Clarke and Niebauer is not satisfied. Therefore, the model proposed by Røed and O'Brien (1983), which considered cross-edge ice velocity proved a better match for the NORSEX CTD upwelling sections, and confirmed the reversal in sign of the upwelling signature under these wind conditions. Johannessen *et al* (1983) proposed that an alternative mechanism for the upwelling seen in earlier data (Buckley *et al*, 1979) could be the increase in wind stress over the open water caused by the unstable atmospheric boundary layer generated during off-ice winds (Reynolds, 1984). Note however, that some of the upwelling signatures seen in the NORSEX data arose from eddy dynamics (section 2.6), therefore care should be taken in defining the dynamics of isolated ice edge sections without some knowledge (possibly remotely sensed) of the synoptic field.

Røed and O'Brien (1983) used a coupled ice-ocean model to investigate the interactions occurring with a mobile ice edge under a number of external forcing conditions. The essential requirement for the formation of a strong upwelling event is a sharp ice edge. The upwelling drives a divergence in the ocean which diffuses the ice, requiring the sharp ice boundary to be maintained by an extra mechanism: internal stress. For their sea ice model, Røed and O'Brien used an ice rheology which produced a geostrophic jet in the ice when no external forcing was imposed (Røed and O'Brien, 1981). The geostrophic balance of the sea ice was used as the initial condition for model simulations. The air-ice and ice-water stresses are parameterized in terms of drag coefficients, quadratic winds and linear relative ice-water velocities. The ocean part of the coupled model is represented by a two layer reduced gravity scheme.

Røed and O'Brien (1983) forced their model using winds which in the earlier models (Gammelsrød *et al*, 1975) had produced upwelling events. Here, the same conditions induced a weak downwelling of the pycnocline by 2 – 4 m. The same result was found when the internal stress and non-linear terms were removed from the sea ice model. The ocean beneath the ice is dominated

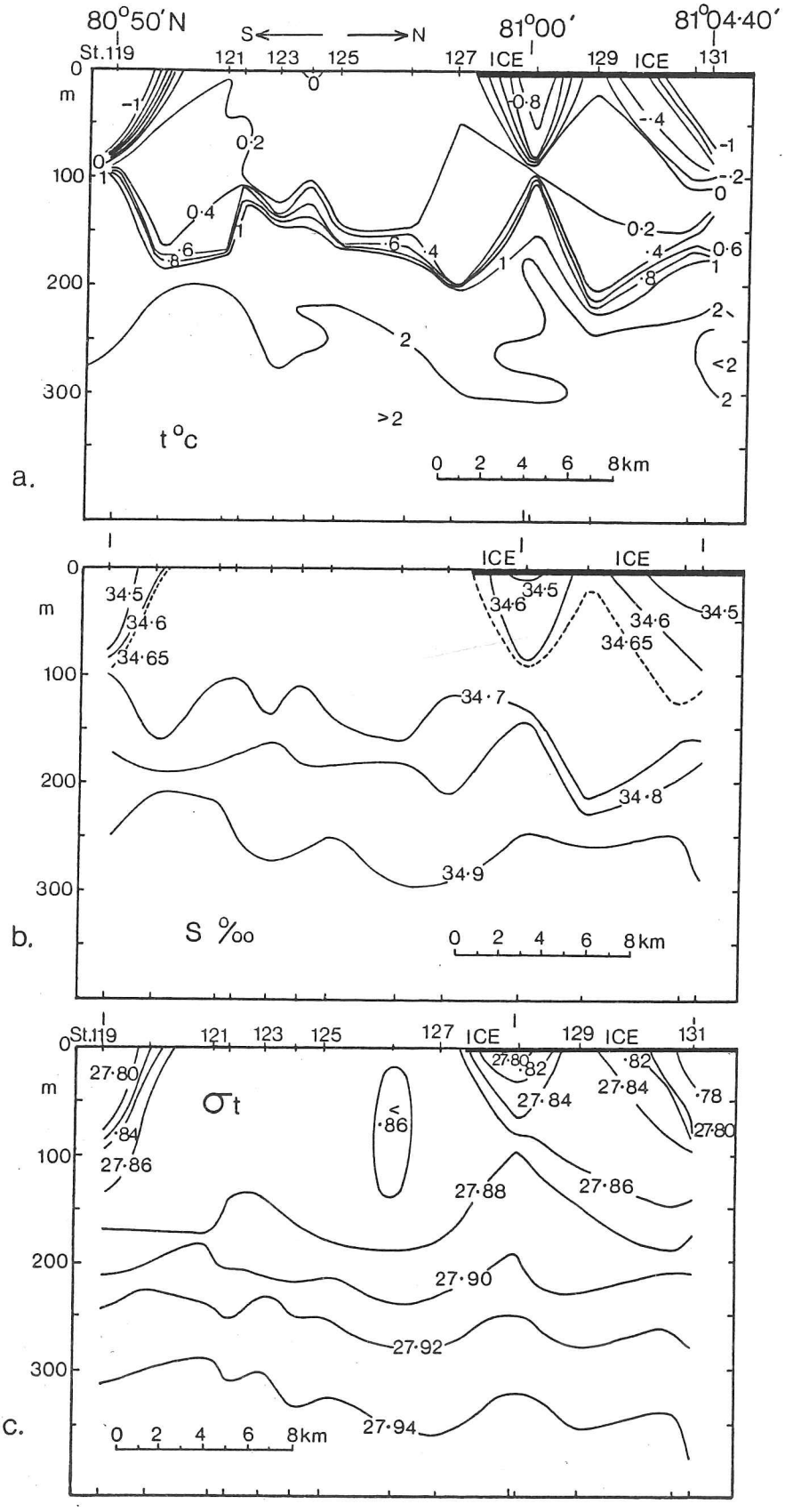

FIGURE 2.2: CTD section observed by Buckley *et al*, 1979 north of Svalbard in 1977. They attributed the changes in pycnocline depth to wind induced upwelling.

by convergent velocities which are a maximum at the ice edge and overwhelm the off-ice transport. An additional experiment was run without external forcing and a strong upwelling region was generated in the ocean, driven by the geostrophic jet in the ice (Figure 2.3). The model results, however, are sensitive to the values chosen for the drag coefficients and the interfacial stress term (Røed, 1983) with changes of 10-20% in the latter term capable of altering an upwelling response to a downwelling in an analytical model of the system.

The magnitude of the upwelling is determined by the net total Ekman transport in the complete area of model integration. The greatest volume of upwelled water is achieved when the available potential energy within the system is a maximum (Smedsted and Røed, 1985). The maximum pycnocline deviation generated, however, can be two or three times greater, with the disturbance confined to a narrower region. This represents the condition when the cross-edge ice velocity is zero, i.e., when a balance between the wind stress and interfacial stress terms is achieved (Smedsted and Røed, 1985).

An ice cover which remains stationary, though capable of transmitting momentum to the ocean via an interfacial stress, can also generate weak downwelling (Markham, 1983) under the Gammelsrød *et al* (1975) upwelling conditions. In Røed and O'Brien's (1983) model, this was only achieved when the ice cover was free to move, emphasizing that the transmission of energy by an interfacial stress is the crucial part of the process. Markham (1983) investigated upwelling circulations under both positive and negative buoyancy input conditions using an embedded mixed layer model (Adamec *et al*, 1981). The negative buoyancy input provided by the meltwater addition led to the shallowing of the mixed layer, thereby enhancing any upward vertical motion already generated by the upwelling processes. In Markham's model, winds blowing along a stationary ice edge with ice on the left initially produced a weak downwelling. This was soon replaced by an upwelling of the pycnocline, induced by a buoyancy force produced by a melt input of $10\,\mathrm{cm\,day^{-1}}$. This situation is reversed if the ice is free to move, with downwelling replacing upwelling after 42 hours of winds. For comparison, Røed and O'Brien (1983) model generated weak downwelling in this case.

If our study of the ice edge included two horizontal dimensions, variations of velocity and ice concentration in the along ice direction could be considered. Hakkinen (1984) investigations have shown that strong gradients in the ice concentration along the edge can produce upwelling and downwelling events of equal weight to those generated by changes in wind stress across an ice edge

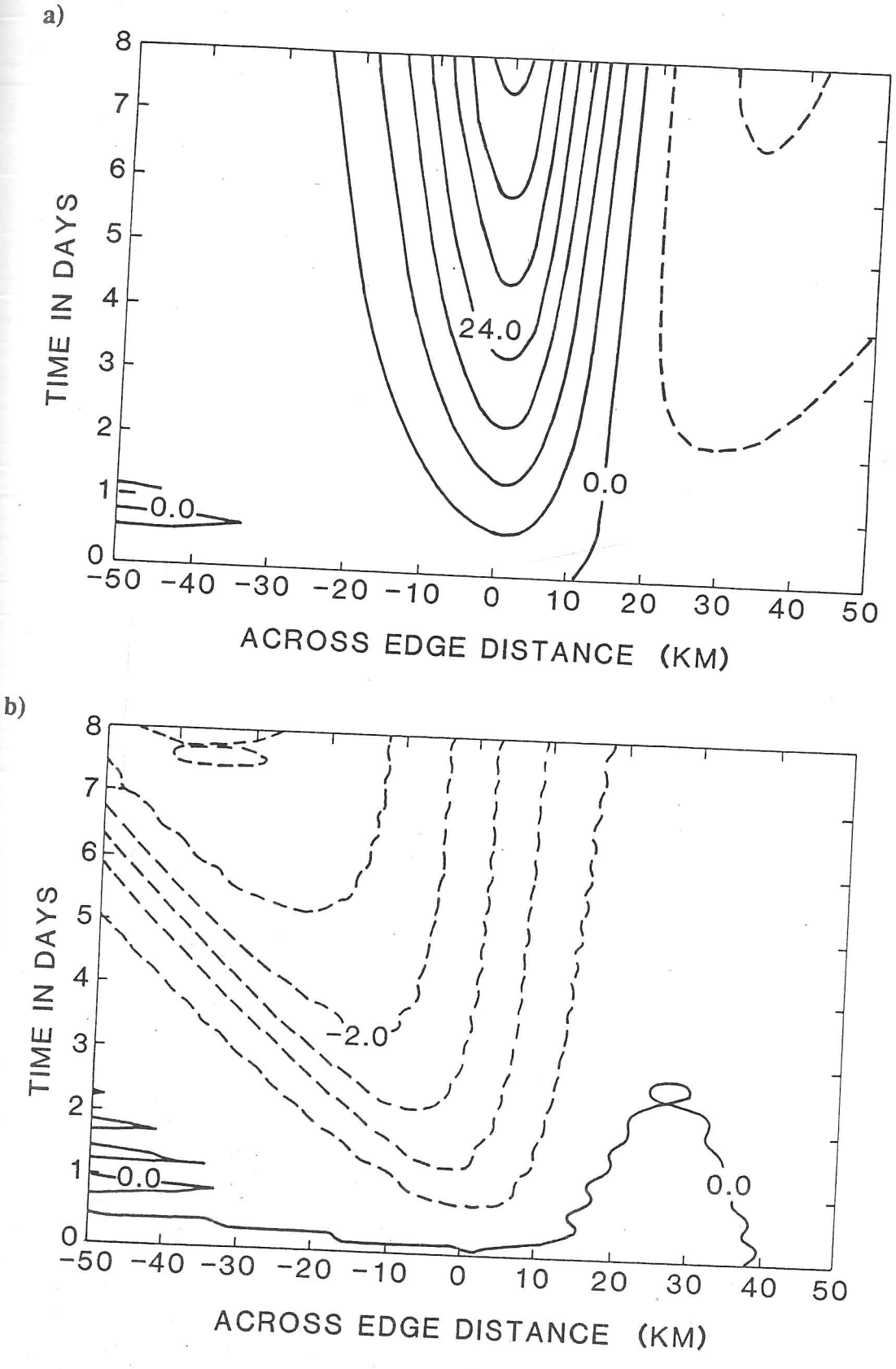

FIGURE 2.3: a) Time series of pycnocline deviation developed by Røed and O'Brien (1983) coupled ice ocean model when model is initialized with a geostrophic jet in the ice cover directed into the page. b) Results when model is forced by an along-edge wind directed out of the page.

(Hakkinen, 1984). The formation of a shallow summer pycnocline can induce changes comparable in size to pycnocline deviations induced by upwelling, necessitating consideration of non-linear dynamics (Hakkinen, 1984). The ocean structure under such conditions demonstrates rapid convergence allowing the pycnocline to break the surface forming an ocean front and strong velocity jet.

All the numerical models discussed above have suggested that the ocean pycnocline response increases linearly with time. However, an analytical model proposed by Sjøberg and Mork (1985) demonstrates that a steady state may eventually be reached if dissipation by inertial gravity waves is included.

In summary, the discontinuity in the wind stress across the ice margin forces the ocean to respond by upwelling or downwelling. An ice edge jet is formed during the geostrophic adjustment process. The presence of an active advective ice cover can alter the dynamics of the pycnocline deviation, changing a simple event into a sequence of upwelling/downwelling events as the ice itself becomes part of the external forcing.

2.5 Ice bands and streamers

Observations

The ice edge is frequently not delineated by a sharp discontinuity in concentration but is diffuse, with 100% ice coverage often not being encountered until more than 100 km from the edge (Ackley and Smith, 1983). Such conditions are particularly common during periods of off-ice winds. Satellite and ship observations show that a divergent ice pack organizes itself into distinct features, termed bands or streamers (Figure 2.4). Up to now, the principal study area for these phenomena has been at the Bering sea ice edge, where most observations have been recorded. The wind conditions there are predictably off-ice for long periods. Throughout this discussion, streamers refer to long strips of ice running parallel to the wind direction whilst bands refer to strips of ice orientated from 40° to 90° to the wind direction.

When the wind speed is low, scalloped meanders may appear along the Bering sea ice edge, though no evidence of eddy type structures have been found in measurements of the ice dynamics. Degenerate eddies, often found at ice edges (Wadhams and Squire, 1983), may be re-formed into streamers and bands by wind/wave herding mechanisms, once the floes have separated from the

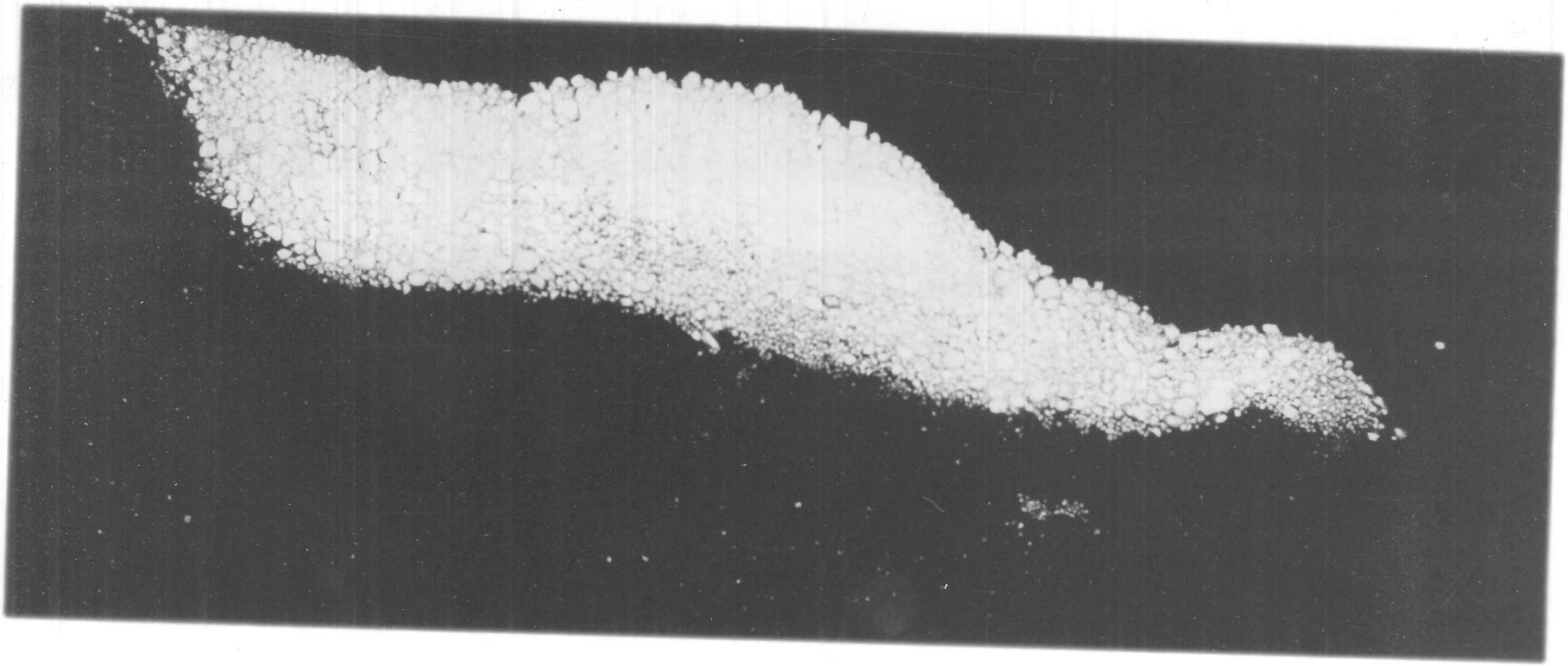

FIGURE 2.4: Aerial photograph of ice band formed at the Bering Sea ice edge (provided by S. Martin).

main pack. Banded regions of ice at the extreme ice margin, have also been reported in the Gulf of St. Lawrence (Bauer and Martin, 1980), Antarctica (in space shuttle photographs, Carsey *et al*, 1986; aerial photographs, Squire personal communication) and at the edge of the East Greenland Current (Squire *et al*, 1983).

The presence of ice edge streamers was first reported by Muench and Charnell (1977) using data collated from weather satellite photographs. They attributed the regular, 10 km spaced features to convection cells in the atmospheric boundary layer, formed during vigorous vertical heat exchange as the off-ice, cold winds interacted with the 'warmer' water. Roll cloud vortices were observed on the same satellite photographs as the streamers. These were aligned in the same direction and had similar length scales. Muench and Charnell discarded ocean convection as the forcing mechanism for the streamers, as the oceanic convection scale is smaller than 10 km. Ocean mechanisms such as wind driven Langmuir circulation cells and brine convection may cause some of the ice features observed from ships on shorter (10 m – 1 km) scales. Visual observations from ships have also shown that ice edge streamers are found to be parallel to the wind, and can be aligned with linear cloud features.

The length scale of ice bands is close to the resolution of NOAA satellite sensors. Hence despite being readily available, satellite photographs are unable to provide a record of band (as opposed to pack ice) divergence.

Observations of the relative motion of ice edge bands with respect to the main pack, were carried out during Winter 1979 from NOAA ship Surveyor (Bauer and Martin, 1980). The ice edge zone consisted of small rafted floes which represent an increase in upper and lower surface roughness compared with floes encountered further into the interior. Bauer and Martin (1980) used aerial photography to track marked floes and revealed that, after initial separation, the band moved 1 cm s^{-1} faster than the main pack. The band accelerated downwind and increased its velocity relative to the interior to 25 cm s^{-1}. The downwind edge of the band was sharpened by the action of water waves and swell whilst the upwind side was diffuse. Bauer and Martin (1980) attributed the initial separation of the bands to increased aerodynamic roughness of the ice surface in the edge zone, and its later acceleration downwind to radiation pressure from short waves generated in the fetch of the open water between the band and the main pack.

A more detailed survey of band movement was undertaken in March 1981 (Martin *et al*, 1983) by tracking transponders on floes within the band, by means of the ship's X-band radar. The band

feature showed no evidence of stretching or rotation, but after destruction of the band formation, the tracked floes diverged rapidly. During the period of the experiment the width of the band decreased due to wave erosion and lateral ablation (Wadhams *et al*, 1979) at a rate of $20\,\mathrm{m\,hr^{-1}}$. The transponder sites within the band moved 30% faster than a station in the interior of the ice pack. This is equivalent to a velocity difference of $13\,\mathrm{cm\,s^{-1}}$. The interior ice pack station also recorded wind and current data which was transmitted to shore by satellite. Using these data, Martin *et al* (1983) were able to calculate a force balance for a typical floe in the interior pack and a floe within the band (Figure 2.5). The resultant extra stress τ_R required to accelerate the band away from the pack was found to be $0.4 - 0.7\,\mathrm{N\,m^{-2}}$ in magnitude in the direction of the wind. Water stress values in this calculation were subject to some error, as the drag coefficient measured at the interior station was used for the band case after scaling for the local roughness and ice-water velocity characteristics. The radiation stress generated in the fetch opened up behind the band, assuming perfect reflection from the ice floes, was adequate to produce this extra force.

Theory

A number of oceanic mechanisms have been proposed to explain features of band formation and development and they will be discussed below.

a) Surface waves

Wadhams (1983) proposed a mechanism by which bands could be generated by the action of surface waves from a random diffuse cover containing 25-50% open water. He calculated that the fetch generated in polynyas aligned with the wind, would be sufficient to herd the floes at the downwind end into a band-type configuration. The short period wave spectrum that is generated in such an open water area transfers nearly all its energy to the ice, as the reflection is near perfect when the floe diameters are greater than half the wave length of the generated waves (Wadhams, 1973). The band's integrity is maintained by the action of open water waves on the downwind side of the band (i.e., waves coming in from seaward). This mechanism of band generation limits the width-wise growth of the band to a value, dependent on the wavelength of waves generated in the neighbouring polynya. The bands observed in the field are normally of a regular width and spacing rather than completely random. To create such a regularly spaced pattern, Wadhams (1983) proposed that narrow bands move faster than wider ones and merge with features ahead.

Although the radiation stress argument explains the forces that accelerate the band away from

Force balance for ice in band

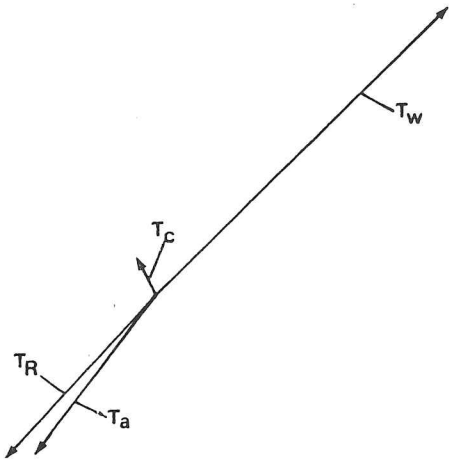

Force balance for ice in interior

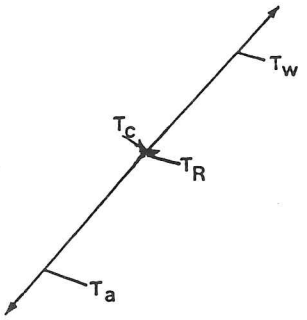

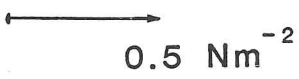

Figure 2.5: Stress balance on an ice floe in the interior pack and that on an ice floe in a band formed at the edge of the Bering Sea based on calculations given by Martin *et al*, (1983).

the ice edge, it does not adequately answer how the original divergence of the ice occurs. Field observations (Martin *et al*, 1983) suggest that when bands are forming at the edge the pack itself is diverging, with leads opening, their long axes orientated perpendicular to the wind.

b) Internal waves

The regular spacing of bands, has led to suggestions that they may be linked to internal wave phenomena (Muench *et al*, 1983; Sjøberg and Mork, 1985). Both laboratory and field data have confirmed the presence of internal waves within the pycnocline at the ice edge (Hachmeister and Muench, 1981). Data obtained from temperature probes on current meter moorings in the pycnocline possess high frequency oscillations which suggest that the probe was positioned alternatively in the upper and lower layers. These data may be aliased, however, as the sampling frequency was close to the frequency of the pycnocline motion. Internal waves can be generated under the ice cover either by the drag of ice keels (Ekman, 1905) or by the propagation of an upwelling disturbance (section 2.4). As the wave propagates under the ice cover it creates divergent regions, while an outgoing wave will collect the newly diffused ice in the convergent zones above the wave troughs. Theoretical calculations of the phase speed of the first mode interfacial waves (Turner, 1973), using stratification conditions found in the Bering and Greenland Seas, gives internal wave speed values of the order of $30\,\mathrm{cm\,s^{-1}}$. When the ice velocity is close to the wave phase speed (a resonance condition), the wavelength of the disturbance is on the same scale as the observed spacing of ice edge bands (Muench *et al*, 1983).

c) Buoyancy effects

Whilst surface wave effects undoubtedly control the structure of the band once formed, other theories have been advanced to explain the initial divergence of the ice pack. McPhee (1983) proposed that the divergence of the ice pack close to the edge is induced by changes in the boundary layer dynamics resulting from meltwater input. The additional freshwater stabilizes the upper layer, reducing both the transfer of heat and momentum across the boundary layer. The reduction in momentum transfer weakens the effective drag on the ice. Hence, when the initial ice floes cross the frontal boundary they accelerate and melt cooling the water mass behind, hence slowing down further ice advance. Countering McPhee's (1983) argument for ice divergence Josberger (1983) has suggested that for reasonable melt rates a stabilizing buoyancy flux has little effect on the turbulent transfer of momentum, heat and salt between the ice and ocean. This is because the Monin-Obukov length scale calculated for the buoyancy flux (Eqn. 5.17) under realistic melt conditions is greater

than the planetary boundary layer thickness (McPhee, 1984b; Josberger 1984).

d) Ice edge jets

Smedsted and Røed (1985) experimenting with Røed and O'Brien's (1983) coupled ice-ocean model were able to demonstrate substantial decreases in ice concentration some 20–30 km from the ice edge. In particular, when imposing the wind stress forcing which generates maximum upwelling of the pycnocline, two ice edges separated by a region of open water occurred in the ice model. The maximum cross-edge ice velocity coincided with the position of ice concentration decrease. The two ice edges formed during the generation of maximum upwelling corresponded to different parts of the ocean jet structure. The negative section of the along-edge velocity drove the outer ice edge, whilst the inner edge was formed by the positive section of the ocean jet. The phenomenon was not only found in specific cases, but was obtained over a range of oblique wind angles (Smedsted and Røed, 1985). The choice of Røed and O'Brien's ice rheology was not crucial to the phenomena as the ice concentrations involved were less than 85%.

From the above discussion on the appropriate driving mechanism for ice edge bands it appears that the initial ice divergence is dependent on the coupling of the wind and the ocean at the ice boundary. The combination of changes in stresses due to the increased roughness characteristics across the ice transition zone (Squire and Moore, 1980), and its discontinuity across the edge, generate divergence and convergence zones in the upper ocean. Subsequent interaction between the ocean and the ice causes the ice divergence. Once the ice has separated from the pack, wave radiation stress, generated in the short fetch of the opening leads, is important in accelerating the ice and the incoming sea acts to maintain the downwind integrity of the band.

2.6 Ice edge eddies

A significant proportion of the kinetic energy of the world's oceans is not contained in the mean flow, but within the turbulent mesoscale eddy field. Consequently, one would also expect ice edge regions to contain turbulent eddies capable of transferring heat across frontal boundaries and into the ice covered areas. Eddies have been observed in the Bering Sea along the shelf break (Paluszkiewicz and Niebauer, 1984), though no evidence of any interaction with the Bering Sea shelf and the accompanying ice cover has been detected. In particular, as both the Labrador and East Greenland currents (LeBlond, 1982; Wadhams and Squire, 1983) are density-driven ocean currents bounded

by strong shear zones, we might expect that eddies would be generated by baroclinic instability along their extreme edges (Griffiths and Linden, 1981) (cf. Norwegian, Californian and Scottish coastal currents). A sea ice cover can often act as a surface tracer for this oceanic phenomenon.

Instances of eddy phenomena at the edge of the Greenland sea ice pack have been observed in satellite photographs over a number of seasons and different years (Vinje, 1977). Satellite tracked buoys in the region have also been trapped within eddy features. The range of eddy scales (10 – 200 km), observed in this area suggests that not all the ice eddies are generated by the same forcing mechanism. Some of the eddies, may not represent ocean phenomena at all, but be derived from local meteorological conditions. The passage of a low pressure cyclone causes the winds to rotate and strip away the outermost part of the ice edge to form an eddy. These ice floes may melt in the warmer open water conditions or may return to the pack, thereby disturbing the normal gradation in floe characteristics which occurs across the MIZ region (Squire and Moore, 1980).

Observations of an eddy in the Denmark Strait between Iceland and Greenland suggests that it is generated when the flow of the East Greenland current is constricted as it enters the strait (Cowan and Ulbricht, 1984). This eddy has been observed in several years' satellite data, under both compact and diffuse ice conditions. The eddy, 100 – 200 km in size, on close inspection reveals an internal vortex sheet of smaller (10 km) cyclonic and anticyclonic eddies.

In the East Greenland Current region ice edge eddy activity has most frequently been detected by satellites in Fram Strait, where the ice stream first enters the Greenland Sea. The width of the current at this point, relative to the local baroclinic radius of deformation, suggests that it may be baroclinically unstable (Griffiths and Linden, 1981). However, eddies of all scales have been observed propagating down the outer edge of the ice boundary. Cloud free periods over the northern section of the East Greenland Current have revealed a large (> 50 km wide) cyclonic eddy in a similar position over many seasons, suggesting that it may represent a stationary phenomena.

Such an eddy, positioned within the polar frontal regime, could have a far reaching influence by transferring warm Atlantic water under the ice and increasing ice decay within the pack. Evidence of warm water lenses under the ice cover were observed in horizontal sound velocity profiles obtained by a submarine (Wadhams *et al*, 1979). The ice cover above the warm lens was marked by reduced ice thickness and concentration relative to the surrounding region. The water column close to this eddy feature showed evidence of small scale structure possibly caused by internal waves or double diffusive processes.

Further evidence of warm water lenses underlying a surface ice eddy configuration was obtained aboard the Swedish icebreaker YMER (Wadhams and Squire, 1983). During a two day period, the area of the eddy was surveyed by helicopter, tracked by four radar transponders, and the underlying ocean was sampled in a cross-shaped CTD pattern. The eddy delineated by the survey was centred at 79° 15′ N, 00° 38′ E, a similar position to the many satellite observations of Vinje (1977). The eddy was situated close to a topographic 'hole', 30 km across and up to 5770 m deep, known as the Molloy Deep. The eddy was shaped like a backward breaking wave with a banded internal floe structure. Bands and streamers were present locally in the open water. The polar surface water beneath the eddy was cold (less than 0° C) and had a relatively low salinity. This water mass extended outside the ice cover as a thin (< 10 m) melt layer, though under the ice the pycnocline deepened to 40 m, except beneath the centre of the eddy. Here, the depth of the mixed layer decreased to 20 m forming two additional frontal regions with some open water areas present at the surface. In both north-south and east-west CTD sections, warm cores of Atlantic water were present in the water column at two locations centred at depths ranging from 40 – 80 m, with maximum temperatures of 4.3° C and 3.9° C, respectively. The salinity in these cores compensates for the temperature anomalies, leaving the vertical density profile stable and undisturbed. This suggested that the inflowing warmer water mass had been transferred to the ice-covered region along isopycnals. The positions of the warm water lenses coincided with the areas of reduced ice concentration, suggesting that this heat source was responsible for the ice decay.

Transponders positioned on ice floes within the eddy structure moved either anticyclonically around a small region or advanced some distance away from their initial position, possibly caught within the cyclic part of an eddy pair. The transponder movement and the calculated geostrophic velocities show that the motion within the eddy was in an anticyclonic direction which is consistent with laboratory and theoretical studies (Griffiths and Linden, 1981). The condition for baroclinic instability, where the energy is derived from the potential energy stored in the horizontal density field, is that the width of the current is very much greater than the local baroclinic radius. Such a condition is met for the complete length of the east Greenland Current, with the 'Ymer' eddy being located close to its narrowest point. The critical wavelength for such a disturbance for given field conditions was calculated to be 50 km, which is close to the observed diameter (Wadhams and Squire, 1985).

The repeatability of the eddy at the same location, and its stationarity in space does unfortunately not fit theoretically with baroclinically-forced instabilities. This suggests that the position and generation mechanism for the eddy may be linked to the local topography, as originally had been proposed by Vinje (Wadhams *et al*, 1979). Such a proposition was followed up by Smith *et al* (1984), who examined, in a qualitative manner, potential vorticity conservation over the topography in the region. The notable features in the area consisted of the 30 km wide depression and three seamounts to its south-west. Following conservation of potential vorticity one would expect a cyclonic feature to be associated with the depression and anticyclonic eddies to be associated with the seamounts. The cyclonic part of the vortex pair which made up the eddy observed by Wadhams and Squire (1983) overlaid one of these seamounts (Figure 2.6). In general, Wadhams and Squire's eddy observations lay further to the southwest than would be expected if the eddy were generated by the Molloy deep. Earlier eddy observations by Vinje (1977), which took place in spring when the ice extent was at a maximum, correlated more closely with this deep depression in the bathymetry. Further evidence that the eddy observations of Wadhams and Squire (1983) are at the periphery of the disturbed region were obtained from details of the potential vorticity changes. The eddy's vorticity increase calculated from field measurements was only a tenth of the value predicted from topographic changes (Smith *et al*, 1984). A model of this bathymetrically steered eddy was made by Smith *et al* (1984) using a two layer ocean model where a Gaussian distribution represented the bottom topography. After 24 days the model had generated an eddy which was similar in shape to the observed phenomena with a smaller cyclonic gyre to one side.

The Greenland Sea MIZEX programme (Johannessen *et al*, 1987) has identified the signature of over 14 independent eddies using data from all available sources (remote sensing, drifting buoys, SOFAR floats and hydrographic sections). Nearly half of the observations were categorized as either barotropic/baroclinic instabilities which advected southwards with the main current at speeds between $1 - 15\,\mathrm{km\,day^{-1}}$. The remaining observations were of eddies which appeared to be trapped by the complex bathymetry of numerous seamounts and depressions of the Molloy Deep. Some of the first group of eddies may also have been generated by the topography but were not trapped within the region.

Eddy phenomena on a smaller scale ($5 - 15\,\mathrm{km}$) were observed by both remote sensing techniques and in the CTD measurements in the NORSEX study region (Johannessen *et al*, 1983). These eddies were probably generated from barotropic instability of the ice edge ocean jet, as the

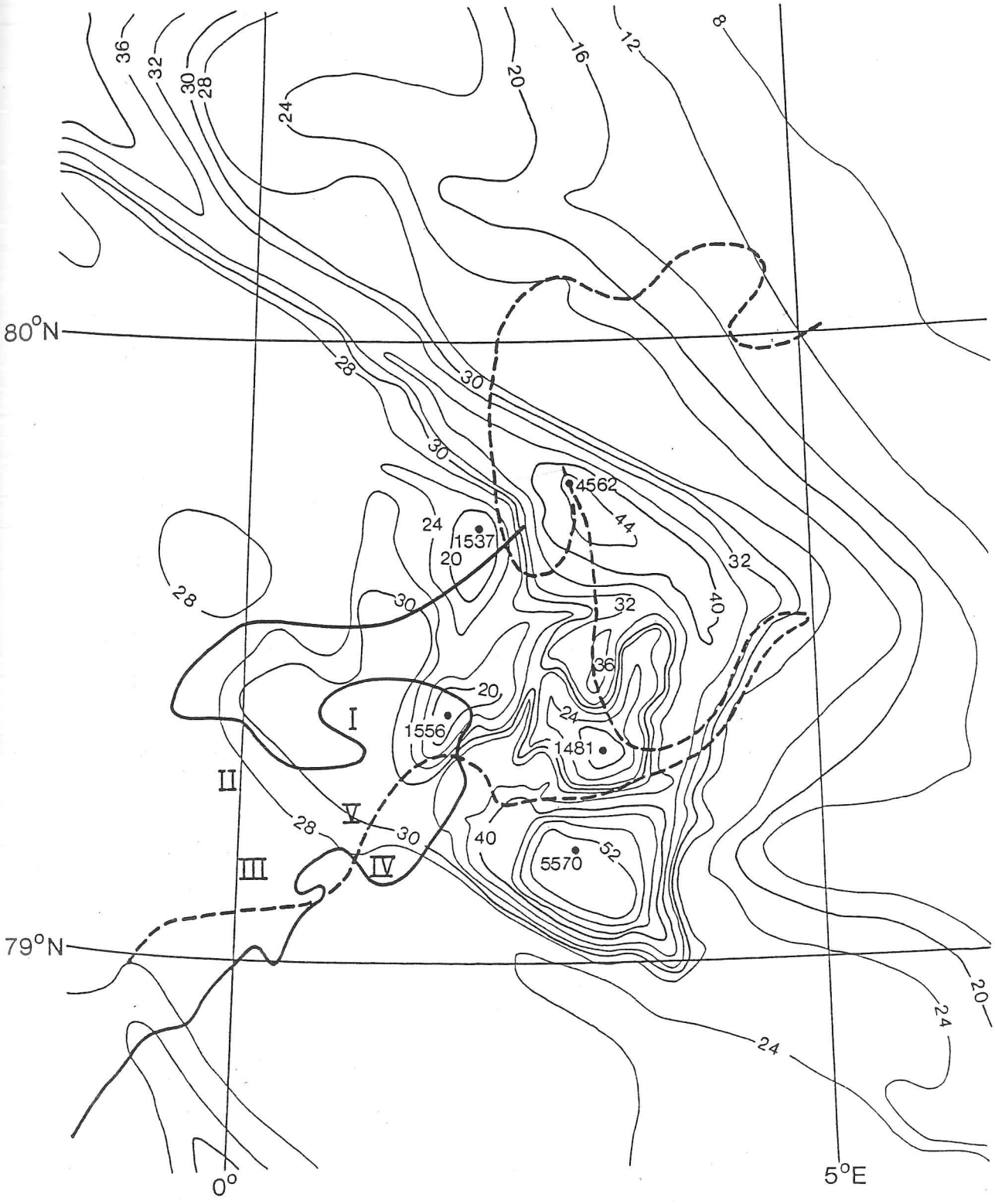

Figure 2.6: Superposition of eddy observed on Ymer-80 expedition to Fram Strait (solid line) and satellite observations of Vinje (1977) (broken line) on the local bathymetry (after Smith *et al*, 1984).

width of the current was close to the baroclinic radius of deformation (Hakkinen, 1984).

With the frequent observations of ice edge eddies now being documented (Johannessen *et al*, 1987), further attempts have been made to model them and to understand their dynamics. Hakkinen (1984) used a non-linear, two-dimensional model in an attempt to generate wind forced eddies. The initial condition for the ice edge was set by either a sinuosidal shaped boundary or by allowing the ice concentration to vary from 100% to zero ice cover in the form of a 50 km sinuosidal wave. Neither of these over-idealized ice conditions led to instabilities but the stress gradients across the margin generated additional upwelling and downwelling motions which were superimposed on to the wind-generated upwelling field. When the wind was forced to oscillate in opposing directions every 3 hours, eddies were shed from the ice edge region Hakkinen (1984).

Killworth and Paldor (1985) observed that the scale of eddy motion in the ocean adjacent to an ice edge was much greater than the baroclinic radius of deformation. They suggested that the ice had a greater role to play than just a passive tracer in the dynamics. They approached the problem in a similar fashion to Røed and O'Brien (1981), and looked to see if the ice front was inherently unstable. The likely scale of the motion, by analogy to the Rossby scale for the ocean is $c_o\, f^{-1}$ where c_o is the speed of propagation of small pertubations in ice of 100% cover. The ice deformation scale with this definition is $40 - 50$ km (Røed and O'Brien, 1981) which is similar to the observed eddy size and significantly greater than the oceanic deformation scale. Killworth and Paldor employed the Røed and O'Brien (1981) ice rheology, where the internal stress (F) is dependent on the wave speed in the ice (c) which in turn is function of the dispersivity, (κ) and ice compactness A.

The internal stress terms in the momentum equation are of the form

$$F(A)A_x, \qquad F(A)A_y \tag{2.1}$$

with the function F(A) defined as

$$F(A) \;=\; c^2/A \tag{2.2}$$

and

$$c^2 \;=\; c_o^2 \kappa A \exp(-\kappa(1-A)) \tag{2.3}$$

The form of the instability is dependent on the value of κ; with low ice dispersivities, in the range 2-4, an unstable wave is generated. As κ increases the mean along edge velocity decreases, in turn

reducing the magnitude of the instability. When κ increases to 15-20 the system becomes stable with the ice effectively at rest. κ in this range is comparable to values chosen for the ice dispersivity by Hibler (1979)).

2.7 Effect of wave-ice interaction on the ocean

As this chapter has studied the effects of the ice on ocean structure, a short summary of interactions between surface waves and the ice floes is in order.

A wave field entering the ice is dampened by the ice floes, with loss of wave energy resulting from scattering by ice floes encountered during the passage. Only long swell reaches a considerable distance into the pack (50 – 60 km). The shorter waves are attenuated by the ice and decay exponentially with e-folding penetrations of 14 km for 9 s swell, and 26 km for 13 s period swell (Wadhams, 1973). The floe sizes encountered in the MIZ range from 10 – 1000 m and are graded by wave action into distinct zones. This gradation is best demonstrated in the Bering Sea where no strong velocity shears exist to disturb the pattern. During a transect across the Bering sea ice margin, Squire and Moore (1980) observed a narrow edge zone of 2 – 4 km with rafted floes broken into 10 – 20 m pieces. The following transition zone consisted of floes > 20 m which had smoother surface characteristics; most of the incoming energy had been absorbed by the outer zone. The interior zone started about 30 km into the pack with most floes greater than 100 m in diameter.

Wave action increases ice ablation by introducing meltwater into the upper ocean in several ways. When a wave breaks up a floe, it increases the available perimeter of ice. This enhances the ability of capillary waves to transfer heat trapped in the shallow surface water to the floe wall, thereby increasing lateral melt rates (Perovich, 1983). Momentum derived from the wind field is also transferred to the ocean by the action of surface waves. As a result the shallow meltwater layer under the ice is stirred and heat transfer to the ice increases. At the same time some of the kinetic energy stored within the waves is transferred to the mixed layer turbulent energy budget.

The other major way in which wave interaction induces melt input into the upper ocean is by creating an oscillatory shear flow beneath the ice (Wadhams *et al*, 1979). This mechanism will only be effective if there is a heat source in close proximity to the ice. Wadhams *et al* (1979) calculated the time for a 3 m floe to melt when placed at various distances from the edge when the incoming wave was of 9 s or 13 s period (Figure 2.7). The most dramatic melting took place at the ice edge,

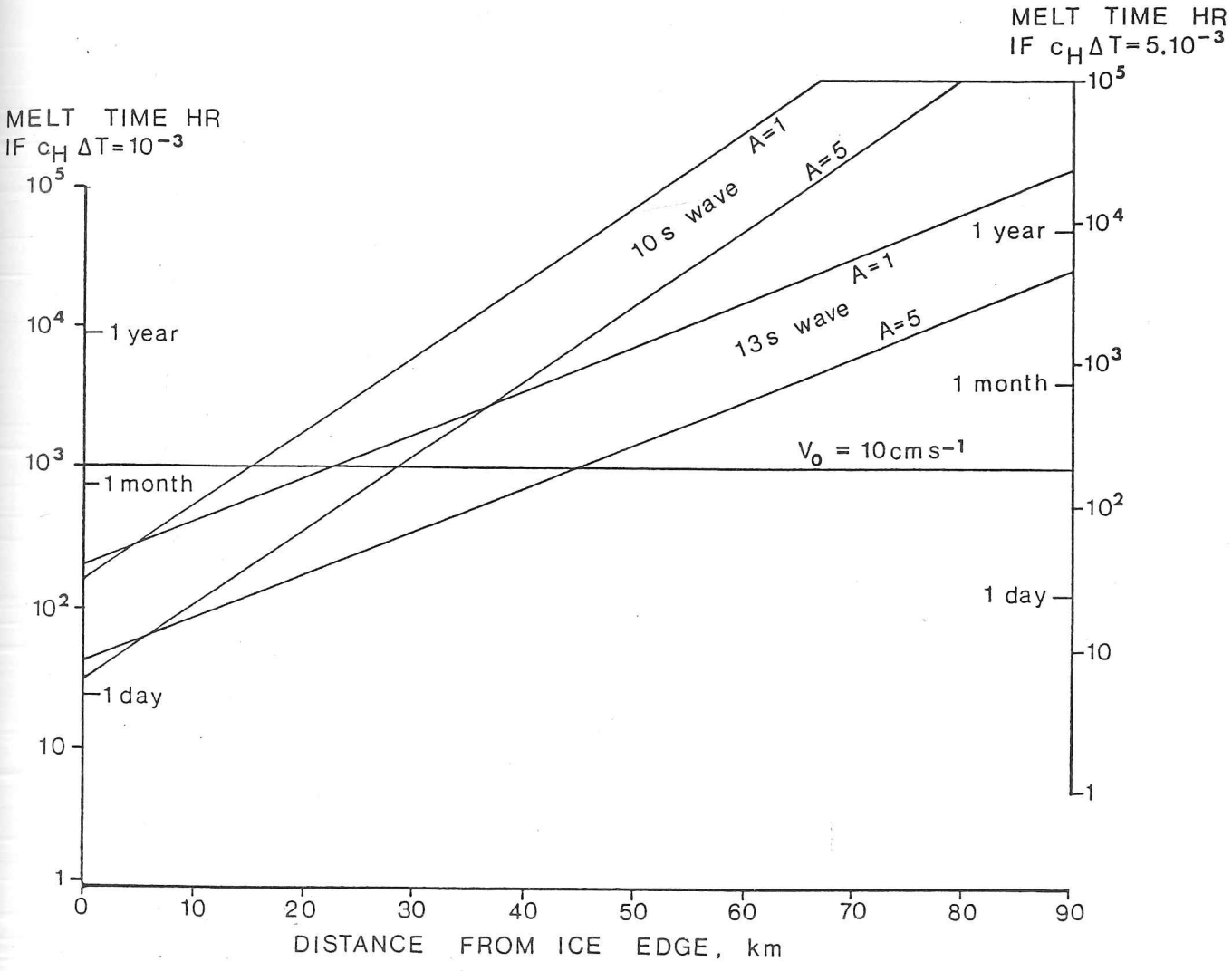

Figure 2.7: Plot of time taken for a 3 m floe to melt in an oscillatory shear flow of periods 10 s and 13 s (after Wadhams *et al*, 1979).

where a 5 m amplitude wave destroyed the ice in $1 - 2$ days whilst a 1 m wave took $6 - 8$ days . Further than 6 km into the ice cover the longer period waves are most effective in causing bottom melt, whilst by 22 km a background shear velocity of $10\,\mathrm{cm\,s^{-1}}$ would dominate any wave-induced shear and hence would control the melting process.

Extremely rapid ice decay results when the ice is located within a diffuse cover or close to open water regions such as in a band. Here, wave-induced erosion and decay of the ice can reach levels of $20\,\mathrm{m\,hr^{-1}}$(Martin *et al*, 1983). Moreover, once the ice has crossed the ocean thermal front, waves washing over the broken floes deposit warm water on the surface causing catastrophic ice decay (Wadhams and O'Farrell, 1985).

3

THE ICE EDGE REGION IN THE BERING SEA

3.1 Introduction to MIZEX-WEST

A comprehensive data set for the Bering Sea ice edge region was collected during MIZEX-WEST (February-March 1983) from a combination of observation platforms which included ships, remote sensing aircraft, and instrumented arrays deployed on the ice (Martin, 1985; MIZEX-West study group, 1983). In addition current meters and pressure sensors were deployed in the region of likely maximum extent of the ice, thereby providing a six month long data set spanning the ice season. These temperature, salinity and current velocity time series were supplemented by intensive oceanographic surveying carried out by the NOAA ship 'Discoverer' and USCG (United States Coast Guard) ship 'Westwind' in February 1983. Later, in March 1983, oceanographic sampling was also undertaken by the USCG ship 'Polar Sea' in an area overlapping the MIZEX study region.

Personnel on board each ship undertook several sea ice-orientated experiments to study the deformation and drift of the pack. Attenuation of waves through the ice cover was measured (Squire and Wadhams, 1985) with a one-dimensional wave buoy and on-ice accelerometers. The deformation of the ice cover was monitored by tracking an array of ice floes using radar transponders and Argos buoys. The Argos buoys was were used to describe deformation in the ice interior. An array of 8 buoys was set up 200 km from the ice edge with separations of 30 km centred on the 'Westwind'. At selected array points additional instrumentation was installed to log and transmit

meteorological data (wind, surface pressure and air temperature), and upper ocean parameters (relative currents and temperatures at 2 m and 6 m below the ice). Ice floe bottom ablation was measured using sonic sensors (Josberger and Meldrum, 1985) and was found to be about 7 mm hr^{-1}. Gust probes attached to a NOAA P3 aircraft measured changes in the air-ice drag across the marginal ice zone due to the increase in surface roughness (Overland and Walter, 1985). Helicopters deployed from 'Westwind' gave an aerial view of ice conditions in the neighbourhood of the deformation array, and mapped ice concentration gradients in the MIZ. A NASA Convair 990 carried out passive microwave experiments at a range of microwave frequencies in order to optimize the ability to discriminate between new and young ice. Preliminary tests were also made of the suitability of an airborne radar altimeter for studying sea ice.

3.2 MIZEX-West field data

Hydrographic data

The oceanographic data obtained from the current meter moorings and hydrographic sections have been examined in some detail by Muench and Schumacher (1985), and Muench *et al*, (1985). The latter publication contains sections of all CTD transects across the ice edge which were carried out during the two month surveying period. Generally, results from the density profiles were in agreement with earlier work, with the ice margin underlain by a two layer section of stratified flow. In the northern part of the basin lay a homogeneous water mass close to freezing. This was capped by a warmer, intruding saline layer which formed the two-layered region (Figure 3.1). The sections in Muench *et al*, (1985) showed that, despite changes in both the location and width of the stratified region, the form of the frontal intersection with the surface and the bed was similar at several positions along the shelf. The strongest frontal gradients are associated with the $-0.5\,^{\circ}$C isotherm, with horizontal temperature and salinity gradients of $10^{-4}\,^{\circ}\mathrm{C\,m^{-1}}$ and 2×10^{-5} ‰$\mathrm{m^{-1}}$ respectively (Muench *et al*, 1985). The lower front is associated with enhanced bottom slopes, between $65 - 95$ m, whilst the position of the upper layer interface is within the reduced ice concentration level or in some cases coincident with the extreme edge of the ice cover. The variability of the upper frontal boundary with respect to the ice edge is a function of the thermodynamic input to the ocean, which in turn is dependent on the rate of ice advection. On short time scales the system is not necessarily in equilibrium.

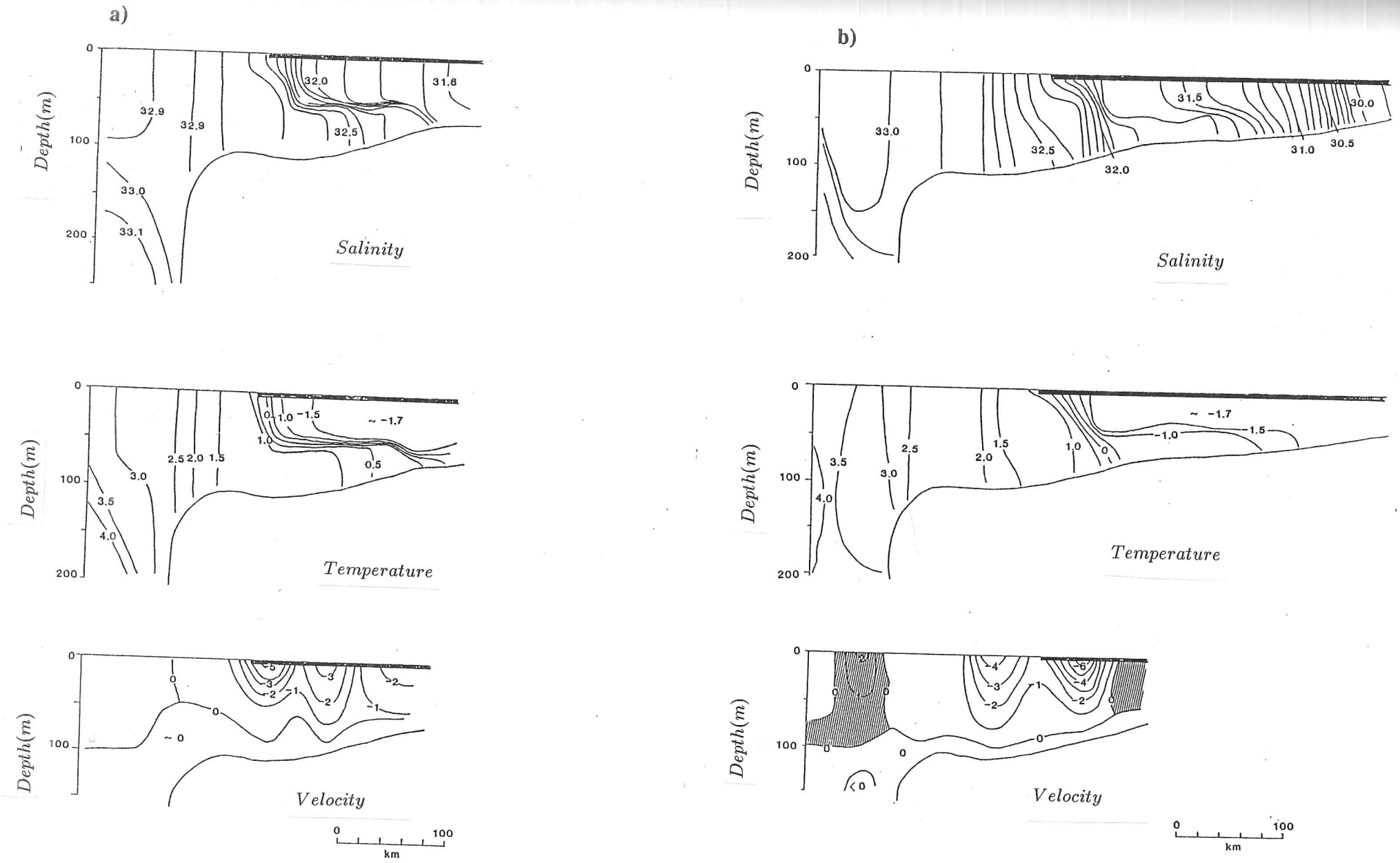

FIGURE 3.1: Salinity, temperature and geostrophic velocity cross-sections for the main MIZEX-West transect obtained by 'Discoverer' and 'Westwind' between a) 6th–9th February 1983 and b) 26th–27th February 1983 (after Muench and Schumacher, 1985).

During the MIZEX-West intensive field study period, the ice edge and associated front advanced 80 km south under the action of strong N/NE $15-20\,m\,s^{-1}$ winds (Muench and Schumacher, 1985). During this advance both the horizontal and vertical temperature gradients were sharpened, as seen by comparing the main CTD section along the line of the current moorings on 6-9th February with that of 26-27th February (Figure 3.1). The bottom frontal intersection moved 30–40 km to the south during this period. Two shorter sections centred about current meter mooring 4 were sampled on either side of the ice advance by Discoverer on the 14th February and by Polar Sea on 21st February. These sections indicated a similar small (10 – 20 km) advance in the lower layer, whilst the ice edge and surface frontal structure had advanced 75 km along the line of the section. We again find the two layers of the stratified region are more distinct with stronger gradients. CTD sections sampled before the ice advance frequently showed the outer part of the front extended to the bed forming a vertical front. A nine day CTD section was sampled by Westwind (Figure 3.2) as she drifted south with the interior array on the western side of St. Matthews island. This section indicates some stratification within the isothermal waters behind the front, with the water getting progressively fresher towards the north.

3.2.1 Current meter moorings

In the autumn of 1982 five taut wire moorings, each consisting of up to three current meters and a bottom mounted pressure sensor, were installed in the MIZEX-West study area south of St Matthew island (Muench *et al*, 1985). The array (Figure 3.3) was organized to define the cross-shelf and along-shelf gradients and fluxes. Current meters were fitted with temperature sensors and the meters at mid-depth also carried salinity sensors. Positioning within the pycnocline allowed the salinity characteristics of both layers to be found. Most of the current meters used were of savonous rotor type, which along with the pressure sensors, sampled at 30 minute intervals. Only three acoustic current sensors, sampling every 5 minutes, were available and were installed to measure currents in the upper layer on three of the moorings. Records from these devices were more reliable than those from the lower layer, the latter being susceptible to contamination from rotor pumping caused by surface waves and also to biological fouling. Fouling severely degraded the data quality, with current speeds beneath the ice probably being underestimated by a factor of 2/3. The current directions, however, are thought to be reliable (Muench and Schumacher, 1985).

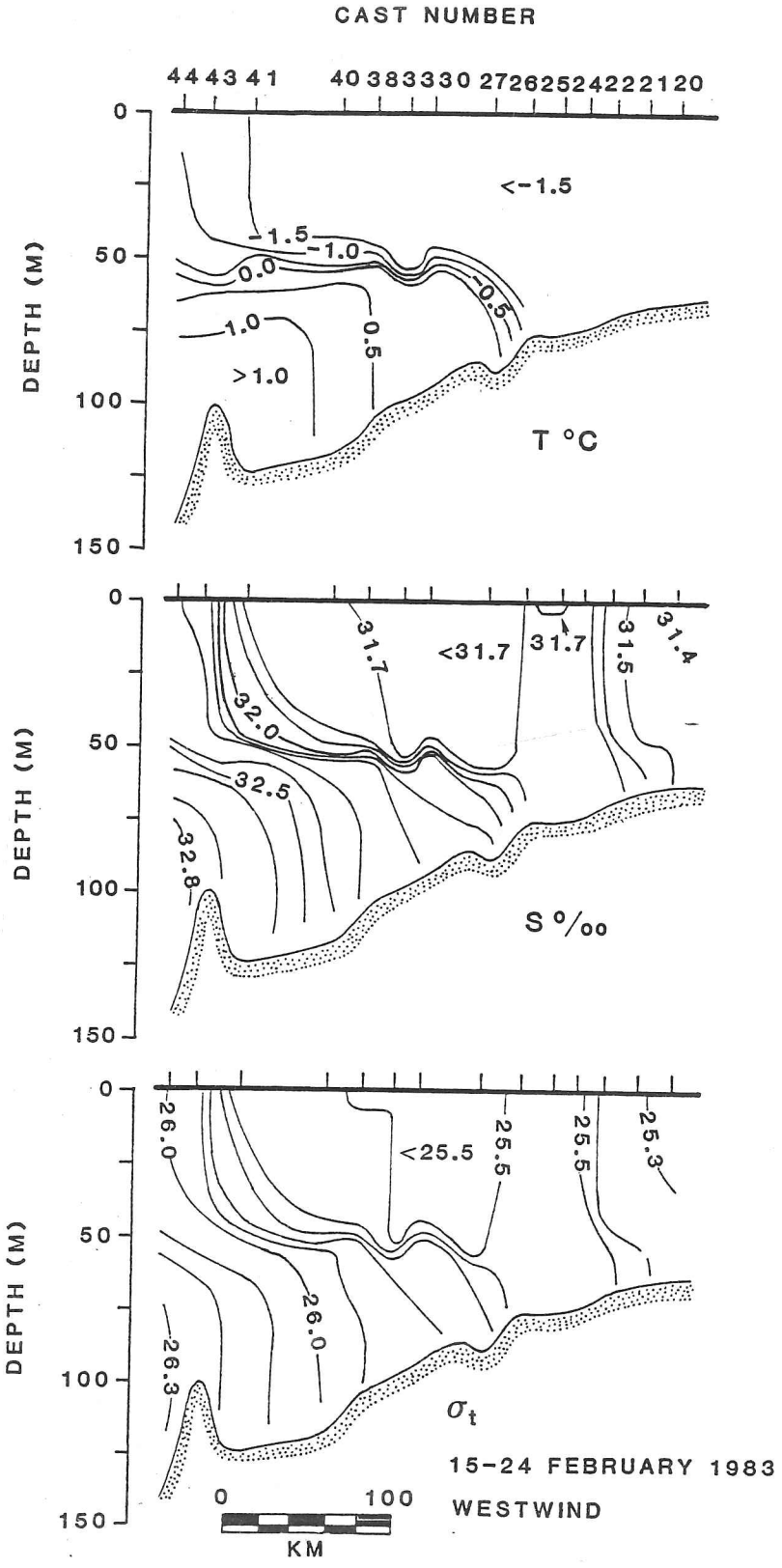

FIGURE 3.2: Temperature, salinity and density section obtained by 'Westwind' between 15th–24th February as she drifted under northerly winds from the interior ice camp to the ice edge (after Muench *et al*, 1985).

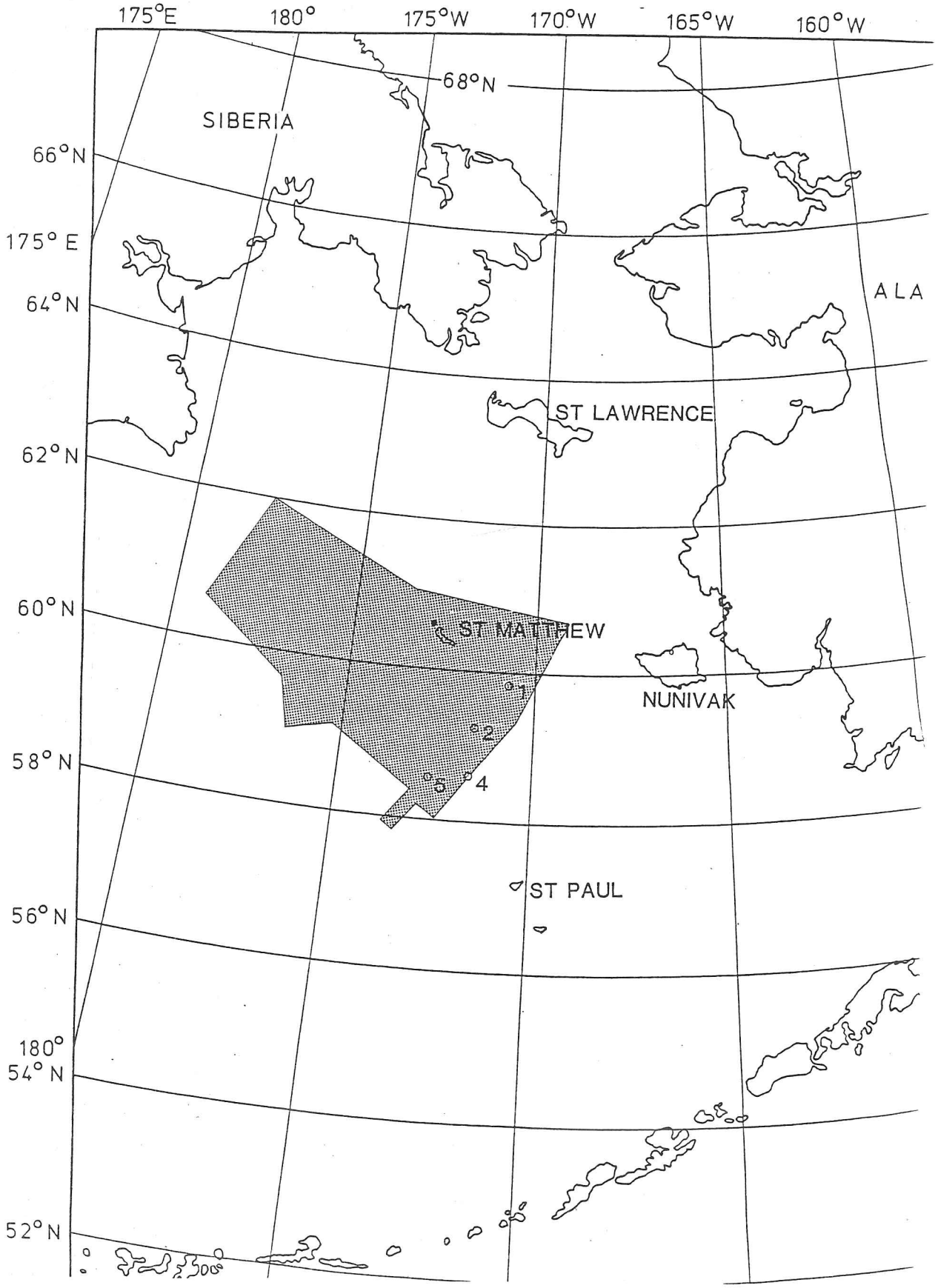

Figure 3.3: Map of Bering Sea region showing the location of the 4 current meter moorings. The shaded area represents the area sampled by the 'Discoverer', 'Westwind' and 'Polar Sea' during the mid-winter period 1983.

3.2.2 Ice edge position

To complement the above datasets information is required on the position of the ice edge and on the state of the ice cover during the season. Aircraft and satellite observations are the obvious source. For the intensive study period of MIZEX-West such observations were available using helicopters, NOAA P3 overflights and the NASA convair 990; detailed information was provided on the ice conditions at the ice edge, across the MIZ and in the interior pack. Daily photographs were also available from NOAA weather satellites. All available remotely sensed data are compiled into weekly ice charts by the Navy/NOAA joint ice centre. From these weekly charts we can determine the periods of greatest ice advance and retreat in the study area. The outermost defined ice type is used to indicate the ice edge, as even banded, broken ice will influence the oceanographic temperature regime monitored by the moorings.

Overlaying consecutive Navy/NOAA ice reconnaissance charts indicates weeks of rapid advance (4-11th Jan, 18-25th Jan), followed by weeks of near stationary conditions when the ice-covered area is consolidated with 'heavier' pack ice. This view of the advance may partly be an artefact of our tracking only the outermost limit of the ice, though oceanographic data from the intensive study period supports this pattern (Muench and Schumacher, 1985). This is because rapid ice advances of the ice edge/frontal system are self-limiting, as additional heat sources will become available to melt the ice, thereby increasing the decay process. Eventually the ice melt will slow to a rate at which ice can thermodynamically coexist with the upper ocean (McPhee, 1983; Hendricks *et al*, 1985). In situations when there was no clear visual images available for the weekly period, the Navy/NOAA charts rely on microwave radiometry data. As there is considerable ambiguity in distinguishing between young ice and open water types at passive microwave frequencies, use of these data will introduce greater inaccuracy to the ice edge position.

3.2.3 Air temperatures

Air temperature data recorded at meteorological stations on local islands were tabulated in Climatological Data Alaska (1983). Values of daily maximum and minimum air temperature at three island stations in different ice regimes (Figure 3.3) are displayed in Figure 3.4. Unfortunately, no similar record of wind speed and direction was available. The stations chosen are the St. Lawrence island meteorological station positioned deep within the pack. Nunivak island, which is in similar position to St Matthews island (where there is no meteorological station), is 200 Km or so inside

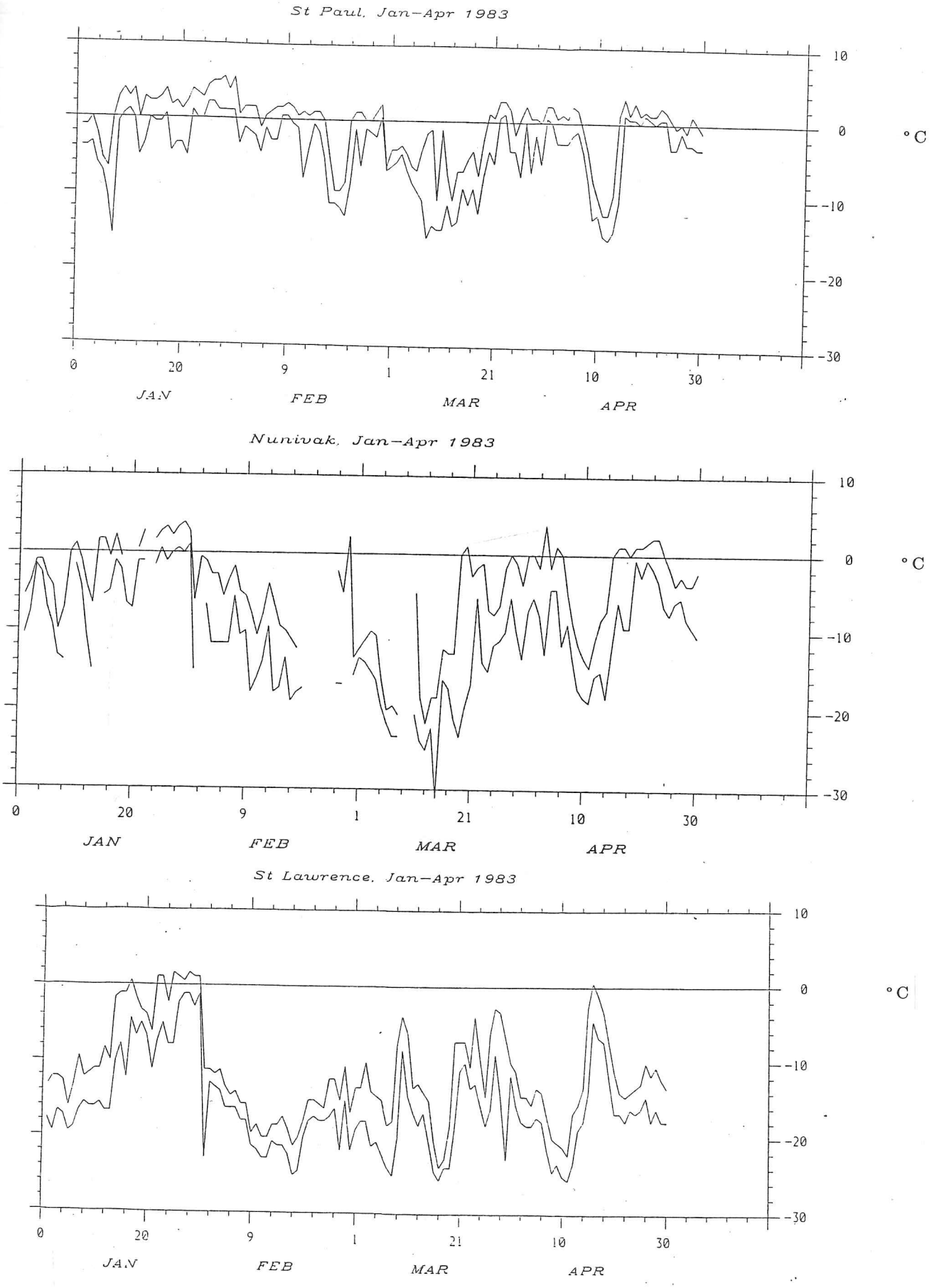

FIGURE 3.4: Maximum and minimum air temperatures recorded at St Paul, Nunivak and St Lawrence island meteorological stations between January–April 1983.

the marginal ice zone, St. Pauls in the Pribilofs is well to the South of the ice cover in a normal winter. Extrapolation of the data collected at these stations to provide a value typical of temperature at the ice edge is hampered because the island measurements include local meteorological effects. However, these records do form a useful guide to the gradients in temperature across the sea ice and open ocean regions, and give some indication of the prevailing atmospheric conditions.

3.3 Synopsis of ice advance across the shelf

In October, when the current meter and pressure recorders were installed, the ocean stratification was dependent on the temperature signal, with the upper layer at values above 5.0 ° C and lower layer around 3.0 ° C. By late November-early December, considerable surface cooling had occurred over much of the Bering sea region and initial ice growth around sheltered coasts is recorded.

Convective overturning of the denser surface water (caused either by surface cooling or by the injection of denser brine from the ice) generates a series of high frequency pulses about a decreasing trend on the temperature time series recorded at the moorings. Such pulses of activity are of 2-3 hours duration and are preceded by high frequency activity on the velocity time series. The amplitude of the pulses rapidly diminishes in magnitude with temperature discontinuities of > 1.0 ° C decaying in a few days.

Convective overturning took place between 18th-24th December and occurred progressively across the shelf; the southernmost mooring showed overturning 3-4 weeks later than similar convection in the area surrounding the northern moorings. Continuous convective mixing will produce isothermal conditions over the whole region. Data from the northernmost mooring indicate that the temperature had cooled below 0 ° C by early January. Step increases in the temperature records show the persistence of warm water in the neighbourhood of the sensors. Such signals are generated in the temperature time series by horizontal tidal excursions of the frontal boundary. Frequent occurrences of such tidal signals were seen in the temperature and salinity time series, particularly at the lower moorings where the tidal currents govern the vertical mixing and hence the horizontal sharpness of the front.

These data allowed us to monitor the horizontal gradients in the frontal zone. If advective exchange across the front can be neglected over the tidal time scale, then a horizontal eddy diffusion coefficient may be calculated from the lapse rate of the amplitude of the temperature signal produced

by these oscillations. If the amplitude of the temperature signal decreases by 0.5 ° C over a semi-diurnal tidal cycle then the horizontal diffusion coefficient is found to be 300 $m^2 s^{-1}$. Hendricks *et al* (1985) have shown that over the season the advective exchange across the front dominates the diffusive flux by an order of magnitude. Their calculation of eddy diffusion across the temperature gradient gave a diffusion coefficient of 2000 $m^2 s^{-1}$ for the upper layer moorings. This was several times larger than those quoted for similar shelf sea regions (Bryden *et al*, 1980; Coachman and Walsh, 1981).

Typical temperature, salinity and density profiles are shown in figure 3.5. They show a) a station where the water is isothermal with slight salinity stratification; b) a well defined two layer section; c) a two layer structure where the pycnocline region is diffuse.

Sensors at the northernmost site indicate that the near-freezing water mass beneath the ice extends to mid-depths from early January, though the bottom layer does not completely overturn and become isothermal until early-March. By then, the ice pack has covered the southernmost mooring. Hence, the array of current meters subtends the whole of the frontal domain.

The rate of ice advance and associated cooling events observed by the temperature sensors peaked both in mid-January, and in mid/late February. The timing of these episodes is controlled by atmospheric changes when cold Arctic continental air is released over the area (Reynolds *et al*, 1985; Wilson *et al*, 1984). All these major periods of ice advance and some of the minor adjustments recorded in the weekly Navy/NOAA ice reconnaissance charts have clear counterparts in the salinity and temperature records.

The ice extent record indicates that the largest weekly advance of the ice cover between St. Matthew and St. Lawrence islands took place during 21st-28th December. Simultaneously a 2.0 ° C cooling was observed in the lower part of the water column at the northern sensors. Subsequently, this advance almost halted when the ice was compressed against the northern side of St. Matthew Island. At about the time the ice first reaches the centre of the array (22nd-23rd January 1983), an increase in temperature was noted at all the lower moorings. A temperature increase (> 0.5 ° C) is also found in the surface waters sampled at the southernmost mooring, still well south of the advancing ice.

Examination of the island air temperature records indicates that these ocean temperature increases are correlated with an atmospheric event on 22-23rd January, with air temperature values above 0 ° C recorded in the vicinity of the ice edge. This warm spell continued into early February at

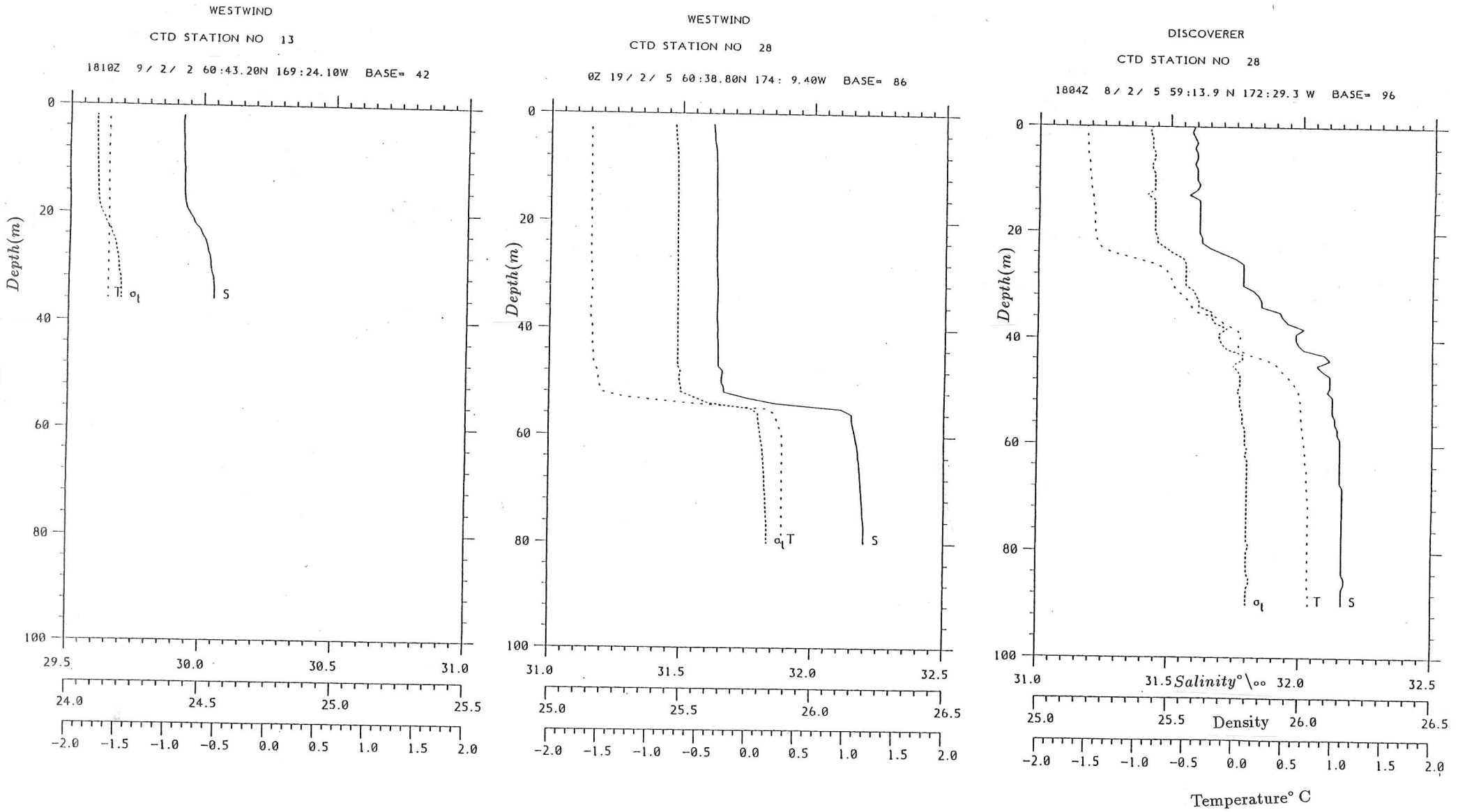

FIGURE 3.5: Typical temperature, salinity and density profiles indicating a) an interior station where the water is isothermal with slight salinity stratification, b) a sharply defined pycnocline creating two distinct layers closer to the ice edge, c) a two layer structure where the pycnocline region is diffuse as there is only sufficient energy available to mix upper 25 m.

the two southern meteorological stations, though maximum air temperatures had decreased rapidly again at the St. Lawrence Island station. The ice charts show that the overall loss of ice volume from the south-eastern sector of the Bering sea during this period was more than compensated by an increase in the area of ice cover on the north western sector of the shelf. By then, the final embayment of open water at the tip of the Bering slope current had been closed (Figure 3.6). All but the outermost mooring's sensors are underneath the ice cover by February though sensors positioned at 12 m depth at the outer mooring indicate the presence of sea ice in the area by recording the passage of a cold water mass ($-1.6\,^{\circ}$ C) on the 28th January . There then followed a further brief surface layer warming signal at this mooring, which is correlated with air temperature conditions, but freezing still occurred in the neighbourhood of the mooring as oscillations in the temperature time series at 12 m indicated the development of a cold, shallow mixed layer.

3.3.1 Ice advance during MIZEX-West

During early February, the ice cover and associated frontal structure migrated slowly across the shelf. After 16th February, winds increased from the northern sector and the pace of events quickened, inducing rapid advance of the complete ice-ocean structure. This ice advance led to a $2.0\,^{\circ}$ C drop in ocean surface temperature in just 20 hours on 22-23rd February at the southernmost mooring. The advance continued until 27th February when a new quasi-steady balance of the ice margin was achieved. Other moorings also indicated significant cooling events during the same 24 hour period (22nd-23rd February). By the end of this cooling episode the northernmost moorings were enveloped by the freezing water mass and remained so with only short interruptions for the rest of the ice season.

The ice cover continued to advance and did not reach maximum extent on the shelf until the week of 15th March. Timing of the maximum ice extent was controlled by a change in atmospheric regime, with the winds slackening, rotating through $120\,^{\circ}$ in direction, and bringing warmer air from the south to the ice edge region. A temperature rise of $> 10.0\,^{\circ}$ C was recorded at all of the island monitoring stations. Although the intensity of this warming event was not sustained, for the remainder of March air temperatures registered at St. Paul and Nunivak Island did not drop sufficiently below freezing to initiate further ice growth. The Navy/NOAA ice charts did not show a substantial ice retreat during this period, rather they showed a consolidation of ice types within the same boundary. Following the attainment of the maximum ice cover, the surface temperature sensor

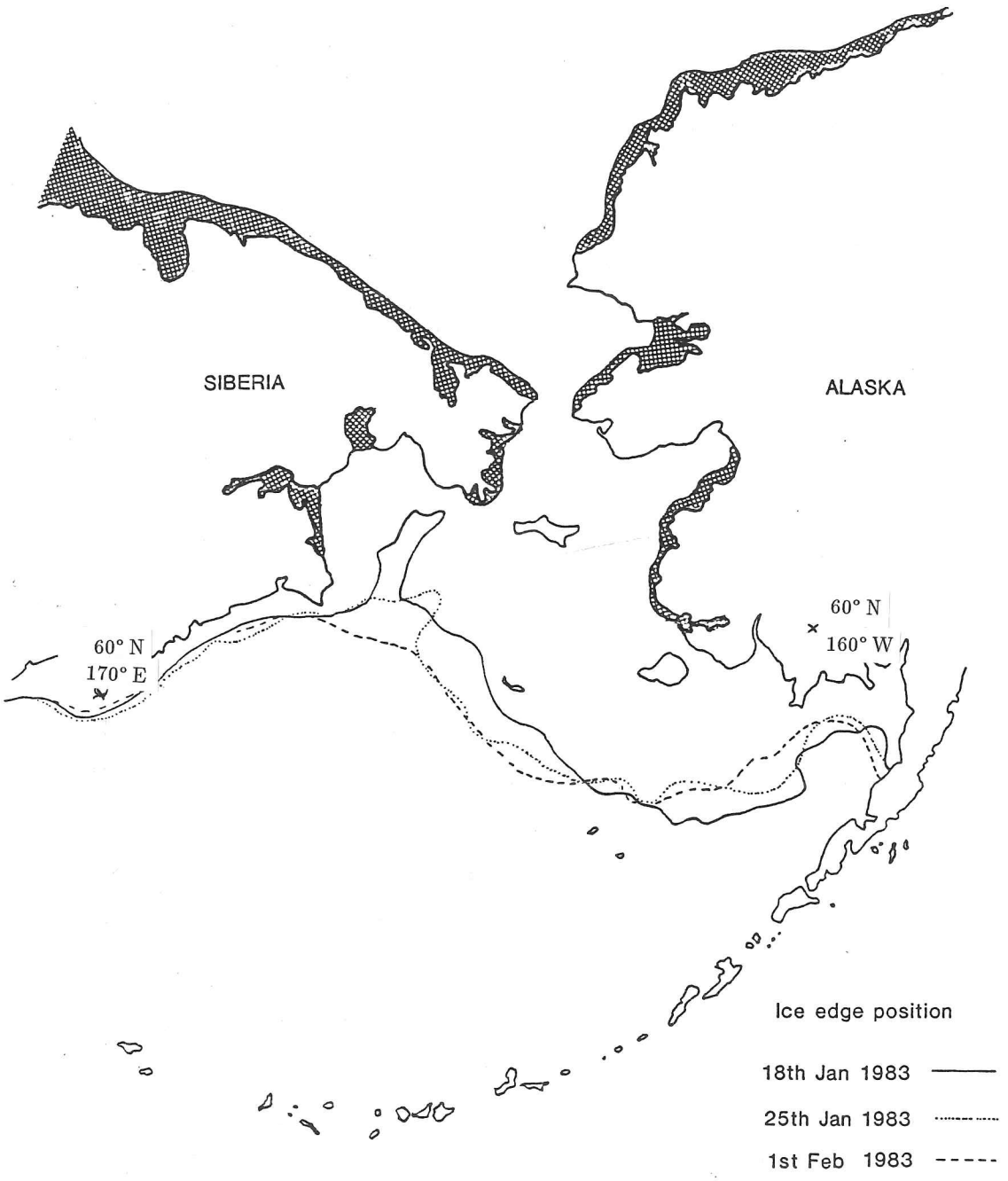

FIGURE 3.6: Bering Sea ice edge positions from NOAA/Navy charts between 18th January–1st February 1983 showing embayment in ice cover caused by the warm water transported by the slope current.

at 12 m depth registered a substantial warming. A further short warming period was observed at the ocean sensors between 30th March and 1st April, an event which correlates with air temperature records. A final atmospheric cooling, simultaneous to near freezing temperatures ($1.7\,^{\circ}C$) being recorded at the southernmost mooring, occurred on April 9th. The main seasonal melt occurred after 19th April at the southernmost moorings with gradual warming as melting ice permitted more insolation to reach the water surface. Decay of the ice cover at the site of the northern moorings occurred during the same period though with a slower rate of ocean temperature rise.

3.4 Baroclinic jets

An ocean front marked by a strong density gradient is balanced by geostrophy with a current jet. The dynamic topography of the MIZEX-West area referred to the 75 dbar reference level compiled from the Discoverer data by Muench and Schumacher (1985) is shown in Figure 3.7. The contours show the variability due to the density structure is seaward of the 0.18 dyn m isoline, and confirm a northwestward trending flow in agreement with the current meter moorings which gave vector-averaged values of $8.0\,\mathrm{cm\,s^{-1}}$. Calculations of geostrophic currents from the density transects gave an ice edge jet of $5-6\,\mathrm{cm\,s^{-1}}$ at the maximum of the horizontal density gradients (Figure 3.1). Other jets were also found within the ice where the density gradient increased. These positions may represent earlier manifestations of the frontal boundary, or be due to aliasing in the CTD transect by internal waves (Muench and Schumacher, 1985).

During the MIZEX-West oceanographic programme several transponder arrays were deployed on the ice to determine the deformation characteristics of the pack with respect to winds and currents. In particular, the baroclinic jet played a significant role in the balance of forces acting on the ice floes when the wind speed was low. The first deployment of the array (Figure 3.8) occurred between 8th-11th February (JD39-42), when winds were winds from the east ($100-110\,^{\circ}$) at $6\,\mathrm{ms^{-1}}$ for 46 hours; thereafter the wind strengthened to $15-20\,\mathrm{ms^{-1}}$ and rotated northwards by $20\,^{\circ}$. The variability in the wind direction decreased as the wind speed increased. Similarly, there was a decrease in the variability of the direction of the ice velocity vectors as the winds strengthened (Figure 3.9). During the early part of the drift several of the transponders underwent inertial oscillations causing the track to loop back on itself. Comparing the ratios of ice velocities to wind speeds, and the turning angle of the ice motion with respect to the wind direction, we find that the variability in the signal is derived

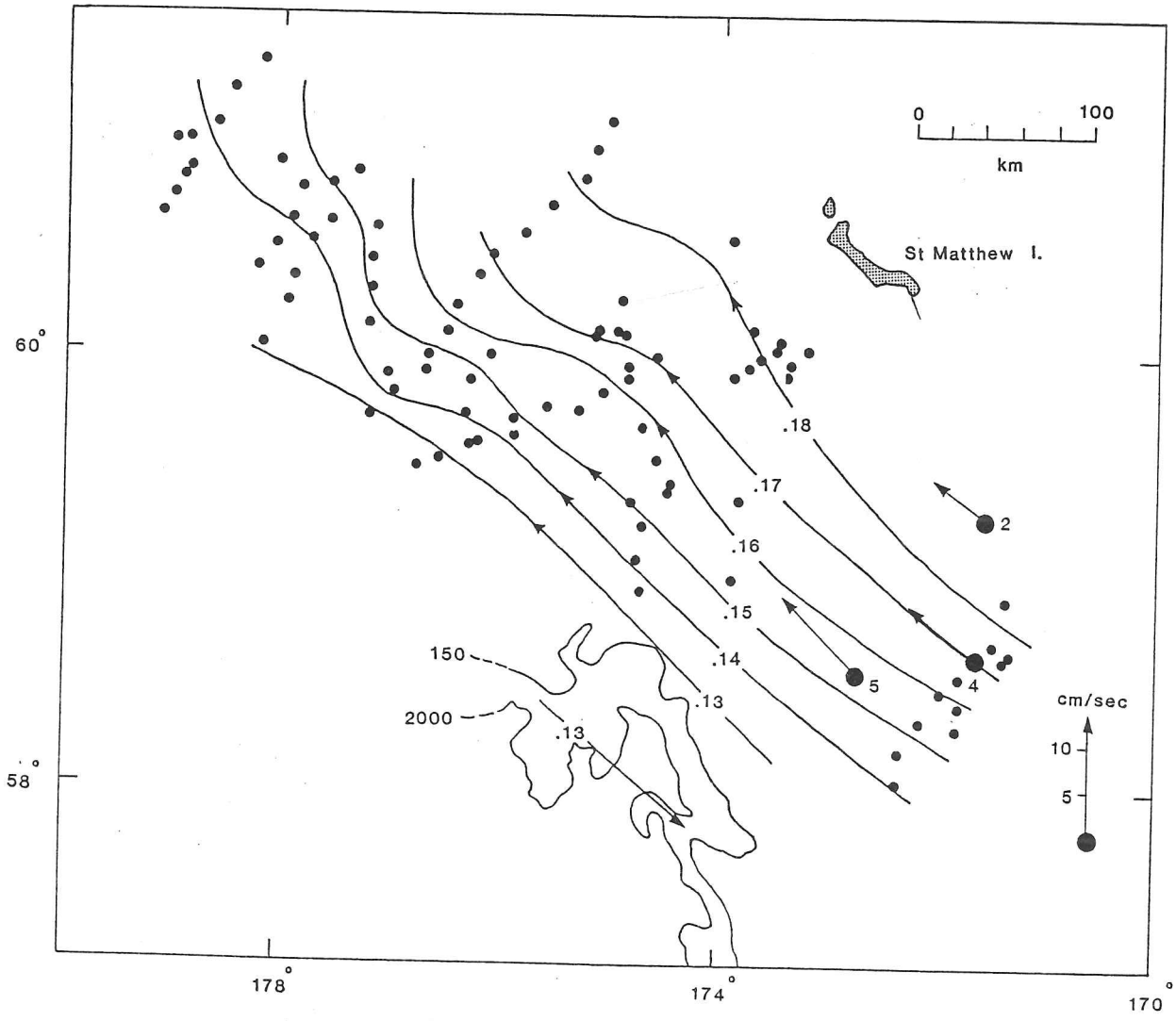

FIGURE 3.7: Contours of dynamic topography relative to 75 dbar calculated from MIZEX-West CTD data. Also shown are the current meter vector averages for comparison (after Muench and Schumacher, 1985).

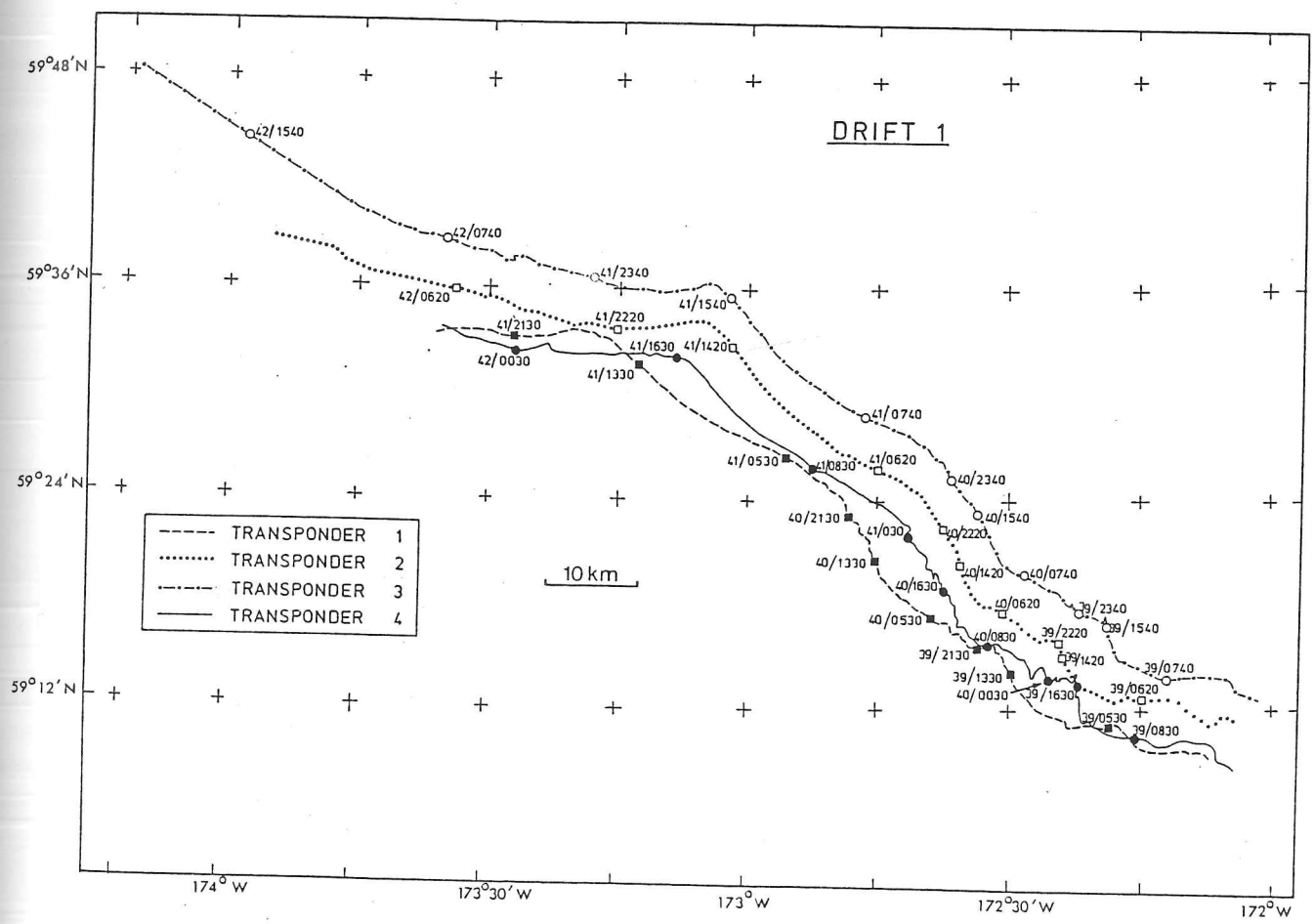

Figure 3.8: Tracks of four radar transponders (drift experiment 1), released by SPRI on JD39 (8th February, 1983) in the Bering Sea MIZ and were followed until JD42.

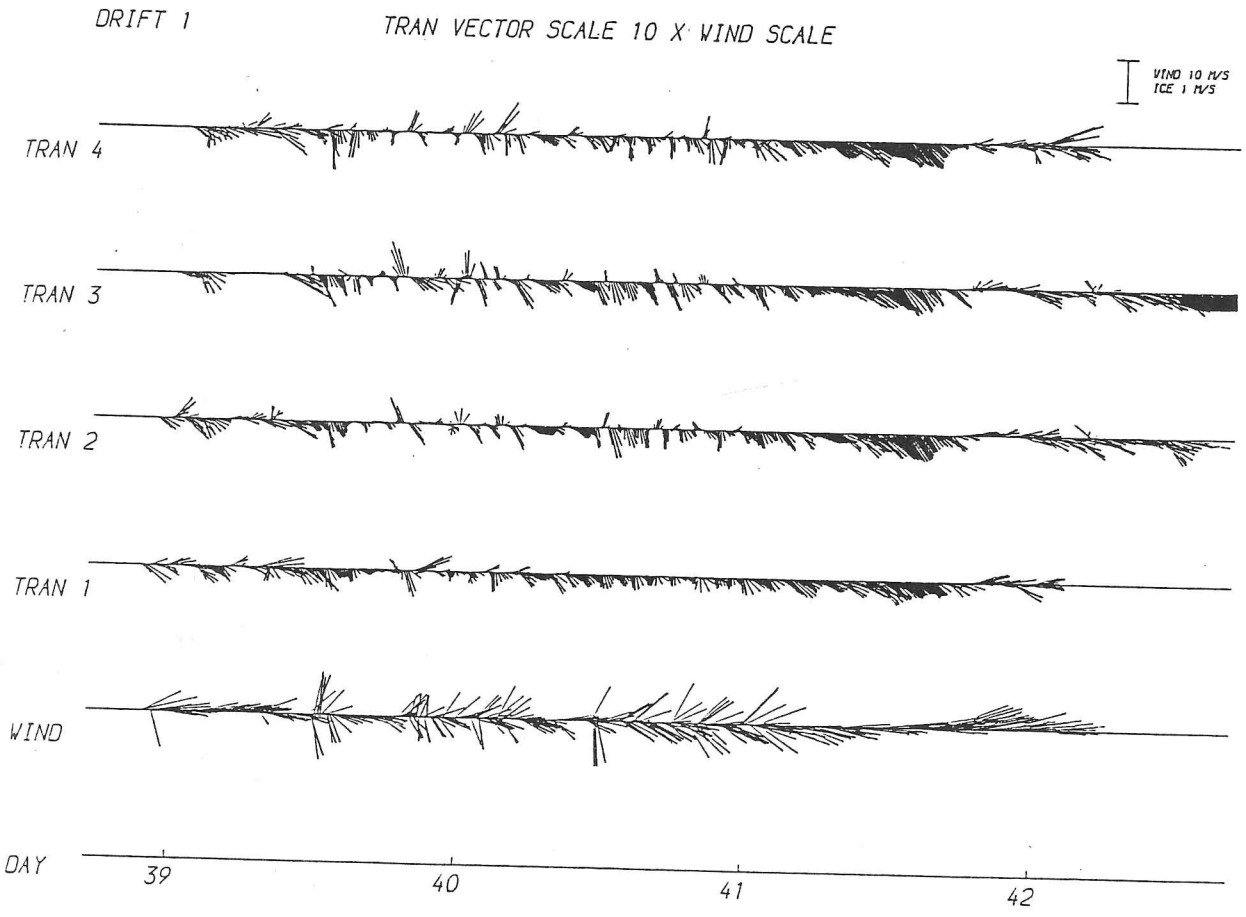

Figure 3.9: Ice velocity and wind vectors from drift experiment 1 (Figure 3.8).

from a source other than the wind. The correlation between the wind speed and ice velocity, and the direction of the wind and ice vectors, does not show a marked increase when time-lagged.

The vector calculated from the ice velocity drift data after wind forcing and Coriolis force have been removed represents the oceanic part of the external forcing (Figure 3.10). The amplitude of this force ($0.1 - 0.2N$) shows little attributable variability, whilst the direction of the vector indicates a tidal/inertial oscillation (which disappears during the final free drift phase) superimposed on the NW trend of the current. During this stage the floes were moving at about 4% of the wind speed at a turning angle between $20 - 40\,°$.

Tidal currents will only allow the floes to oscillate back and forth along the tidal ellipse causing loops in the track of the floes. Therefore, after the wind advection has been accounted for, the ice translation must be governed by the mean baroclinic and barotropic currents which act in the same north-westward direction as the array movement.

3.5 Distribution of mixed layer depths under consistent NE wind pattern

The study of mixed layer development in ice-covered regions is hampered by the lack of a continuous time series of temperature and depth changes similar to time series gathered by open ocean weather stations (Denman and Miyake, 1973). Measurements taken from stationary fast ice would not be appropriate, as the movement of the ice is an inherent part of the energy transfer process which maintains the turbulence in the mixed layer. Mixed layer data from the AIDJEX camps needed to be corrected for advective processes before use in a seasonal mixed layer model (Lemke and Manley, 1984). Turbulent flux measurements from the mixed layer under drifting ice were obtained in the inner Greenland Sea MIZ during the summer of 1984 (McPhee, 1984a, Erlingsson, personal communication, 1984).

No turbulent flux measurement devices were deployed during MIZEX-West and no specific mixed layer study was undertaken. Therefore the data on mixed layer depth are collated from shipboard CTD profiles. The distribution of surface mixed layer depths between 17th-28th February when winds were consistently from the northeast will be considered. This period was chosen because all three ships were operating CTD instruments in the area at that time.

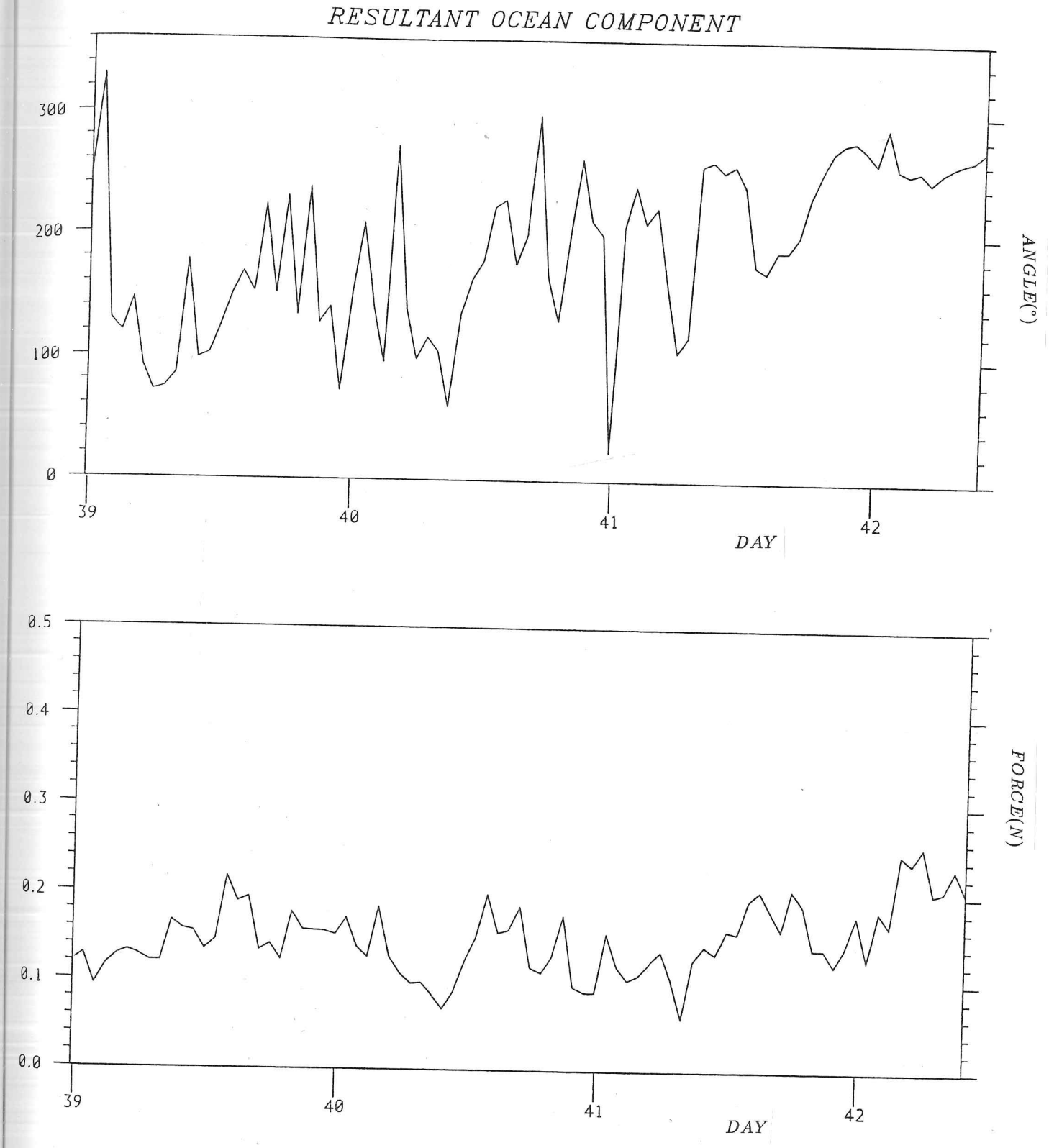

Figure 3.10: Residual external forcing after wind driven motion has been removed from data of drift experiment 1 (Figure 3.8).

Contouring spot points of mixed layer depths is impossible as the data are not synoptic. However, we can divide the data into specific areas where the mixed layer depths can be ascribed to particular affects. All the stations on the shelf north of 60 ° in water depths $< 60 - 70$ m were homogeneous in temperature and salinity (area A). An intermediate regime where the mixed layer is between $40 - 60$ m depth occurs, with the thickness of the upper layer decreasing as we move further south. This shallowing of the mixed layer occurs when the external mixing forces are opposed by an increased buoyancy flux from melting ice (area B). The shelving isopycnals eventually break the surface and form a front. Stations sampled in area B several days previously, just after a change in the wind direction and strength, indicated that no mixed layers existed and the water column was nearly homogeneous. Hence, these earlier points cannot be included in our picture as they represent an impulsive reaction to the onset of the wind forcing. We note, that the period selected does not represent a steady state response to the imposed wind condition.

Most of the stations obtained above the slope region had very deep (> 100 m) mixed layers or displayed homogeneous conditions remnant from the autumn, with water temperatures at least 2 ° C above freezing (Area C). By the beginning of March, the winds had rotated through 90 ° and the mixed layer results will react to this change. The only ship operating then, in the north-western part of Bering shelf, measured mixed layer depths of $30 - 40$ m in depths of $150 - 200$ m. From the strength of the wind at this time and the local bathymetric conditions one would expect to find a homogeneous water column (Area D). A small cluster of shallow mixed layers was sampled centred on 176 °W and 60 ° N (Area E). These shallow mixed layers ($12 - 24$ m) had surface water temperatures over a degree above ambient freezing temperatures. This warm source contributed to the rapid ablation rates of the ice floe monitored by Josberger and Meldrum (1985) during the same period.

In summary we note that, except at the extreme ice edge, enough turbulent energy is generated by bottom keels and through convective overturning to create a mixed layer of up to 50 m depth against the balancing force created by the buoyancy input of the meltwater from the ice.

3.6 Advective and Turbulent heat fluxes

Despite the strong advection of ice across the Bering shelf, cross-shelf currents are weak and the current fluctuations u', v', are correspondingly small. Hence, significant fluxes of temperature and

salinity are found only within the frontal zone. Hendricks *et al* (1985) calculated from the MIZEX-West data set a representative value for the turbulent heat fluxes across the shelf. They ignored the turbulent transports in the lower layer as the current meter records were unreliable.

Even though the density front in the lower layer is not as sharp as in the surface layer, significant turbulent transfer can occur at this boundary. In order to help with the interpretation the velocity vectors were resolved into components relative to the alignment a) of the front and b) of the bathymetry. The direction of the front was taken from the contours of surface temperature values in mid-February (Muench and Schumacher, 1985) in the vicinity of the moorings using the $-1.0\,^{\circ}\mathrm{C}$ isotherm as a guide. The angle of $50\,^{\circ}$ between the alignment of the local front and the bathymetry may not, however, be representative of conditions for the entire season. The flow resolved in the direction of the bathymetry may help us understand the current system. In particular, maximum positive turbulent salinity fluxes in the pycnocline are directed across the bathymetry and along the axis of the front in our calculation.

The weekly averages of the along and cross-shelf (cross-bathymetry) velocity components show a significant drop in the amplitude of the signal with depth, which is not simply the result of instrumental errors. However, with only three data points it is difficult to match any particular velocity/depth profile. There is also strong correlation of the daily averaged velocity components over depth on 3-6 day time scales.

Even though 90 % of the velocity variations are at diurnal and semi-diurnal frequencies, the temperature variance is largely in the sub-tidal range, i.e., long term cooling dominates the temperature statistics (Hendricks *et al*, 1985). The maximum monthly turbulent flux was calculated for the upper layer at the outer mooring in February, with a value of $0.8\,\mathrm{MWm}^{-1}$ (Hendricks *et al*, 1985). This calculation assumes that the properties at the upper mooring were representative of conditions over an upper layer of constant density and velocity characteristics of 50 m depth. From comparisons with CTD's gathered by ships in the area during the same period, this estimate of the mixed layer depth is not unreasonable. The time when the maximum positive flux is attained is governed by the horizontal gradient across the temperature sensor.

The across-shelf temperature and salinity gradients also govern the advective transport of heat. Our region of ocean does not appear to act as a local recirculation system because the mean upper and lower layer currents are on-ice for most of the season. The likeliest position for a return flow is in the bottom layer and, although rotation in the direction of the lower monthly velocity vectors

occurs, it is related to the superposition of the baroclinic flow associated with the front on the upper layer currents.

Some reversals to southerly flow were noted in January, particularly at the more northerly moorings (Muench and Schumacher, 1985). In the weekly averaged current data several records show a reversed flow in the lower layer. Evidence has been cited for return flow by Newton (1982) who observed a high salinity bottom flow. Hence we could assume (following Coachman, 1982) that at some time a local recirculation system existed allowing us to set the depth-averaged, time-averaged velocity $< \bar{u} >$ to zero. To achieve this we would need to assume that the reverse flow was within a layer not monitored by the instrumentation. Hence, we could calculate the advective flux for each layer about the instrument using

$$F_A = \rho_w c_p \int_0^h (\bar{u} - < \bar{u} >)(\bar{T} - < \bar{T} >) dz \qquad (3.1)$$

where $(< >)$ represents the average over depth and an overbar the average with respect to time for the velocity variable u and temperature T (Bryden *et al*, 1980).

Such advective fluxes were calculated to give a qualitative picture of the flow using weekly averaged data from moorings 2 and 5. At the inner mooring (2) on-shelf advective fluxes were found in the upper layer, and off-shelf fluxes at mid-depth until the frontal feature was present. The outer mooring (5) showed on-shelf fluxes until early April when the current changed sign. The lower two sensors at this position and the bottom sensor at the inner mooring alternated in sign, mirroring the change in sign in the weekly mean currents. (Note. The direction of the currents from the lower sensors is not degraded by instrument errors; only the current magnitudes are suspect).

Daily turbulent fluxes were calculated by averaging the daily temperature, salinity and polarized velocities, calculating the deviation from the mean, and combining all data into a flux term of the form

$$F_x = \rho_w c_p \overline{u'T'} \qquad (3.2) .$$

Insufficent space is available to plot data for each sensor and polarization, so as an example the values for current meter 9 in the surface layer at the outermost mooring is selected for display in Figure 3.11. The most striking feature of the daily flux values in the early part of the season is a cycle at about 10-14 days. This is at a longer period than the peak of the current variance spectrum which occurs between 2-4 days (Muench and Schumacher, 1985), though some energy does exist

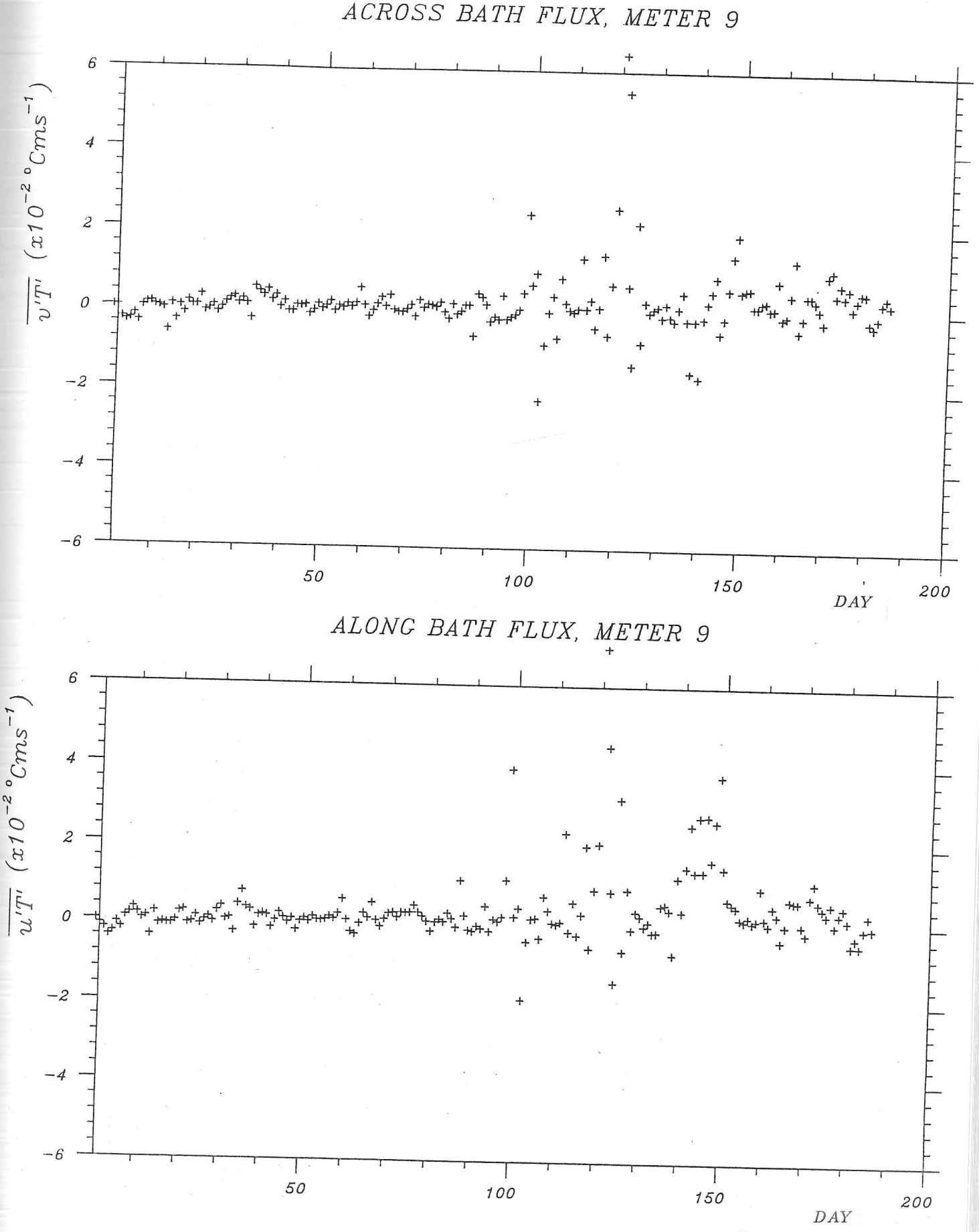

FIGURE 3.11: Scatter plot of daily averaged turbulent component $\overline{u'T'}$ for along and across bathymetric polarizations using data from current meter 9 in the surface layer of the outermost mooring. (Time axis is days from the start of the record.)

at this frequency in their spectral calculation for this sensor. Some of this current signal is the effect of the spring/neap cycle. Periods of increased frontal activity where the gradient region is advected back and forth across the sensor are indicated by a wide scatter of daily flux values. This extreme variability may be dependent on how the horizontal tidal temperature oscillations about the moorings are weighted in the daily average.

Although the velocity variances are at a maximum at diurnal and semi-diurnal frequencies, almost all the temperature variance is at longer periods (Hendricks *et al*, 1985). Hence, to obtain a clearer seasonal view the daily fluxes have been grouped into monthly averages (Figure 3.12). The values so calculated are slightly different from the results of Hendricks *et al* (1985) who used monthly means in their derivation of the turbulence terms.

As expected from our earlier discussion in section 3.2, the largest heat flux across the northernmost mooring (mooring 1) of $2.4\,\mathrm{MW\,m^{-1}}$ occurred in January. The maximum flux vector was found to be parallel to the direction of the front with a compensating cross-front heat flux developing in February. Mooring 2 demonstrated a maximum surface heat flux ($1.8\,\mathrm{MW\,m^{-1}}$) in January, though in the middle layer the maximum heat transport was in December before formation of the ice edge front. The lowest sensor at this mooring had an off-ice turbulent heat transport of about $1\,\mathrm{MW\,m^{-1}}$. Minimal heat transport ($< 0.4\,\mathrm{MW\,m^{-1}}$) occurred in the lower part of the water column at the outermost mooring as no strong frontal gradient formed during the season at this depth. The surface layer, at this position indicated the strongest cross-frontal diffusive transports ($> 5.0\,\mathrm{MW\,m^{-1}}$) with a maximum occurring in March, though substantial density gradients and hence fluxes did occur in adjacent months ($2.0\,\mathrm{MW\,m^{-1}}$). In contrast, sizeable temperature fluxes were measured both by the surface and mid-depth sensors at the central mooring (4). Maximum fluxes at this depth occurred in January and April when the greatest ice edge and associated frontal variability occurs, though the surface sensor at this position does not display the late season signal. (Note. This discussion should be read with the understanding that if the the current speeds are low, the velocity variances will similarly be affected.)

3.7 Horizontal and vertical velocity coherence

Covariance spectra were calculated for all neighbouring pairs of contiguous velocity records measured by the mooring strings during the winter months (January-April). The strongest coherences

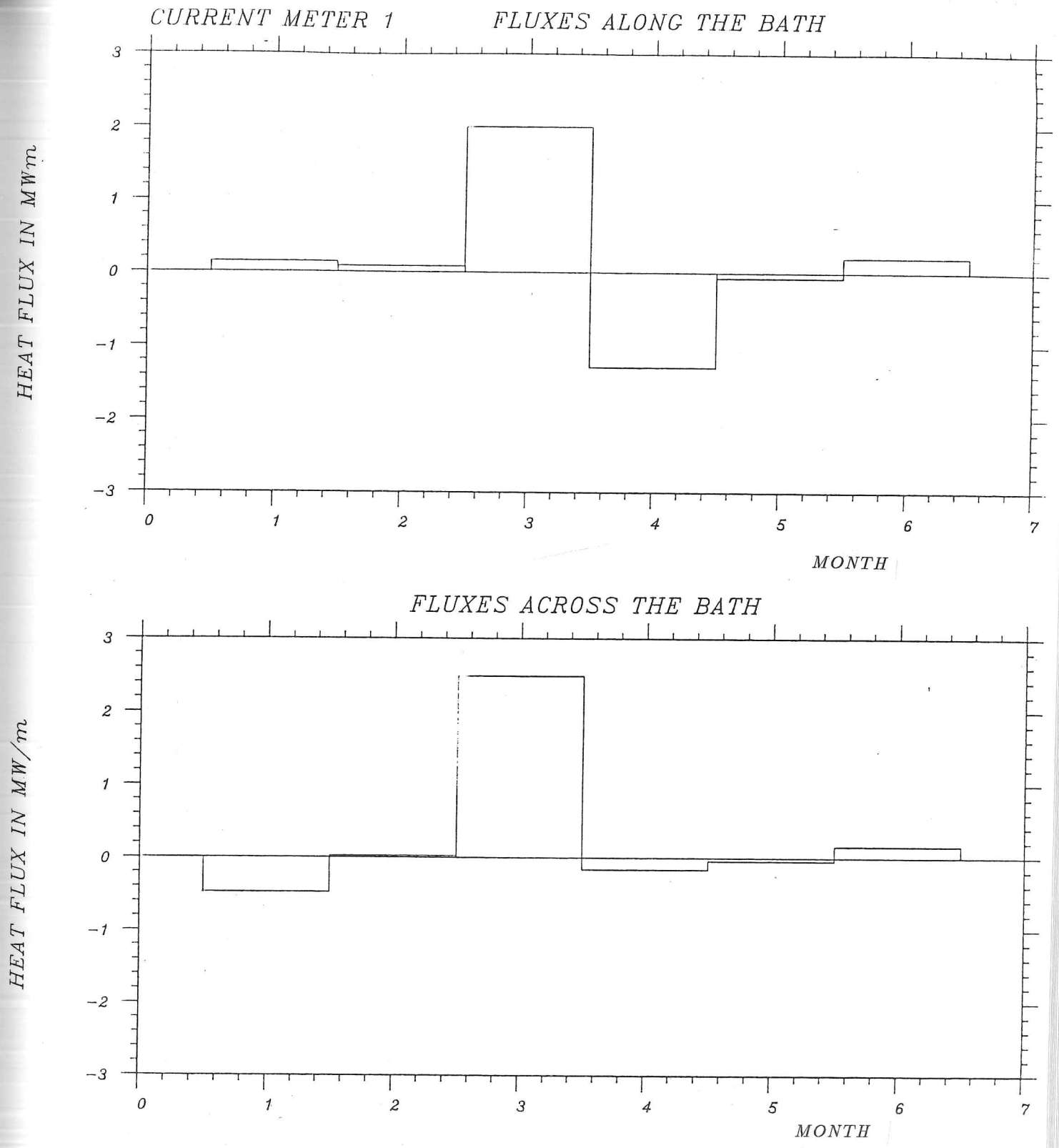

FIGURE 3.12: Histogram of monthly averaged temperature fluxes polarized along and across the bathymetry using data from the northern most record. (Time axis is months since the start of the record).

were at tidal frequencies, but consistently high coherences occurred in higher frequency bands. Coherences in low frequency bands were not examined at this point and would not be well-resolved in the monthly segments. Muench and Schumacher (1985) had used this dataset earlier to examine low frequency variability, finding a dominant spectral peak between 2-4 days. They also calculated cross-correlations between the surface currents and winds and found that only 22% of the velocity fluctuations were correlated with the winds, and that there was no major change during ice free and ice covered periods. The remainder of the low frequency velocity variance is probably due to barotropic forcing, and possibly to dynamic instabilities which play no active role in the ice edge system.

Comparing the coherences and associated gains for the north-south and east-west polarizations we find similar response patterns for any given month. Comparisons have been made of vertical coherence of velocities between sensors on the same mooring 5 (meters 9, 4, 2) and with the interior mooring 2 (8, 3, 5). Both encountered a variety of density and ice compactness regimes during the season, particularly the outer mooring which experienced the effect of ice break-up in April. We would therefore expect to see fundamental differences in the way that energy (especially at high frequencies) alters over depth. Examination of the records shows that in nearly all pairings the two major tidal components have significant coherence, specifically in the range 0.9 to 0.95. The gain or amplification at these frequencies was always close to unity, i.e., no energy is removed or added. The same is not true for some of the higher coherent frequencies (>0.8) where significant gain in energy is acquired, centred at periods of 4.17 and 2.76 hrs. (The filter to cut off current meter noise levels for the 30 minute samples was centred at 2 hrs). Therefore, these signals represent energy coherences in the current meter record at the higher tidal harmonics of 3 and 4 hour periods.

At the outermost mooring, vertical gains at these tidal harmonics ranged from 2.0-8.0 for the surface-pycnocline comparison, and a smaller amplification (< 3.0) is experienced with the mid-depth and lower layer pair. By contrast, at the inner mooring (in more consolidated pack ice for the entire period) the vertical comparisons rarely showed gains outside a ratio of 3:2.

We also examined the horizontal coherences of velocities calculated between the current meters in the surface layer, at mid-depth and at about 20 m above the bed. Coherences at mid-depth between sensors on the outer 2 moorings, did not produce gains greater than 1.0-2.0. However, if the innermost current meter (1) is included, higher gains (up to 5.0) are found for the same sub-group of frequencies. Therefore we are encountering amplification at these frequencies as we proceed

into the ice pack which is in contrast to the change in vertical coherence at high frequencies that we observed above. A similar result is found in the lower layer, though no amplification of horizontally coherent signals appeared in the surface layer at these frequencies.

3.8 The wind driven and tidal current regimes under the ice cover

We would expect the presence of a seasonal ice cover on the Bering sea shelf to modify both tidal and wind driven currents. Earlier observations in the northern section of the basin have shown frequent reversals of the flow regime driven by atmospheric forcing during the ice-free period in early winter. After an ice cover is formed the reversals are suppressed, and the correlation between wind and surface ocean velocity is reduced (Salo *et al*, 1983).

When the MIZEX-West moorings were covered with ice the upper layer currents increased significantly. This can be attributed to the development of a baroclinic jet in the frontal regime, and also to additional barotropic flow as the intensity and frequency of storms increase.

The addition of the baroclinic component to the current vector causes a shift in the direction of the current to the left of the isobars in the surface layers, whilst in the deeper layers the flow is still aligned with the bathymetry. Muench and Schumacher (1985) also observed a trend across all the moorings to a more northerly flow during the ice-covered period. During this period, there was only one major reversal to southerly flow, which occurred in the deeper layer during January 1983. The correlation of the velocity fluctuations with the wind measurements decreased slightly during the ice-covered period, with a mean correlation of 0.47 over the 6 month period (Muench and Schumacher, 1985).

During the months when no ice cover was present to inhibit transmission of wind energy, strong coherent inertial oscillations ($> 40\,\mathrm{cm\,s^{-1}}$) were observed (Muench and Gunn, 1985). These were frequently up to 180° out of phase in the separate layers, creating considerable shear across the interface.

Tidal constituents also appear to change phase and magnitude under a winter ice cover (Pearson, 1981). This fact has a bearing on the characteristics of the ice edge front because the lower part of the water column is mixed by tidal energy. Although we have stated in section 3.6 on heat fluxes that the temperature variance is dominated by the long term changes, it was thought that tidal variations in the temperature record may conceal signals related to changes in the position of the isopycnals

at non-tidal frequencies. In an attempt to remove these effects it was necessary to reconstruct the tidal signal from its harmonic constituents. In practice this was unsuccessful as the temperature time series was highly non-stationary in nature, with quiescent periods interspersed with periods of vertical and horizontal tidal mixing and frontal advection. As an aside to this work, however, we obtained the results from the harmonic analysis which both revealed and confirmed the variability of the constituents throughout the winter months (Muench and Mofjeld, 1985).

The 1977-1978 tidal current dataset examined by Pearson (1981) demonstrated a decrease of 35% in the amplitude of the M2 tide at 24 m depth with only a 12% decrease at 40 m. The phase lag at the upper meter decreased by 20 ° during the same period, whilst the lower meter increased by 18 °. The change in amplitude of the tidal constituents was at first dismissed as an effect arising from the suppression of surface waves (rotor pumping) during the ice covered period, but this did not explain the change in phase. Several mechanisms have been proposed for this variability which have included:

1) the frictional effects of the ice cover on the ocean which in turn will be a function of the roughness elements of the under-side of ice floes. This frictional effect of the ice will alter between light and heavy ice seasons;

2) Mofjeld *et al*, 1984 have suggested that the frictional forcing in the bottom boundary layer is altered by the surface waves and this in turn will be modified by the presence of the ice floes.

3) non-linear interaction with the stratification;

4) variations may occur in the tidal constituents in either the North Pacific or the Arctic ocean during the winter season and impinge upon the tides in the Bering Sea (Muench and Mofjeld, 1985).

Variations in tidal constituents have been monitored over several winter seasons (Muench and Mofjeld, 1985). In each of these years there has been some variability in maximum ice extent, time of formation, and break-up of the ice, confirming that the interactive mechanism causing the change in the tidal constituents is dependent on the concentration and type (roughness) of ice present.

30 major tidal harmonic constituents were fitted to 29 day sections of pressure level and current meter records from each winter month. We generated a large amount of tidal constituent data which cannot all be discussed. As biological fouling and wave pumping has degraded data from most of the current meter sensors, we will concentrate our discussion on the constituents for the bottom pressure sensors. If the current meter data had been more reliable the variation in the tidal coefficients with depth might help to distinguish between the proposed mechanisms.

Four of the major constituents of the local tide (K1, O1, M2, N2) are selected to display the monthly changes at the three pressure sensors. In all the graphs phase and amplitude are plotted relative to their means, thereby indicating the trend for any given month. (In the graphs in Figure 3.13 the full line represents amplitude deviation using left hand scale, and the dotted line is phase deviation graduated on the right hand side. (Graph style adapted from Mofjeld, 1986).) The mean phase across the pressure sensors for the selected constituents did not show wide variability indicating that the mooring sites were not close to basin tidal amphidromes for those frequencies. The most striking feature is the large ($> 20°$) phase deviation in February for all selected constituents. As a check that this was not the result of aliasing by the least squares fit procedure, the frequencies in each tidal species were altered. Apart from February, smaller compensating negative deviations from the mean phase were found for each month with the exception of the pressure sensor on mooring 2, where all the constituents had a positive deviation in April, the ice break-up period.

The amplitude variations are more complex with each of the constituents following a particular pattern: K1 has minimum amplitudes in January and April with a maximum in February; M2 also has a minimum in January with a maximum in March; O1 again has minimum amplitude in January, with a maximum in December and a maximum in March/April; and N2 has only one turning point in its amplitude curve for the winter months with a maximum value in January/February.

These results show clear differences in the tidal constituents during the ice season, with the understanding that the monthly divisions cut across changes in the characteristics of the ice cover. In particular, at maximum ice cover (February-March) there is a distinct change in phase at all sensors and for all the selected constituents. Moreover, the ice break-up period also has a distinct signal. However, these results do not discriminate between the four mechanisms advanced.

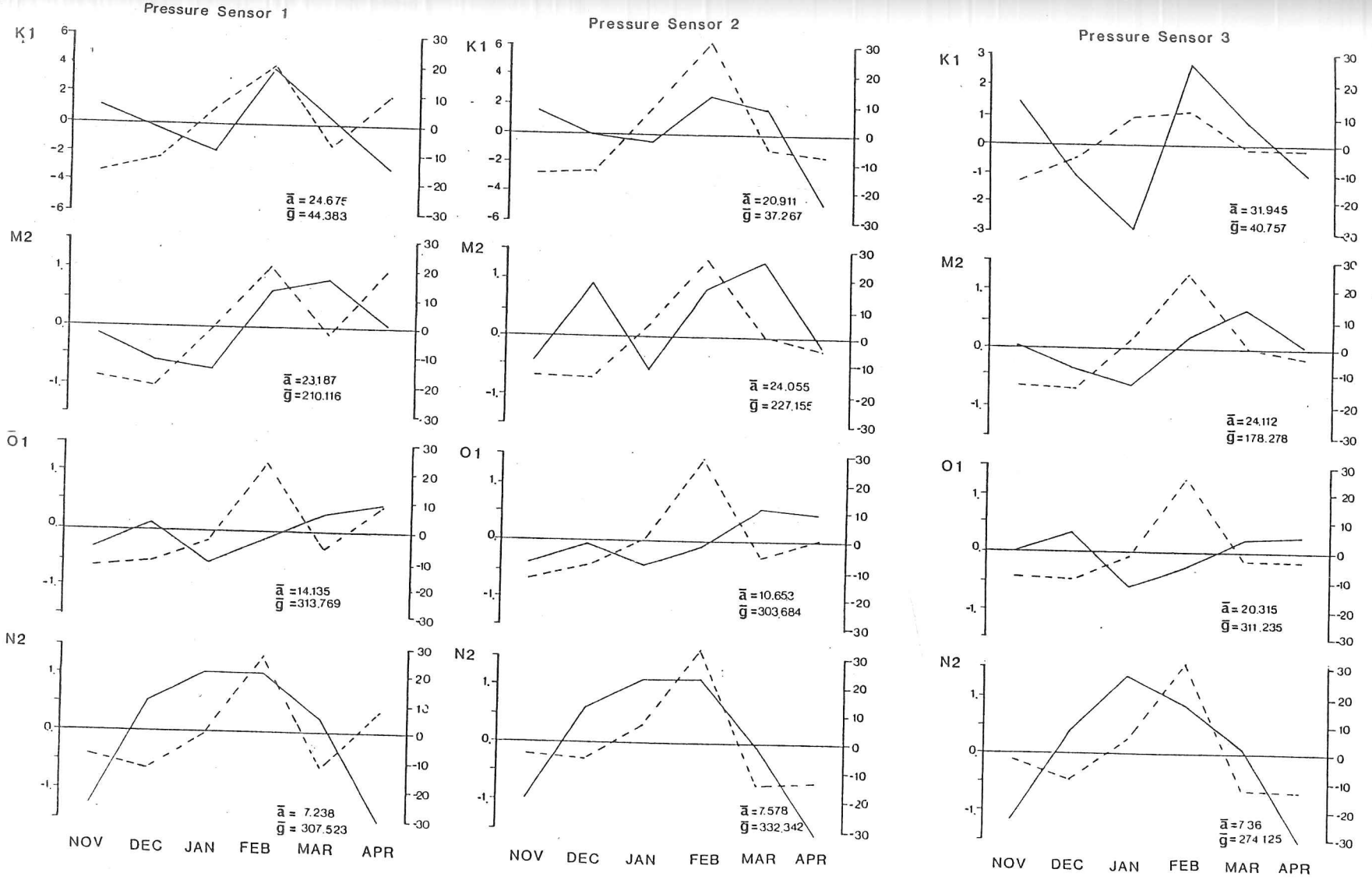

Figure 3.13: Amplitude and phase variability for the major tidal constituents seen in the bottom pressure sensor data obtained with the current meter moorings. The 6 month winter record was analyzed in 29 day sections.

4

ICE-OCEAN MODELLING

4.1 Introduction

The emphasis in modelling studies of ocean dynamics in the Bering Sea basin has either been with homogeneous ocean models forced by external tides (Hastings, 1976; Liu and Leendertse, 1978), or with models of ice motion which use simple atmospheric and oceanic boundary layers with respect to the ice cover (Overland *et al*, 1984). The previous work most relevant to our study of ocean processes at the ice edge is the two dimensional multi-level model with stationary ice cover developed by Niebauer (1982) to examine upwelling at the Bering Sea ice edge. Table 4.1 gives a summary of the mechanisms included in ice-ocean coupled models by several other authors.

In this chapter of the thesis we aim to build up a hierachy of models which examine different facets of the ice/ocean system, in an effort to understand the governing processes in the Bering Sea Marginal ice zone. We will discuss in turn, a one-dimensional model describing the momentum and buoyancy fluxes between the ice and upper ocean, a two-layer geostrophic model capped by a partial ice cover, and a two-dimensional multi-level ocean model with both dynamic and thermodynamic coupling to an ice model.

The impact of the sea ice cover is transmitted to the deep ocean through the oceanic boundary layer (McPhee, 1982). Hence, many large scale modellers who have parameterized the interaction between the ice and ocean have represented the ocean by a mixed layer of constant depth (Hibler, 1979; Bratchie, 1984; Parkinson and Washington, 1979). Hence, the first stage in examining the ocean structure beneath the ice in the Bering Sea was to adapt a mixed layer model which had been

TABLE 4.1: Mechanisms included in coupled ice-ocean models

Author	Ice model	Ocean model
Hakkinen (1986)	Reiner-Rivlin rheology	reduced gravity
Hibler and Bryan (1984)	Elastic-plastic rheology	3-D primitive equation
Ikeda (1985)	shear stress along ice edge pressure term across ice edge	2-D primitive equation
Ikeda (1986)	Thermodynamic forcing for ocean	2nd order turbulent closure mixed layer model
Lemke and Manley (1984)	Seasonal cycle of buoyancy and surface stress	Mixed layer model with advection
Markham (1983)	Buoyancy input and surface stress	Mixed layer model embedded in primitive equation model
Niebauer (1982)	Stationary ice cover	2-D primitive equation
Røed and O'Brien (1983)	Ice pressure term for rheology Solved along equation characteristics	reduced gravity
Semtner (1987)	Ice resistance during convergence	3-D primitive equation
Sjøberg and Mork (1985)	ice cover represented by semi-infinite plane transmitting stress discontinuity	2 layer

developed for central Arctic conditions (Lemke, 1979) to the Marginal ice zone. The model concentrates on how the balance between the buoyancy input from melting ice and the turbulent mixing forces alter the characteristics and depth of the upper ocean layer. The ocean is assumed to be horizontally homogeneous, a reasonable approximation for the long term average temperature and salinity fields well away from major dynamical features. The only feedback from the ocean model to the ice cover is a temperature dependent melt rate; ice velocity and ice concentration remain unaltered in the simplest configurations of the model. The budgets of heat and salt are maintained separately in the model as the heat flux is necessary to calculate melt rates. The buoyancy value is calculated from a linear function of the salinity and temperature values. The heat budget includes short and longwave radiation, sensible and latent heat fluxes, transfer through the ice, and heat losses due to melting (section 1.3).

A one-dimensional model such as this indicates the short-term response of the ocean (less than one inertial period) to changes in the wind, ice velocity or heat budget terms, or to the initiation of buoyancy input after ice has ice advected across an ocean thermal front. However, the one-dimensional model does not provide an ideal base for examining the case of the ocean thermal front. Therefore, once the results indicating the relative importance of the heat budget terms and

the division between mechanical and convective mixing had been analyzed, the model was not developed further.

A more realistic approach to the ice edge frontal problem, bearing in mind the two distinct layers in the Bering Sea frontal section, was thought to be a two layer ocean with the isopycnal allowed to intersect the surface. Several simple layer models for shelf frontal systems have been proposed (Ou, 1983, 1984a,b; Stommel and Veronis, 1980). In section 4.3 we describe attempts to formulate similar quasi-steady state models for a two layer ocean bounded by homogeneous water masses and capped by a partial ice cover.

Neither of these simplified models gives the information on ice edge evolution that we require in order to explore feedback between the ice cover and ocean. The two layer model has several problems. Firstly, the faster response of the ice model to an impulsive change in external conditions, and secondly, our inability to set appropriate matching conditions at the moving frontal boundary for the model to represent a reasonable analogy to the field situation.

We progressed to using a multi-level ocean model with the density distribution defining the boundary of the frontal feature. However, we again must invoke simplifications to the full three dimensional problem, the most obvious being to ignore along-edge gradients. We can justify this approach in the first instance by examining the CTD transects made at several points across the ice edge (Muench *et al*, 1985) and the aerial photographs of the ice cover. These show that the density and ice floe characteristics are principally determined by the distance from the ice-water boundary. Further, the focus of our study is on *how* the frontal features change as the ice advances across the shelf, rather than on three-dimensional structures such as eddies which would complicate the dynamics. Instabilities of the ice ocean frontal jet do exist however, a 2-4 day spectral peak in the current meter data was attributed by Muench and Schumacher (1985) to baroclinic instabilities. There is no evidence that these instabilities play an active part in the ice-ocean interaction process in the Bering Sea. This latter statement is not true of other ice edge regions. In the Greenland Sea, Labrador Sea and Antarctica strong currents shed numerous eddies (section 2.6). Hence this model is not suitable for such regions, and can only be adapted to localized regions away from strong shear zones where the processes can be considered two-dimensional .

4.2 One dimensional mixed layer models of the upper ocean under ice

Models of the mixed layer under ice, considering only salinity changes, have been developed on a seasonal time scale by Lemke (1979) (extended in Lemke and Manley, 1984). Pollard *et al* (1983) extended to polar latitudes a transect from north to south across the globe by calculating mixed layer depths at high latitudes using salinity conservation equations. Disregard of the temperature changes that occur in a salinity stabilized mixed layer may be a reasonable first approximation for the central Arctic, but in the marginal ice zone the ice edge location is determined by its proximity to ocean heat sources. These sources may increase the heat supply to the ice either by entrainment from below the pycnocline or across a horizontal density front.

We have confined the preliminary part of our one-dimensional study to an extension of the Lemke (1979) model to a partially ice covered region. It is an attempt to complement other work by MIZEX researchers in which turbulent boundary layer theory has been used to describe the transfer of heat from the upper ocean needed to melt ice (McPhee, 1983; Josberger, 1983). Following Lemke's earlier model we use an ice keel mechanism to generate turbulence under the ice and will compare the effectiveness of this ice-ocean stress with directly imposed wind stress as the amount of open water increases.

The model used is the simple bulk mixed layer formulation originally proposed for the ocean by Kraus and Turner (1967) and reviewed by Niiler and Kraus (1977). The entrainment velocity in the model is derived from the turbulent kinetic energy budget. At this initial stage we are primarily interested in the properties of the density layer under the ice, and since we have no field observations of velocity shear in the mixed layer we have set the mean horizontal velocity to zero. The temperature fluxes (section 1.3) used in the model have been weighted with respect to the percentage of open water present. We have assumed that some heat is transmitted through the ice cover. The temperature calculation for the ice-covered section includes the latent heat transfer equivalent to the proscribed ice melt/growth rate. The salinity flux is related only to ice process, with no allowance for evaporation or precipitation.

4.2.1 The equations

The principal assumptions in the derivation of mixed layer models are:

1) the temperature and salinity can be considered to be uniform over a given layer of water column

and also uniform in the horizontal;

2) the pycnocline can be modelled by a discontinuous step in the temperature and salinity properties;

3) during deepening of the mixed layer, water is entrained from the fluid beneath.

If however, the turbulent generating forces are not sufficient to overcome buoyancy input, the mixed layer rapidly shallows to the Monin-Obukhov length (equation 4.18). Derivation of the basic equations used in the model will now be given.

The equations of continuity for the temperature (T) and salt (S) budgets when horizontal gradients are neglected are given by

$$\frac{\partial \bar{T}}{\partial t} + \frac{\partial \overline{(w'T')}}{\partial z} = 0 \tag{4.1}$$

$$\frac{\partial \bar{S}}{\partial t} + \frac{\partial \overline{(w'S')}}{\partial z} = 0 \tag{4.2}$$

The quantities marked by overbars are averages whilst the turbulent deviation from the mean is marked by a prime. No velocity budget is calculated as the mean horizontal velocity has been set to zero.

By assumption (1) the temperature and salinity characteristics within the layer are independent of z, so we can integrate from the surface $z = 0$ to the time dependent depth $z = -h$, then

$$h\frac{\partial \bar{T}}{\partial t} = \overline{(w'T')}_{z=-h} - \overline{(w'T')}_{z=0} \tag{4.3}$$

$$h\frac{\partial \bar{S}}{\partial t} = \overline{(w'S')}_{z=-h} - \overline{(w'S')}_{z=0} \tag{4.4}$$

By assumption (2) the flux condition for temperature and salinity at the base of the mixed layer across the pycnocline is represented by a discontinuous step ΔT and ΔS, respectively.

$$\overline{(w'T')}_{z=-h} = -w_e \Delta T \tag{4.5}$$

$$\overline{(w'S')}_{z=-h} = -w_e \Delta S \tag{4.6}$$

where w_e is the entrainment velocity, the rate at which the mixed layer is deepening.

$$\begin{aligned} w_e &= dh/dt \text{ when } dh/dt > 0 \\ &= 0 \text{ when } dh/dt \leq 0 \end{aligned} \tag{4.7}$$

The surface salinity flux is given by

$$\overline{(w'S')}_{z=0} = \frac{(S_o - S_i)R}{h} \tag{4.8}$$

where S_o is the salinity of the surface layer (a function of time only), S_i is the salinity of sea ice (5-10 ‰), and R is the melt rate (a function of the heat available in the mixed layer to melt or accrete ice). The surface boundary condition for temperature is a combination of an open water flux value for all the heat budget terms, and a term proportional to the ice concentration which includes the heat transfer through the ice (exchange coefficient κ_i) and latent heat exchange (L_m) during melt/growth processes.

$$\begin{aligned}\overline{(w'T')}_{z=0} &= \frac{(1-A)\rho_a C_T U(T_{sfc}-T_a)}{\rho_o c_p h} + (1-\alpha)(1-0.6\mathrm{cld}^3)F_R \\ &+\rho_o L C_T U(Q_a - Q_{sfc}) - \epsilon_I \sigma T_{sfc}^4 \\ &-\epsilon_I \sigma T_a^4 (1-0.261\exp(-7.77\times 10^{-4}(T_a-273)^2)) \\ &+\frac{AL_m R}{\rho_w c_p h} + \frac{AR(T_o-T_B)}{h} + \frac{\kappa_i(T_B - Tsfc)}{h_i} \end{aligned} \tag{4.9}$$

The nomenclature for the above heat budget terms is defined in section 1.3 and in glossary.

The entrainment velocity w_e is calculated by integrating the turbulent kinetic energy budget over the mixed layer. Invoking the simplifications detailed by Niiler and Kraus (1977) the energy budget becomes

$$\underset{(A)}{\frac{1}{2}\frac{dh}{dt}(q^2+\ \Delta bh)}\ \underset{(B)}{=m_1 u_*^3}\ \underset{(C)}{+\frac{1}{2}hB_o}\ \underset{(D)}{-\int_0^{-h}\epsilon dz} \tag{4.10}$$

where the terms in the equation represent

(A) is the rate of energy needed to agitate the entrained water mass

(B) work per unit time to mix the entrained dense water through the layer

(C) Rate of working of the external forces (wind, waves)

(D) Rate of potential energy changes introduced by the surface fluxes (buoyancy forcing)

(E) Dissipation

4.2.2 Parameterizations

The primary difference between all the bulk mixed layer models is the method by which dissipation of the turbulent energy is represented. Intuitively the dissipation should be a function of the turbulent generating terms, i.e., the wind mixing (C) and Buoyancy forcing (D) when convection occurs ($B_o > 0$). Hence, we chose to incorporate the effect of the dissipation into the unknown coefficients already associated with these terms, e.g., the m_1 for the wind generating term. Both the wind and ice keel mixing terms are given in the form of constant (m_1) times the third power of the friction

velocity u_*, making it easier for the relative contribution of the wind mixing and ice keel stirring to the total mixing to be assessed. Values of m_1 of O(1) are quoted for most mixed layer situations with $m_1 = 1.25$ providing a good match for field profilesDenmanand Miyake, 1973). Alternatively, the ice keel drag can be used to calculate the rate of working ($\tau_i \times \mathbf{u}_i$) where $\tau_i = c_D \mathbf{u}_i \mid \mathbf{u}_i \mid$. With a suitable choice of c_D this form is equivalent to the earlier friction velocity term. The convective energy can either be non-penetrative (coefficient $n = 0$) or fully penetrative ($n = 1$). Data collected by Farmer (1975) on mixed layer deepening beneath ice in a freshwater lake gave an average value for the convective dissipation coefficient n of 0.036 which we will use in our standard model runs.

Another view is that the dissipation can be expressed as an exponentially decreasing function of depth with a residual background dissipation (Alexander and Kim, 1976). Here

$$\int_0^{-h} \epsilon dz = \epsilon_o h + e^{-\gamma z}. \tag{4.11}$$

This background dissipation (ϵ_o) accounts for all the dissipation not included in the coefficient (m_1) of the friction velocity representing wind mixing/ice stirring. If dissipation does not cease at some point the mixed layer will deepen towards infinity, and when subjected to cyclical seasonal wind and buoyancy forcing will be unable to repeat the same cycle the following year. Several authors (Gill and Turner, 1975; Stevenson, 1979; Niiler, 1977) have addressed this infinite deepening question. Niiler (1977) has suggested that if the sum of the background dissipation and half the maximum buoyancy input in the sinusoidal forcing term remains positive throughout the cycle then infinite deepening is arrested. However, Stevenson argues that a non-zero background dissipation is sufficient for the deepening to cease at some depth. Hence, we also need to invoke some relationship between the dissipation and depth in our model to prevent infinite deepening. Lemke (1979) model used a linear relationship between dissipation and depth, with a cut off at depth H_r to prevent infinite deepening, of the form

$$m_1 = m_2(1 - h/H_r), \tag{4.12}$$

He suggested, however, that an exponential form might be more reasonable, as too much energy was available for entrainment causing rapid deepening at the beginning of the freezing period. Similarly, Lemke set n, the partially penetrative convection coefficient, to cut off at the same depth H_r, giving

$$n = (1 - h/H_r). \tag{4.13}$$

These different dissipation forms will be compared in the model runs below. Although we have not using cyclical forcing in our mixed layer simulations, the model continues to deepen after melting ceases as both the convective mixing from brine input and ice stirring act simultaneously.

The set of equations to be solved in the model are

$$\frac{dT_o}{dt} = \frac{w_e \Delta T}{h} - \frac{Q}{\rho_o c_p h} \tag{4.14}$$

$$\frac{dS_o}{dt} = \frac{w_e \Delta S}{h} - \frac{R(S_o - S_i)}{\rho_i h} \tag{4.15}$$

where Q represents all external thermal forcing, and R is the melt rate.

The entrainment velocity

$$w_e = \frac{dh}{dt} = \frac{(2mu_*^3 + nhB_o)}{(q^2 + \Delta bh)} \tag{4.16}$$

where m is a function of depth and

$$\begin{aligned} n &= 1 \quad \text{if } B_o \leq 0.0 \\ n &= 1 - h/H_r \quad \text{otherwise} \end{aligned} \tag{4.17}$$

In the limit as the entrainment velocity $w_e \rightarrow 0$, the mixed layer shallows to the Monin-Obukhov length (L) which is given by rearranging equation 4.18 to give

$$L = \frac{2m_1 u_*^3}{nB_o} \tag{4.18}$$

Seasonal mixed layer models are normally driven by the solar insolation cycle and hence they display a gradual shallowing of the layer depth as the buoyancy reaches a maximum, with the minimum depth occurring in summer. In the ice edge situation we wish to simulate the transition is more abrupt, with the buoyancy input to the upper ocean a function of the horizontal temperature gradient in the ocean front. The ice is probably being advected too rapidly through this narrow zone for an appreciable change in melt characteristics to occur. So, we initiate our model with an impulsive input of buoyancy. The meltwater input which enters the ocean is cooler than the ambient fluid which in turn cools thereby reducing the melt rate. Thus, our buoyancy function starts impulsively at its maximum value, decreases as the water cools, and then keeps alternating in sign once freezing is reached and brine convection is temporarily switched on.

If the buoyancy forcing is greater than turbulent generating forces, the mixed layer should in theory, shallow instantaneously. In a numerical model, however, we weight the rapid detrainment

of the layer by local turbulence (q^2), as given in the denominator of equation (4.16). Although the local turbulent velocity scale is unknown, it is normally estimated to be related to the friction velocity with Kim (1976) choosing $q = \max\{3 \times 10^{-2}\,\mathrm{ms}^{-1}, 3u_*\}$. This parameterization hardly alters the entrainment phase as $\Delta bh >> q^2$ whilst successfully arresting the rapid detrainment.

4.2.3 Results from parameter sensitivity tests

We have run the one-dimensional model for several sensitivity tests to examine both the various mixing and dissipation parameters, and also to look at suitable functional forms for the melt/growth rate. The buoyancy flux is imposed by allowing a temperature step to represent the change as the ice drifts across the front. Very rapid shallowing is induced, producing mixed layer depths less than 5 m when the temperature step is of order 1 °C and the wind conditions are moderate.

However, at the edge of the Bering Sea few shallow mixed layers persist for more than a few hours, indicating that they are quickly destroyed by the wind-dominated regime. In contrast, in the Greenland Sea during summer melt conditions, slack winds prevail and the existance of very shallow mixed layers is widespread.

Results from our standard runs are fairly predictable: the shallowest depths reached are equivalent to the Monin-Obukhov length, (eqn. 4.18); and the density of the entrained fluid is determined by the salinity/temperature profile formed during the retreat (Fig 4.1). For our sensitivity tests of the various dissipation coefficients and heat terms we have considered the case when the model is most stretched. This is when the temperature is near to freezing, and there is a switch between positive and negative buoyancy input. All the other model runs will reach this situation eventually, for the meltwater is continuously cooling the upper layer and there is no compensating increase in insolation included in the model. The same external conditions are imposed throughout the model run. Thus if the air temperature remains below freezing, the upper mixed layer eventually cools to the point where ice will grow if there are no additional heat source terms. The ice melt rate function used changes sign when the surface water temperature drops below freezing. In simulations away from the freezing point we defined the melt rate as an exponential function of temperature. However, close to freezing this is not suitable and the melt rate is given by a linear function of the thermal driving, i.e., the excess temperature above freezing point (Josberger, 1983). Details of the control parameter set are given in Table 4.2. The initial conditions selected for the upper layer of the ocean were a salinity of 32.2 ‰ and a water temperature of -1.55 °C. The calculated melt

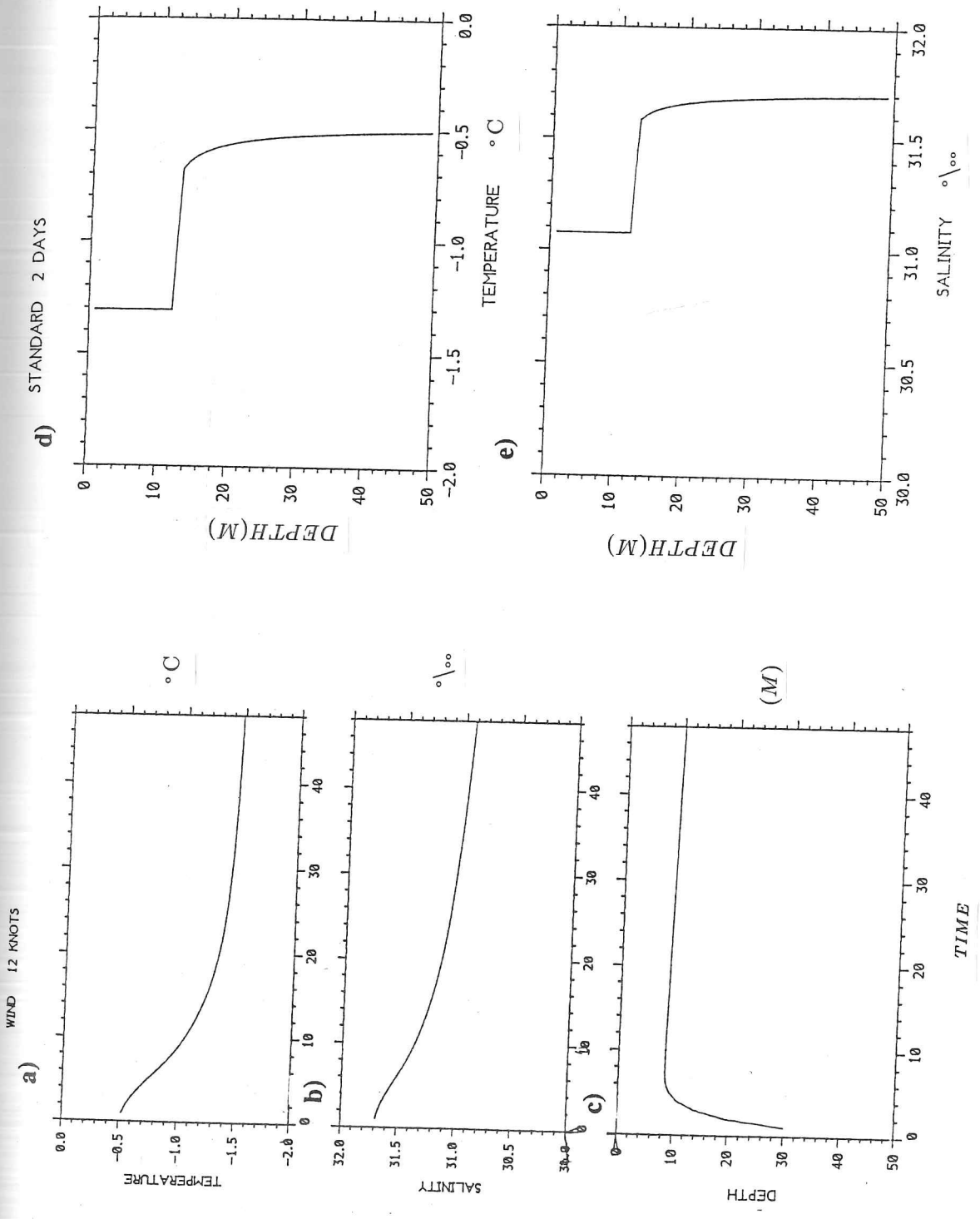

FIGURE 4.1: Results from one dimensional model simulations after 2 days forcing with 12 m s^{-1} winds. The change seen in 48 hours are shown for a) mixed layer temperature, b) mixed layer salinity and c) mixed layer depth. The vertical profiles after 48 hours are indicated for d) temperature and e) salinity.

TABLE 4.2: Model parameters for standard model runs

ice speed		$0.24\,\mathrm{m\,s^{-1}}$
wind speed		$10.0\,\mathrm{m\,s^{-1}}$
ice concentration		0.7
air temperature		$-20.0\,^{\circ}\mathrm{C}$
initial mixed layer depth		50 m
initial mixed layer temperature		$-1.55\,^{\circ}\mathrm{C}$
initial mixed layer salinity		32.4 ‰
ice temperature		$-0.288\,^{\circ}\mathrm{C}$
ice salinity		5.0‰
initial melt rate		$0.12\,\mathrm{m\,day^{-1}}$
density of air	ρ_a	$1.225\,\mathrm{kg\,m^{-3}}$
density of water	ρ_w	$1026.0\,\mathrm{kg\,m^{-3}}$
specific heat of air	C_a	$1004.0\,\mathrm{J\,kg^{-1}\,K^{-1}}$
specific heat of water	c_p	$4.187 \times 10^3\,\mathrm{J\,kg^{-1}\,K^{-1}}$
longwave emmisivity of ice	ϵ_w	0.97
Stefan-Boltzman constant	σ	$5.67 \times 10^{-8}\,\mathrm{W\,m^{-2}\,K^{-4}}$
water albedo	alb_w	0.1
cloud cover	cld	0.5
solar radiation	Q_o	$205\,\mathrm{MW\,m^{-1}}$
coefficient for sensible heat	C_T	3.3×10^{-3}
latent heat of freezing	L_m	$3 \times 10^8\,\mathrm{J\,m^{-3}}$
thermal conductivity	κ_i	$2.04\,\mathrm{W\,m^{-1}\,K^{-1}}$
Dissipation for standard runs		
m	$m_1(1 - h/150)$	
n	$n_1(1 - h/150)$	
n_1	0.036	
m_1	1.25	

rate for these properties was to $12.5\,\mathrm{cm\,day^{-1}}$ for a water temperature of $-1.55\,^{\circ}\mathrm{C}$ (equivalent to $50\,\mathrm{cm\,day^{-1}}$ in waters of $-1.0\,^{\circ}\mathrm{C}$, cf. Josberger, 1983).

Most of the results generated with the parameter changes are as one would expect, with increasing wind mixing and surface buoyancy flux causing deepening and shallowing respectively when compared to the mixed layer depth in the standard case. These runs do however, indicate the range of values over which the main parameters may be varied whilst still achieving a realistic balance between melt-derived buoyancy and typical MIZ ice/wind speeds. If no dissipation terms are included in the model the mixed layer depth will initially shallow and will then deepen continuously

out of the model grid. The temperature cools to freezing and the salinity value decreases by up to 0.1‰ during the melt period. Then the salinity gradually increases once the water column reaches the freezing point. Over a 14 day period a 20 cm decrease in the average ice thickness is induced by the variable melt/freeze rate.

Allowing linear dissipation of wind generated terms with a cut-off at a depth of 150 m produces a decrease in the shallowest depth of 10%. When dissipation of buoyancy is included, no change in the minimum depth profile is recorded, as the convective energy is only available when buoyancy becomes positive. If however, we allow the decay of wind energy to be an exponential function

$$m_1 = m_3 \exp(-Kh/150) \tag{4.19}$$

with K in the range of 1 to 15, then the minimum depth can be reduced by up to 50%. However, the mixed layer deepening will continue at a slower rate. Inclusion of a background dissipation term (Alexander and Kim, 1976) only increases the infinite deepening of the mixed layer with more energy available. In order to arrest infinite deepening both wind-generated and buoyancy-generated turbulence must decay with depth.

If buoyant dissipation is ignored in the above runs the mixed layer is able to shallow again after reaching the maximum given by the wind energy decay. Hence, the maximum depth to which deepening occurs is dependent on convective energy. Though the convective dissipation cannot be ignored, the model is not very sensitive to the choice of coefficient n, as the dissipation of convective energy is only invoked for short periods when freezing occurs.

A doubling of the wind mixing coefficient will cause the mixed layer to be 50% greater than the standard case, but a 10-fold increase in wind-derived energy will hardly disturb the mixed layer from its initial position. Hence, the coefficient ($m_1 = 1.25$) used in our control experiment is reasonable for the range of wind/ice velocity conditions encountered. Because the ice velocity and wind speeds are represented in the entrainment equation as a friction velocity term to the third power, a doubling of our standard wind and ice velocity parameters will give an 8-fold increase in the available turbulent energy and there will be little alteration to the mixed layer depth with this level of buoyant influx. An increase in wind speed of 50% in the open water, without an associated increase in ice speed, causes an increase in the deepening rate of about 30%.

The magnitude of ice velocity and wind speeds in the standard runs have been chosen to give the same friction velocity. If however, we change the initial ice concentrations then the effect of

velocities will be altered. Decreasing the initial ice concentration causes an increase in the rate of deepening, as extra freezing occurs. The opposite effect occurs if the initial ice concentration is greater than the standard simulation. In none of these simulations does the minimum mixed layer depth change by more than 20%. An increase in initial ice concentration from 7/10 to 9/10 introduces equivalent changes in the temperature, salinity and mixed layer depth time series as would an increase in the air temperature by 10 ° C. Other heat budget parameters were also tested, but if the incoming radiation remains constant then the air temperature (through its inclusion in the sensible heat flux and longwave radiation terms), has the most significant effect on the overall heat budget.

4.3 Two layer geostrophic model

The frontal region beneath the Bering Sea ice edge is divided into two well-defined water masses, separated both vertically and horizontally by sharp density fronts. Similar frontal configurations are encountered in most branches of coastal dynamics, both at the scale of estuarine plume fronts (Garvine, 1974) and seasonal fronts formed at the shelf break (Flagg and Beardsley, 1978). In both these instances, the stratification is dominated by the lighter coastal water which can be treated as a continuous inflow at the inner boundary.

In the case we wish to consider, however, the buoyancy is input from above, reaching a maximum at the surface manifestation of the front. Details of flow in such two layer frontal systems have been described using simple analytical and numerical models. In each case, the models are very idealistic with only some of the pertinent mechanisms affecting the flow included in any one model. These mechanisms include earth's rotation, entrainmment and diffusion across the interface, freshwater buoyancy, wind forcing, and bottom topography.

A principal factor in many of these two layer models is the choice of initial configuration. Frequently, the initial condition chosen is for the two fluids to be considered at rest separated by a hypothetical barrier. On removal of this barrier the lighter fluid flows over heavier and vice-versa until an equilibrium state is reached. The adjustment process takes place over several inertial periods, with the energy dissipated by inertial oscillations. Details of the equilibrium layer depths, the layer velocities and the shape of the front can be obtained by invoking both conservation of mass and conservation of vorticity alongside the momentum equations in the two fluids.

Several boundary conditions are required to close the problem but these must be imposed at the yet unknown extents of the front. Possible conditions are setting one of the layer depths to be zero outside the bounds of the front, we could for example, impose geostrophic flow at the front or a condition on the surface displacement. In order to close the system, further conditions involving continuity in some of the variables may be needed. These extra matching conditions may include constraints on derivatives of variables across the frontal interface.

The simplest case to consider is when two fluids are positioned over a flat base and the water column height is confined (rigid lid), then four matching conditions are sufficient to solve problem. In some models, particularly those over sloping beds, (Stommel and Veronis, 1980; Hsueh and Cushman-Roisin , 1983) the solution is found by an iterative technique with progressive matching at each boundary. The error introduced by this approach is calculated using the final matching condition and then the initial estimate is updated so that eventually the solution converges.

In the most basic two layer models no mixing across the vertical and horizontal interfaces is permitted. The upper fluid will then only change density during the simulation if there is a source of lighter coastal fluid in the model. We have to invoke the full momentum and conservation equations if we wish to consider the case of a continuously stratified fluid, though the solution can be obtained numerically (Kao, 1981; Wang, 1984). In such models the frontal boundary is defined either by the region of strongest gradient or by a particular isopycnal.

Some models have included mixing between the two layers. Ou (1983) included an entrainment flux in the pycnocline generated by the surface stress, whilst Csanady1984) also allowed detrainment of the fluid from the upper to the lower layer particularly at the head of the front (Garvine, 1979). Entrainment in the Ou (1983) model balances the along-front current shear, thereby enhancing off-shore transport. The transports induced in the geostrophic adjustment process are baroclinic with the exception of the bottom topography case, where the surface barotropic mode is included in the adjustment process if the rigid lid assumption is relaxed. Stommel and Veronis (1980), in comparing solutions of the flat bottom case with and without the rigid lid condition, concluded that little difference was made to the overall dynamics of the front. This, they felt, justified the use of the rigid lid assumption in more mathematically complex frontal systems.

When a wind impulse is imposed at the start of the simulation, the effect on a simple flat bottomed, rigid lid model of a front is to shift the position of the interface across the shelf by a distance related to the additional transport generated by the wind impulse. No alteration is made to the

frontal shape or to the depth of the upper layer (excluding wind induced entrainment). If, however, the front overlies a slope, different wind impulses will be imposed on each section causing a narrowing or broadening of the frontal region which is dependent on the sign of the impulse (Hsueh and Cushman-Roisin, 1983). If the shelf/slope frontal system is forced by an along-front wind, the boundary is advected offshore on to the slope region and the depth of the upper layer is only slightly altered. If, however, the wind is forcing the fresher water to be constrained to the shelf zone, the upper layer deepens and along-shelf flow is increased (Ou, 1984b).

Below we outline a time-dependent 2-layer ocean model which is overlain by a simple advective ice model. In the initial integration the densities for each layer remain constant since the interfacial entrainment flux is set to zero. Only dynamical aspects of the ice-ocean interaction are included. Time derivatives for along-front and cross-front velocities, and the layer depths derived from the continuity and momentum equations, are obtained in each of 3 sections; in advance of the front, in the two-layered section, and behind the front (Fig 4.2). A fourth sub-division is introduced by the ice edge boundary.

The ice parameters (velocity and compactness) are calculated from a simplified ice momentum equation without internal stress and sea surface slope (see Eqn 1.6) and a conservation equation for the ice compactness (A). The position of the frontal interface and the ice boundary which bound the integration regions of the model (points a, b and c) are relocated at the end of each time step using the cross-frontal velocity calculated by the model just behind the front. No matching conditions were imposed at these boundaries except in the model runs where a rigid lid is assumed whence the total depth H remains constant across the two boundaries.

The equations for this model are similar to those of the wind driven model developed by Ou (1984b), where the time-dependent wind advection of a front is considered. We have simplified the system by ignoring bottom topography.

The system of equations used, with the ice edge placed ahead of the front without loss of generality are

y > c

Ocean model:

$$\frac{\partial U_2}{\partial t} = fV_2 + \tau_x \qquad (4.20)$$

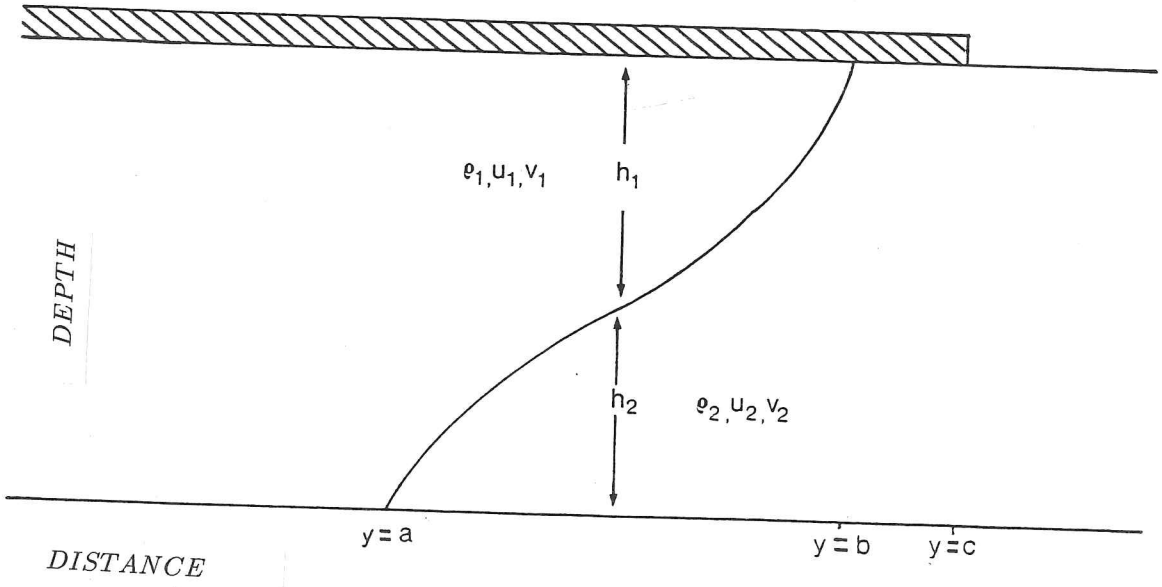

FIGURE 4.2: Configuration of two layer frontal model. The front extends between points $y = a$ and $y = b$ and the ice position is marked by point $y = c$.

$$\frac{\partial V_2}{\partial t} = -fU_2 + \tau_y \tag{4.21}$$

$$\frac{\partial h_2}{\partial t} + \frac{\partial (V_2 h_2)}{\partial y} = 0 \tag{4.22}$$

c > y > b

Ocean model:

$$\frac{\partial U_2}{\partial t} = fV_2 + ((1-A)\tau_x + A\alpha(u - U_2)) \tag{4.23}$$

$$\frac{\partial V_2}{\partial t} = -fU_2 + ((1-A)\tau_y + A\alpha(v - V_2)) \tag{4.24}$$

$$\frac{\partial h_2}{\partial t} + \frac{\partial (V_2 h_2)}{\partial y} = 0 \tag{4.25}$$

Ice model:

$$\frac{\partial u}{\partial t} = fv + \tau_{xi} + \alpha_i(U_2 - u) \tag{4.26}$$

$$\frac{\partial v}{\partial t} = -fu + \tau_{yi} + \alpha_i(V_2 - v) \tag{4.27}$$

$$\frac{\partial A}{\partial t} + \frac{\partial (vA)}{\partial y} = 0 \tag{4.28}$$

b > y > a

Ocean model:

$$\frac{\partial h_2}{\partial t} + \frac{\partial (h_2 V_2)}{\partial y} = 0 \tag{4.29}$$

$$h_1 V_1 + h_2 V_2 = 0 \tag{4.30}$$

$$\frac{\partial U_2}{\partial t} = fV_2 + \frac{w_e(U_2 - U_1)}{\rho_2 h_2} \tag{4.31}$$

$$\frac{\partial V_2}{\partial t} = -fU_2 + g\frac{\partial (h_2 + (1 - (\rho_2 - \rho_1)/\rho_2)h_1)}{\partial y} + \frac{w_e(V_2 - V_1)}{\rho_2 h_2} \tag{4.32}$$

$$\frac{\partial U_1}{\partial t} = fV_1 + (1-A)\tau_x + A\beta(u - U_1) - \frac{w_e(U_2 - U_1)}{\rho_1 h_1} \quad (4.33)$$

$$\frac{\partial V_1}{\partial t} = -fU_1 + g\frac{\partial(h_1 + h_2)}{\partial y} + (1-A)\tau_y + A\beta(v - V_1) - \frac{w_e(V_2 - V_1)}{\rho_1 h_1} \quad (4.34)$$

Ice model:

$$\frac{\partial u}{\partial t} = fv + \tau_{xi} + \beta_i(U_1 - u) \quad (4.35)$$

$$\frac{\partial v}{\partial t} = -fu + \tau_{yi} + \beta_i(V_1 - v) \quad (4.36)$$

$$\frac{\partial A}{\partial t} + \frac{\partial(vA)}{\partial y} = 0 \quad (4.37)$$

y < a

Ocean model:

$$\frac{\partial U_1}{\partial t} = fV_1 + ((1-A)\tau_x + A\beta(u - U_1) \quad (4.38)$$

$$\frac{\partial V_1}{\partial t} = -fU_1 + ((1-A)\tau_y + A\beta(v - V_1)) \quad (4.39)$$

$$\frac{\partial h_1}{\partial t} + \frac{\partial(h_1 V_1)}{\partial y} = 0 \quad (4.40)$$

Ice model:

$$\frac{\partial u}{\partial t} = fv + \tau_{xi} + \beta_i(U_1 - u) \quad (4.41)$$

$$\frac{\partial v}{\partial t} = -fu + \tau_{yi} + \beta_i(V_1 - v) \quad (4.42)$$

$$\frac{\partial A}{\partial t} + \frac{\partial(vA)}{\partial y} = 0 \quad (4.43)$$

where α is $\rho_2 C_{WL}/H, \alpha_i$ is $\rho_2 C_{WL}/\rho_i D$, and similarly for β and β_i with respect to ρ_1, u, v are ice velocities, U_1, U_2, V_1, V_2, are the velocities in the respective layers, h_1, h_2, and H are layer depths and total depth respectively, ρ_1 and ρ_2 and ρ_i are the densities of the water masses and the

ice density respectively, and τ_x and τ_y are the wind stresses in x and y directions. The far field boundary conditions are no slip, i.e., $u = v = 0$.

This model has unfortunately not proved to be successful, principally because the processes we are trying to describe are non-linear. In particular, the depth functions h_1 and h_2 produce negative ripples at the extreme end of the region, as the advection equation for layer depths contains numerical diffusion. Our method of defining the advection of frontal boundaries using the local velocities is also not widely used (only Ou, 1984b). The conservation of volume condition (4.14b) linking the layer depths in the 2-layer section (b,c), was replaced by a rigid lid constraint. Despite this changed condition, negative values of depths h_1, h_2 still occurred. Further, the inclusion of non-linear advection and dissipation terms into the momentum equations, which might have dampened the ripples, did not produce any overall improvement. No account of vorticity changes to the water column have been made in the model, which would be an additional set of constraints on the two layers.

The spin-up of the ice model from rest occurs more rapidly than in the associated ocean due to the different inertia of the systems. This is a problem in that insufficient ocean stress is available at the start of the model run to retard the ice acceleration generated by the wind forcing. The result is that the ice is capable of advecting out of our integration region before the ocean velocities have reached reasonable values. Finally, we note that the two-layer system could have been considered as a series of quasi-steady-state time steps, with changes in frontal location being instigated by an increase in buoyancy or by a change in the external stress. The equations derived would be similar to those solved by Csanady (1978) for each time step.

4.4 Multi-level ocean model

4.4.1 The model grid

We constructed a standard multi-level ocean model (Bryan, 1969) on a rectangular grid with x representing the direction parallel to the ice edge, y the direction normal to the ice edge, and z directed vertically downwards. The region of the ocean we wish to consider with the model is at most 400 km long, when located at a latitude of 60° north. It is therefore unnecessary to use either spherical co-ordinates in space, or a β-plane approximation for the coriolis term. In early model runs undertaken to test parameters of the model we used a horizontal grid 80 km wide with 1 km

grid spacing. At an intermediate stage, in order to give more resolution in the region of our primary interest close to the ice edge, the use of a variable horizontal grid was explored. The grid consisted of 1 km spacing in the centre 40 grid points, gradually increasing via an exponential relationship to $4-5$ km at the boundaries. In the final group of model runs we represented a 400 km long swathe of the Bering Sea, stretching from St Lawrence Island in the north of the basin to St Paul Island in the south, with a hundred 4 km horizontal grid points.

As we explained in the introductory section of this chapter, it was found that the computational time for the model runs was reduced by initially ignoring along edge gradients. Even though, the problem is two-dimensional in form, details of the along-edge baroclinic jet formed at the ice edge by the geostrophic balance with the density gradients is still simulated by the model.

The Bering Sea shelf is broad and shallow so in the model has been represented by a constant depth of 100 m. No bottom gradients have been included to represent the shelf slope, though this would be necessary if we wished to include a barotropic flow directed at an angle to the baroclinic current. This barotropic current has been suggested to be the major source of heat transport directed under the ice (Hendricks *et al*, 1985). However, it cannot be explicitly accommodated in this model as it has a non-zero gradient parallel to the ice edge. An attempt to include the effect of the heat flux from the current was made in the Bering Sea model runs (section 5.1) using a bottom heating term. No tidal currents are included in the model in spite of the major role they play in the shelf seas. In particular, these currents control the mixing in the lower part of the water column and hence the position of the lower front. We would therefore not expect the model to correctly represent the dynamics of the lower front.

4.4.2 Model Equations

The u and v momentum equations for the ocean model are given below. In order to complete the model we require the conservation equations for temperature and salinity, the equation of continuity and the hydrostatic equation. Density is determined from the salinity, temperature and pressure values, and as we are working within a low temperature range the full equation of state is used (Fofnoff and Millard, 1983).

$$\frac{\partial u}{\partial t} + v\frac{\partial u}{\partial y} + w\frac{\partial u}{\partial z} = fv + \tau_x + A_H\frac{\partial^2 u}{\partial y^2} + A_z\frac{\partial^2 u}{\partial z^2} \tag{4.44}$$

$$\frac{\partial v}{\partial t} + v\frac{\partial v}{\partial y} + w\frac{\partial v}{\partial z} = -fu + \frac{1}{\rho}\frac{\partial p}{\partial y} + \tau_y + HA_H\frac{\partial^2 v}{\partial y^2} + A_z\frac{\partial^2 v}{\partial z^2} \tag{4.45}$$

$$\frac{\partial w}{\partial z} + \frac{\partial v}{\partial y} = 0 \tag{4.46}$$

$$\frac{\partial T}{\partial t} + v\frac{\partial T}{\partial y} + w\frac{\partial T}{\partial z} = K_H\frac{\partial^2 T}{\partial y^2} + K_z\frac{\partial^2 T}{\partial z^2} \tag{4.47}$$

$$\frac{\partial S}{\partial t} + v\frac{\partial S}{\partial y} + w\frac{\partial S}{\partial z} = K_H\frac{\partial^2 S}{\partial y^2} + K_z\frac{\partial^2 S}{\partial z^2} \tag{4.48}$$

$$\frac{\partial p}{\partial z} = -\rho g \tag{4.49}$$

$$\rho = \rho(T, S, z) \tag{4.50}$$

where A_H, A_z are the horizontal an vertical eddy viscosities and similarly K_H, K_z are the horizontal and vertical eddy diffusivities.

The ocean surface stresses in the partially ice covered region are given by

$$\tau_x = (1 - A)C_D \mid U_g^x \mid U_g^x + A\rho_w C_w(u_i - U) \tag{4.51}$$

$$\tau_y = (1 - A)C_D \mid U_g^y \mid U_g^y + A\rho_w C_w(v_i - V) \tag{4.52}$$

where the drag on the ice C_D is set to be twice the drag coefficient for the open ocean C_w (Røed and O'Brien, 1983). Values used for each of the non dimensional drag coefficients are

$$C_w = 1.5 \times 10^{-3}; C_D = 3.0 \times 10^{-3}.$$

As we have followed the standard multi-level approach for the ocean section of the model the above equations are similar to those used by Niebauer (1982) to model ice edge upwelling. They differ, however, in that by ignoring along edge gradients we have retained the pressure gradient term only in the cross-edge momentum equation. With the pressure term present in only one of the equations the usual fluid dynamical technique of taking the curl of the momentum equations to eliminate the pressure term cannot be applied here. Direct integration of the hydrostatic equation gives a term dependent on the density structure through the water column, and an unknown surface pressure term. It is the effect of this latter term which we wish to determine.

We approach this indirectly. If we differentiate the y-momentum equation with respect to z we can directly substitute the density term in place of the lateral pressure gradient. The equation is now solved in the time domain for $\partial v/\partial z$ by the conventional finite difference method. This leaves us with $\partial v/\partial z$ defined at each vertical grid point. We invoke a rigid lid condition that implies that the vertically integrated flow is zero, and then we can solve the resulting difference equations. Hence, the surface velocity value is determined as a sum of the vertically differentiated components.

$$\frac{\partial w}{\partial z} + \frac{\partial v}{\partial y} = 0 \tag{4.46}$$

$$\frac{\partial T}{\partial t} + v\frac{\partial T}{\partial y} + w\frac{\partial T}{\partial z} = K_H\frac{\partial^2 T}{\partial y^2} + K_z\frac{\partial^2 T}{\partial z^2} \tag{4.47}$$

$$\frac{\partial S}{\partial t} + v\frac{\partial S}{\partial y} + w\frac{\partial S}{\partial z} = K_H\frac{\partial^2 S}{\partial y^2} + K_z\frac{\partial^2 S}{\partial z^2} \tag{4.48}$$

$$\frac{\partial p}{\partial z} = -\rho g \tag{4.49}$$

$$\rho = \rho(T, S, z) \tag{4.50}$$

where A_H, A_z are the horizontal an vertical eddy viscosities and similarly K_H, K_z are the horizontal and vertical eddy diffusivities.

The ocean surface stresses in the partially ice covered region are given by

$$\tau_x = (1 - A)C_D \mid U_g^x \mid U_g^x + A\rho_w C_w(u_i - U) \tag{4.51}$$

$$\tau_y = (1 - A)C_D \mid U_g^y \mid U_g^y + A\rho_w C_w(v_i - V) \tag{4.52}$$

where the drag on the ice C_D is set to be twice the drag coefficient for the open ocean C_w (Røed and O'Brien, 1983). Values used for each of the non dimensional drag coefficients are

$$C_w = 1.5 \times 10^{-3}; C_D = 3.0 \times 10^{-3}.$$

As we have followed the standard multi-level approach for the ocean section of the model the above equations are similar to those used by Niebauer (1982) to model ice edge upwelling. They differ, however, in that by ignoring along edge gradients we have retained the pressure gradient term only in the cross-edge momentum equation. With the pressure term present in only one of the equations the usual fluid dynamical technique of taking the curl of the momentum equations to eliminate the pressure term cannot be applied here. Direct integration of the hydrostatic equation gives a term dependent on the density structure through the water column, and an unknown surface pressure term. It is the effect of this latter term which we wish to determine.

We approach this indirectly. If we differentiate the y-momentum equation with respect to z we can directly substitute the density term in place of the lateral pressure gradient. The equation is now solved in the time domain for $\partial v/\partial z$ by the conventional finite difference method. This leaves us with $\partial v/\partial z$ defined at each vertical grid point. We invoke a rigid lid condition that implies that the vertically integrated flow is zero, and then we can solve the resulting difference equations. Hence, the surface velocity value is determined as a sum of the vertically differentiated components.

The other velocity values can be determined using this upper value as a starting point (Killworth, personal communication, 1985).

The advective terms in the momentum and continuity equations have been finite differenced on the grid to conserve energy to second order. The variables are positioned on the grid as shown in Fig (4.3), with velocity calculated at half grid points and passive tracers (salinity, temperature, ice concentration and ice thickness) at whole grid points (Simmons, 1980). Fortunately, as we are using the model grid only in two dimensions we have fewer problems than would arise with a three dimensional grid. In that case u and v velocities are defined at different points in the grid, so that additional averaging is needed when calculating the Coriolis term in the momentum equation (Mesinger and Arakawa, 1976). The scheme used to calculate the Coriolis terms is the Sielecki (1968) semi-implicit scheme (Røed and O'Brien, 1983; Hamilton and Rattray, 1978), where the u velocity is calculated at the current time step and is then used in the $v$momentum equation.

All space derivatives in the equations (4.44–4.50) are centre differenced, whilst time derivatives are evaluated either by a leap-frog scheme where the calculation moves from the $n-1$ step to to the $n+1$ time step using advective terms calculated at the n th time step or by the Lax-Wendroff scheme which calculates the full time step of the model using two stages (Mesinger and Arakawa, 1976). In this latter scheme, the first stage uses the $n-1$ values to generate velocities and salinity and temperature fields at $n-\frac{1}{2}$. The second stage to produce the n th time step values is to use these updated values in the iteration for all but the diffusive and viscosity terms. The advantage of the Lax-Wendroff scheme is that it avoids the growth of the computational mode which causes the solutions in the Leap frog scheme at the n th and $n+1$ th time step to diverge.

4.4.3 Model parameters and boundary conditions

The horizontal viscosity and horizontal diffusion were set at a value of $200\,\mathrm{m^2\,s^{-1}}$ for a horizontal grid size of 1 km. The Vertical viscosity and diffusion are determined from the Munk and Anderson (1948) formulae developed for vertical mixing in the deep ocean, though they have been used successfully in other situations.

$$K_H = K_o(1+3.33\mathrm{Ri})^{-1.5} \tag{4.53}$$

$$K_o = 0.005\,\mathrm{m^2\,s^{-1}} \tag{4.54}$$

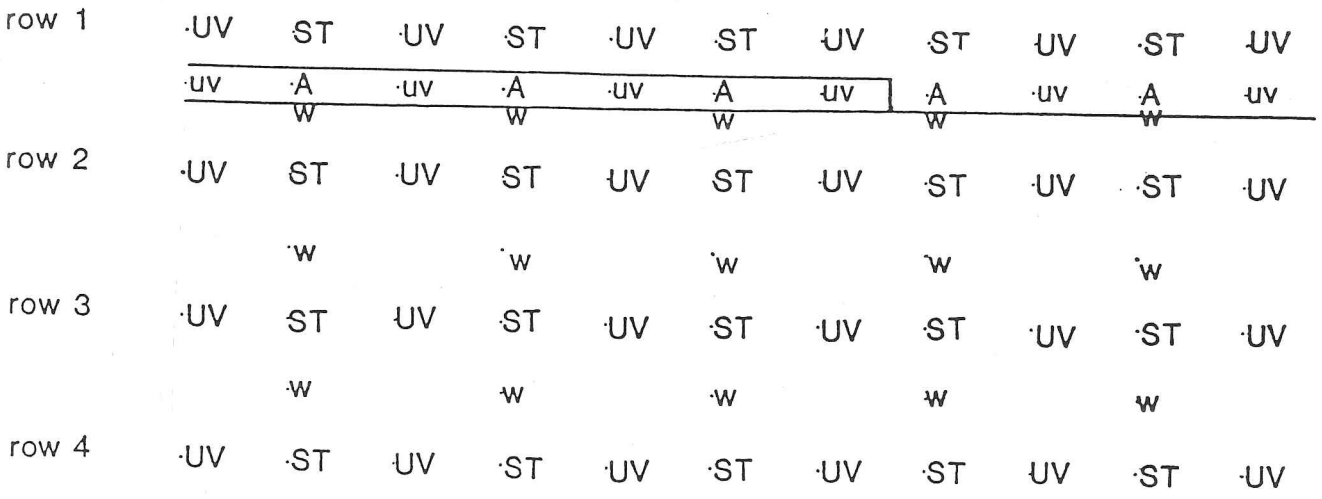

Figure 4.3: Diagram showing the layout of the variables for the finite difference scheme used by the multi-level model. Velocities are calculated at the 1/2 grid point position and the scalars at the edge of the grid points.

$$A_H = A_o(1 + 10\mathrm{Ri})^{-0.5} \tag{4.55}$$

$$A_o = 0.03\,\mathrm{m}^2\,\mathrm{s}^{-1} \tag{4.56}$$

where Ri the Richardson number is given by

$$\mathrm{Ri} = -\frac{g}{\rho}\frac{\partial \rho}{\partial z}\Big/\left(\frac{\partial u}{\partial z}\right)^2 \tag{4.57}$$

James (1984) compared several shelf sea models containing Richardson number vertical mixing formula with a similar series of models where vertical mixing was dependent on higher order turbulence closure schemes (Mellor and Yamada, 1974). Through simulating data representing a number of field situations, he found that Richardson number-based mixing was adequate to maintain the observed frontal gradients; but that the turbulent closure approach may be a better representation for some of the sub-grid scale processes. Until our knowledge of the parmeterization of small scale vertical mixing processes within multi-level ocean models improves the easiest implementation for the case of continuously evolving stratification is to use the mixing formulae dependent on the Richardson number. Early test runs of the model used constant vertical viscosities and diffusivities, with values chosen to be the maximum given in the stratification dependent coefficients.

In the early runs the simplest lateral boundary conditions have been imposed. These are a no slip condition for the velocity fields in the momentum equations

$$\frac{\partial u}{\partial y} = \frac{\partial v}{\partial y} = 0 \tag{4.58}$$

and a no flux condition for the salinity and temperature fields in the continuity equations

$$\frac{\partial T}{\partial y} = \frac{\partial S}{\partial y} = 0. \tag{4.59}$$

At the bed a frictional quadratic bottom mixing term is used in the momentum equation, and there are no heat or salt fluxes in the general model runs. The surface heat and salt fluxes, which will be discussed more fully in a later section, are dependent on whether the grid point is ice-covered or represents open water. In the early runs we only considered stress coupling between the ice and ocean, with τ_x and τ_y representing the sum of an open water wind stress component and an ice-water stress term. The sign convention used for the surface wind forcing is 180° representing the off-ice direction, whilst 0° represents on-ice winds. A 90° angle represents a wind along-ice with the ice on the right.

4.5 Ice model

In the simple ice-ocean models of sections 4.2 and 4.3 we considered the effect of the ice to be minimal. First it introduced a thermodynamic flux from the ice to the ocean in the one dimensional model, and second there was an ice-ocean stress coupling in the 2-layer model. In large scale seasonal ice-ocean models where the coupling only involves the ice thermodynamics (Manabe *et al*, 1975; Parkinson and Washington, 1979), the ice coverage is underestimated as ice advection is not allowed. The inclusion of ice dynamics in the model permits advection of ice into the ice edge region, where it encounters warmer ocean water and subsequently melts (Hibler, 1984b).

The momentum equation which governs ice dynamics was given in section 1.6 and is repeated here (nomenclature as in 1.6) for completeness

$$m\frac{\partial \boldsymbol{u}}{\partial t} = -m\boldsymbol{u}.\nabla\boldsymbol{u} + \boldsymbol{\tau}_a + \boldsymbol{\tau}_w + m\boldsymbol{k} \times f\boldsymbol{u} + \boldsymbol{F} - mg\nabla H \qquad (4.60)$$

Over seasonal time scales all the terms in this equation are necessary to provide a reasonable model for central Arctic sea ice dynamics. In these large scale simulations, the momentum equations are dominated by the external forcing from the atmosphere and ocean which impinge on the ice through stress terms. Thermodynamic changes in ice mass are also an important factor in the ice dynamics on such time scales. Several complex ice rheologies have been used to describe successfully the internal stresses in the ice which occur during the convergent ridge building process and also the conditions representative of divergent ice dynamics where leads develop. These rheological constitutive relations have been extensively reviewed and implemented in models by Hibler (1984b) and Bratchie (1984).

However, in our study of the marginal ice zone, we are dealing with simpler ice dynamics, for the ice is not confined by any solid boundaries and is frequently divergent so that floe interaction is minimal. Hence, we may not need to implement the full rheologies considered by Hibler (1979). Instead it may be sufficient to consider only the decay in the magnitude of ice resistance at the edge.

In a recent Arctic basin coupled ice-ocean model experiment undertaken by Semtner (1987) the internal stress effect was adequately represented using only an ice resistance term during convergence of the flow. Semtner describes this ice resistance term using a shear viscosity which is several orders of magnitude larger than that used for the associated ocean model. As we wish to concentrate on the ice-ocean interaction process we do not consider the use of more sophisticated ice models which calculate the evolving ice thickness and floe size distribution fields (Bratchie, 1984).

4.5.1 Model equations

The ice model is given by the following equations :-

$$\frac{\partial u_i}{\partial t} = f v_i - \frac{\partial (u_i v_i)}{\partial y} + (\tau_i^x + F_x)/\rho_i D \tag{4.61}$$

$$\frac{\partial v_i}{\partial t} = -f u_i - \frac{\partial (v_i v_i)}{\partial y} + (\tau_i^y + F_y)/\rho_i D \tag{4.62}$$

$$\frac{\partial A}{\partial t} + \frac{\partial (v_i A)}{\partial y} = 0 \tag{4.63}$$

$$\frac{\partial h_i}{\partial y} + \frac{\partial (v_i h_i)}{\partial y} = 0 \tag{4.64}$$

Stresses imposed on the ice are given by

$$\tau_i^x = \rho_a C_d \mid U_g^x \mid U_g^x + \rho_w C_w (u - u_i) \tag{4.65}$$

$$\tau_i^y = \rho_a C_d \mid U_g^y \mid U_g^y + \rho_w C_w (v - v_i) \tag{4.66}$$

The initial conditions for the ice model used in most of the following simulations are such that half the model grid is covered by stationary ice of compactness 0.9, with the ice concentration and ice thickness curves decreasing by either a quadratic or by a hyperbolic tangent relationship as we approach the ice edge.

One of the main aims of our coupled ice-ocean model was to compare the effect of different parameterizations of ice rheology on the development of the ocean dynamics, and thereby discover which rheology is most suitable for representing marginal ice zone conditions. Røed and O'Brien (1983) have shown that measurable differences are simulated in their reduced gravity ocean model when a simplified internal stress term is included in the ice momentum equation.

Comparison of ice rheologies was started with one of the earliest ice models (Campbell, 1965) where ice resistance was modelled by a linear viscous term, paralleling the eddy viscosity term used in the ocean models. We have also considered using the form for the ice resistance proposed by Nerella and Liu (1979)

$$\rho_i h_i \nabla (K_L \nabla u)$$

where the viscous term K_L is proportional to ice compactness.

As we are coupling our ice model to an ocean model where along edge gradients are ignored, we can make the same simplification in implementing more complex ice rheologies. Hence, the rate of strain tensor fundamental to the Hibler rheology (eqn 1.8) is reduced to a one dimensional form

after Lepparanta and Hibler (1985). We were reluctant to implement Hibler's full ice model i.e., the viscous-plastic rheology of equation 1.8 as the equations need to be solved implicitly through successive iterations making this model expensive to run computationally.

We considered several other simplifications of the internal stress form which do not include the dependence on the rate of strain tensor, though the exponential decay of ice strength with respect to the ice concentration is retained. Even though, these forms of the internal stress lose some of the detail of the ice-ice interaction, they do represent reduced ice coherence at lower concentrations and further, they permit an explicit solution of the ice momentum equations which can be solved in parallel to the ocean model. Despite the smaller time steps required for these explicit solutions to the momentum equation they are normally more cost-effective on computer time.

Røed and O'Brien (1981) have represented their internal stress term in the momentum equation by a 'pressure/strength' term of the form $\partial P/\partial y$ thereby ignoring the shear and bulk viscosity terms of the full constitutive equation (1.8). This pressure term can be expressed in terms of the propagation speed of a wave through the ice cover, c.

$$\frac{\partial P}{\partial y} = c^2 \quad = \quad c_o^2 A e^{-\kappa(1-A)} \tag{4.67}$$

where c_o is the speed of propagation of the fastest wave ($6\,\mathrm{m\,s^{-1}}$)

$$c_o^2 \quad = \quad \kappa^2 (P_*/\rho_i D)/(e^{-\kappa} + (\kappa - 1)) \tag{4.68}$$

where A is the ice compactness and κ is the ice dispersivity. When the ice model is run with this rheology without any coupling to an ocean model, the ice adjusts towards a geostrophic equilibrium condition and develops an associated ice edge jet. Røed and O'Brien (1981) also examined the analytical solution to this ice model using phase portraits over a range of dispersivity coefficient κ. They confirmed that if a sharp front is to be maintained at the ice boundary the value of the ice dispersivity κ should be set high ≈ 20.

4.5.2 Ice thermodynamics

Ice growth rates for the coupled ice-ocean model are calculated using the zero-level thermodynamic code developed by Semtner (1976b). This model produces reasonable results for the seasonal ice growth/decay cycle when compared with the more complex multi-layer model of Maykut and Untersteiner (1971). Since in the present model we are concerned with time scales of order of days,

rather than months, it was felt unnecessary to use a model which includes heat trapped in brine pockets in the ice lattice (Semtner, 1984a).

Implementation of the thermodynamic model followed the approach of Bratchie (1984), where the heat budget equation was solved iteratively for the surface ice temperature using a shooting method. This value of the temperature was subsequently used to calculate melt/growth rates. No parameterization of the lateral melting of ice floes has been included in our model. For the marginal ice zone, particularly, this may be an oversight as lateral melting is an important form of ice decay there (Wadhams, 1981). The only theoretical study to date which has a lateral melting mechanism dominating the ice thermodynamics is the study of Røed in 1984, where the physics of the heat transfer process between atmosphere, ice and ocean was simplified to single terms for each component part of the system. Bratchie (1984) also included a parameterization for the lateral growth melt/rate in his model, set to a value proportional to that calculated for vertical melt/growth rate.

Thermodynamic loss and gain of the ice were included in the ice compactness and ice thickness conservation equations by calculating both the growth in open water with these conditions and also the growth of standard ice thickness h/A for each grid point (after Hibler, 1979)

The ice thickness changes are calculated as

$$S_h = f(h_i/A)A + (1-A)f(0) \tag{4.69}$$

where $f(x)$ is the ice growth function. The change in ice compactness is composed of two components; one dependent on the sign of the ice growth function in open water, and the other on the changes to the ice thickness S_h in the grid cell.

$$S_A = \begin{array}{ll} (f(0)/h_o)(1-A) & if\ f(0) > 0 \\ + & \\ 0 & if\ f(0) < 0 \\ & \\ 0 & if\ S_h > 0 \\ + & \\ (A/2h_i)S_h & if\ S_h < 0 \end{array} \tag{4.70}$$

The cutoff value for open water ice thickness h_o is set to 0.05 m considerable less than 0.5 m used

in Hibler's two layer thickness model.

In several model runs, especially when cold off-ice winds are blowing, the ice compactness does not increase by realistic quantities under the control of these thermodynamic equations. If, however, we avoid using the above weighting for growth to thick and thin ice layers, and add the new ice growth more directly, we do not significantly alter the results as it is the size of the ice growth function which is too small under these external forcing conditions. This could be overcome to some extent in the model by allowing ice to grow to a threshold thickness and concentration, if freezing conditions persisted.

In summary, we consider several versions of the ice model including different forms for the internal stress term in the ice dynamics. In some of these model runs ice thermodynamics have also been included in the model.

A) Full momentum equation, no ice rheology;

B) Rheology included in the form of a linear-viscous term (Campbell, 1965; Semtner, 1987);

C) Rheology modelled by a viscous term which is dependent on ice compactness. (Nerella and Liu (1979);

D) A one dimensional version of Hibler's rheology (Lepparanta and Hibler, 1985);

E) Rheology determined by an ice 'pressure' term which is a function of the phase speed of propagation in ice, and the ice model is solved along the equation characteristics (Røed and O'Brien, 1983).

4.6 Initial ocean model conditions

4.6.1 Model time step

We initially ran the ocean model without coupling to an ice model in order to test various model parameters, and also to examine appropriate initial and boundary conditions for the model. In particular, we investigated the magnitude of the upwelling/downwelling of the pycnocline caused by a given discontinuity in the external stress which we used to represent the ice edge. It was also of interest to use the largest possible time step for the model whilst still maintaining the stability of the system. A particular focus was the understanding of the physics behind the propagation and growth of wave-like features in the velocity fields which could degenerate into model instabilities.

The time step of the model was restricted using two criterion: the first related to the maximum

velocity resolved by the model — commonly known as the CFL criterion (Cauchy-Fredricks-Lewy); and the second dependent on the amplitude of the diffusion/viscosity coefficients in both horizontal and vertical directions.

Mathematically these conditions are

$$\Delta t \leq \Delta x/v \tag{4.71}$$

where v is the speed of the fastest wave. The velocity of the surface gravity wave is often given as an upper limit. This speed is given by $\sqrt{(gH)}$. However, as we have removed the surface barotropic wave from the model by imposing a rigid lid condition, the speed of first internal baroclinic wave $\sqrt{(g'H)}$ is the critical velocity (where g' is the reduced gravity).

The second condition is based on the magnitude of the diffusivity/viscosity coefficients and is normally less restrictive in ocean models. In general the condition takes the form

$$\Delta t \leq \frac{(\Delta x)^2}{4A_x}. \tag{4.72}$$

This condition applies equally to the vertical grid size and the vertical eddy diffusivities/viscosities. As the same time step will be used for both ocean and ice models this latter restriction may become more important when the amplitude of the ice resistance is considered.

Test runs for acceptable horizontal viscosity and diffusion were considered successful after several thousand time steps were run using a variety of spin-up conditions without causing numerical instabilities.

4.6.2 Initial density conditions

Two sets of initial density conditions will be considered. The ocean velocity field was started from rest, but the density structure was either linearly stratified or initialized as two homogeneous fluids of different densities, separated by an invisible barrier in a 'lock gate configuration'. When the barrier is removed impulsively at the start of the integration the two fluids flow in opposing directions generating two mutual gravity currents which became rapidly unstable at the head (Wang, 1984). We had chosen to study this problem as a base mark for the model parameters (horizontal diffusivity/viscosity) particularly because the frontal structure observed under the Bering sea ice edge is similar in form to a single density current with strong horizontal gradients at the head of the flow,

though without the gravitational forcing mechanism. In contrast, when we examined the model conditions required to test for the size of stress discontinuity to produce realistic upwelling/downwelling of the pycnocline, the density field was initialized with linear stratification.

We also investigated the ability of the model to propagate a strong density interface whilst maintaining its coherence during the advection of the front. The requirement of a coherent density interface was important in the model, for although the winter Bering Sea density regime is derived primarily from the thermodynamic input, the rate of diffusion and horizontal entrainment (Garvine, 1979) across the interface is significant in maintaining the physical structure of the front.

In order to retain a strong density gradient in the model without the front developing ripples we used a technique, commonly used in other branches of fluid dynamics to maintain strong gradients known as 'flux corrected transport' (Book *et al*, 1975) This approach was not entirely successful and was not used in any further simulations of the ocean model.

A second reason to examine the linearly stratified initial density conditions is a requirement for an appropriate steady state starting point for the model. We cannot use climatological density fields to initialize the density structure (the technique normally employed in larger scale models) as we will not be running the model simulation until an equilibrium state is achieved. Further, as the model simulations only last 3-6 days, we have to select an initial condition anticipating the final situation, without imposing the solution that we expect.

The initiation of the model from a geostrophic equilibrium state containing an inner two layer section surrounded by homogeneous regions was also considered but led to further problems. Specifically, the appropriate velocity cross-section initialized at geostrophic velocities, still has to re-adjust after external conditions are impulsively started. Under such conditions, this velocity cross-section appears to be more unstable than the case when the velocity field was started from rest.

As early model runs did not include interactive thermodynamic forcing (section 4.10) we could not initiate the density structure from a homogeneous state which would most closely represent the Bering Sea shelf after autumnal convection. An initial density distribution with a constant horizontal density gradient maintained across the integration domain was considered but in a similar manner to the above geostrophic adjustment case, this density distribution was balanced by a jet structure in the along-edge velocity field which again tended to be more unstable than a velocity field started from rest when new external conditions are imposed.

A vertical stratification for our initial density configuration with stratification set as a linear

function of depth was eventually used. At the surface of the model we imposed a mixed layer of $25 - 30$ m in depth. This surface mixed layer had a temperature of $-1.5\,^{\circ}$C and a salinity of 31 ‰. These values increased to $+1.0\,^{\circ}$C and 32.0 ‰ at the bottom of the model. The vertical resolution in the model was set initially to 5 m. This gave 20 levels over the 100 m depth water column. Within this vertical resolution, changes to mixed layer depth derived from buoyancy forcing are reasonably well represented.

Whilst the 1 km horizontal resolution is sufficient to define typical ocean density scales in the Marginal Ice Zone, at this resolution we still treat the ice cover as a continuum with the floes in the MIZ being of order $20 - 50$ m across. Unfortunately, using 1 km resolution, we are unable to resolve processes at shorter length scales (100 m), such as leads and the dynamics of 'ice bands' (section 2.4) in spite of their importance in the flux transport of ice, (and hence heat and salt) in the Bering sea.

4.6.3 Spin-up conditions

Another major question for these initial simulations was to determine how quickly the model could be spun up. In effect we wish to set an upper bound on the amplitude of the wind impulse. Specifically, when we used an integration domain only 80 km wide we had to scale down the size of the wind impulse from values that would be more realistic in the field. In the later, more realistic model runs with a larger grid more appropriate wind forcing is used.

A second question was whether the wind should be impulsively switched on or gradually increased during the model spin-up period. After a change in stress forcing the model undergoes inertial oscillations lasting for 5-6 periods, equivalent to 2-3 days of model simulation. Some model simulations, particularly the simpler runs where no ice rheology was included, were continued well past this stage. The scalar fields of salinity and temperature are not contaminated by these oscillations. Most of the field data available to compare with our model output consist of density sections. Hence, data fields from this spin-up period are useful even though the velocity fields will be aliased by the inertial signal. Also, the cost in computer time of running the model past this adjustment period in all the planned simulations was prohibitive, particularly as many of the flow features and their development were discernable after the first 2-3 inertial periods. Numerical techniques for removing inertial oscillations involve solving the equations semi-implicitly with respect to the Coriolis term (Bryan, 1969) Despite the smaller time steps needed for explicit

schemes, implicit schemes were not used because of the ease with which additional terms can be included in the explicit formulation as required.

It soon was clear that a model grid of 80 × 1 km horizontal spacing and 20 × 5 m vertical spacing was not broad enough to encompass the dynamics required. Hence, a variable size model grid was incorporated in the code for test purposes, although eventually the grid was replaced by wider spacing at all points of the model. In choosing the variable grid we were limited by store constraints so we elected to use a grid of 100 horizontal points by 14 vertical points. Horizontal grid spacing remained detailed at the ice margin, with the innermost 30 grid points set at 1 km spacing and grid size expanded via an exponential relationship to approximately 5 km at the boundaries. The vertical grid was altered in the region beneath the mixed layer where resolution increased from 5 m to 8 m and then to10 m with increasing depth. Care was taken to minimize errors introduced by having a gradient in the grid spacing, for derivatives in the finite difference scheme will no longer be conservative to second order.

The horizontal viscosity coefficient ($200\,m^2\,s^{-1}$, in the 1 km grid) was altered in these outer zones in proportion to the grid spacing. By dimensional arguments we should use a change proportional to the square of the length ratios.

4.7 Initial model runs

Before coupling the ice model to the ocean model we undertook some model runs representing a stationary ice edge with a sharp stress discontinuity. Several short model runs were examined to find appropriate levels for a freshwater flux term, and also by a similar approach to determine the value of salt flux necessary to break down the stratification by brine convection. Figure 4.4 is the temperature and salinity cross-sections from a model simulation where the only forcing was from an influx of cold, freshened water.

When forced with a stress discontinuity the model produces significant deviations of the isotherms at the ice edge dividing point (Figure 4.5), also the disturbance which is generated by the stress forcing in the velocity field propagates in both directions in a similar way to the upwelling disturbance in the model of Sjøberg and Mork (1985). If the wind stress impulse used to initiate the run was greater than $5\,ms^{-1}$ then the wave generated within the velocity field amplifies sufficiently before reaching the boundary to destabilize the simulation. Upwelling/downwelling of the isotherms/isohalines

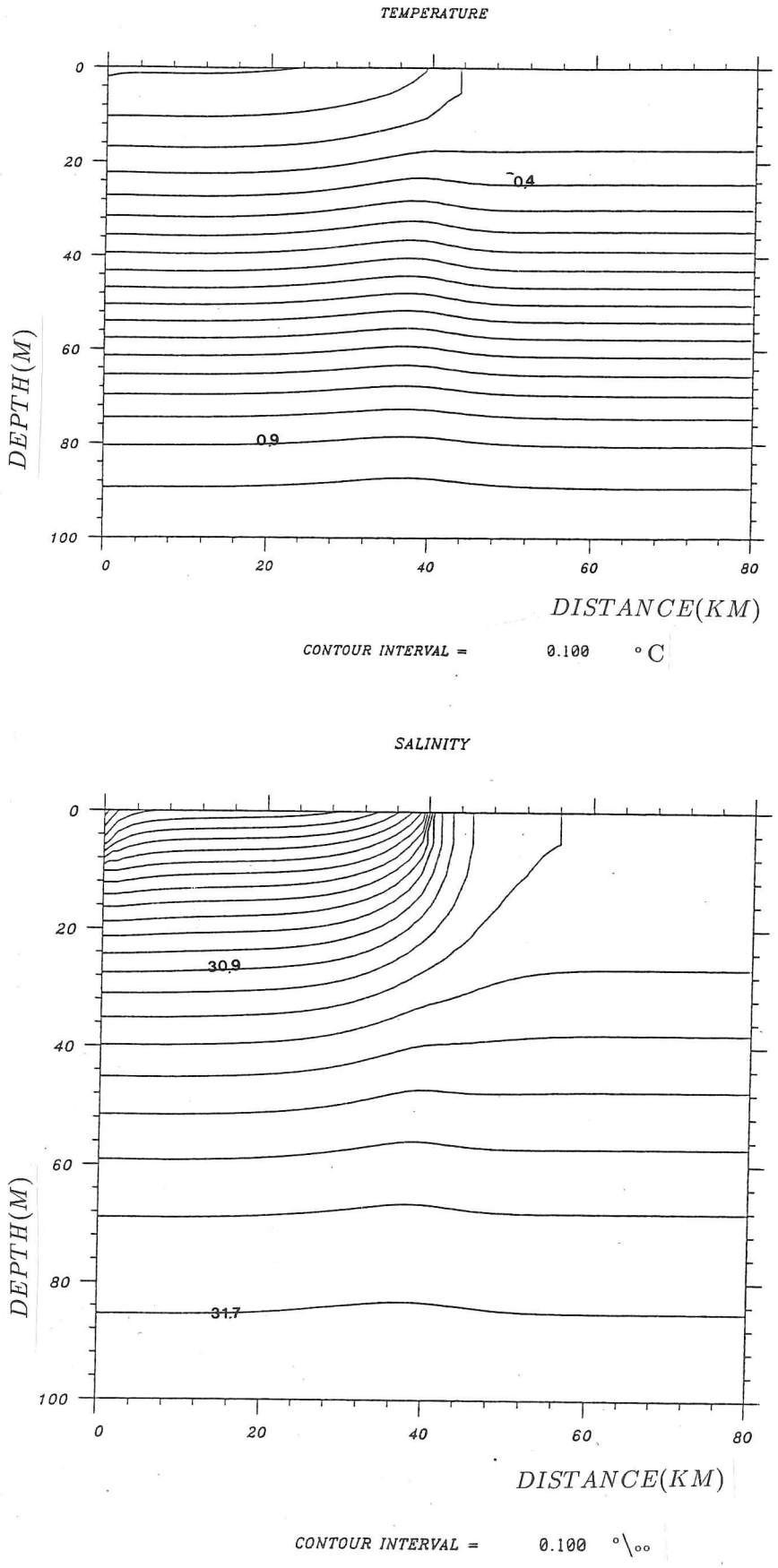

FIGURE 4.4: Temperature and salinity output from test model simulation when the only forcing from the ice is represented by a surface buoyancy flux of less saline, cool meltwater.

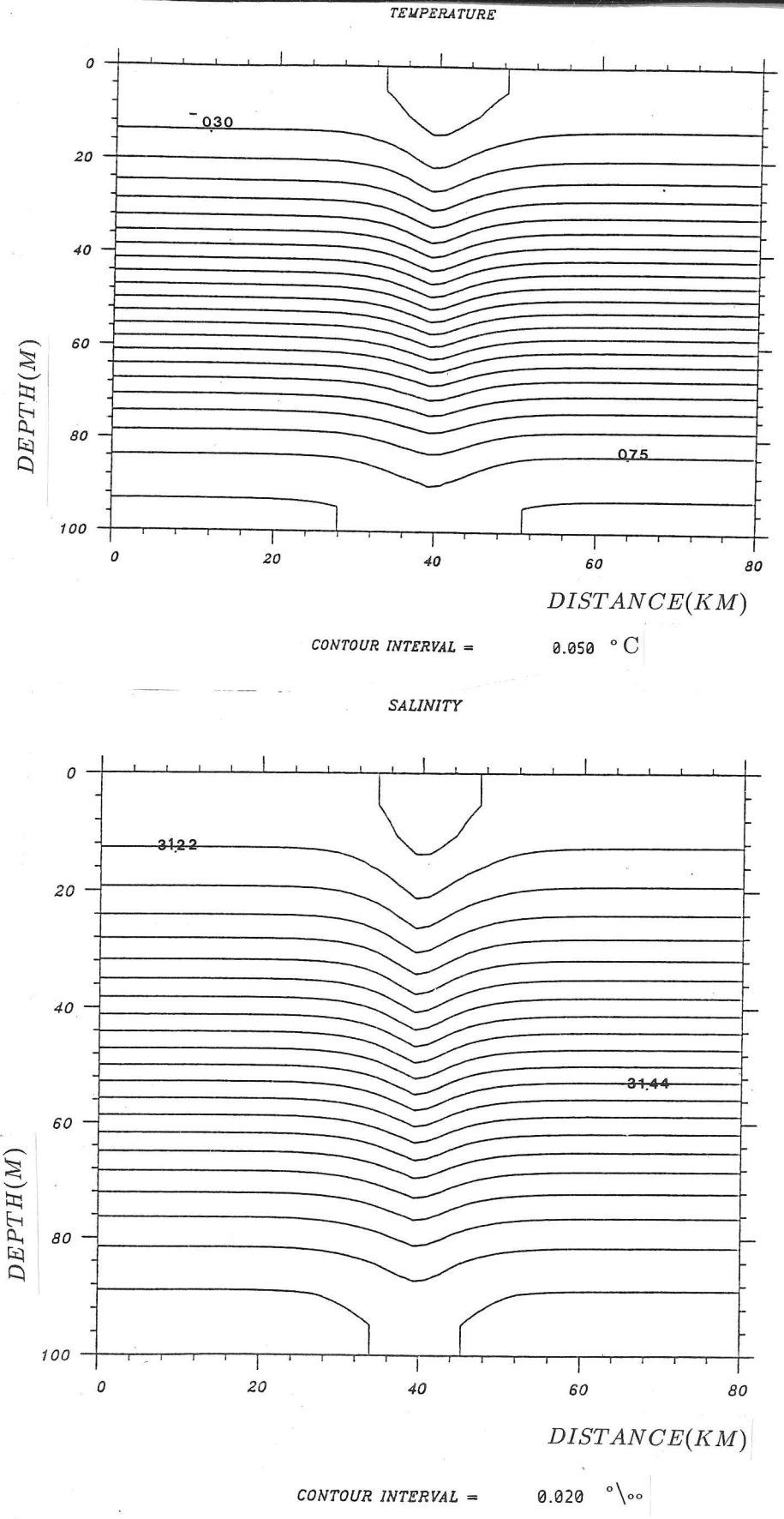

FIGURE 4.5: Temperature and salinity output from a test model simulation where the forcing from the ice is represented by a stress discontinuity generating downwelling of the pycnocline.

was considerable ($5 - 10$ m) under wind forcing of amplitude $5\,\mathrm{m\,s^{-1}}$ during the first inertial period (Figure 4.6). However, in later test runs the external forcing is scaled down, firstly, by choosing smaller initial wind amplitudes ($2\,\mathrm{m\,s^{-1}}$); and secondly, by removing the discontinuous step in the wind stress. In the coupled ice-ocean model the stress transmitted to the ocean is a combination of open water wind stress and under ice stress. Hence, there is a less sharp change in the external stress reaching the ocean which becomes a function of the ice concentration distribution.

Adjustment of model after spin-up

After the ocean model had been spun up for 3 days with $2\,\mathrm{m\,s^{-1}}$ off-ice winds several different external conditions were imposed. The model was then run for a further 12 hours to see how rapid an adjustment took place under the new conditions. These included both an increase in wind speeds and a change in its direction. These runs suggested that if the model was to remain within the bounds of the 80 km grid and was to remain stable, then the strength of the wind increase was limited to less than a further $2\,\mathrm{m\,s^{-1}}$. Ideally new external conditions should be gradually imposed on the model.

4.8 No ice rheology run

A comparison of ice-ocean model runs with the ice model not including rheological terms was undertaken, forced by different magnitude winds in an off-ice direction. The first 24 hours of simulations after an impulsive imposition of winds at the start are shown in Figure 4.6. The ice and ocean velocity regime forced by the larger wind of $5\,\mathrm{m\,s^{-1}}$ (Figure 4.6b) had magnitudes up to 3 times greater than for the slacker $2\,\mathrm{m\,s^{-1}}$ case shown in Figure 4.6a. However, the overall velocity pattern is the same in both cases, though the inertial oscillations take longer to decay for the stronger winds.

The gradient observed in the cross-edge surface ocean velocity data is confined to a narrower zone for the $5\,\mathrm{m\,s^{-1}}$ wind. This maximum gradient region in both the ice and ocean velocity patterns is linked to the translation of the ice edge and is found to be coincident with the 0.6 ice concentration contour in both wind cases. When forced by $5\,\mathrm{m\,s^{-1}}$ winds, all the marked ice concentration contours advanced over 15 km in this first 24 hour period. If the model is allowed to continue running the leading edge of the ice concentration contours (lowest value drawn 0.1) soon reaches the edge of the integration box. However, the coupled model is unable to cope with such a rapid change in

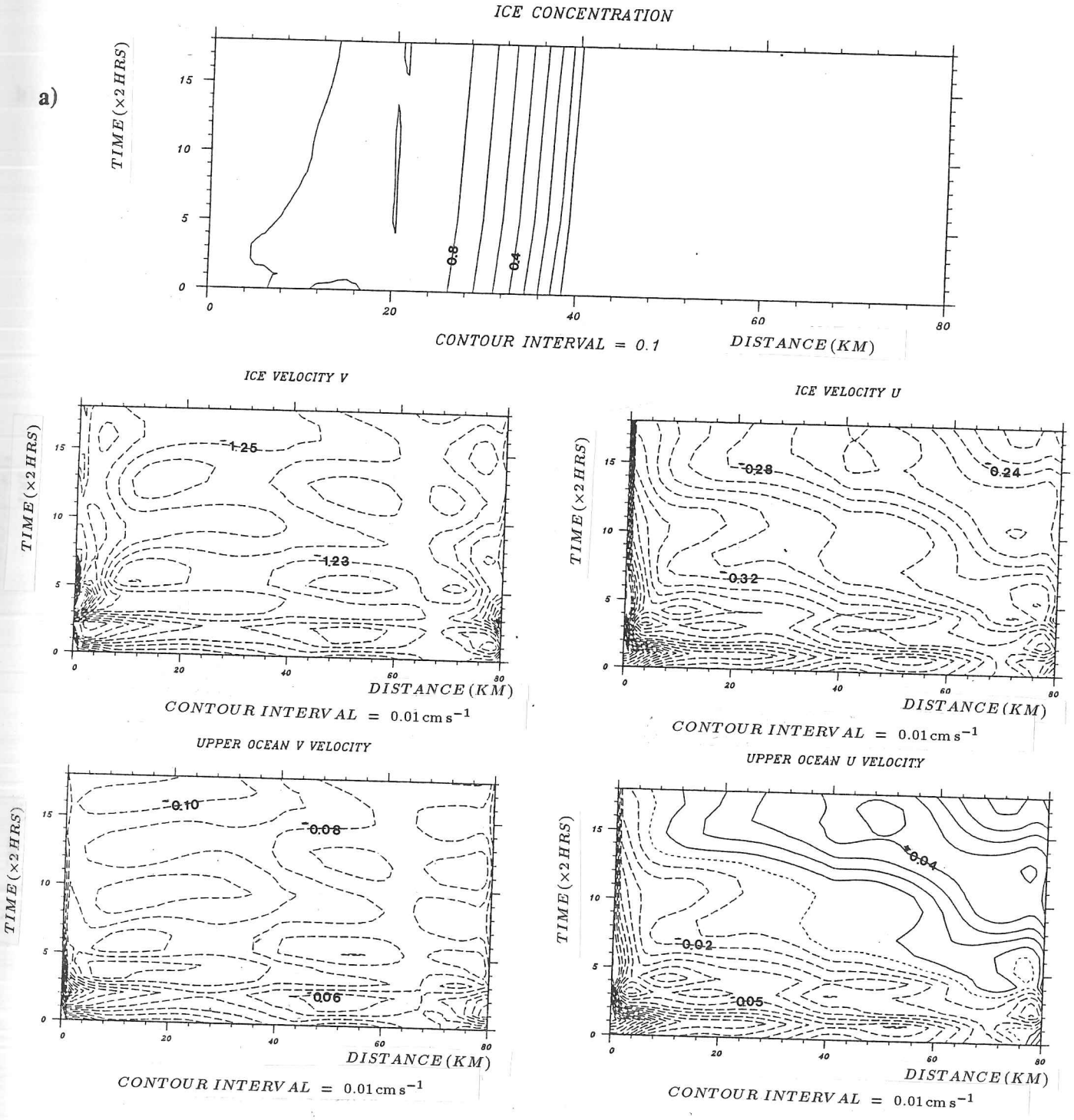

FIGURE 4.6: 24 hour (18 records) contoured time series of model simulation when forced by a) $2\,m\,s^{-1}$, b)$5\,m\,s^{-1}$ off-ice winds.

b)

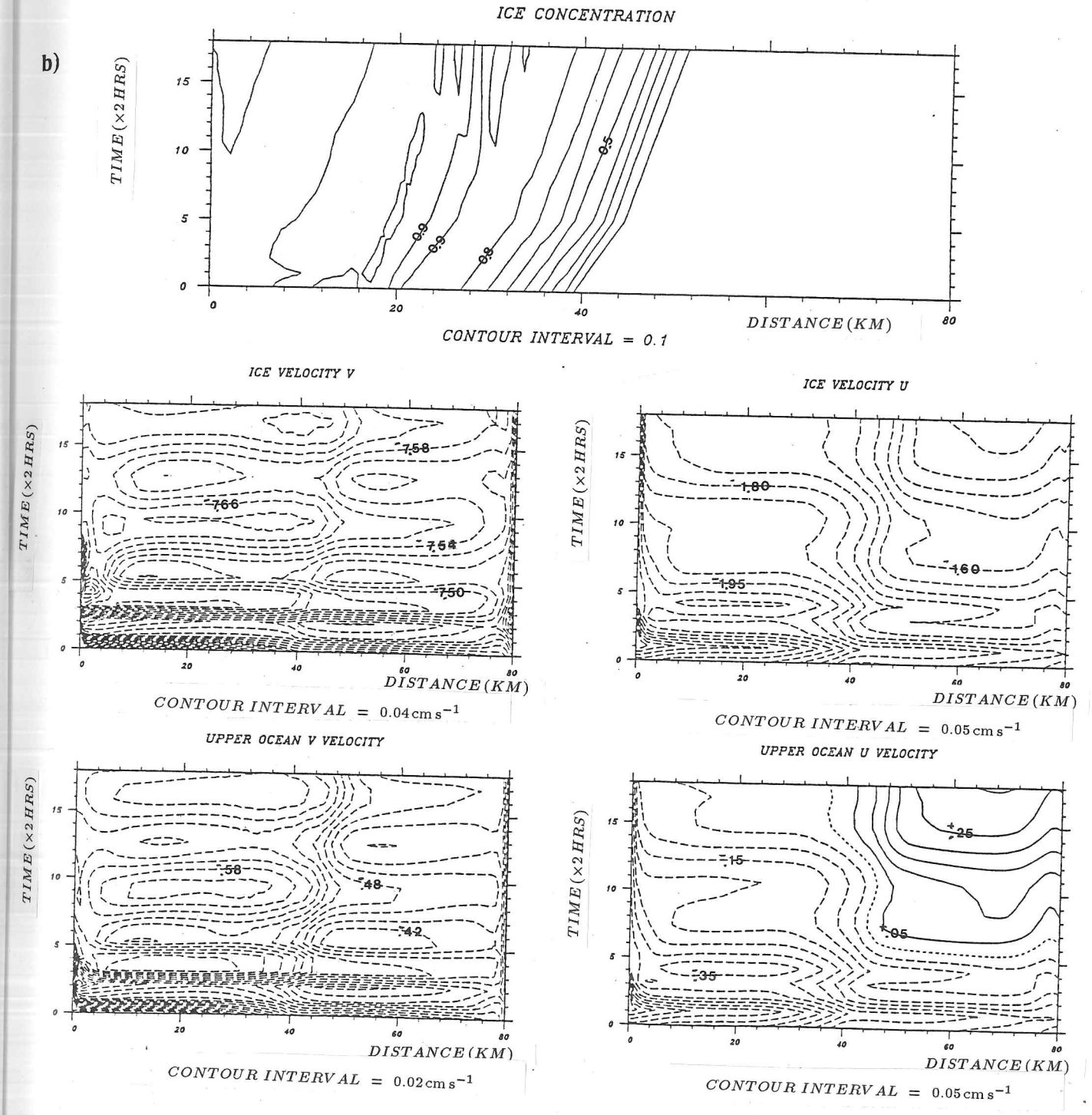

Figure 4.6: continued.

conditions, as is indicated by a growing wave-like disturbance represented by frequent contours in the region above 0.9 compactness.

4.8.1 Format of model output plots

We display the model output in our figures in two ways; firstly, as contoured cross-sections of the data with depth plotted against horizontal distance across the grid frame. The majority of the graphs in this chapter are time series contour plots with changes in the model variables in time plotted in relation to the horizontal position in the model domain. Due to space restrictions and the large amount of data generated by the models we can only display a restricted number of integration variables; those chosen for the ocean model are the upper ocean velocities, temperature and salinity in the mixed layer, whilst velocities and concentration are used to represent the ice model. In order to construct these time series plots, all the data fields are stored on tape at regular intervals (normally hourly) during the model run. On a few of the time series graphs there are discontinuities arising from data gaps when recovery of the hourly fields from the output was disrupted due to computer system errors. In many simulations, the most instructive model output fields to examine are the along-edge and cross-edge velocity fields which are directly linked to the ice velocity fields and the ice concentration curves (in models where ice thickness is calculated the contours follow the ice concentration curves in all but extreme cases).

4.9 Model simulations with on-ice and off-ice wind forcing

4.9.1 Contour sections

We ran the coupled ice-ocean model, with the ice model containing no rheological terms, for a range of wind angles ($0°, 60°, 90°, 120°, 180°$) and time series for the first 128 hours are shown in the sequence of figures 4.7-4.11 (In the graphs time axis represents records of 2 hours duration). Several of the plots show errors at around 30 records due to data loss and changes in model time step after the initial adjustment (strictly speaking this step should not have been undertaken as a change in time step will alter the model response). As the velocity contours are small, $\pm 0.0002\,\mathrm{m\,s^{-1}}$, they are not correctly indicated in the captions beneath the plots.

The velocity field generated in the on-ice (0°) and off-ice (180°) forcing cases are in the opposite sense with the on-ice winds generating strongest gradients in the open water domain whilst the

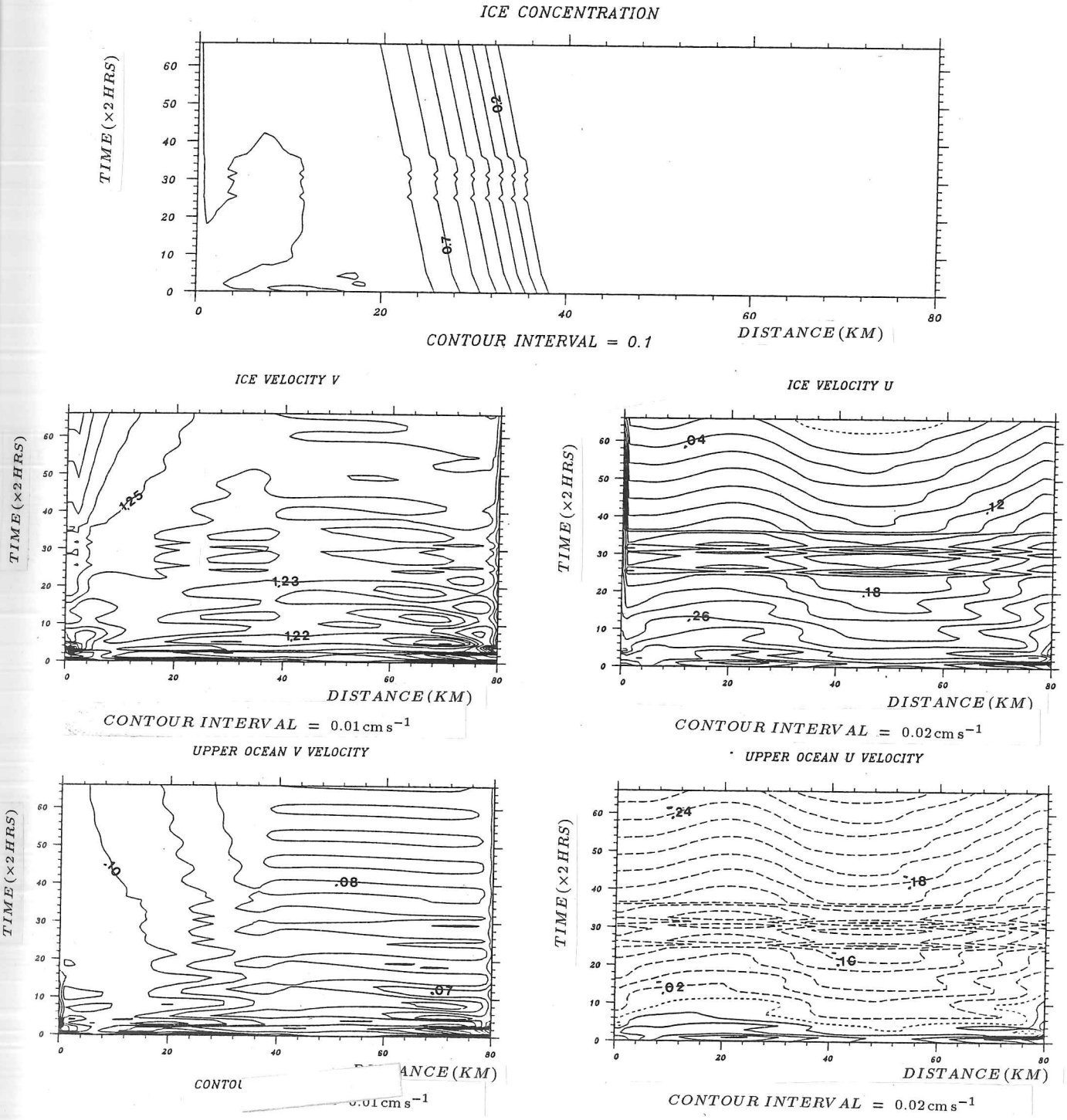

FIGURE 4.7: Contoured time series of output from 128 hours simulation (64 records) when model was forced by winds from 0° (on-ice) of 2 m s^{-1} amplitude. No rheology is included in the ice model. The horizontal grid is 80 km wide.

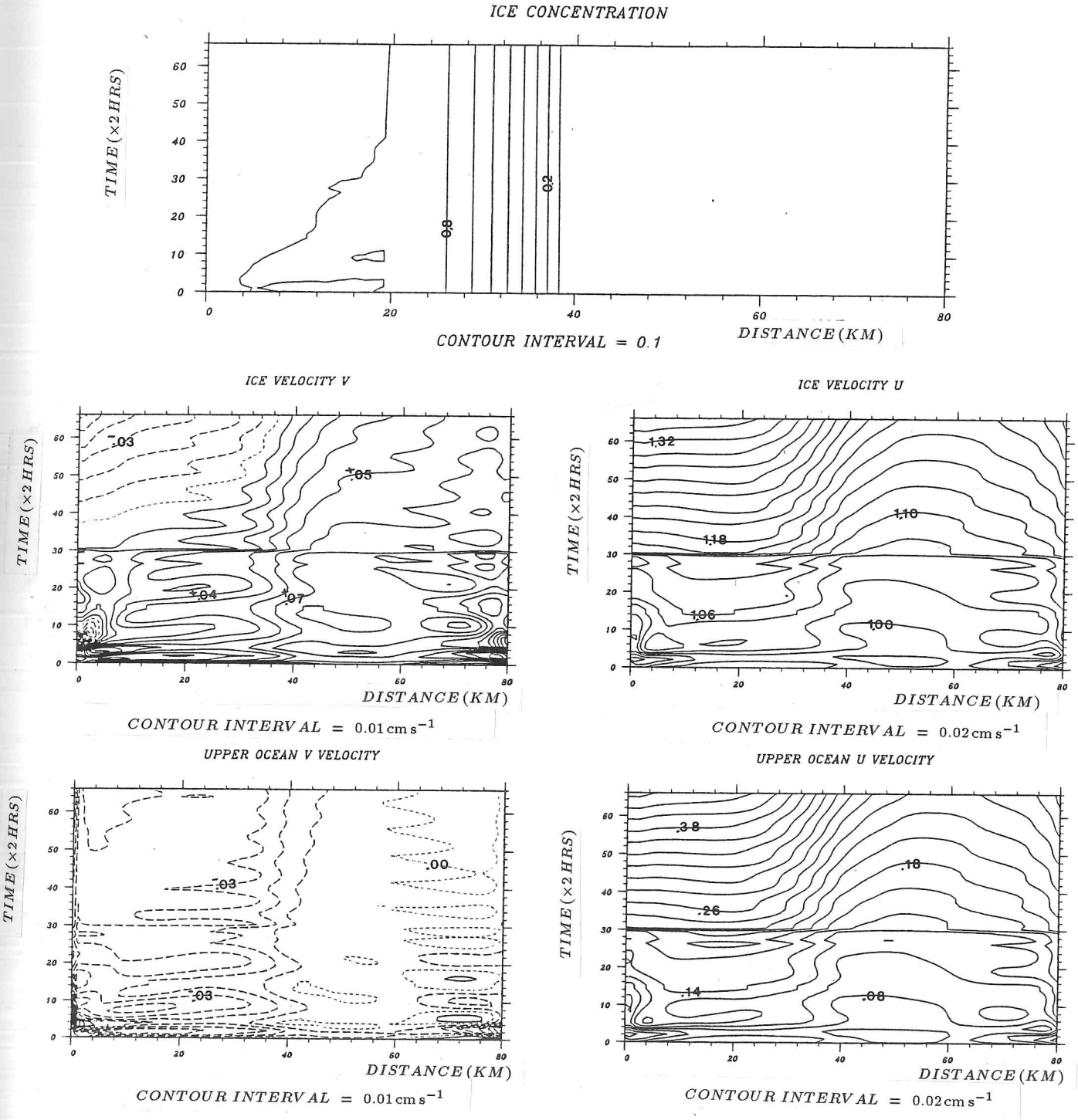

FIGURE 4.8: Contoured time series of output from 128 hours simulation (64 records) when model was forced by winds from 60 ° (obliquely on-ice) of 2 m s^{-1} amplitude. No rheology is included in the ice model. The horizontal grid is 80 km wide.

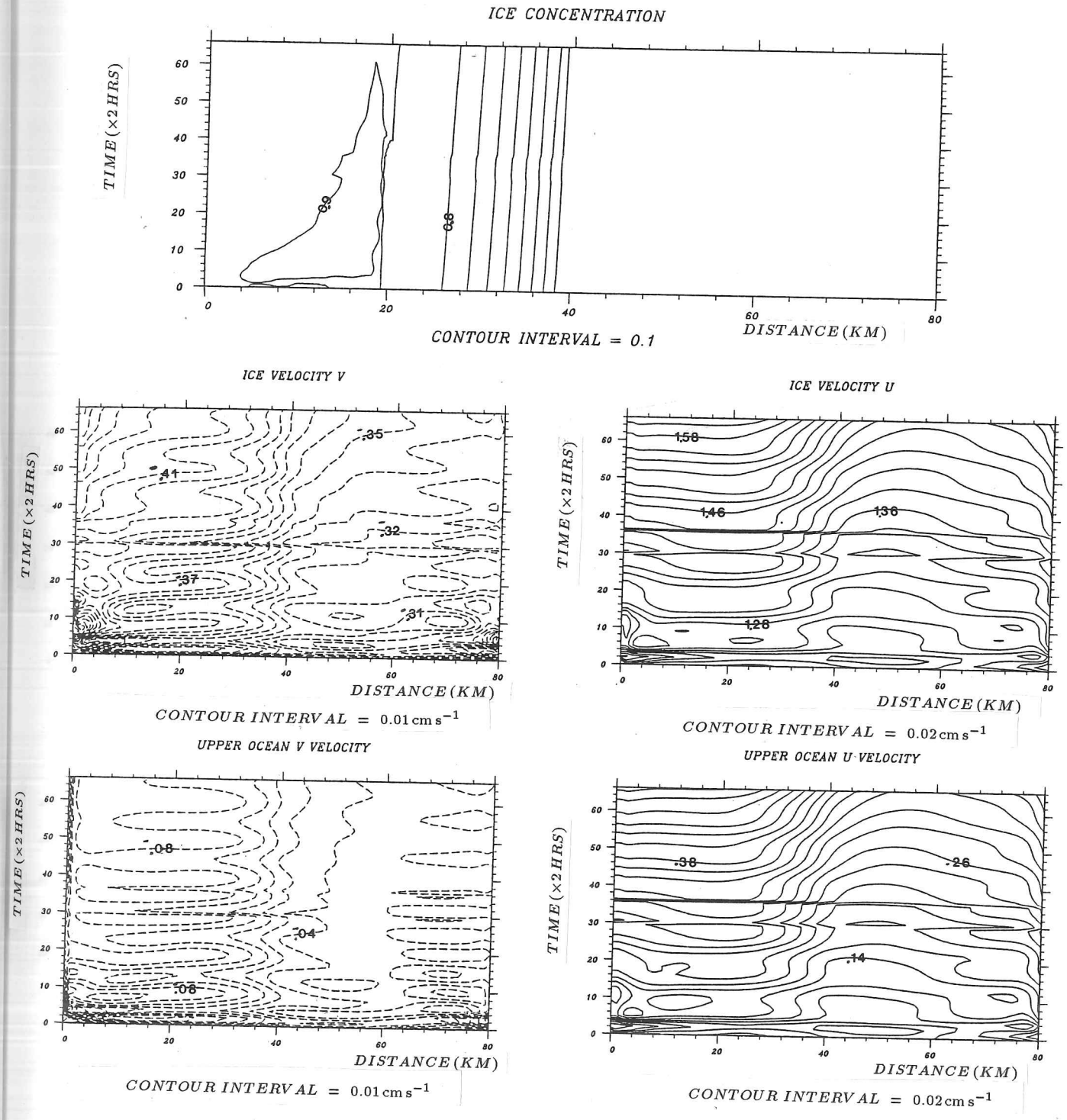

FIGURE 4.9: Contoured time series of output from 128 hours simulation (64 records) when model was forced by winds from 90 ° (along-ice) of 2 m s^{-1} amplitude. No rheology is included in the ice model. The horizontal grid is 80 km wide.

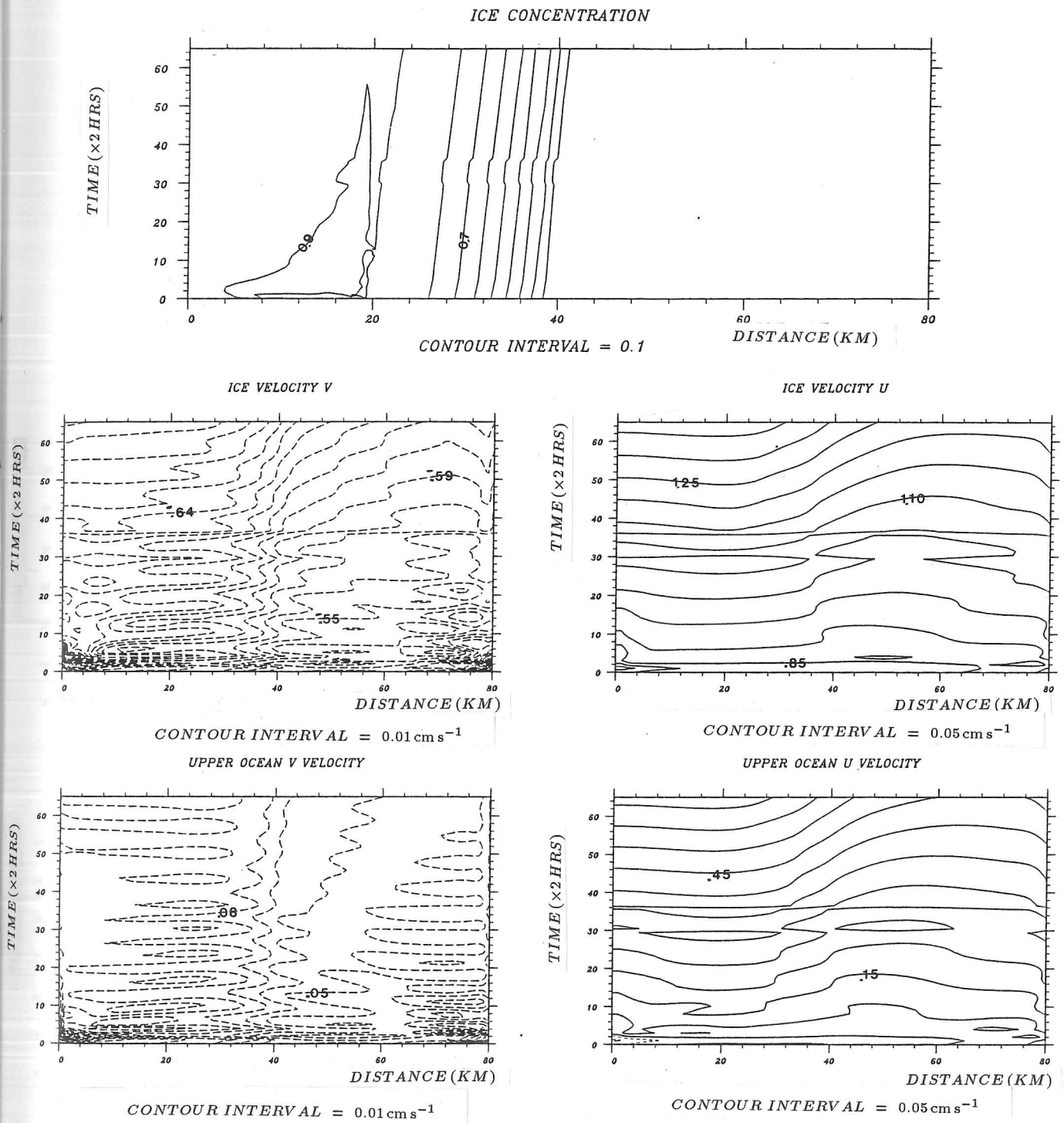

FIGURE 4.10: Contoured time series of output from 128 hours simulation (64 records) when model was forced by winds from 120° (obliquely off-ice) of 2 m s^{-1} amplitude. No rheology is included in the ice model. The horizontal grid is 80 km wide.

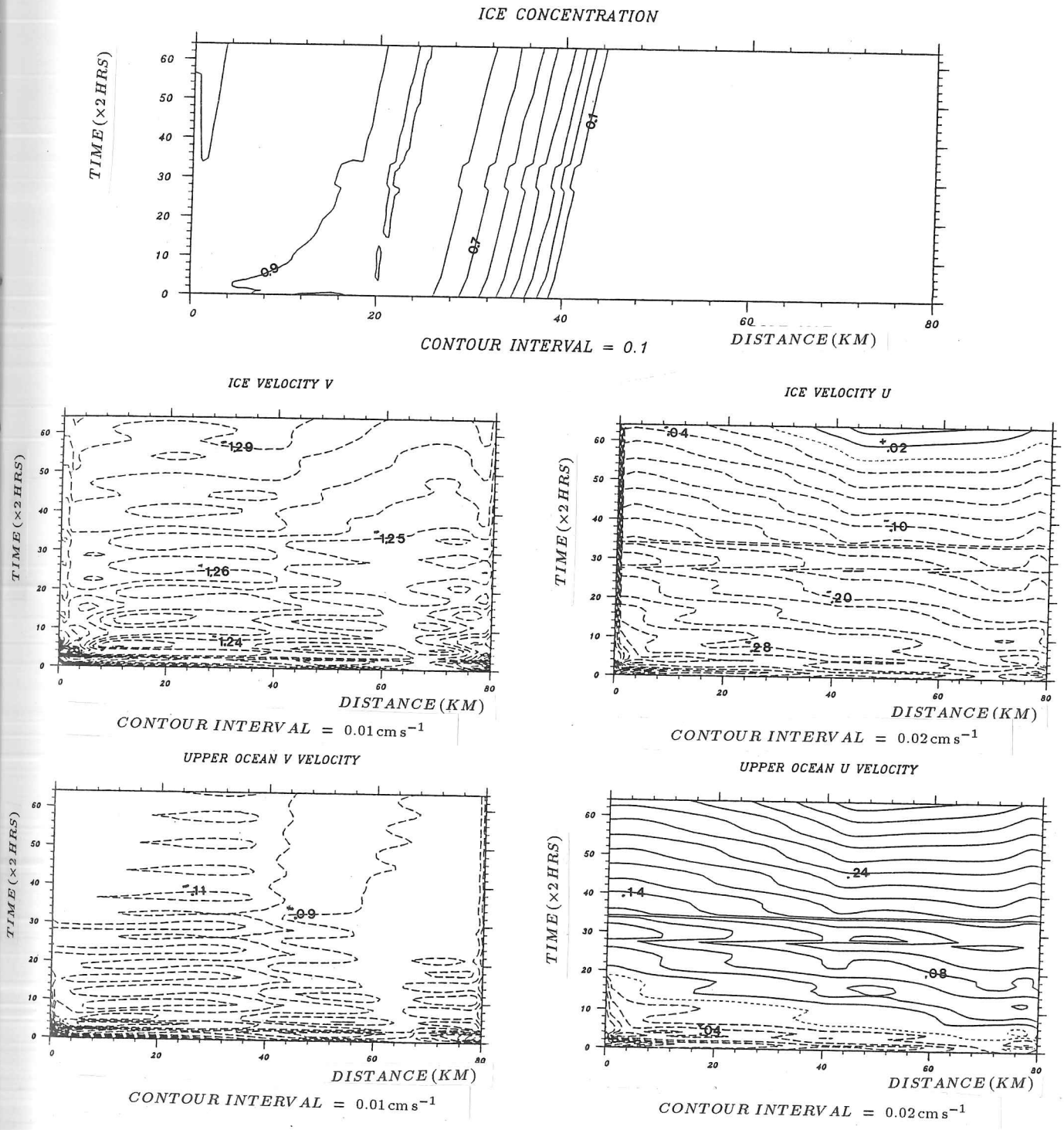

FIGURE 4.11: Contoured time series of output from 128 hours simulation (64 records) when model was forced by winds from 180° (off-ice) of 2 m s^{-1} amplitude. No rheology is included in the ice model. The horizontal grid is 80 km wide.

reverse is true in the 180° case. One can clearly see the effect of the inertial signal appearing every 6 records in the velocity time series. We also considered the model response for the case of along edge winds (ice on the right) and for two oblique wind angles 60° (slightly on- ice) and 120° (the same degree off-ice). The along ice winds barely advance the ice edge position in the 5 day period of the model simulations. The velocity gradients in the open water are of equal magnitude but there is still a recognizable signal in the ocean velocity fields to mark the ice edge. When the model is forced at an oblique wind angle of 60° the ice edge remains stationary throughout the simulation. The velocity fields again indicate a gradient region associated with the ice edge.

Immediately after the model start strong velocity gradients develop within $10 - 15$ km of the model boundaries. This indicates that the no slip boundary condition we are using may not be suitable if strong velocity gradients are present.

4.9.2 Velocity cross sections

Velocity cross-sections were plotted approximately every 12 hours from the model fields stored on tape in the simulations with no ice rheology for wind angles (0°, 60°, 90°, 120° and 180°). During the original simulation u and v velocity fields were plotted to help in tracing back errors and instabilities. For all of the above group of model runs, the salinity and temperature fields showed little change during the simulation because there are no active thermodynamic process included and no significant upwelling/downwelling events. The along and cross edge velocity fields also suggest that the boundary conditions (in this case no slip) can alter the interior solution (see above). The strongest velocity gradients in the cross section are found at the outer grid points. As the models were forced with only $2\,\mathrm{m\,s^{-1}}$ winds to keep the solution within the 80 km grid, the maximum velocities generated by the model are correspondingly small in the range $\pm 0.002\,\mathrm{m\,s^{-1}}$.

With the velocity data plots being produced at 12 hour intervals they are strongly aliased by the inertial oscillations, with patterns of positive velocity contours being replaced by negative contours in the subsequent plot of the sequence. There are, however, greater similarities between the velocity fields plotted 24 hours apart, particularly in the on-ice and off-ice (0°and 180°) cases. The plots of cross-sections for two such instances are shown in Fig 4.12 for an on-ice simulation.

We examine further the velocity data from the simulation forced by the oblique wind angle of 60° which maintained the ice edge at a constant position throughout the simulation (Fig 4.8). A sequence of 8 velocity cross-section plots for this model run obtained at 12 hour intervals of the

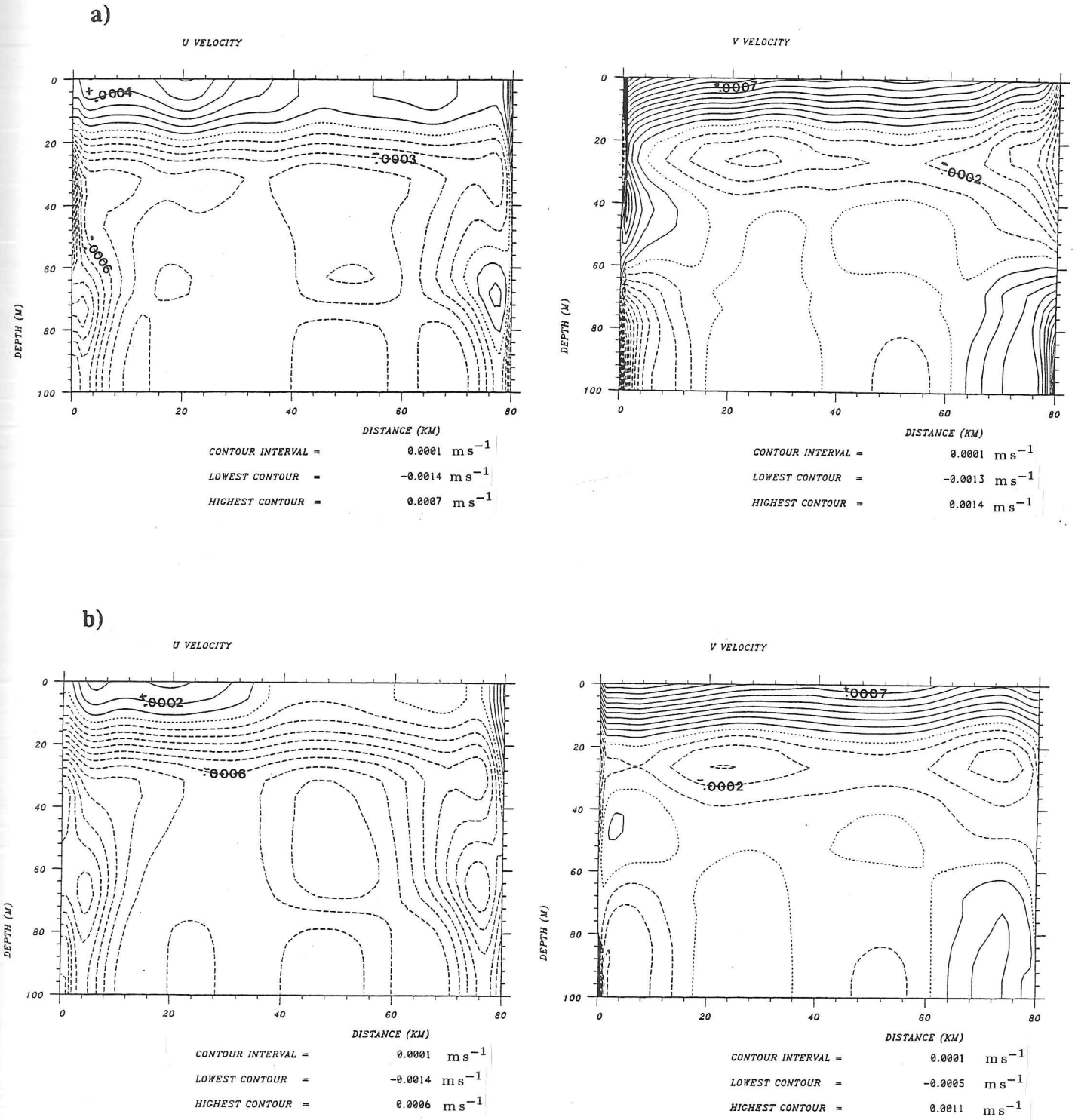

Figure 4.12: U, V velocity cross sections for a) 12 hours and b) 36 hours into model simulation forced by on-ice 0° winds (Figure 4.7). There is little evidence of aliasing by inertial currents with sections 24 hours apart.

velocity fields is displayed in figure 4.13. By the second day of the simulation the u velocity field has reached a settled pattern with only the contour values of the velocity increasing on subsequent sections. However, no steady state is reached as the external forcing continually adds energy to the system. The v velocity field approaches a quasi-steady pattern after two and a half days which is approximately the expected decay time for the inertial currents at 60° north.

4.10 Thermodynamic coupling of ice-ocean model

4.10.1 Vertical fluxes

Before the thermodynamic equations for ice growth were implemented, we needed to prescribe the heat and and salt fluxes between the ice and ocean. We would intuitively expect some relation between the ice concentration and the heat/salt fluxes to the ocean. The heat flux was taken to be linearly related to the ice concentration and several experiments were undertaken in order to find suitable values for the salt flux which would generate a) deep enough brine convection in the code or b) melt-water layers on the time scale of our simulations (2-5 days). Unfortunately, the setting of the fluxes in both cases as functions of the ice concentration leads to incompatibilities. At low concentrations both brine convection in leads and polynyas, and ice melting at the ice edge can occur, the processes involved depending on the prevailing air temperature conditions.

Initially, the salt flux was set such that twice the negative (freshwater) buoyancy flux would occur at the ice edge as would occur the interior (0.9 compactness). This flux gradient across the ice edge domain is realistic, but if it were to continue indefinitely it would leave denser water trapped at the innermost grid points. The magnitude and sign of the flux values are reversed when we are considering brine convection. Here the greatest influx of brine is in the innermost section of the model, where even though we are at maximum, ice concentration the open water within leads and polynyas provide an area for new ice growth and hence brine expulsion. Although some new ice growth occurs at ice edge, it melts when there next is a change in air temperature or ocean flux conditions. Also, this direction of the salt flux gradient again introduces denser water to the area which represents the northern end of the model. As no bottom topography is included in the model along which the denser water could flow down-slope away from the region the denser water remains trapped at the innermost grid points.

Initially we used a linear relationship between ice concentration and the flux magnitude in the

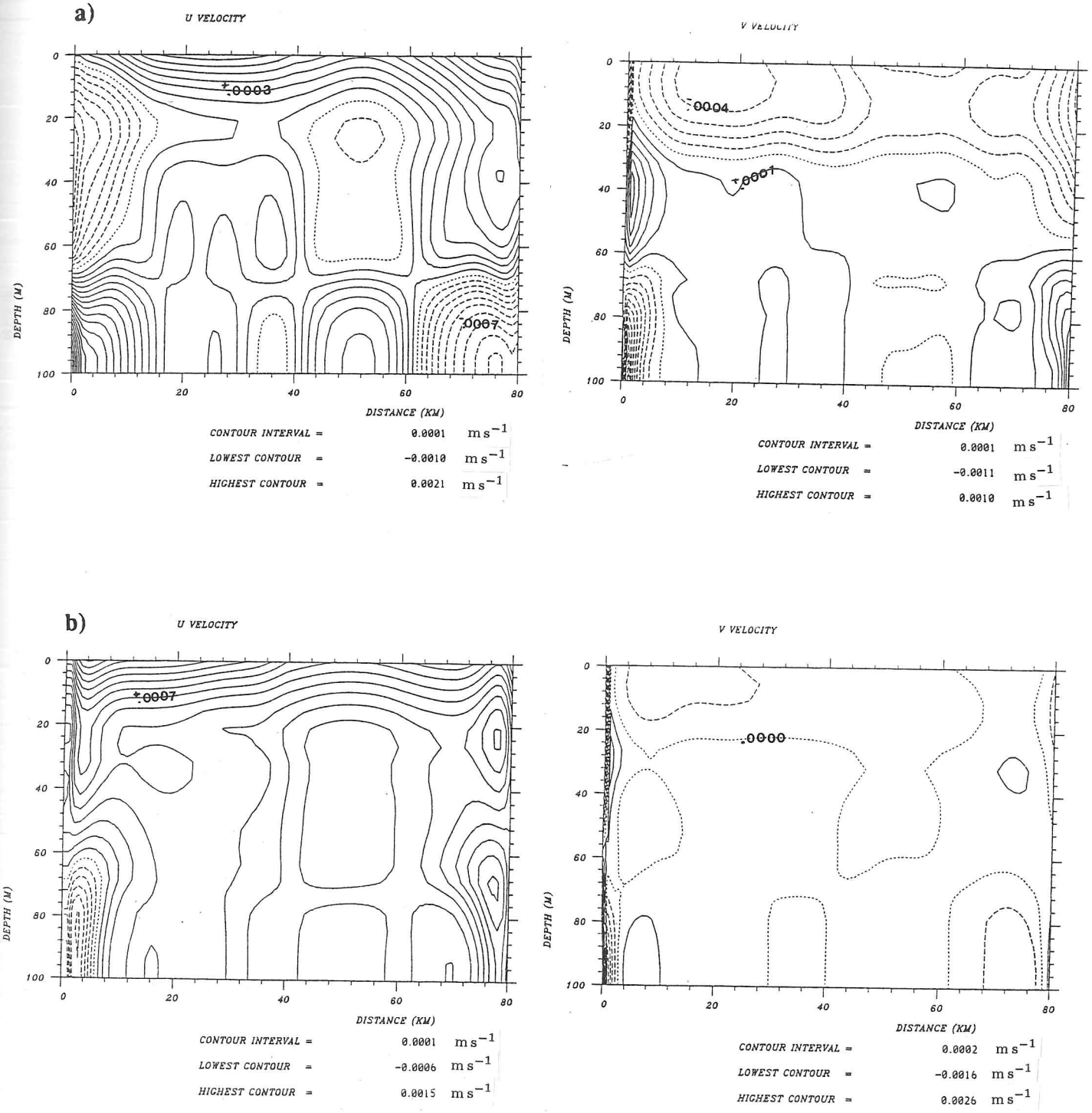

Figure 4.13: Sequence of 8 (a-h), u, v velocity plots obtained every 12 hours during model simulation forced by wind from a direction of 60° (obliquely on-ice). The time taken for the velocity fields to reach a quasi-steady state, 60 hours, is approximately equal to the decay time for the inertial currents.

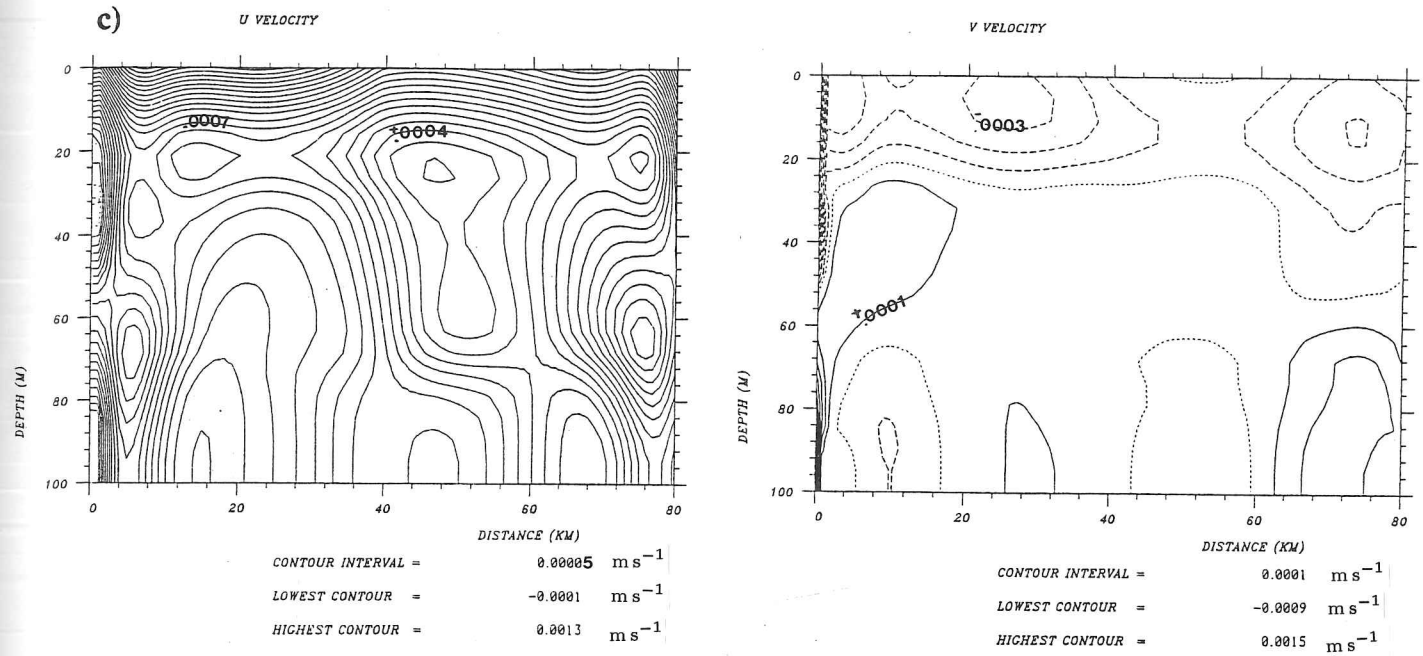

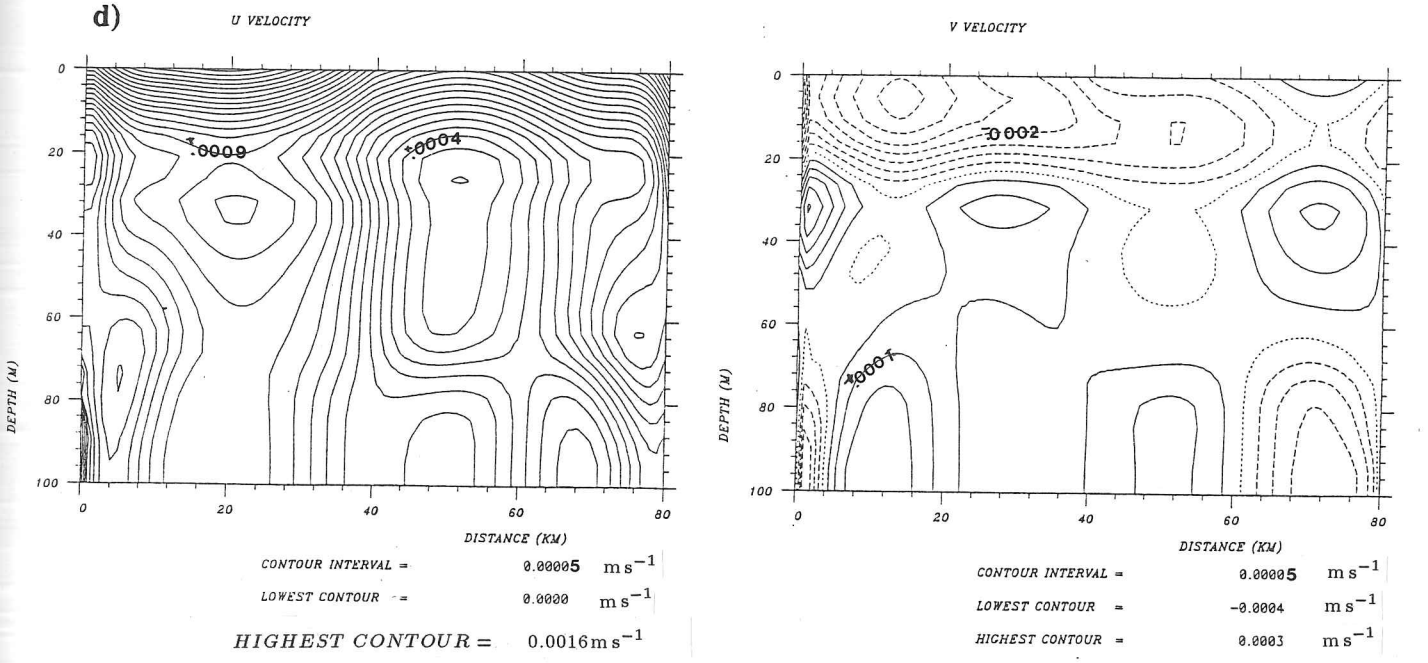

Figure 4.13: continued.

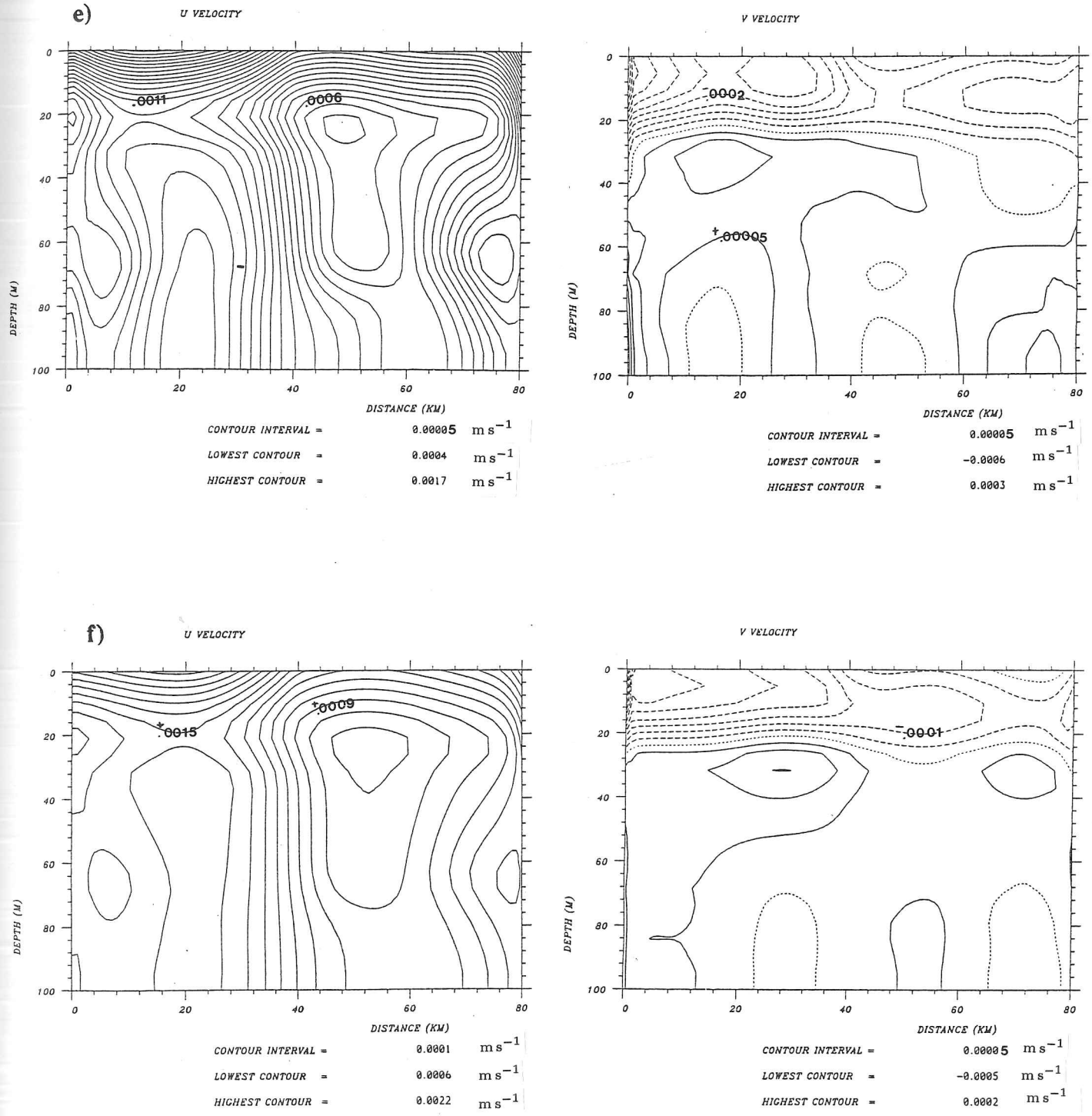

Figure 4.13: continued.

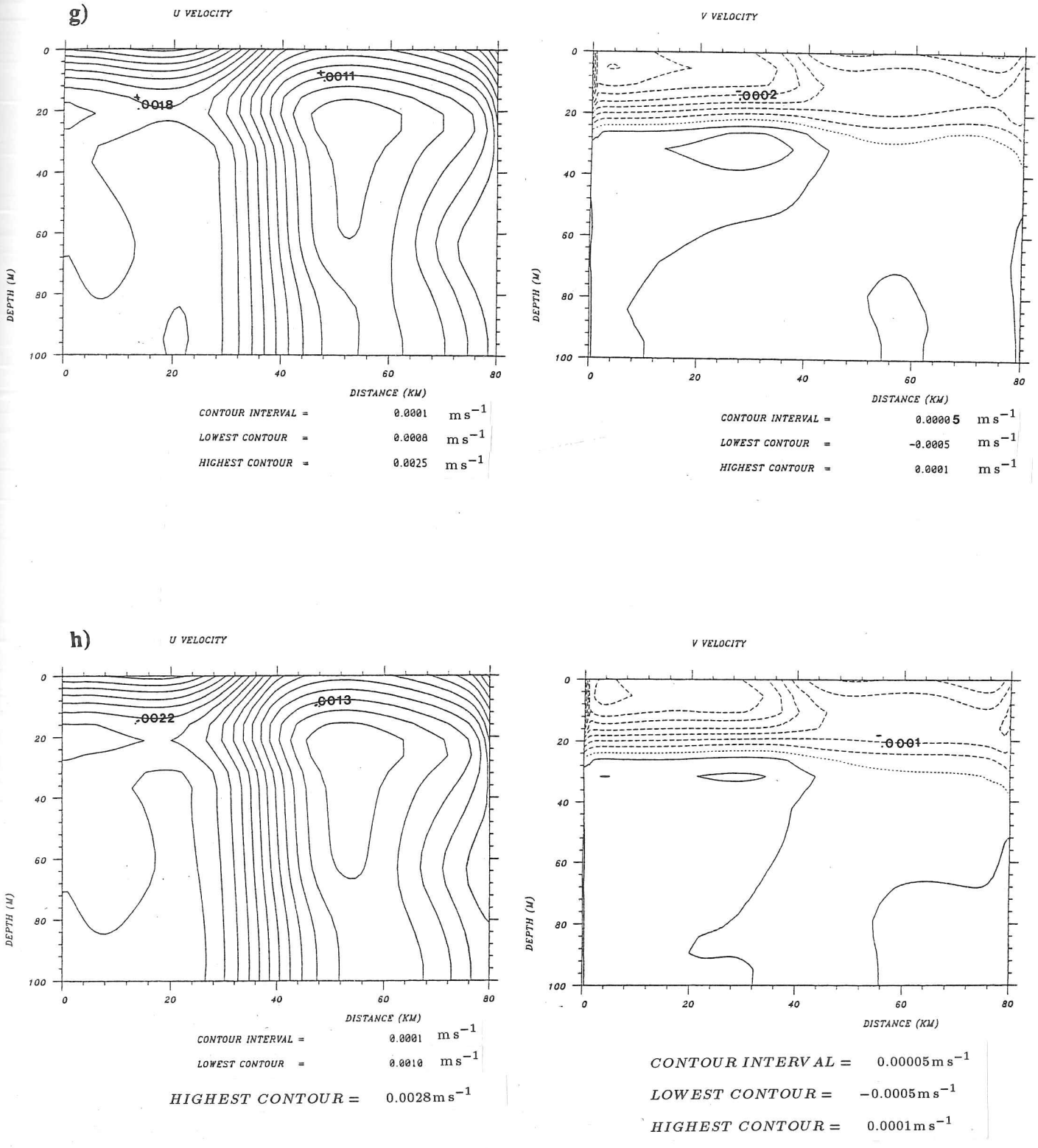

Figure 4.13: continued.

brine convection case. However, this soon proved unsatisfactory and was replaced by an exponential relationship between the two variables with a 25% drop in salt flux magnitude occurring between 0.9 and 0.1 ice compactness levels. Moreover, as the Bering Sea ice edge regime is determined by ice advection rather than by local ice growth rates, the control of the ocean density regime by such a strong dependence on the surface flux condition may be inappropriate.

4.10.2 Ice growth

Ice growth rates are calculated from a zero-level Semtner (1976b) model forced by the air-sea exchange and radiation terms introduced in section 1.3. The heat flux from the ocean to the ice was taken as the difference of the surface water temperature from freezing point, with an ice-water conductivity coefficient of $200\,\mathrm{J\,m^{-2}\,s^{-1}\,(^{\circ}C)^{-1}}$. The value of the ice growth calculated by the thermodynamic model is used to evaluate the latent heat transfer to the ocean.

When the surface waters are very close to the freezing point, salt released to the water column during ice growth will lower the freezing point and thereby increasing the heat flux. Hence, in a similar way to the one-dimensional model (sec 4.2) a stable state is never reached. A possible solution would be to hold the freezing temperature at a fixed value which would in turn prevent excessive heat loss and ice growth.

Ice concentration is restrained from ever reaching 100%, so some minimal open water thermodynamic transfer is always included in the model. Any additional sea ice growth which would bring the ice compactness to the 100% value is added instead to the ice thickness profile when one is maintained by the model.

In a similar way to the field data the largest heat flux in the model occurs through the open water areas, where heat transfer is at least an order of magnitude greater than that through 1 m thick ice. The ice ablation/accretion rate had a maximum value of $1 \times 10^{-5}\,\mathrm{m\,s^{-1}}$ which is equivalent to a growth/melt rate of $8\,\mathrm{cm\,day^{-1}}$. This is small by MIZ standards where melt rates of $0.5 - 1.0\,\mathrm{m\,day^{-1}}$ are found from melt gauge records at the extreme edge (Josberger and Meldrum, 1985). However, these high values were observed after the instrumentation had drifted across an ocean front. Measurements made at the start of the experiment further into the ice cover were closer to $10\,\mathrm{cm\,day^{-1}}$. Hence, the maximum value of $8\,\mathrm{cm\,day^{-1}}$, calculated by our thermodynamic model, is not an unreasonable estimate. Also, as we were only considering ice growth at a latitude of 60° N we would not expect a more rapid freezing rate.

No diffusion terms were routinely added to the ice thickness and ice compactness equations in our model. The large scale basin models used by Hibler (1979) and Bratchie (1984) have included both a second order diffusion term and a bi-harmonic diffusion term to filter out errors introduced at higher wavenumbers by numerical diffusion during the ice advection process. However, when an ice accretion/ablation rate of the order of 5 cm day^{-1} is calculated as the appropriate thermodynamic change in an off-ice edge grid point, this is often less than the change arising from numerical diffusion within the conservation equations.

Hence, we ran some experiments with a corrective diffusion term with several different coefficient values arranged to cancel out the numerical diffusion. However this approach eventually led to ripples in the ice concentration curve at low ice values. Eventually, it was decided that it was better to tolerate small order numerical diffusion terms in the off-ice grid points than to generate ripples which could lead to instabilities.

An attempt to parameterize the growth in leads within the pack was made by weighting the fluxes to ice concentration levels using the two layer thickness form proposed by Hibler (1979) (eqn. 4.70). The lower level, representing open water conditions was set at < 5 cm . These formulae do not produce the new ice growth rates that are expected at low ice concentrations during prolonged cold periods of off-ice winds. As in the case of the prescribed fluxes, most ice growth occurs in polynyas and leads at the high concentration values.

For these reasons, the choice and implementation of the ice growth algorithm in the model is crucial when considering thermodynamic changes on short time scales. Climate based thermodynamic algorithms do not respond fast enough to new conditions. In contrast, the ocean model responds rapidly to cooling events (convection) generated by the presence of the ice, with the ice reacting more slowly to heat increases which are derived from changes in the ocean model. This may seem a contradiction to our original supposition based on field data that it is the advection of ice across the ocean front which causes the ice to melt. However, this is a consequence of the initial temperature condition used in the model, where the upper horizontal homogeneous layer reduced the heat available from the ocean to the ice significantly below levels found in field data. When we later increase the flux into the open water grid points using the surface heat budget we alter this horizontal homogeneity significantly.

4.10.3 Thermodynamic dependent ice ocean fluxes

In the longer model runs it was inappropriate for the fluxes to be directly coupled with the local ice concentrations values. Therefore, the heat flux in longer runs was related to the thermal driving i.e., the difference of local temperature above freezing. The salt flux was a function of the melt/growth rate and appropriate salinity driving.

In longer simulations when the ice-ocean fluxes were dependent on the ice growth rate, some the grid points close to the edge encounter both ablation and accretion conditions on a daily basis. In implementing flux conditions which are dependent on ice growth rates which change sign during the model simulation, a reasonable level of horizontal diffusion is required in order to smooth out the density changes which could be introduced by having opposing flux gradients at adjacent grid points. If this diffusion is inadequate and the gradients in the influx continue to be considerable, narrow patches of warm/cold water form at neighbouring grid points.

4.10.4 Model simulations under variable external conditions

The initial surface temperature was chosen at $-1.5\,^{\circ}\mathrm{C}$ to reduce the adjustment during spin up in the ice-covered domain. In choosing horizontally homogeneous initial conditions for the model, we expected that the surface fluxes would alter the density structure to produce a more appropriate cross-edge distribution. Hence, we imposed an open water heat flux including the daily insolation cycle. In this group of model runs the far field temperature was also heated from below by a flux into the base grid points. This heat flux was introduced to represent the heat contributed to the shelf region by the barotropic along slope current. Hendricks *et al*, (1985) had proposed that the on-ice component of this current was a major source in the overall heat budget for winter shelf conditions.

Gradients in wind forcing and surface air temperatures were used as external forcing conditions for these model runs. With a gradient in the wind forcing and no ice rheology to maintain ice coherence, the gradient in wind stress will cause either a convergence or divergence zone in the ice cover. This in turn will alter the combined stress of wind and ice reaching the upper ocean. If this wind gradient is coincident with the maximum ice gradient the convergence/divergence will be amplified. The end result of the combined ice/wind stress curl on the ocean velocities is to rapidly destabilize the ocean model.

Though the gradient in air temperature in the Bering Sea is normally directed north-south, the gradient in wind speed is less uniform as weather systems are often dominated by the presence

of cyclonic and anticyclonic pressure structure as well as frontal weather features. Furthermore, a gradient in the wind stress alters both the open water percentage in the ice cover and (indirectly) the turbulent fluxes reaching the ocean in such a manner that the salt and heat flux gradients changes sign within the ice covered region. If we are unable to diffuse strong horizontal gradients that may be created by such conditions, baroclinic ocean currents will develop. These in turn will disturb and possibly amplify the ice field variation.

4.11 Initial condition for ice distribution

The original ice distribution curve used in the early coupled simulations consisted of a constant compactness value of 0.9 up to 20 grid points (20 km) of the prescribed initial ice edge position. Over this interval the value of ice concentration was allowed to decrease smoothly to zero via a quadratic relationship. Within this ice distribution only the outer 10 grid points had concentrations less than 75%. The width of this outer zone was not easily varied with the quadratic. Hence, other initial relationships between the ice compactness value and its relative distance from the ice-edge were examined. Throughout our search the smoothness of the ice concentration curve was of primary importance, so that the function was differentiable to the accuracy of the finite-difference approximation. This is because several of the more complex ice rheologies are dependent on ice compactness and its derivatives. Two forms we considered for the ice concentration distribution were a) an exponential function and b) a hyperbolic tangent functions Overall, the hyperbolic tangent form was more useful, with the width of the ice edge zone (area of ice concentration less than 80%) easily altered. Using this relationship the ice concentration at grid point J was determined by

$$A_J = \tanh(M^2 + M + 4) \tag{4.73}$$

where $M = (MJ - J)/RM$, (MJ is the original ice edge position). The parameter RM was normally set to a value of 15, but when RM was allowed to take on a range of values from 8–30, the function A_J generated a set of diffuse-through-to-sharp ice concentration curves. When necessary, the initial condition for the ice thickness distribution was set to be proportional to the ice concentration distribution with a maximum ice thickness of 1 m.

4.12 Internal stress simulation in the ice model

In the first instance internal ice stress in the ice model momentum equations was in the first instance represented by an ice resistance/viscosity coefficient analogous to the eddy viscosity term in the ocean model (Campbell, 1965). However, choice of a suitable amplitude for this coefficient, which one would intuitively expect to be at least an order of magnitude greater than the viscosity in the ocean, created problems in the implementation in the model. Hence, the ice resistance term was removed until other features of the model which were not dependent on the rheology had been considered.

An upper limit for the viscosity value is set by the time step restriction of equation 4.72. The value of the 'ice eddy viscosity' at which the 1 km grid model rapidly became unstable was $10^3\ m^2\ s^{-1}$. Ice rheology terms with coefficients of this magnitude have been successfully used in several fine resolution models (Hakkinen, 1984; Røed and O'Brien, 1983), yet our time step of two minutes was below half the value required by condition 4.72 to maintain stability. This constraint on the size of the 'resistance term' was cross-checked by increasing the grid spacing to 2 km whilst leaving both the time step and ice viscosity unchanged. When the model was run with these conditions an identical instability was created twice as far into the integration (Figure 4.14).

Our value of $10^3\ m^2\ s^{-1}$ for the ice viscosity is smaller than those favoured by large scale modellers who considered more appropriate values for the 'ice strength' to be $2.5 \times 10^4\ N\,m^{-1}$ (Lepparanta and Hibler, 1985). The units we have used for the (kinematic) viscosity coefficient are $m^2\ s^{-1}$ whilst other authors give their resistance in terms of a strength value in $N\,m^{-1}$. The difference arises because we have divided throughout our momentum equation by the ice mass term which was retained in the equations of Hibler (1979). Røed and O'Brien (1983) studying ice-ocean processes at 1 km resolution considered an ice strength value in the range $5 \times 10^3 - 10^4\ N\,m^{-1}$ to be appropriate for their model. Hakkinen (1984), however, justified reducing the amplitude of both the shear and bulk viscosity coefficients in her model in comparison to the large scale models with a dimensional analysis argument. Measurements during MIZEX-83 in the summer pack of the Greenland sea have demonstrated, by measuring the strain across an array of accurately positioned transponders over a month, that an ice strength of order $10^3\ N\,m^{-1}$ may be a reasonable estimate for the MIZ and that values in the range $10^4 - 10^5\ N\,m^{-1}$ may be more appropriate to interior Arctic ice which is more constrained (Lepparanta *et al*, 1986).

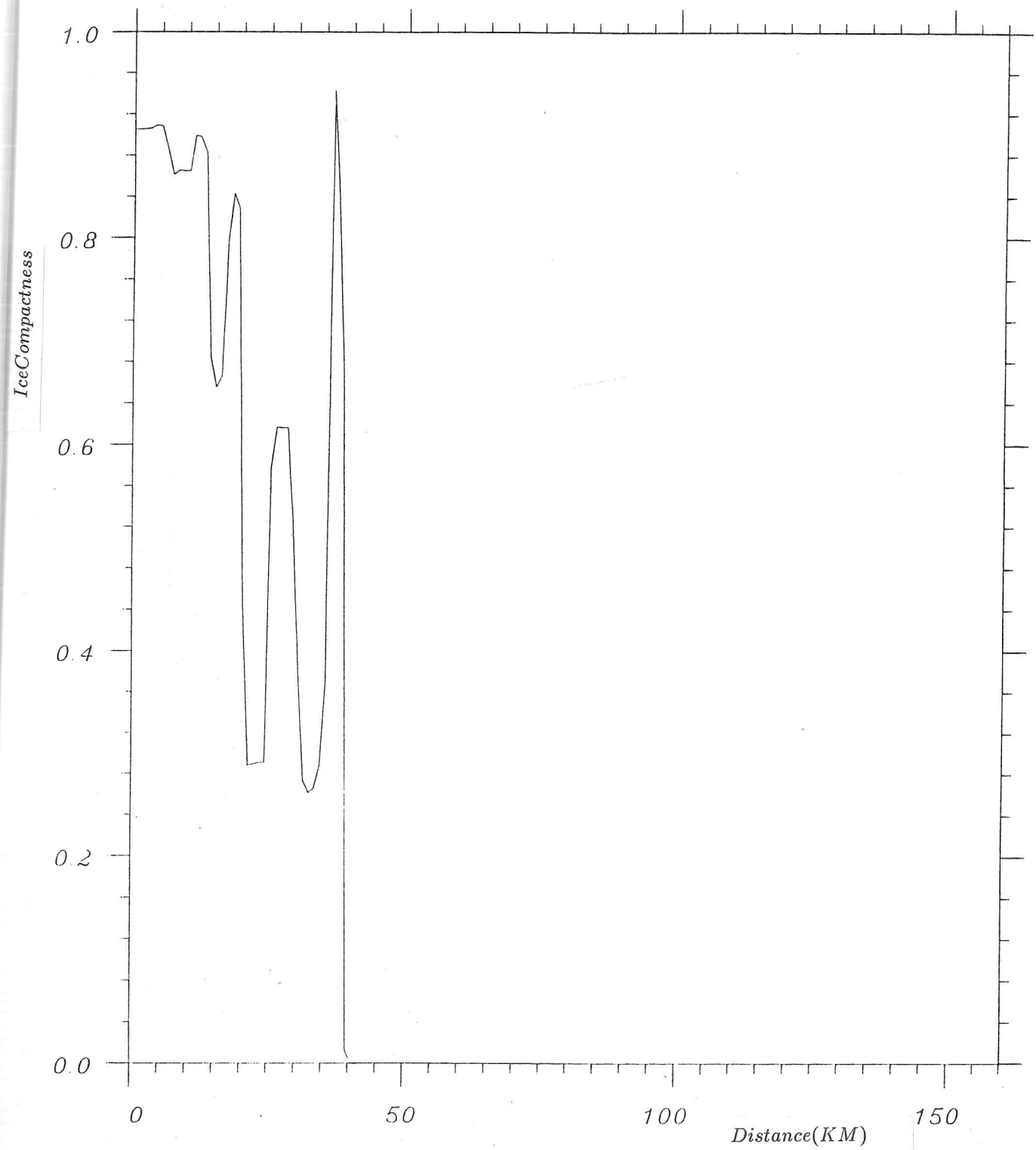

FIGURE 4.14: Ice compactness distribution 18 hours into simulation when rheology includes an ice pressure term exponentially dependent on the ice compactness. The initial ice distribution dropped to zero over 5 grid points. Model domain is now 160 km wide.

We have emphasized the importance of the magnitude of these 'viscosity' coefficients in the above paragraphs because when our ice model simulation includes the Hibler (1979) rheology, simplified for one horizontal direction, it rapidly becomes unstable. Close investigation of the balance of terms in the momentum equations indicates that the major impact of the rheology was not from the strain rate tensor values derived from the velocity field (equation 1.8), but was due to the amplitude of the internal stress discontinuity at the ice edge. In particular the term $\partial P/\partial y$ in the momentum equation, where P the ice strength is given by $P_* \exp -\kappa(1-A)$, could easily amplify any ripples which develop in the ice concentration distribution. In addition, as both the shear and bulk viscosity terms are functions of the ice strength they will also generate problems if the gradient of the ice strength term is excluded from the equations.

Whilst we acknowledge that there were problems with an ice resistance of order $10^3\,\mathrm{m^2\,s^{-1}}$ in our 1 km model grid, we often used a value of $500\,\mathrm{m^2\,s^{-1}}$ for which the model remained stable after several thousand time steps. We continued using this value for the ice strength/viscosity coefficient while we gradually increased the rheological complexity of the model.

After considering a simple viscosity-like form for the ice resistance the next step was to allow the internal stress to be a function of ice concentration. Following Nerella and Liu (1979) we set the stress term to be

$$\frac{\partial(AK_L)}{\partial y}\frac{\partial u}{\partial y}.$$

If the resistance coefficient K_L is constant across the domain then this equation can be further simplified.

The importance of a smooth initial ice concentration distribution should now be clear, as any sharp gradients that evolve in the ice concentration distribution will be amplified by this internal stress and will eventually lead to a model instability. However, a linear relationship between the ice resistance and ice compactness does not sufficiently emphasize the rapid reduction in internal stress that occurs at the ice edge. We can achieve a suitable reduction in coherent ice motion at lower concentrations by allowing the ice resistance to be proportional to an exponential function of ice compactness. The decay constant κ within this exponential function was called the 'ice diffusivity coefficient' by Hibler (1979). Hence, we set the ice strength P to be

$$P = P_* \exp(-\kappa(1-A)) \tag{4.74}$$

We chose to continue using a value of 20 for the ice diffusivity κ in our model, after Hibler (1979)

and Røed and O'Brien (1983). Røed and O'Brien (1981) showed that this value of κ was the most suitable to maintain a sharp ice edge.

Unfortunately, this improved definition of the internal ice stress form did not increase the stability of the model. Altering the value of the ice diffusivity κ_s only shifted the grid point at which the instability first formed. The instability in this instance arose because the finite difference approximation of the ice strength was not well discretised by the 1 km model grid.

In normal circumstances the first approach to solve such a problem would be to develop finer grid spacing for this region of the model. However, the reduction in the model grid size also requires a smaller time step and a smaller ice viscosity/strength amplitude. Moreover, the extra storage requirements make this approach prohibitive as we would need to subdivide the grid in this region by a factor of 10.

4.13 Nature of instability developed by coupled ice-ocean model

Throughout the above discussion of our multi-level coupled model we have referred somewhat arbitrarily to a point when the model has become unstable, even though this instability often arises from a number of sources. Once initiated, unstable waves will propagate and grow both in the ocean and ice velocity fields. This occurs most often when too rapid a gradient in external stress is forcing the ocean. Also, the instability can originate in the density field, which in extreme cases can produce alternate patches of warm/cold water when there are significant gradients in the surface flux condition.

Eventually these instabilities will act to reinforce one another; a velocity disturbance will alter the density field which in turn will increase the velocities. This amplitude feedback of the instabilities is especially strong between the ice model and the ocean model. A disturbance in the ocean velocity field causes convergence/divergence of the ice, which in turn increases the stress gradient reaching the ocean. The fact that the ice compactness is restrained to lie between the limits of 0.0 and 1.0 makes the ice model more susceptible to break down as the advection of ice into an area of compact ice is prevented.

One particular feature of the instability generated by any of the complex rheologies which include an exponential decrease in ice strength at the edge is that the model breaks down in a similar way each time. The sequence of events leading to the instability begins with the outer edge of the

ice cover advecting away from the initial edge position, leaving a reduced ice cover behind. This depression in the ice concentration value creates the expected oscillation in the cross-edge velocity field. A further disturbance in the ice concentration distribution curve then develops some way into the main ice mass as the first disturbance separates away from the ice pack (Figure 4.14).

This 'numerical band' is not linked in any way to the physical case of banded regions of ice that occur at the Bering sea ice edge which we described in detail in section 2.5. However, the generation of the 'numerical band' does illustrate the point that once such a velocity disturbance is formed in the ocean it is possible that it could break down a constrained ice mass into several separate zones. (Muench *et al*, 1983; Sjøberg and Mork, 1985) Also, the coherence of the ice grouping in the band appears to be maintained by the ice rheology term, for each of the following ice zones has a similar smoothed leading edge. Whenever this model or simulations by other authors show a tendency to develop divergent ice 'banded' structures, the role played by the ice rheology terms in the momentum balance equation, and the relative size of each term, should be examined in detail to ensure that the feature is not a numerical artefact.

Numerical methods for propagating strong gradients

The instability problem addressed in the above paragraphs is a result of trying to parameterize the abrupt change in internal coherence of the ice pack as we encounter the ice edge. In other branches of fluid dynamics, particularly those associated with moving shock waves, several numerical techniques have been developed to tackle analogous problems. Two of these methods are be employed in our ice model.

Firstly, a technique known as flux corrected transport (Book et al, 1975). Here, extra diffusion is added at particular points in the system to correct miscalculation of the ice concentration by the dynamics. Using this technique we can theoretically propagate a discontinuity through the fluid. This scheme was mentioned briefly earlier in this chapter, where we were trying to maintain a sharp gradient zone in early versions of the ocean model (section 4.6.2).

The second technique we wish to pursue is the method of characteristics successfully implemented by Røed and O'Brien (1983) in their coupled ice-ocean model. This method is widely used in gas dynamics when there is a moving shock wave disturbance. O'Brien and Reid (1967) also used the method when simulating the effect of a moving hurricane on the upper ocean.

4.14 Flux corrected transport

The flux corrected transport method (FCT) is designed to circumvent problems generated in finite difference schemes when a steep gradient is propagated, without needing to implement finer grid spacing in the region of difficulty (Book *et al*, 1975). Essentially FCT involves applying a corrective diffusion to the parts of the model grid where unphysical ripples are formed after the advection of a steep gradient. If left untreated these ripples would grow into instabilities. The authors suggest that this method is most successful when advective processes dominate the diffusive processes in the conservation equations. However, Book *et al* (1975) state that the method can be used to treat other equations. During operation of the scheme the fluid is conserved. For at a particular time step when mass is added by the scheme to one grid point an equal amount is removed from a neighbouring one.

The advection, diffusion and anti-diffusion operations occur in three stages and are not commutative. The FCT scheme applies diffusion throughout the grid and then the anti-diffusion process cancels this diffusion out, in the regions where it is unnecessary. The anti-diffusion is limited to be no greater than the maximum forward diffusion. The anti-diffusion value will be set to zero when it would otherwise enhance any local maximum or minimum in the profile. Hence, repeated application of the diffusion and anti-diffusion process forms a plateau over a number of grid points, where previously an extremum occurred.

We have chosen to determine our anti-diffusion values using the 'phoenical' scheme (Book *et al*, 1975) where the diffusion effect disappears if there is no advection present in the equation. The implementation of the scheme within the model code is dependent on the time stepping scheme used by the model. To use FCT appropriately in a leap-frog time scheme there needs to be interaction between the two time levels of the scheme. Instead, we continued to use two separate time levels with only the advection term linking the two time stages. However, for this approach to succeed we require half the grid spacing and consequently half the time step. Hence, if we adopt this version of the scheme we do not avoid using a finer model grid. Alternatively, we could implement the FCT scheme using a Lax-Wendroff time scheme, where the time step is split into two halves, with the advection terms at the final stage dependent on the half point calculation.

The stages in the scheme are firstly to calculate the diffusive fluxes f_j

$$f^0_{j+1/2} = \eta_1(v^n_{j+1} - v^n_j) \tag{4.75}$$

where η_1 is the normalized diffusion coefficient. The rest of the momentum equation is advanced in the normal way

$$v_j^{n+2} = v_j^n + \ldots \tag{4.76}$$

We then calculate the anti-diffusive fluxes by

$$f_{j+1/2}^1 = \eta_1(v_{j+1}^{n+2} - v_j^{n+2}) \tag{4.77}$$

The diffusion is applied by

$$\hat{v}_j^{n+2} = v_j^{n+2} + f_{j+1/2}^0 - f_{j-1/2}^0 \tag{4.78}$$

The first differences of $\hat{v}$ are then used to calculate

$$\Delta_{j+1/2} = \hat{v}_{j+1}^{n+2} - \hat{v}_j^{n+2} \tag{4.79}$$

We limit the anti-diffusion flux to be applied using

$$f_{j+1/2}^c = S.\max\{0, \min(S.\Delta_{j-1/2}, \mid f_{j+1/2}^1 \mid, S.\Delta_{j+1/2}\} \tag{4.80}$$

where $S = \mathrm{sgn}(f_{j+1/2}^1)$. The flux corrected velocity field is given by

$$\tilde{v}_j^{n+2} = \hat{v}_j^{n+2} - f_{j+1/2}^c + f_{j-1/2}^c. \tag{4.81}$$

where $\tilde{v}_j^{n+2}$ represents the flux corrected value of v_j^{n+2}.

Implementation of the FCT occurs across the entire model grid even though the region which needs the scheme is at the ice edge in the centre of the domain. Moreover, the extra diffusion introduced by the scheme upsets the solution at the model boundaries, hence we avoid implementing the scheme at the outermost grid points. The value of the normalized diffusion coefficient η_1 used in both diffusion and anti-diffusion fluxes was in the range 0.1-0.4 with a value of 0.35 being the most appropriate.

Although some improvement was found in the ice model results when using FCT scheme, with the rate at which an instability arose being delayed, the coupled ice-ocean system still eventually became unstable. This suggests that the decrease by two orders of magnitude in the internal stress term within two to three grid points, is too sharp to be even considered by this technique.

It was thought that the choice of initial condition for the ice model might be an important factor in the rapid model destabilization. For, if all the velocities start the simulation set to zero there is no

term in the momentum equation which can balance the magnitude of the internal stress gradient at the ice edge. Hence, the discontinuity introduced by the internal stress will propagate outwards in the velocity field (initially by diffusive processes) and will eventually develop into an instability. As a different initial condition we spun up the coupled model, preventing the ice compactness from adjusting by advection by the ice velocity field. This technique ought to improve the overall stability, since as soon as small changes in ice compactness are created they are converted to large changes in the ice strength magnitude because of the exponential relationship between ice strength and ice compactness. Thus rapid changes in sign in the pressure gradient term $\partial P/\partial y$ are produced which are associated with ripples in the ice concentration distribution. However, neither this approach nor a second attempt which used the results of a rheology-free model as initial condition proved successful. This is because the gradient of the ice strength term was still an order of magnitude greater than other terms in the momentum equation at the ice margin. Following, our earlier discussion on the magnitude of the ice resistance term, a scaled-down (scaled by the square of the ratio of the sizes of the two model grids) ice strength coefficient P_* from Hibler (1979) was used. This value still proved to be too large a gradient to be sustainable in the model however. Moreover, if we remove the $\partial P/\partial y$ term in the constitutive equation for the ice rheology, because it dominates the balance in the momentum equation and initiates the instability, we can then concentrate our efforts on choosing appropriate values to use for the shear and bulk viscosity coefficients. These coefficients are themselves a function of the strain rate values and the ice strength. We again used a scale factor of 10^3 on Hibler's (1979) creep limit, which was used to scale his values for the shear and bulk viscosities in equation 1.8. We had a greater degree of success with this form of rheology for now the strong gradients in the viscosity terms of the momentum equations are weighted by three ice concentration values. However, this model did eventually produce excessive ice velocity values and became unstable in the same manner as before.

As a final point we note that if our ice rheology had been chosen such that the ice strength was a function of the floe size distribution (Bratchie, 1984), as well as being dependent on ice compactness, we may have avoided some of the abruptness in the change in internal stress at the ice edge, whilst more realistically modelling the ice-ice interaction. Unfortunately, the complexity of the floe size distribution model proposed by Bratchie (1984) made it unsuitable for use in our coupled ice-ocean model.

term in the momentum equation which can balance the magnitude of the internal stress gradient at the ice edge. Hence, the discontinuity introduced by the internal stress will propagate outwards in the velocity field (initially by diffusive processes) and will eventually develop into an instability. As a different initial condition we spun up the coupled model, preventing the ice compactness from adjusting by advection by the ice velocity field. This technique ought to improve the overall stability, since as soon as small changes in ice compactness are created they are converted to large changes in the ice strength magnitude because of the exponential relationship between ice strength and ice compactness. Thus rapid changes in sign in the pressure gradient term $\partial P/\partial y$ are produced which are associated with ripples in the ice concentration distribution. However, neither this approach nor a second attempt which used the results of a rheology-free model as initial condition proved successful. This is because the gradient of the ice strength term was still an order of magnitude greater than other terms in the momentum equation at the ice margin. Following, our earlier discussion on the magnitude of the ice resistance term, a scaled-down (scaled by the square of the ratio of the sizes of the two model grids) ice strength coefficient P_* from Hibler (1979) was used. This value still proved to be too large a gradient to be sustainable in the model however. Moreover, if we remove the $\partial P/\partial y$ term in the constitutive equation for the ice rheology, because it dominates the balance in the momentum equation and initiates the instability, we can then concentrate our efforts on choosing appropriate values to use for the shear and bulk viscosity coefficients. These coefficients are themselves a function of the strain rate values and the ice strength. We again used a scale factor of 10^3 on Hibler's (1979) creep limit, which was used to scale his values for the shear and bulk viscosities in equation 1.8. We had a greater degree of success with this form of rheology for now the strong gradients in the viscosity terms of the momentum equations are weighted by three ice concentration values. However, this model did eventually produce excessive ice velocity values and became unstable in the same manner as before.

As a final point we note that if our ice rheology had been chosen such that the ice strength was a function of the floe size distribution (Bratchie, 1984), as well as being dependent on ice compactness, we may have avoided some of the abruptness in the change in internal stress at the ice edge, whilst more realistically modelling the ice-ice interaction. Unfortunately, the complexity of the floe size distribution model proposed by Bratchie (1984) made it unsuitable for use in our coupled ice-ocean model.

4.15 The method of characteristics

Following the lack of success with FCT, we examined further the approach used in Røed and O'Brien's (1983) ice model where the ice cover had maintained coherence during a variety of wind forcing conditions. The rheology in this model is represented only by an ice pressure gradient term with an amplitude an exponential function of the ice concentration. When there is no other external forcing the pressure term causes the ice model to undergo geostrophic adjustment (Røed and O'Brien, 1981)

The method Røed and O'Brien (1983) used to solve their momentum equation involves solving along the characteristics (Figure 4.15). We have two real characteristics as the momentum equation is a second order hyperbolic equation. Using this approach we reduce our second order quasi-linear partial differential equation to two ordinary differential equations along the set of characteristics (Smith, 1978). We quote both the original and characteristic form of the ice-model equations directly from Røed and O'Brien's (1983) paper, and refer the reader either to Røed and O'Brien's appendix or a standard text (Smith, 1978) for the derivation of the characteristic equations.

The original momentum equations are

$$\frac{\partial u}{\partial t} + v\frac{\partial u}{\partial y} - fv = \rho C_w(U-u)/\rho_i D + \tau_a^x/\rho_i D \tag{4.82}$$

$$\frac{\partial v}{\partial t} + v\frac{\partial v}{\partial y} + fu + (\frac{c^2}{A})\frac{\partial A}{\partial y} = \rho C_w(V-v)/\rho_i D + \tau_a^y/\rho_i D \tag{4.83}$$

Where c the speed of wave propagation through the ice is given by

$$c^2 = c_o^2 A e^{-\kappa(1-A)}. \tag{4.84}$$

The speed of propagation of the fastest wave, c_o is ($6\,\mathrm{m\,s^{-1}}$)

$$c_o^2 = \kappa^2(P_*/\rho_i D)/(e^{-\kappa} + (\kappa - 1)) \tag{4.85}$$

$$\tag{4.86}$$

where κ is the ice dispersivity.

We also use the conservation of ice compactness

$$\frac{\partial A}{\partial t} + v\frac{\partial A}{\partial y} = 0. \tag{4.87}$$

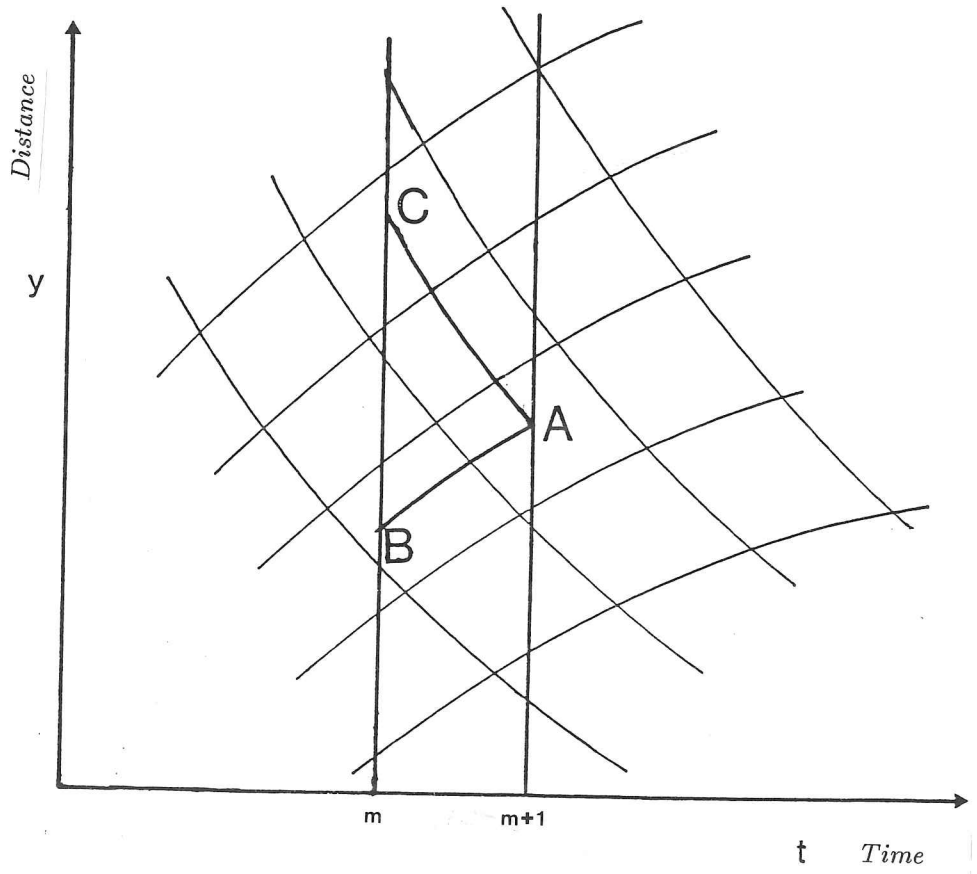

Figure 4.15: Diagram showing lattice of characteristics for hyperbolic second order differential equations. The variables calculated on the characteristics can be interpolated onto a regular grid by allowing the variables at point A, time step $m+1$, to be dependent on the variables a points B and C, time step m, where the characteristics intersect the previous time level.

The equations are combined to give a set of equations to be solved along the characteristics of the form:

$$\frac{Dv}{dt}_{-} - \frac{c}{A}\frac{DA}{dt}_{-} = G(u,v,A) \tag{4.88}$$

$$\frac{Dv}{dt}_{+} + \frac{c}{A}\frac{DA}{dt}_{+} = G(u,v,A) \tag{4.89}$$

$$\frac{Du}{dt}_{s} = F(u,v,A) \tag{4.90}$$

$$F(u,v,A) = fv + \rho C_w(U-u)/\rho_i D + \tau_a^x/\rho_i D \tag{4.91}$$

$$G(u,v,A) = -fu + \rho C_w(V-v)/\rho_i D + \tau_a^y/\rho_i D \tag{4.92}$$

Derivatives are evaluated along characteristics slopes, i.e.,

$$\begin{aligned} C_+ : (Dy/dt) &= v + c \\ C_- : (Dy/dt) &= v - c \\ C_s : (Dy/dt) &= v \end{aligned} \tag{4.93}$$

In implementing the method of characteristics for the ice model we had to consider how the coupling between the ocean model, which is calculated on a regular finite difference grid, and the ice model, where the solution is only calculated along the equation characteristics, is achieved. At some point interpolation onto the grid must occur so that the terms common to both models, particularly the stress coupling, can be calculated. We know that once ice concentration and cross-edge velocity values are known along the characteristic curves, they can be theoretically determined in any region bounded by the curves.

An interpolation method for use in solving along characteristics when one of the variables is available at regular grid intervals, was proposed by Hartree (1952). In this method shown diagrammatically in (Fig 4.15) we can trace back from the current time step (m+1) to find the values for grid point A using the pair of characteristics which pass through A. These intersect the previous time level m at points B and C. As points B and C will not normally be coincident with regular points in the finite difference grid we need to interpolate the required values (ice velocities, ice concentration, G_B and G_C).

Hartree (1952) suggests linear interpolation along the space axis should be suitable for most situations. However, in practice it was found that interpolation over 3 points produced smoother

results, particularly at grid points where the local propagation speed c is small, with both characteristics intersecting the previous time level between the same pair of grid points. Quadratic interpolation worked successfully in all cases with one exception, which involved interpolating the ice concentration at the extreme edge. To avoid spurious negative values, it was therefore necessary to use linear interpolation for these points.

When solving along characteristics we have to assume in the first instance that the characteristics can be represented by line segments. We need to use the velocity value from the previous time step to calculate the gradient of the line. We can then estimate the intersection points of the characteristic with the grid at the previous time step. Using the interpolated values we can calculate the velocity and ice concentration (and hence the propagation speed c) for the current time step and use the new values to update the previous estimate of the characteristic gradient. This procedure continues until the calculated cross-edge velocity and ice concentration values converge, which normally takes no more than 5 iterations per time step. The additional computer time used when the ice model is solved by the method of characteristics, particularly when it is necessary to iterate to a solution, is small as the ice model only represents a 1/15th of all the grid points for which values have to be calculated at each time step.

Although, we could have solved the along edge velocities in a similar manner to the cross-edge velocity using a single characteristic, it would produce the same result as a normal finite difference technique. This is because the solution along the characteristic represents the calculation due to the advective term in the earlier model runs. We also needed to define the ice edge position so that we could determine the grid points at which the characteristic equations needed to be solved. This was achieved by redefining the ice edge location at the end of each time step by advecting it a distance determined by the velocity at the outermost ice grid point. A new grid point enters into the characteristic scheme after the ice has advected over half-way across the grid spacing. The calculations of velocity in the grid points outside the ice margin were retained after using a conventional finite difference scheme, so that continuity in the higher order derivatives is maintained at the ice edge boundary. We could have continued with a characteristic solution across the whole domain. This was done later, producing little overall difference in the velocity results to the conventional case for which the computer code already existed.

A further point to consider is that Røed and O'Brien (1983) initiated their ice simulations from the geostrophic equilibrium state, which resulted when no external terms were available to balance

the pressure term (Røed and O'Brien, 1981). They showed that this initial condition was sufficient to cause considerable pycnocline deviation (over 20 m in 4 days of simulation) without any external stress discontinuity (Røed and O'Brien, 1983). However, in our model simulations we found that the ice concentration curve developed small ripples in the region of less than 0.7 compactness. These errors may arise from the closeness of the characteristic intersections from the previous time level, and the quadratic interpolation scheme we used to match the characteristic solutions with a regular finite difference grid. As we were relying principally on external (atmospheric forcing) to drive the coupled model we felt it was unnecessary to persue this initial geostrophic condition any further as it would involve us in more-elaborate interpolation schemes. We therefore reverted to spinning up the model with both the ice and ocean model at rest.

One factor which appeared to be strange when comparing runs with this rheology with those without any rheological forcing is that there is a difference in the direction the ice moves with the same wind forcing (Figure 4.16, 4.17). Winds which have previously acted in the off-ice direction now act as if they are on-ice. In spite of this, the stress forcing and the velocity fields were continuous at the ice edge. Unfortunately, though this phenomenon was noted at this stage its significance was not fully investigated until later, when use of the solution along characteristics produced strange results when forcing the model with realistic winds.

After carefully checking the algebra of the model, a solution to the problem concerning the difference in wind directions was attempted by examining the effect of a change in the sign of all non-characteristic terms on the RHS of the momentum equation (G). This change in sign only produced excessive cross-edge velocities. Further, a reversal of the sign of the wind stress alone advected the ice in the expected direction. At this point, the original sign convention was retained for all subsequent simulations.

On returning to the problem of this change in direction of ice advection under given wind forcing later, we observed that the stress forcing in the solution along characteristics produced a velocity field of the same sign and magnitude as in the non-rheology case. This suggested that the increase and decrease in ice concentration must depend on the ice velocity gradient, which affects the changes in ice compactness through the advective term in the conservation equation. Close examination of the velocity field for the non-rheology case revealed minimal gradients, with values of the order 10^{-5} m s^{-1} in the early stages of model spin up. The cross-edge ice velocity became progressively more negative as ice concentration decreased. A small maximum in ice velocity, again of

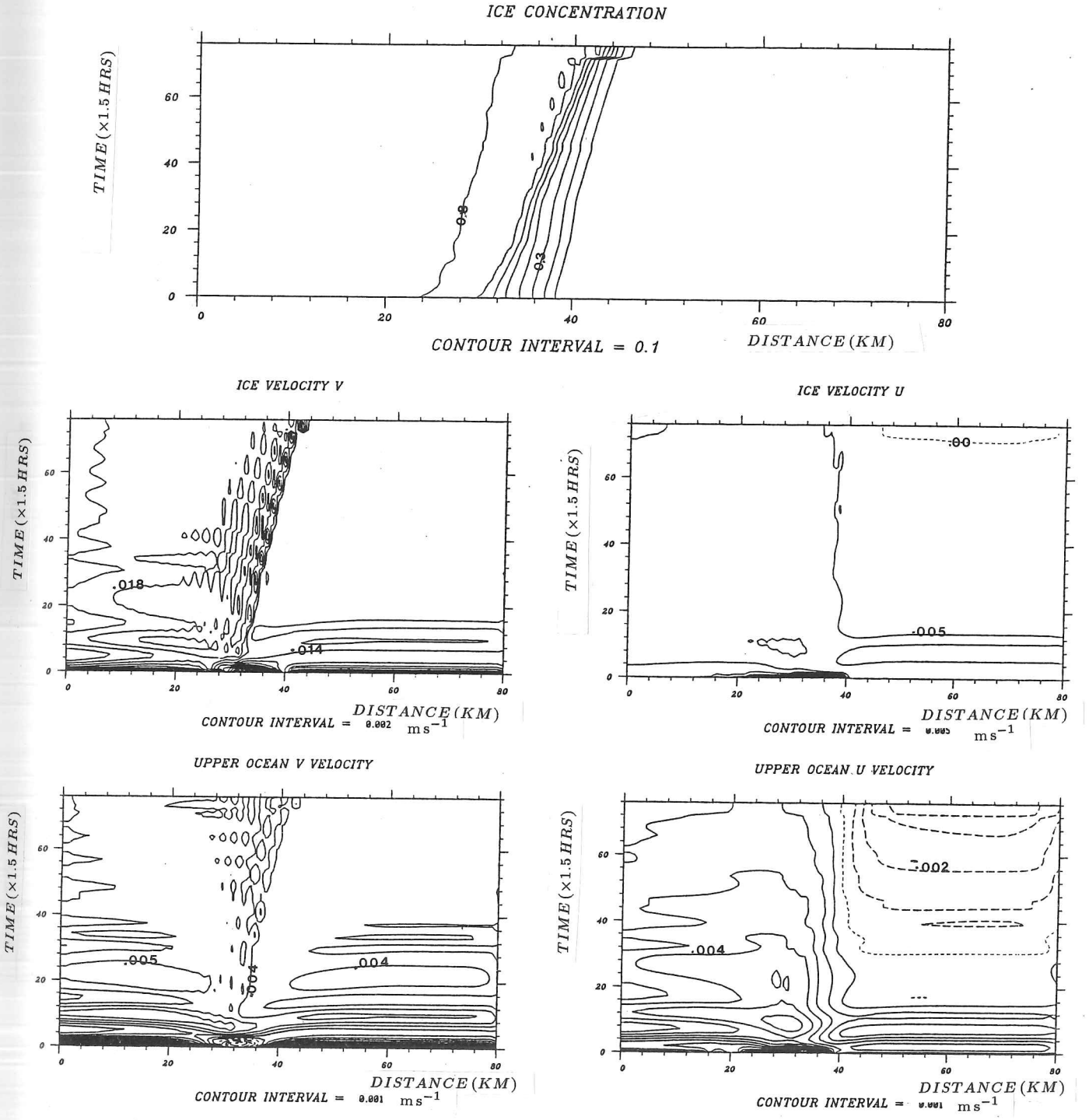

FIGURE 4.16: Contoured time series (1 record = 90 minutes) for model solution when the method of characteristics is used for the ice model. Wind forcing is from a direction of 0° and the model domain has reverted to 80 km.

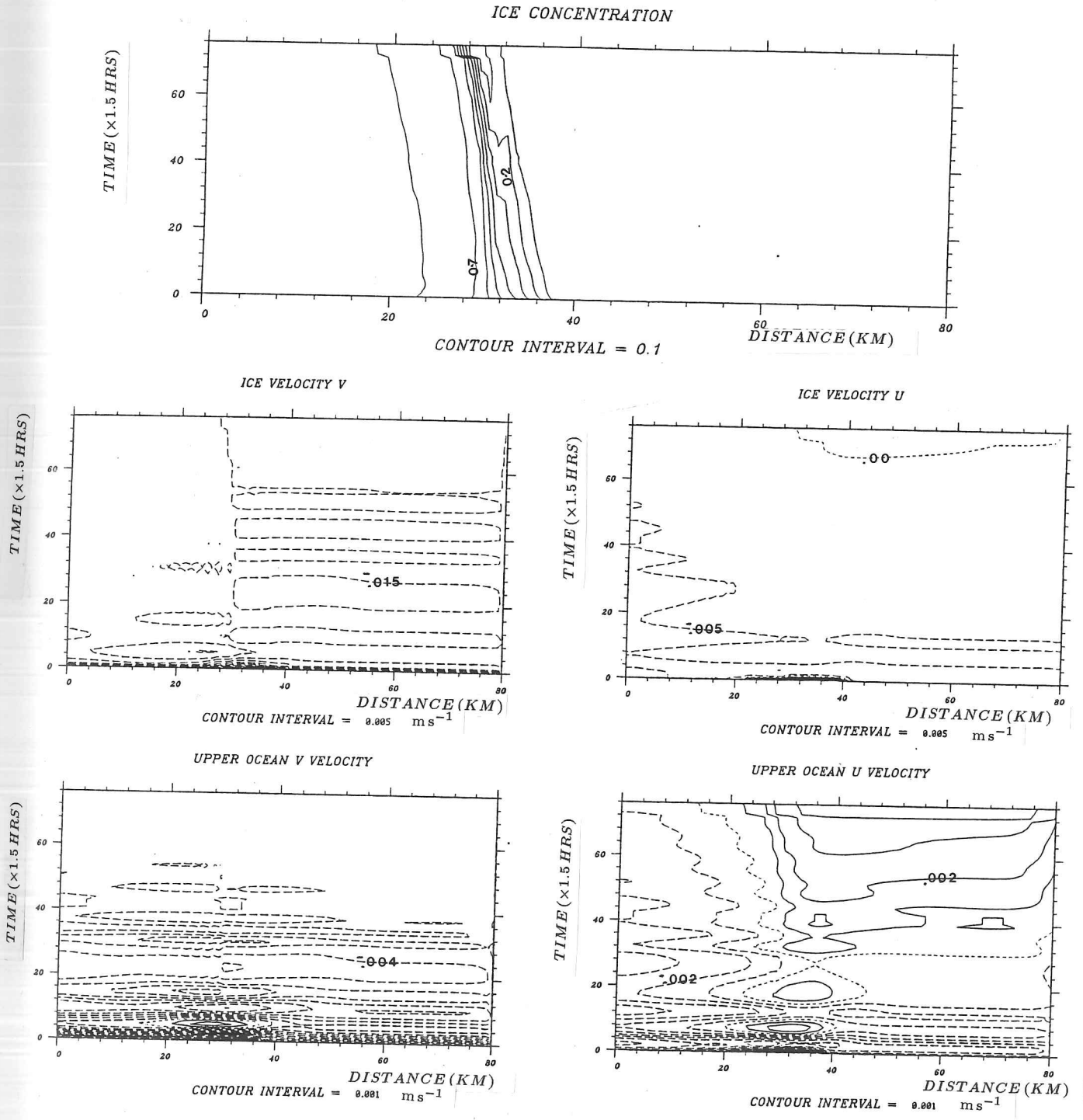

FIGURE 4.17: Contoured time series (1 record = 90 minutes) for model solution when the method of characteristics is used for the ice model. Wind forcing is from a direction of 180°.

$O(10^{-5}\,\mathrm{m\,s^{-1}})$ formed at the grid point where the constant ice concentration merged with the region of decreasing concentration. In contrast, in the cross-edge velocity fields from the model run solved along the equation characteristics, a pronounced ice edge jet with a maximum of $O(10^{-3}\,\mathrm{m\,s^{-1}})$ forms at the point where the ice concentration starts to decrease. There is also a velocity minimum of similar magnitude where the compactness drops below the 0.5 level. The main observation however, is that there is a general trend to a velocity increase as we approach the ice edge. This would explain the ice retreat under off-ice forcing conditions.

The above simulations also indicate that the first development in the ice model is the adjustment to form a geostrophic jet, i.e., the initial condition for the ice selected by Røed and O'Brien (1983). Perhaps if our interpolation scheme had involved weighting over 4 data points, either directly or by averaging two consecutive quadratic fits (O'Brien and Reid, 1967), we could have avoided the development of ripples in the ice concentration when model simulations were started from geostrophic equilibrium

One further point to observe is that, in a similar way to Røed and O'Brien's (1983) model, under both on-ice and off-ice winds the ice concentration curve became sharper as the model developed. This is also true in the case when the wind direction is at 60° Figure 4.18 shows the case where the outermost ice position remains steady throughout the integration (cf. Figure 4.8 for no ice rheology). The ice edge jet developed by the ice model with this rheology is visible in the time series of the ice velocity field as a moving wave train approximately coincident with the 0.6 ice compactness curve.

Parameter studies of ice configuration

Some short runs were made to test some of the parameters used in this ice model. We were particularly interested in the magnitude of the ice strength within the ice rheology term when solving along the characteristics of the momentum equation. Other important parameters are the ice 'diffusivity' (Hibler, 1979), κ, used in the exponential function of the rheology term. This coefficient determines the gradient of the ice stress. We were also interested in the degree of sharpness required in the initial ice concentration distribution when it is represented by a hyperbolic tangent function.

When the diffusivity coefficient was halved from a value of 20 to 10 showed little effect on the model scalar fields (salinity, temperature, ice concentration and thickness). However, the ice velocity distribution in the ice gradient region was reduced by up to 15% in the cross-edge direction, and by 3% in the along-edge direction. Values above and below these ice diffusivities

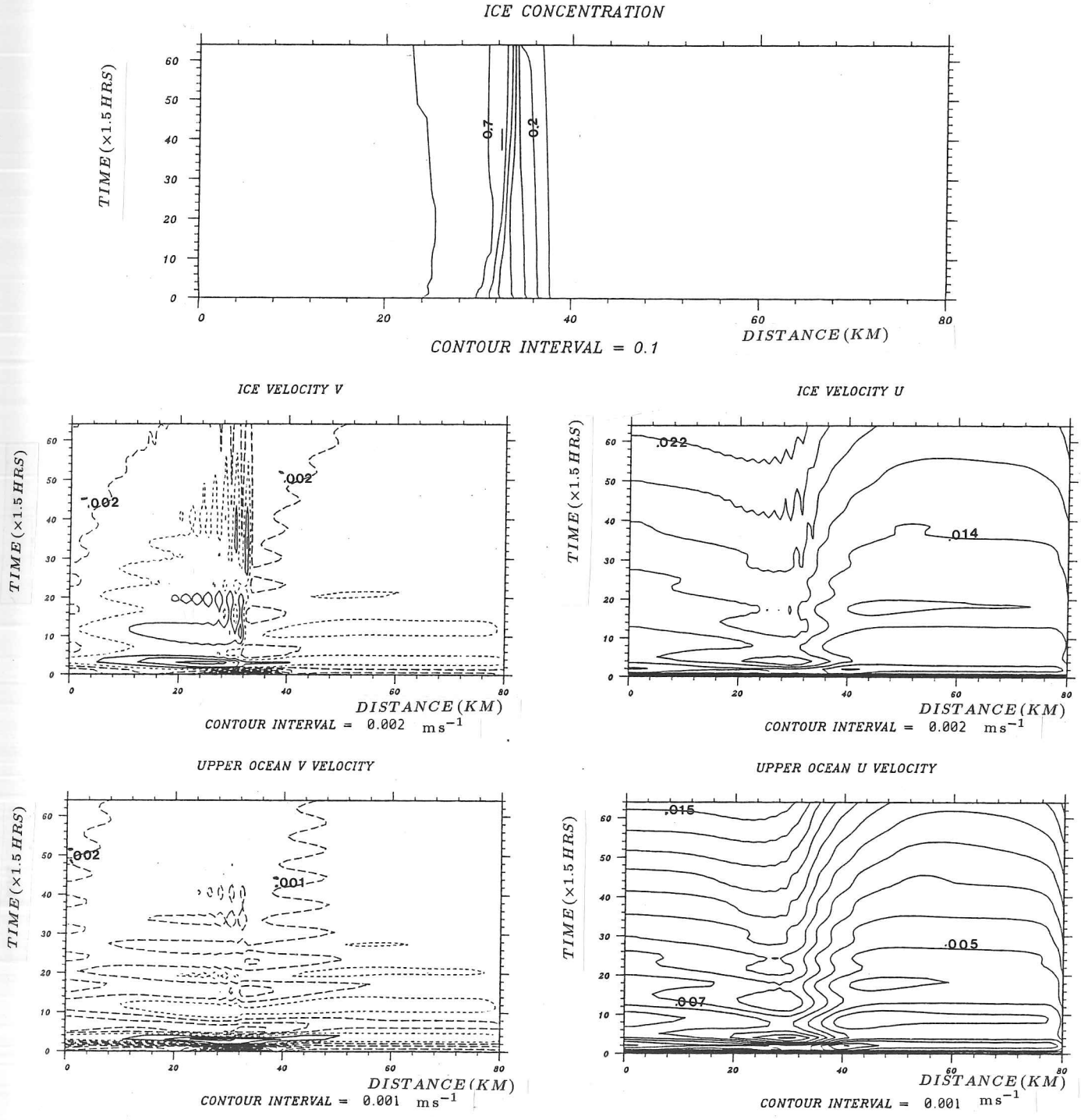

FIGURE 4.18: Contoured time series (1 record = 90 minutes) for model solution when the method of characteristics is used for the ice model. Wind forcing is from a direction of 60°.

were not considered suitable as the former would not give a reasonable decay in ice resistance below 80% concentration, whilst lower values of the ice diffusivity within a pressure term ice rheology have been shown to be easily unstable when perturbed (Killworth and Paldor, 1985).

An increase in the amplitude of the strength function by a factor of three did not have the disastrous consequences seen in earlier simulations when solving along the equation characteristics. Again only velocities in the cross-edge direction in the region of the ice gradient were noticeably affected, this time by a rise of order 10% in cross-edge direction.

Changing the shape of the initial ice concentration by altering the constant divisor RM, in equation 4.73 in the kernel of the hyperbolic tangent function shifted the point of maximum ice gradient, and hence the maximum ocean and ice velocities, but had minimal effect (2%) on the magnitude of those velocities when the model was solved along characteristics.

4.16 Open boundary conditions

We noted in earlier simulations that there were problems at the boundaries of our finite difference domain when we allow a disturbance propagating outwards to be reflected or distorted by the presence of that boundary. Also, no slip boundary conditions lead to the development of strong velocity gradients at the boundary during the start of the simulation.

In this study, we were mainly concerned with the dynamics at the ice margin, so one would expect that events occurring at the boundaries should not raise too much concern. However, the development of ripples at the boundary in the ice covered region could lead to a larger scale model instability because ripples in ice concentration will create gradients in the total stress reaching the ocean and in the internal stress terms. This suggested that a further investigation on the choice of boundary condition was necessary to limit any amplification of the ripples that might occur.

In some of the early model runs we chose to impose a highly viscous layer at the exterior grid points to damp any waves at the boundary. However, as the damping in this layer needed to be gradually imposed, and since at this stage we were using variable grid spacing in the outermost grid points, we could have been at risk of introducing further errors into the model by creating high gradients in the ocean eddy viscosity coefficient values.

The aim is to impose open boundaries in the coupled model, so that waves travelling from inside the model are allowed to pass out of the domain and no wave from exterior to the domain

is allowed to enter and disturb interior points. A suitable scheme for this task was proposed by Orlanski (1976) and simplified by Carlomongo and O'Brien (1980). The main difference between the above two schemes and other possible open boundary conditions are discussed by Chapman (1985). Both Orlanski, and Carlomongo and O'Brien considered the simplest case of a barotropic ocean where a single value of wave propagation speed is defined for the complete depth. Direct application of such a scheme to a level model is theoretically incorrect as we cannot associate a wave speed with a density level in the model only with density layers. In spite of this argument we used a variant on an Orlanski scheme at each level for the main ocean variables to see if any improvement could be had. Although this approach was incorrect, and we found it not to be entirely successful, some improvement in the noise in the velocity field was found in comparison to the no slip boundary condition. We considered, therefore, that it was necessary to formulate an appropriate open boundary condition in both the open and ice model, and further to allow for the situation where the free and forced waves of the system are treated separately (Røed and Smedsted, 1984). In order to provide a framework for this discussion we first state some of the theory governing the condition we are trying to satisfy on the boundary, and give details of how the appropriate wave speeds are calculated.

After Orlanski (1976), the condition to be satisfied by the wave at the boundary is the Sommerfield radiation condition

$$\frac{\partial \phi}{\partial t} + C\frac{\partial \phi}{\partial x} = 0 \tag{4.94}$$

where ϕ is the variable in question. An identical equation has to be invoked for each model variable that we require to set with an open boundary condition.

The phase velocity C is calculated at each time step for the variable under consideration using the values from previous time steps at adjacent grid points. This method gives a reasonable approximation to the local phase speed which does not vary rapidly during the period of a few time steps.

Mathematically C is given for end point J by

$$C_\phi = -\frac{[\phi^t(J-1) - \phi^{t-2}(J-1)]}{[\phi^t(J-1) + \phi^{t-2}(J-1) - \phi^{t-1}(J-2)]}\frac{\Delta x}{2\Delta t} \tag{4.95}$$

substituting this back into a finite difference solution of the Sommerfield radiation condition, we

find that

$$\phi^{t+1}(J) = \frac{[1-(\Delta t/\Delta x)C_\phi]}{[1+(\Delta t/\Delta x)C_\phi]}\frac{\phi^{t-1}(J)+2(\Delta t/\Delta x)C_\phi\phi^t(J-1)}{1+(\Delta t/\Delta x)C_\phi} \tag{4.96}$$

In the limit as $C \to 0$, $\phi^{t+1}(J) = \phi^{t-1}(J)$, and in the opposite extreme when $C \to \Delta x/\Delta t$ we get $\phi^{t+1}(J) = \phi^t(J-1)$.

To apply these conditions to density layers, i.e., not model levels the model code included extra subroutines enabling us to convert from level to modal structure and vice-versa. Hence by using the normal modes of the density structure we were able to calculate the appropriate wave speeds for each density layer. Eigenvector matrices had to be calculated for each of the appropriate density structures to be used in the Orlanski (1976) scheme. The routines to derive the eigenvector matrices came from the NAG (Numerical algorithms Group) package.

Once the velocity and scalar values in the level space had been split into their constituent modes, an Orlanski type procedure similar to that outlined above for the barotropic case was carried out. The boundary vector in modal space was then converted back to level space using the most recent eigenvector matrix available. The use of the eigenvector matrix from the current time level involved additional storage and produced little improvement in the calculation.

Whilst using this scheme, we encountered yet further problems. It was necessary to retain the eigenvectors associated with the smaller wave speeds if we were to correctly make the reverse step back to model levels. However the accuracy in the smaller wave speeds, representing the higher wave modes, was dependent on the algorithm chosen to calculate the eigenvectors and could introduce errors to the scheme overall. It is also probable that the lower wave modes dominate the physical processes that occur at the boundary.

The initial stratification of the model was chosen so that a reasonable depth mixed layer pre-existed. Hence, it was not an ideal density structure to be resolved into normal modes. The open boundary approach using normal modes would be more successful if a stratification containing 2 - 3 well defined modes was chosen.

Other problems with this open boundary condition arose when using the leap-frog method of time-stepping for the model computation. The two solutions formed during this time stepping process diverged considerably, so that the eigenvector matrices used for the mapping between the modal and level forms of the density structure amplified this divergence even further. It was therefore possible to derive a boundary value using this Orlanski scheme that does not resemble any of the internal grid points.

The documentation in the NAG manual suggests that the procedure chosen to solve the eigenvector problem, which we have expressed in the general form $Ax = \lambda Bx$, gives a correct result. However, on examining the details of the of the NAG routine used (Moler and Stewart, 1973), the authors only claim that the scheme attempts to find a solution which would be subject to round off error. This in turn is dependent on which matrix point the scheme pivots about. Hence, we obtained copyright of the original routines in order to edit them to operate at increased precision in an attempt to overcome the problems introduced by round-off error.

We also switched our time stepping scheme from Leap-frog to Lax-Wendroff (Smith, 1978) in order to prevent the computational mode. In this second time scheme the simulation is progressed for half a time step. Then these new values are used in the advective and coriolis terms in the full time step. Use of this time-stepping scheme increases the computation time for the model run by a factor of 2. Overall the scheme is computationally expensive because of the need to calculate several sets of eigenvectors for the level-modal-level conversions. In particular, in the extended precision version of the Lax-Wendroff code slows the model run time considerably. By including all the refinements we have mentioned in this section we increased the model run time by a factor of 10. As we were strictly limited by the availability of computer time, extensive runs of the model with this boundary condition were now out of the question.

In spite the extra precision available in the eigenvector conversion from level to modal domains, the scheme was still prone to round off error and at an arbitrary point (> 400 time steps) the eigenvector matrices become ill-conditioned Also, comparisons with model runs using 'level-type' Orlanski and no-slip boundary conditions did not suggest that the scheme produced sufficient improvement to justify using the extra computational effort.

As mentioned in the introduction to this section, we were intending to split the boundary condition into free and forced components after Røed and Smedsted (1984). An attempt was made to do this in the leap-frog time code. The open boundary condition under this scheme is only imposed on the free wave mode of the model after the values for the velocities resulting from the external forcing have been subtracted from the solution. The scheme did not show sufficient improvements to justify implementing it with a Lax-Wendroff time scheme, where additional array storage would be required to calculate the necessary model variables at both full and half time steps.

5

Discussion of coupled model runs and conclusions

5.1 Bering sea model runs

The aim throughout this thesis in both the field programmes and the modelling studies was to produce a model of conditions in the Bering sea during the winter season of 1982-1983. To do this, we employed many of the numerical techniques used to describe ice edge processes as discussed in Chapter 4. We have already stated in that chapter that some of these processes can cause conflicting effects in the model when used in conjunction with one another. However, our aim in these model runs was to include all the effects we had studied, and only exclude them from the combined model runs if it was obvious that their inclusion had caused the model to become unstable or collapse.

The atmospheric data used for the external forcing terms in the model were derived from the surface pressure fields, surface winds and air temperatures given by the model output of the PMEL METLIB package for the relevant data period (Wilson *et al*, 1984). The region we wished to represent was a 400 km long swathe starting just south of St Lawrence island, passing through St Matthew Island (though not explicitly included in the model) to just off the shelf. As in earlier runs, no topography was included and gradients of variables along the ice edge were ignored. In increasing the size of the model area it was also necessary to increase the horizontal grid spacing to 4 km. Hence, the model we used had a grid of 100×4 km points in the horizontal and 14 vertical grid points with spacing of 5 m, 8 m, and 10 m. The meteorological data collated from the PMEL report covered the

period from the 4th February to 17th March 1983 (JD35-JD76). The data were digitized by hand and then linearly interpolated to produce a value for each of the 100 grid points in the integration domain.

The Bering Sea model runs were initiated impulsively from rest, with the atmospheric forcing from JD35 (Table 5.1) which coincided with the start of the MIZEX-West field programme. For these model runs we used an active ice model which contained no rheological terms. By JD37 after approx 72 hours of model simulation the system had gone unstable (Figure 5.1), though large oscillations in the ice compactness distribution had appeared after 40 hours. (Note, numbers in graphs on the time axis should be multiplied by a factor of 2). There are also strong variations in the base of mixed layer temperature and salinity (not shown in Fig 5.1) particularly 2-3 time records before final model collapse. A further point to note is the effect of the impulsive change in external forcing conditions on the ice and ocean velocity fields. The model fields do not have time to adjust via inertial currents before new conditions are imposed. The banded regions seen in the velocities time series plots are the result of this slow adjustment.

A second attempt to use the coupled model in this mode was made by starting the integration with forcing data beginning on JD40. In this simulation the ice compactness distribution developed large scale oscillations after 44 hours with loss of mass to the area off the ice edge. During the period JD40-42 of this second model run the winds strengthened and were blowing primarily from the north eastern sector. A very noisy signal developed in the velocity and temperature fields at the southern boundary where there were significantly stronger winds ($18\ m\ s^{-1}$) than in the central sector. As with the previous simulation the whole system degenerated into several instabilities by 72 hours after the start (Figure 5.2).

The instabilities generated in this model run are similar to those we had previously seen when the gradient in the forcing wind field was continuously changing sign, so we should have anticipated the presence of these oscillations when imposing the external forcing fields in Table 5.1 as there are considerable gradients in the wind fields moving across the model domain. However, as we were interpolating the values of wind speed and direction used for external forcing of the model the gradients were not expected to be too strong. We had specifically avoided forcing the model with external conditions which represented atmospheric fronts, where abrupt changes in the gradients of the wind field might occur.

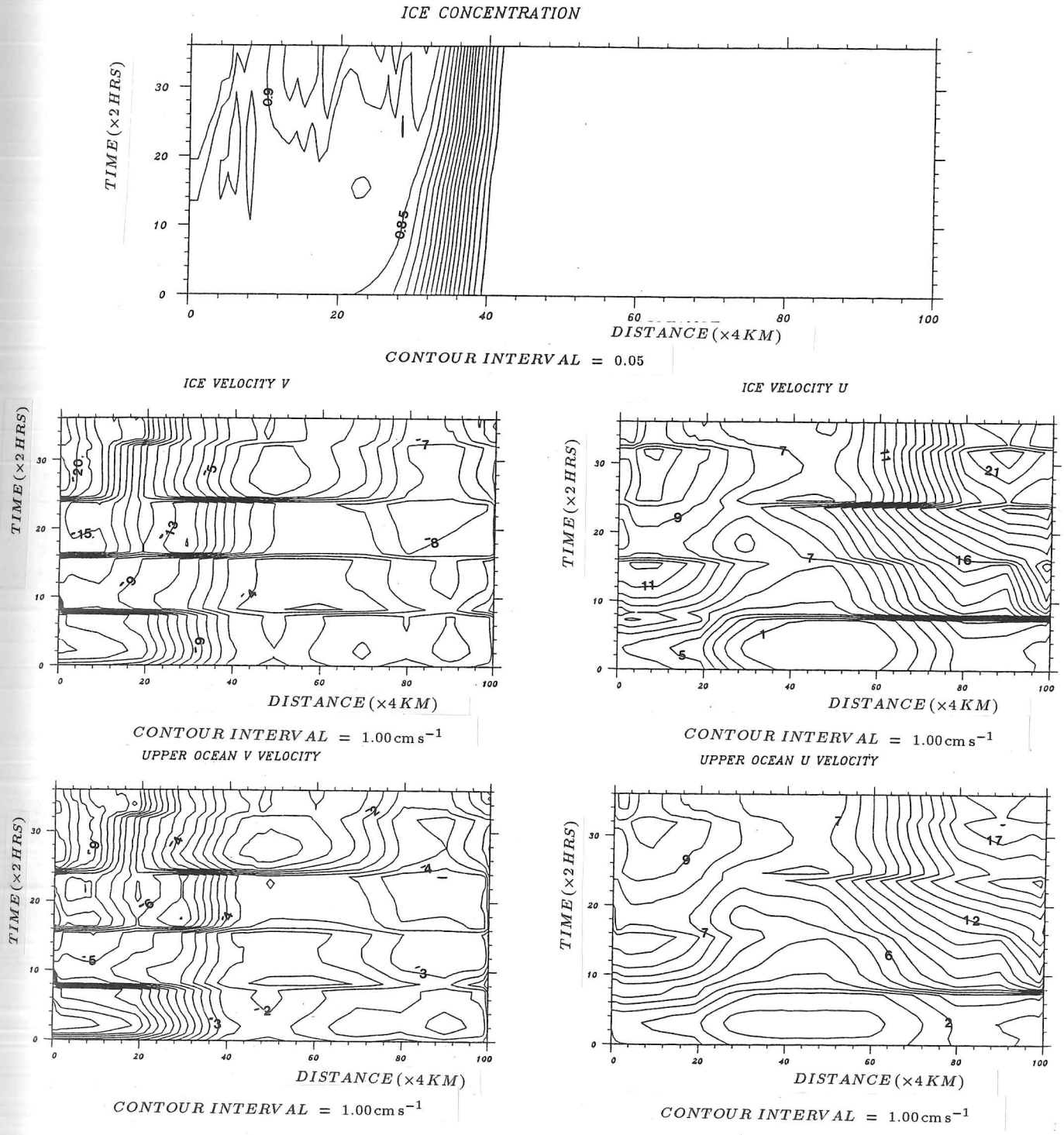

FIGURE 5.1: Contoured time series results from model simulations of Bering Sea conditions between JD35-37. The model does not include any ice rheology. Records on the time axis are every 2 hours and the 100 horizontal grid points represent 400 km.

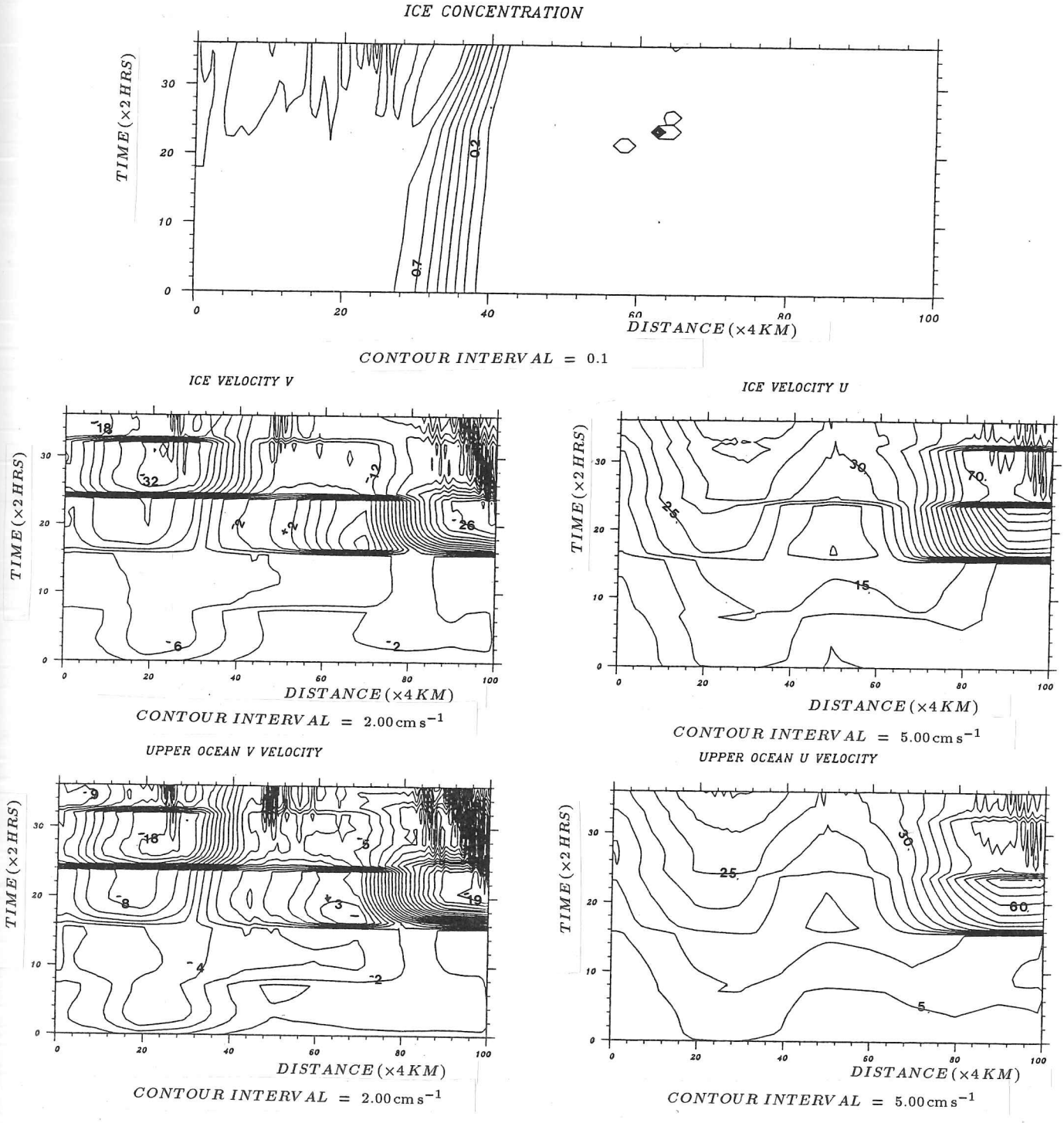

FIGURE 5.2: Contoured time series results from model simulations of Bering Sea conditions between JD40-42. The model does not include any ice rheology. Records on the time axis are every 2 hours and the 100 horizontal grid points represent 400 km.

We then made a third attempt to initiate the model, this time beginning the run at the end of the month of February (JD59-61), after the winds had decreased in magnitude. However, the simulation followed the same pattern as the earlier runs though in this case even stronger oscillations in the ice concentration field developed, closer to the start of the simulation (Figure 5.3). By 60 hours the system had degenerated so far that the ice concentration values had become alternately 0% and 100%. The velocity fields also displayed strong oscillations in this model run. On the output plot these were superimposed on the inertial currents generated with each change in external forcing conditions.

Some degree of success was achieved earlier when we treated the ice cover like a moving shock wave and included an ice rheology term dependent on the gradient of 'ice pressure'. We were able to solve for the cross-edge ice velocity and ice concentration by reducing the system to ordinary differential equations along the equation characteristics. A major disadvantage of using this method of solution in a direct comparison with the no-rheology case is that the forcing of the model, which one would expect to generate off-ice flow, reverses in the characteristic case and develops on-ice flow (see section 4.15). However, not realizing the seriousness of this effect at this stage we spun up the model with external forcing representing the conditions for JD35-37, JD40-42 and JD59-61 discussed above along with a further mid-March data set JD 74-76 (ice at maximum extent). In all the model runs using the method of characteristics for the ice model we find a much stabler ice edge system (Figure 5.4-5.6).

In a similar way to the single wind forcing cases the model now produces ice retreat when previously there was ice advance. Also, areas of ice convergence in the earlier model runs are now divergent ice regions. Overall, the patterns in the velocity time series contour diagrams are similar to those of earlier runs. As stated in section 4.15, it is the gradients in the geostrophic jet produced by the ice rheology which turn the previous ice advance regime into the ice retreat. However, in using variable wind forcing conditions we do not get the same strong jet type signal displayed in the time series plots as is seen in the case of steady winds (Fig 4.16, 4.17). Even though the model is more stable than in the earlier case it cannot run on indefinitely as divergent zones in the ice cover have started to develop in the JD35-37 run, and more particularly in the JD74-76 simulation where there is no non-rheology case available for comparison. Figure 5.6 indicates that the wind conditions representing the mid-March situation of maximum ice extent did not cause any advance or retreat of the ice edge. There was also no major thermodynamic change in the ocean

TABLE 5.1: External forcing for the Bering Sea model runs

Temperature	Pressure	Wind Speed	Wind Direction	Temperature	Pressure	Wind Speed	Wind Direction
JD 35AM				JD 35PM			
-9.3	997.5	9.07	131.0	-5.0	997.1	6.85	129.5
-6.9	994.9	8.88	132.0	-3.8	995.1	7.03	129.0
-4.7	992.2	8.51	133.0	-2.8	993.6	6.48	129.5
-3.2	990.7	6.85	139.0	-1.9	991.8	6.11	130.0
-1.7	988.8	5.37	144.0	-0.9	990.3	5.55	124.0
-0.9	987.3	4.81	144.0	-0.0	988.7	5.00	119.0
-0.2	985.8	5.37	143.5	0.8	987.4	5.37	111.5
0.5	984.3	6.05	135.0	1.7	985.7	6.11	106.0
1.0	982.9	6.11	125.0	2.5	984.0	6.85	108.5
1.6	981.8	6.50	128.0	3.3	982.2	6.85	113.0
2.1	978.9	5.92	128.5	4.1	981.2	7.22	92.0
JD 36AM				JD 36PM			
-8.8	997.4	7.59	144.5	-7.7	993.5	9.25	142.6
-7.3	995.6	7.77	143.5	-6.3	991.4	8.70	141.0
-5.9	994.0	6.85	142.5	-5.4	989.7	6.66	141.0
-4.8	992.4	7.59	141.7	-4.6	987.9	5.18	143.5
-3.6	990.8	7.03	133.5	-3.6	987.1	3.50	149.0
-2.3	989.2	6.66	125.0	-2.6	986.2	2.22	145.5
-1.1	988.0	7.03	117.5	-1.7	985.4	3.33	132.0
0.2	986.2	7.22	114.0	-1.6	984.4	5.00	118.0
1.7	984.3	7.77	116.5	0.3	983.2	6.84	116.2
3.2	982.4	7.77	112.5	1.6	981.6	7.22	115.0
4.2	980.5	7.40	112.0	2.3	980.0	5.92	112.0
JD 37AM				JD 37PM			
-11.0	989.2	9.07	149.8	-7.1	987.8	7.77	155.5
-9.7	987.6	8.07	150.2	-6.5	986.1	5.92	156.5
-8.2	985.8	7.59	150.7	-5.9	984.6	4.44	161.2
-6.9	984.2	5.18	156.1	-5.5	983.8	4.07	166.6
-5.8	983.4	4.07	161.0	-5.1	983.1	2.59	171.0
-4.6	982.7	3.70	161.7	-4.6	982.7	2.40	172.5
-3.5	981.8	3.33	129.8	-4.1	982.1	2.22	172.8
-2.2	980.7	4.07	119.4	-3.5	981.5	3.33	157.0
-1.3	980.0	6.11	119.5	-2.7	980.7	2.96	144.0
-0.2	979.1	5.92	117.3	-1.9	979.9	2.22	147.2
0.2	978.2	4.25	110.0	-1.0	979.2	1.66	146.0

Temperature	Pressure	Wind Speed	Wind Direction
JD 40AM			
-14.2	1007.6	3.88	126.5
-12.1	1006.1	5.00	115.4
-9.7	1004.7	7.03	110.5
-7.1	1003.3	6.85	104.6
-5.0	1001.8	6.29	97.5
-3.1	1000.1	4.25	92.5
-1.7	999.1	4.62	88.3
-0.4	998.0	5.18	83.5
0.6	997.2	5.37	83.0
1.5	996.3	4.81	85.0
2.2	995.6	5.00	89.0
JD 41AM			
-17.2	1011.3	6.66	124.4
-14.4	1009.1	8.70	117.2
-11.3	1006.7	9.07	113.4
-8.2	1004.2	7.77	107.8
-5.7	1002.9	4.44	86.6
-3.5	1001.5	4.07	36.8
-1.8	1001.0	7.77	28.2
-0.4	1000.5	12.96	38.1
0.7	1000.2	15.92	61.0
1.8	999.1	18.33	80.5
2.5	996.2	18.70	91.2
JD 42AM			
-18.7	1010.9	8.88	128.0
-16.1	1008.6	9.25	125.5
-12.8	1006.0	10.37	119.0
-9.5	1003.1	10.00	116.5
-6.2	1000.3	10.74	116.4
-3.6	997.2	10.18	117.0
-1.3	994.3	9.81	113.9
0.2	991.6	9.07	110.0
1.5	989.0	7.59	105.5
2.1	987.5	5.55	98.5
2.4	986.4	3.33	90.0

Temperature	Pressure	Wind Speed	Wind Direction
JD 40PM			
-19.1	1010.9	5.18	128.5
-17.3	1009.3	5.55	122.8
-12.8	1007.8	6.11	114.0
-9.2	1005.7	6.66	110.3
-6.0	1003.8	7.59	108.4
-3.2	1001.3	7.40	108.2
-1.3	999.2	7.22	104.0
0.2	997.4	7.40	102.0
1.6	995.9	5.92	96.0
2.5	995.5	3.70	84.5
3.6	995.0	2.40	82.7
JD 41PM			
-18.2	1012.8	9.25	137.5
-15.3	1010.5	11.66	130.3
-12.3	1007.1	12.59	126.6
-9.6	1003.4	12.40	123.0
-6.9	1000.0	11.11	118.5
-4.8	997.0	8.88	106.5
-3.1	994.8	9.07	99.2
-1.5	992.5	9.29	90.5
-0.1	990.2	11.66	90.6
1.2	988.0	11.48	91.5
2.2	985.8	9.81	89.8
JD 42PM			
-18.2	1012.0	10.55	119.6
-16.3	1008.8	12.77	116.8
-14.4	1005.7	13.14	112.0
-12.6	1002.1	12.77	106.8
-10.7	998.7	12.03	100.4
-8.0	995.3	10.74	96.1
-5.1	992.9	9.81	90.3
-2.7	991.0	7.40	86.1
-0.2	989.7	5.74	58.4
1.2	989.6	4.62	30.0
2.1	989.7	4.24	-3.5

Temperature	Pressure	Wind Speed	Wind Direction
JD 59AM			
-12.0	1000.0	7.03	160.7
-10.0	998.1	7.96	162.0
-8.7	996.0	6.48	159.4
-7.5	994.8	6.85	164.5
-6.5	993.2	6.11	165.2
-5.7	991.9	3.88	170.9
-4.9	991.1	3.70	151.9
-4.2	990.3	3.33	135.6
-3.5	989.7	2.77	112.5
-2.2	988.9	3.70	108.0
-1.0	988.2	3.88	95.2
JD 60AM			
-9.8	1004.8	7.40	128.4
-7.5	1002.4	7.59	123.6
-5.4	1000.2	7.40	121.4
-3.6	998.3	7.22	115.0
-2.2	996.2	7.03	109.5
-1.5	993.8	7.77	101.0
-0.9	991.6	7.96	93.2
-0.3	989.3	8.51	77.0
0.2	987.8	8.70	59.8
0.8	986.8	9.07	47.6
1.1	986.0	9.44	39.2
JD 61AM			
-6.9	1009.2	9.44	116.5
-5.3	1006.3	12.77	113.8
-4.8	1002.4	12.96	111.6
-4.2	999.0	12.77	106.3
-4.1	995.9	10.92	100.8
-3.8	992.4	8.88	89.5
-3.1	989.8	9.44	75.0
-2.2	988.0	10.00	62.0
-1.3	986.1	12.77	47.6
-0.6	984.9	12.40	63.0
0.0	984.0	14.48	38.2

Temperature	Pressure	Wind Speed	Wind Direction
JD 59PM			
-9.4	1007.1	11.29	136.5
-8.1	1004.0	11.11	136.4
-7.7	1001.0	10.92	131.2
-7.2	998.2	9.62	131.1
-6.8	995.6	9.25	127.4
-5.8	993.1	8.88	120.8
-4.7	990.6	7.77	112.5
-3.7	988.2	7.96	103.3
-2.5	985.8	8.70	97.0
-1.5	983.6	9.07	94.5
-0.4	981.0	9.25	84.2
JD 60PM			
-9.6	1009.6	8.14	106.7
-7.4	1007.2	9.25	106.1
-5.2	1004.3	9.07	99.2
-3.5	1001.8	10.37	97.8
-2.1	998.4	12.22	98.4
-1.2	995.2	12.59	100.9
-0.3	991.8	12.96	102.1
0.3	988.2	12.77	100.8
1.0	985.0	11.29	103.2
1.7	982.0	10.95	98.6
2.1	979.2	9.25	93.8
JD 61PM			
-8.2	1009.6	7.22	118.9
-6.3	1007.2	8.88	107.1
-4.6	1004.5	9.07	101.1
-3.1	1002.2	8.70	94.8
-1.9	1000.2	8.80	86.5
-1.0	998.4	8.14	77.8
-0.1	997.1	7.40	68.6
0.4	996.1	7.59	61.7
1.1	995.1	7.96	56.5
1.6	994.0	7.95	66.1
2.1	993.8	7.77	67.8

Temperature	Pressure	Wind Speed	Wind Direction
JD 74AM			
-16.7	1017.3	4.81	156.0
-16.2	1016.0	4.07	177.8
-16.0	1015.3	3.70	178.2
-15.7	1014.8	3.88	188.0
-15.1	1014.3	4.07	187.2
-14.1	1014.1	3.33	176.4
-12.8	1013.8	2.77	119.5
-11.3	1013.3	2.59	103.1
-9.8	1012.9	3.70	63.6
-8.0	1012.5	3.88	46.2
-6.0	1012.1	5.00	39.2
JD 75AM			
-16.7	1017.0	7.03	115.2
-14.8	1015.2	6.11	108.2
-12.7	1013.8	5.74	102.3
-10.6	1012.2	5.92	97.6
-8.7	1010.8	5.55	90.5
-6.8	1009.2	5.92	83.4
-5.1	1008.3	6.11	78.1
-3.6	1007.1	7.22	65.8
-2.0	1005.9	7.77	61.6
-0.5	1004.1	8.88	59.2
1.1	1003.8	9.25	55.5
JD 76AM			
-6.2	1014.2	7.77	92.8
-4.0	1012.2	9.62	92.0
-2.0	1009.4	9.63	84.5
-0.4	1007.3	9.07	75.0
0.3	1005.4	8.88	57.8
0.9	1004.8	8.90	36.1
1.3	1004.6	8.85	27.2
1.7	1004.5	9.62	27.4
2.2	1004.5	11.11	40.4
2.6	1004.0	11.29	51.5
3.1	1003.1	12.59	62.1

Temperature	Pressure	Wind Speed	Wind Direction
JD 74PM			
-16.2	1018.1	4.62	166.8
-15.1	1017.2	2.40	183.4
-13.9	1017.1	2.03	203.1
-12.8	1016.5	2.22	172.5
-11.9	1016.0	5.37	107.9
-11.3	1014.1	5.74	92.5
-10.7	1012.8	6.66	79.8
-10.0	1012.0	6.70	68.0
-8.7	1010.6	8.51	51.0
-7.0	1009.8	8.88	37.0
-4.6	1007.4	9.81	31.7
JD 75PM			
-12.3	1017.6	6.85	101.4
-10.8	1015.6	7.03	90.0
-8.6	1013.5	7.59	87.0
-6.5	1012.0	9.07	82.5
-4.9	1009.9	11.85	83.4
-3.2	1007.4	12.77	85.4
-1.9	1004.9	11.66	86.1
-0.9	1002.8	10.92	85.0
0.2	1000.7	7.77	75.4
1.1	999.8	6.48	56.4
2.0	999.3	5.92	42.2
JD 76PM			
-1.8	1016.1	7.96	73.4
-0.3	1014.8	9.07	71.9
0.2	1013.2	8.88	71.4
0.5	1012.0	9.62	75.4
0.7	1010.3	10.74	77.4
0.9	1008.4	9.81	84.0
1.2	1007.0	9.62	88.5
1.5	1005.1	8.88	91.2
1.8	1003.5	8.33	95.6
2.2	1001.9	7.55	97.0
3.1	1000.2	7.03	94.5

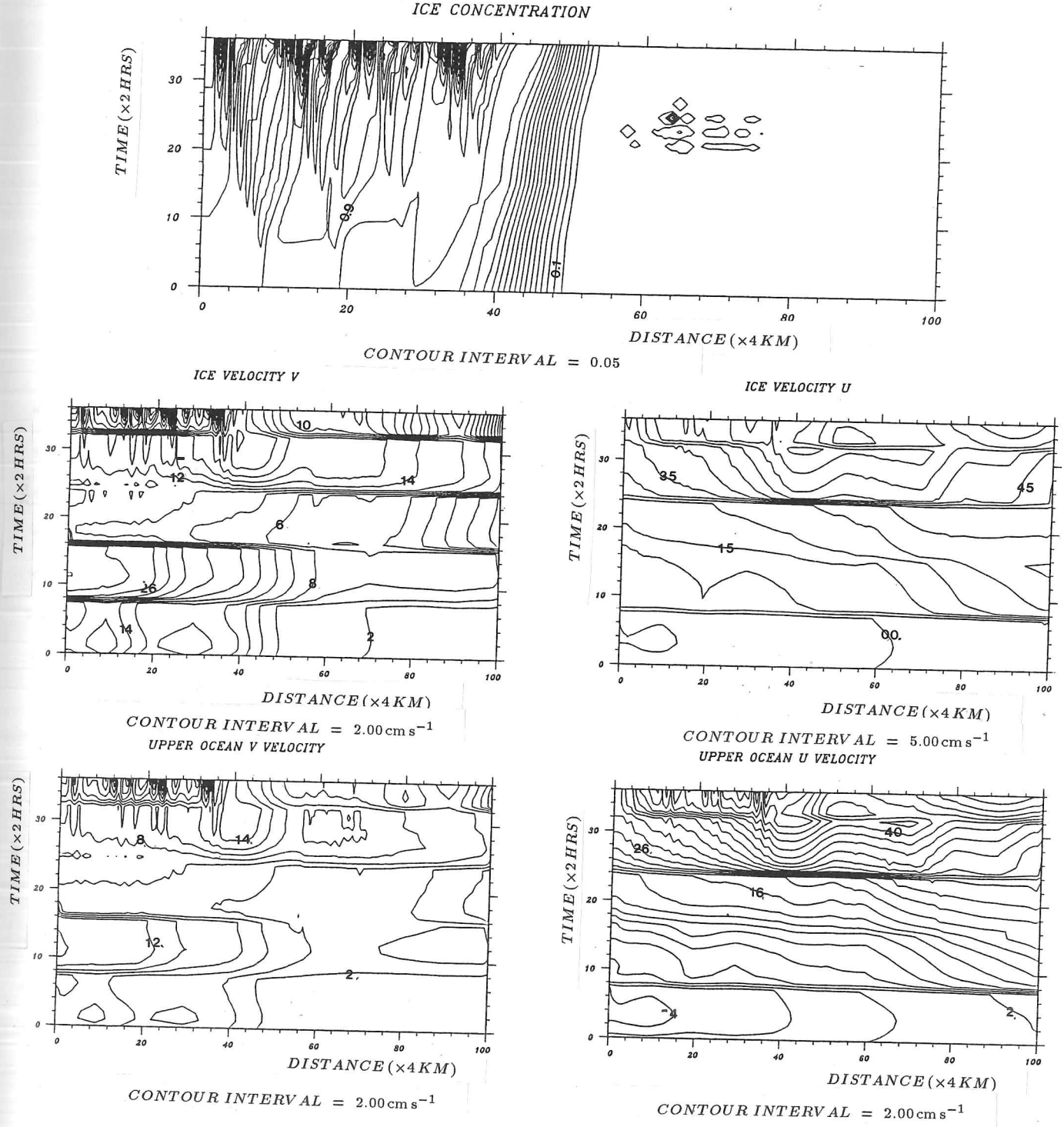

FIGURE 5.3: Contoured time series results from model simulations of Bering Sea conditions between JD59-61. The model does not include any ice rheology. Records on the time axis are every 2 hours and the 100 horizontal grid points represent 400 km.

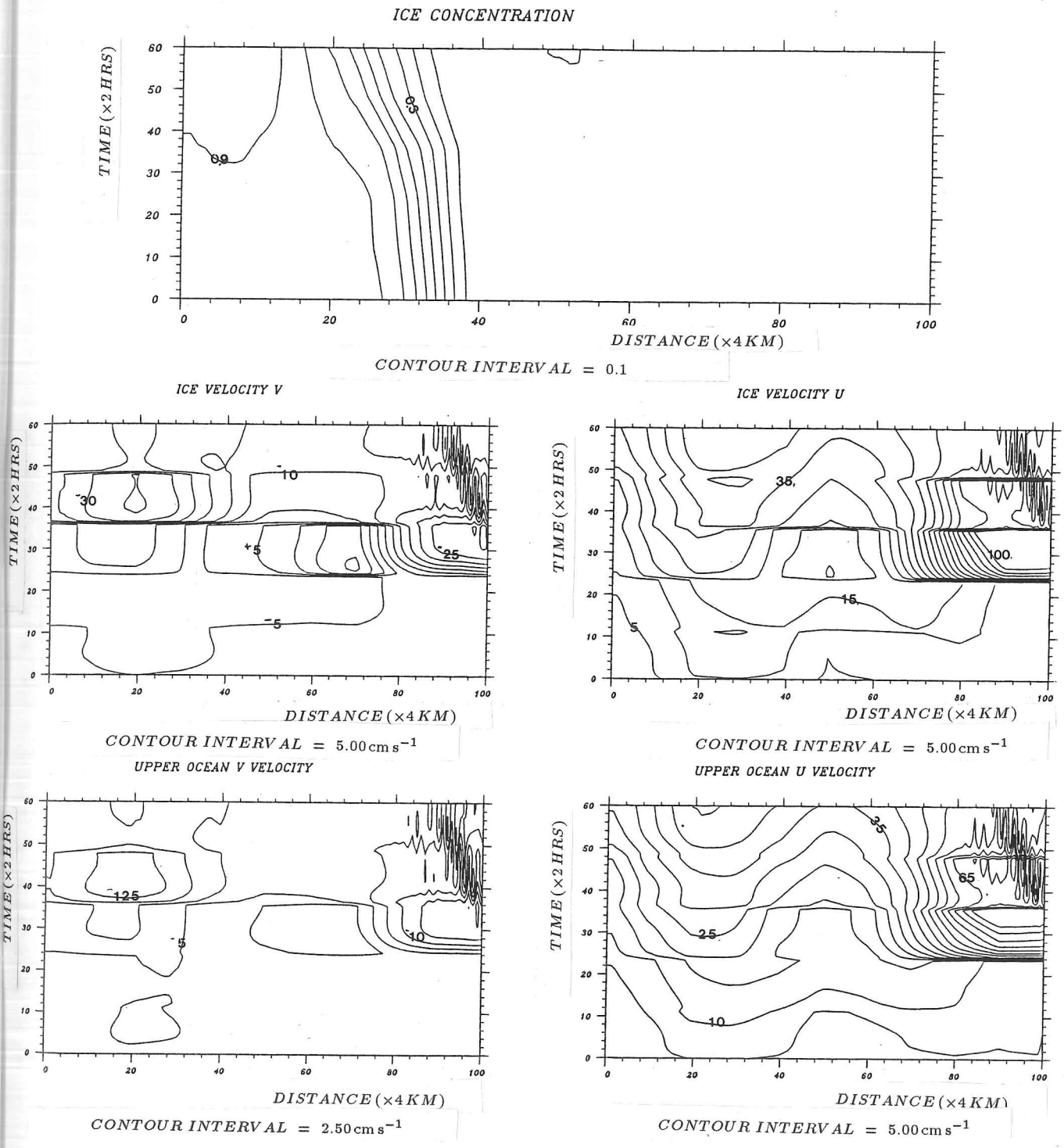

FIGURE 5.4: Contoured time series results from model simulations of Bering Sea conditions between JD40-42. The ice model is solved by the method of characteristics.

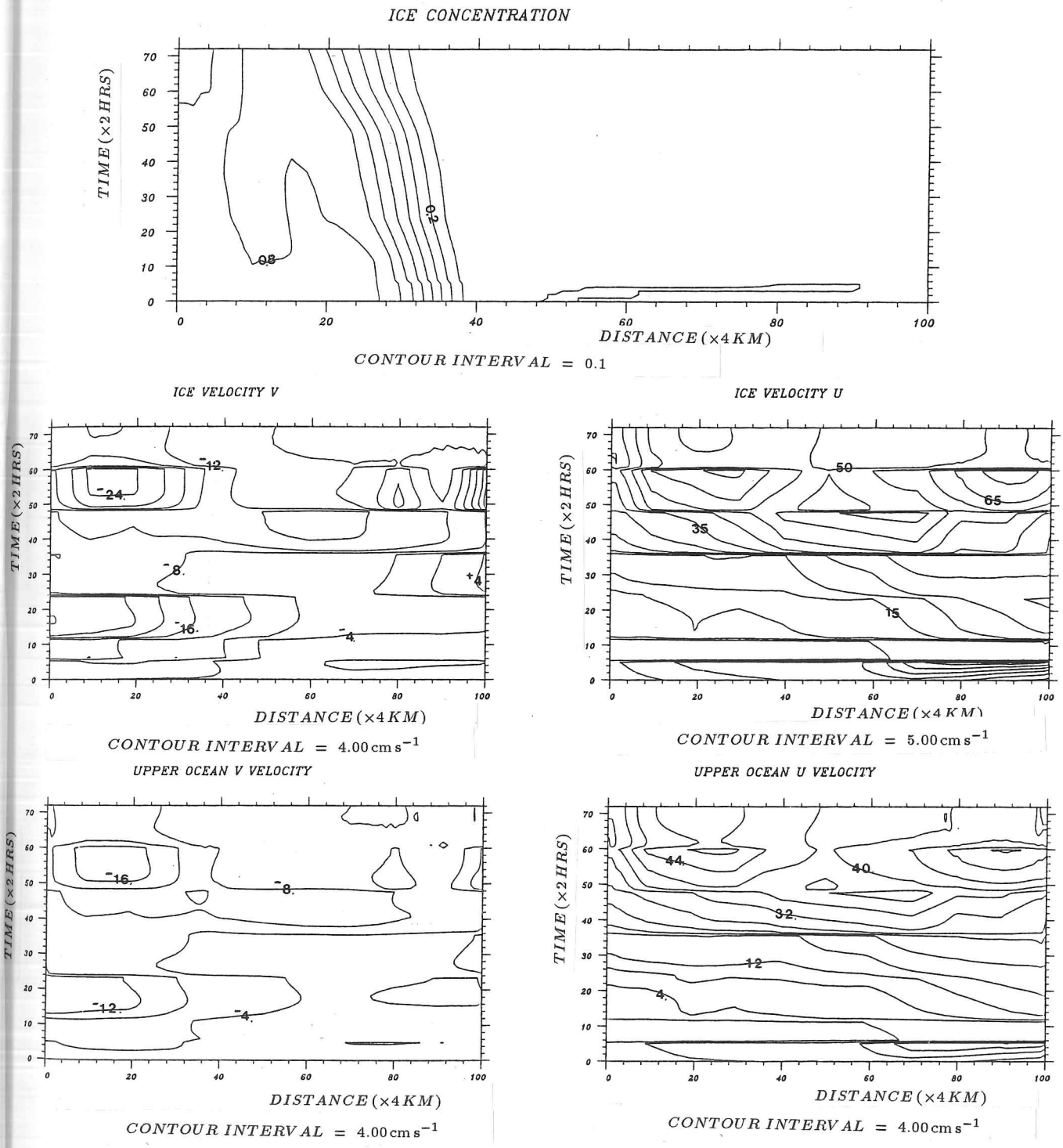

FIGURE 5.5: Contoured time series results from model simulations of Bering Sea conditions between JD59-61. The ice model is solved by the method of characteristics.

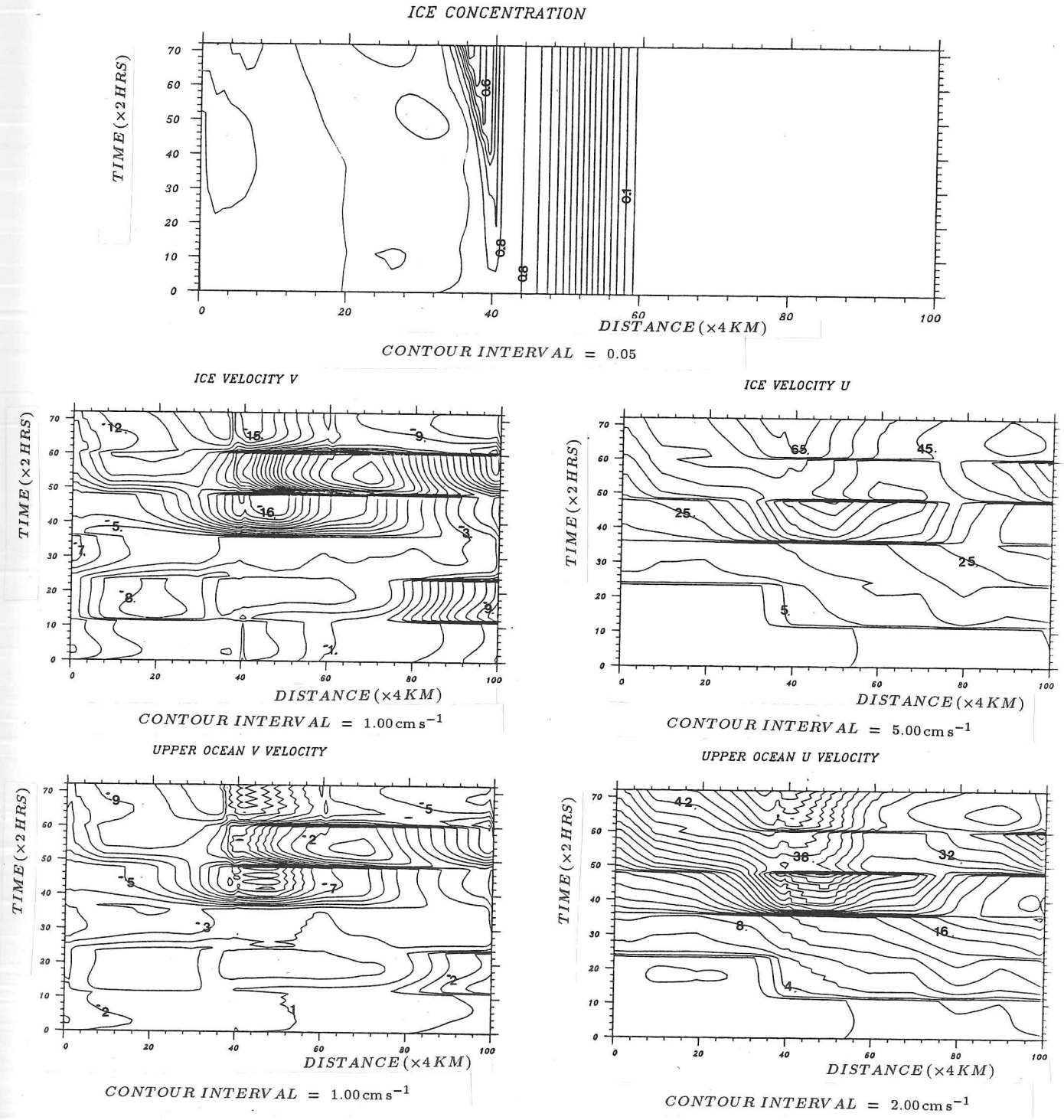

FIGURE 5.6: Contoured time series results from model simulations of Bering Sea conditions between JD74-76. The ice model is solved by the method of characteristics.

during this simulation with the base of the mixed layer temperature only indicating the effect of surface warming in the off-ice grid points.

Although the inertial oscillations caused by changes in the external forcing did not lead directly to instabilities in the model simulation, they did mask the underlying trend in the velocity fields during model development. In order to reduce the effect of the inertial oscillation, the forcing data were linearly ramped from one 12 hour external data set to the next at hourly intervals. This change proved successful, with inertial oscillations dampened in all but the strongest changes in wind gradient Unfortunately due to a change in computer resource allocation the model could only be re-run for a single case.

We chose to use the external forcing data set for JD 40-42 as it represented the strongest sequence of off-ice winds of all the 3-day periods considered, and we again solved the ice model by the method of characteristics. After 72 hours we see in Figure 5.7 that the ice edge has again retreated due to the change in sign of ice motion with this form of the model. In the open water area there is a signature representing new ice growth which is mirrored in the contours of salinity and temperature at the base of the mixed layer time series. It is this change in density from the new ice growth which generates a baroclinic signal in the ocean velocity field. The development of this disturbance in the velocity field may lead to the instability of the earlier non-rheological ice model runs.

The external forcing data for the four periods used in the model runs discussed above are given in Table 5.1. We can briefly look at how these different forcing fields affected the model simulation. Throughout the first period JD35-37 the winds were from the east to North-east sector alternating between data sets with a constant magnitude of $6 - 7\,\mathrm{m\,s^{-1}}$ and data sets where there was a decreasing off-ice trend ranging from $3 - 9\,\mathrm{m\,s^{-1}}$ which introduced cooler air from the north over the region.The ocean evolved in response to these wind fields with maximum velocities in the range $15 - 20\,\mathrm{cm\,s^{-1}}$. These velocities are much more realistic than those seen in the earlier test runs (Figure 4.12) where the winds had been restricted to $2\,\mathrm{m\,s^{-1}}$.

The period between JD40-42 was characterized by ENE winds of $3\,\mathrm{m\,s^{-1}}$ with cold air of approximately $-14\,^{\circ}\mathrm{C}$ in the northern sector, with more easterly winds ($5\,\mathrm{m\,s^{-1}}$) as we move southwestward along the sector (in a perpendicular direction to the average ice edge position) used for forcing the model grid. On the second day in this 3 day period the winds strengthened to a value of $9\,\mathrm{m\,s^{-1}}$ in the northern sector, are slack from the SE in the centre of the model domain, and are very strong easterlies of magnitude $15 - 18\,\mathrm{m\,s^{-1}}$ in the off-ice region. The strength of the wind

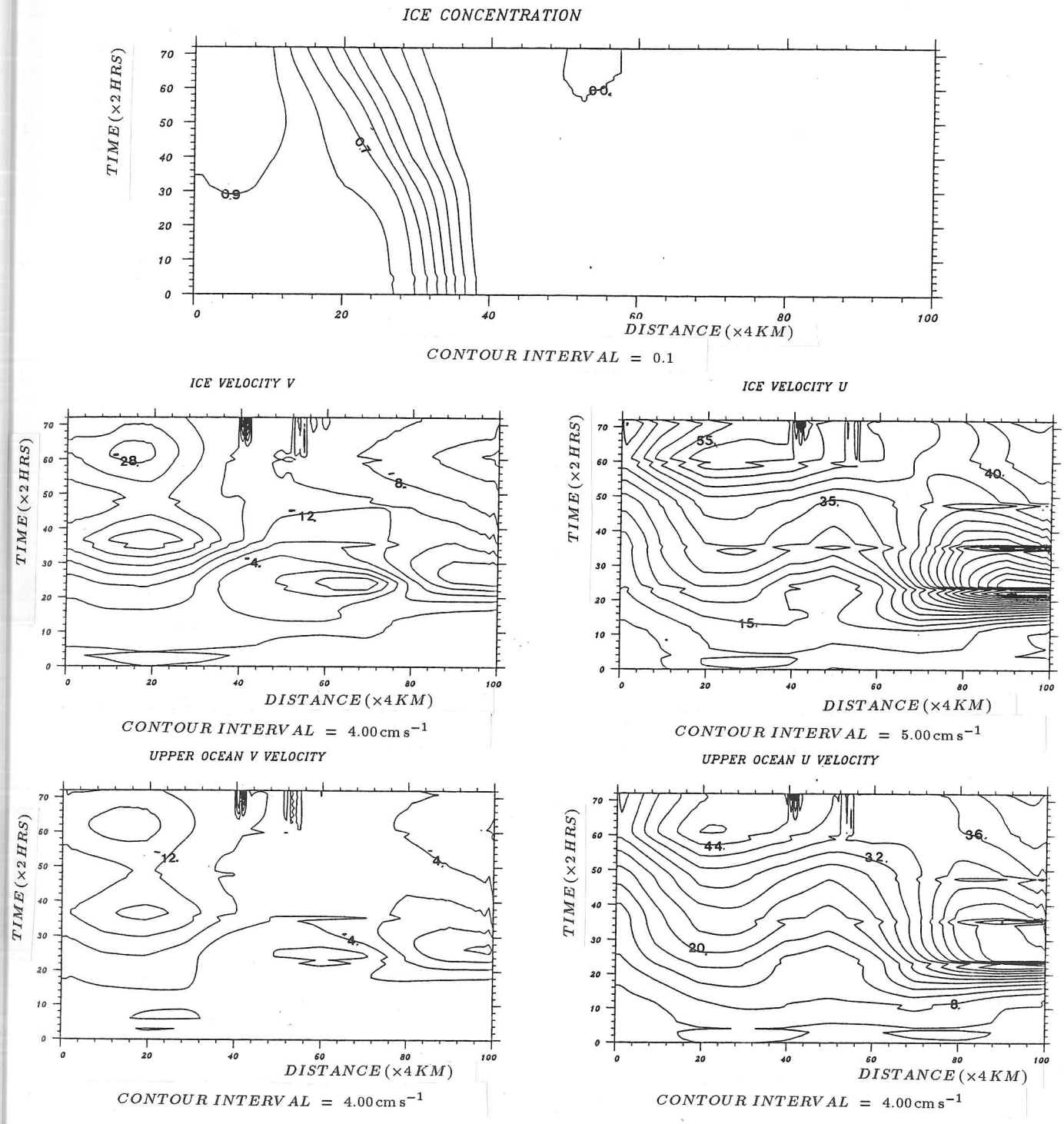

FIGURE 5.7: Contoured time series results from model simulations of Bering Sea conditions between JD40-42. The ice model is solved by the method of characteristics. The external forcing is now ramped between 12 hour data changes.

in this region explains the presence of inertial waves at the off-ice grid points even after the wind fields imposed on the model have been ramped. These stronger winds moved northward over the grid during the remaining days of the simulation, with the slacker wind values in the centre of the atmospheric system disappearing. In contrast, the data for the periods at the end of February and mid-March showed significant atmospheric warming over the 3 day duration. Air temperatures at an approximate ice edge location increased from -5.1 to $-1.0\,^{\circ}$C in the three day period starting on the 28th of February, and from -14.1 to $0.7\,^{\circ}$C in the three days from 3rd March. The winds were $7-11\,\mathrm{m\,s^{-1}}$ from the ENE within the ice cover, from the east along the ice edge, and from ESE at the ice-free grid points. One would expect that this wind pattern would prevent any rapid advance of the ice cover and the model simulation for the JD74-76 period (Figure 5.6) confirmed this conjecture.

There has been little discussion in this chapter so far on how the thermodynamic coupling between the ice and ocean models has reacted to the complex forcing fields. We can best address this question by examining the temperature and salinity cross sections at selected times, and also the salinity and temperature time series at the base of the mixed layer. The latter data mirror the surface temperature and salinity time series, but advance at a slower pace. The cross-sections two days into the 'no ice rheology' simulation will be considered as representative of the processes involved. In general, there is little difference in the salinity and temperature fields between the 'no ice rheology case' and the 'solution along characteristics' case, except where instabilities are generated as these are superimposed on the main temperature distribution.

The temperature cross-sections (Figures 5.9–5.12) show that the effect of the open water heat flux, which we had hoped would make the simulations more like reality, was not as successful as anticipated as strong temperature gradients are generated. We also see the signature of the bottom heat flux used to represent the effect of the barotropic current at the outer grid points. The size of this flux increased as we moved away from the ice, destabilizing a larger section of the lower part of the water column, thereby creating a bottom mixed zone. If this change to a bottom mixing mechanism was confined to a narrower zone, our final temperature cross section would more closely resemble the structure seen in the lower front (Fig 3.1,5.8) where the mixing is controlled by tidal currents.

The surface temperature flux is calculated using an open water budget at each time step. This flux gradually changes the surface water temperature value by direct insolation, sensible and latent heat fluxes, and direct heat transfer. The coefficient value in the latter process is unknown but we

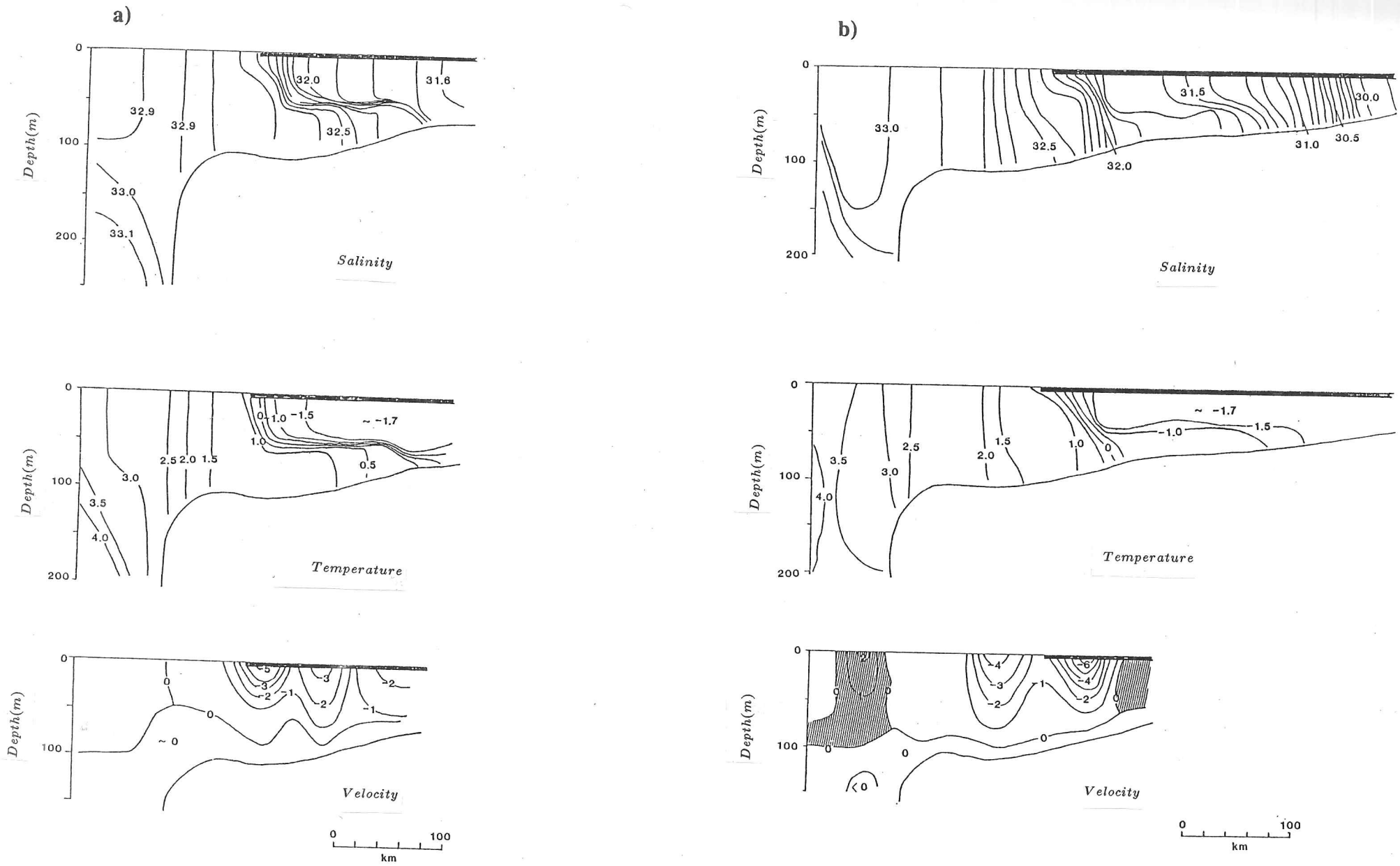

FIGURE 5.8: Repeat of Figure 3.1, Temperature, salinity and geostrophic velocity sections obtained during MIZEX-West on a)6-9th and b)26th-27th February, 1983

initially used an order of magnitude estimate which gave a realistic increase in temperature during test runs. However, examining the data in the temperature cross sections we see that the surface temperature closely mirrors the imposed air temperatures. This effect is most clearly indicated in the simulation forced by data from the period JD47-49, (which is not shown in any of the Figures or Table 5.1), when an initial warming in the open water grid points is followed by a cooling trend. The surface temperature responds rapidly to external conditions imposed over the 12 hour period. Also, the build up of high surface temperatures ($> 4°C$) in the outermost open water area is unrealistic.

In this model, convective mixing is stronger than wind-induced mixing which is included only in the vertical mixing term where the viscosity coefficient is dependent on the stability. The increase in surface temperatures reduces both of these mixing processes so that the incoming heat is effectively trapped at the surface and will only reach the rest of the ocean by diffusion. These results appear to show that the value assigned to the unknown heat transfer coefficient was too high, a lower value would slow the response time to the external conditions to more realistic rates.

The close association between the surface and atmospheric conditions is demonstrated in the temperature fields in Figure 5.9 showing the data 24 and 48 hours into the model run for the simulation period of JD59-61. During the first 24 hour period all the air temperatures in the off-ice zone were below zero, and the ocean responds giving surface temperatures of $-1.7\,°\,\mathrm{C}$ well away from the ice edge. The ice model does not indicate any rapid new ice growth at this time. However, after a further 24 hours the air temperatures had warmed and the surface ocean temperatures had increased in response.

We may gain further insight into the model simulation by examining the u and v velocity fields in conjunction with the temperature and salinity cross sections, and in particular look at the upwelling/downwelling signatures in the data and their relationship to the wind gradients in the forcing field. We find that the strongest velocity gradients in the along edge direction represent geostrophic velocity currents which are affected by the open water heat flux condition discussed above. Other features in the cross-section 2 days into the JD35-37 simulation (Figure 5.10) are a region of open contours in the along-edge velocity distribution associated with the ice edge which may represent a baroclinic jet. In contrast, the cross-edge velocity field indicates that the most negative velocities ($-8.0\,\mathrm{cm\,s^{-1}}$) are confined to a surface layer $15 - 20\,\mathrm{m}$ beneath the ice cover. Moreover, the velocity contours converge upwards outside the ice edge. Velocities in the lower 60 m of the water column are in the positive sense, but are considerably slacker than at the surface. This velocity

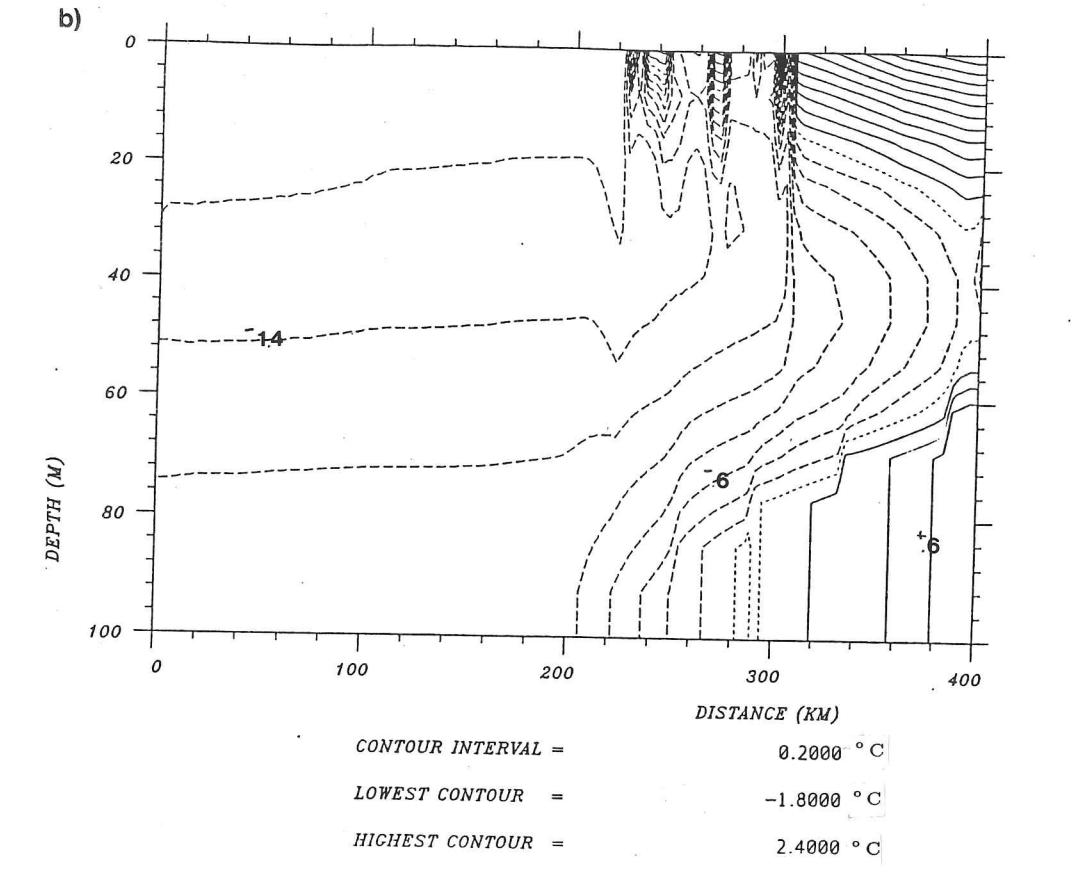

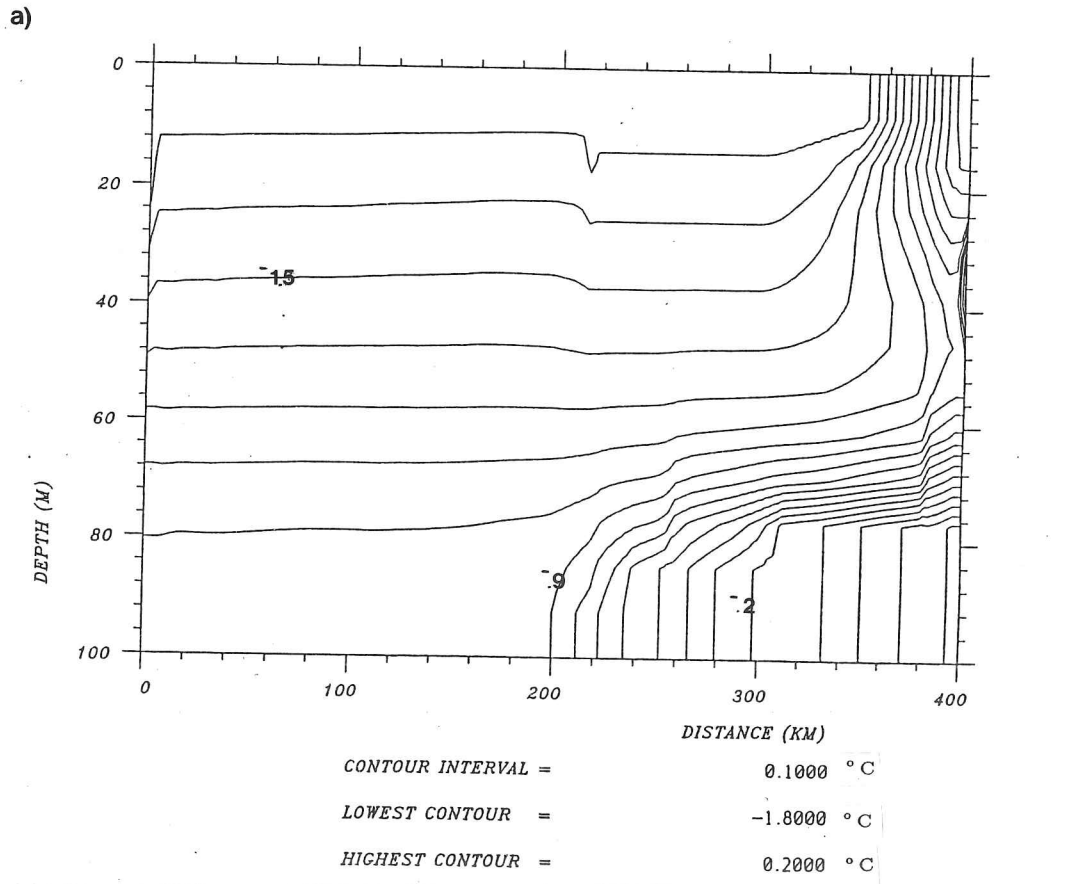

Figure 5.9: Temperature sections obtained a) 24 hours and b) 48 hours into model simulation forced by data from JD59-61 period. The sections show the effect of the off-ice atmospheric cooling during the first 24 hours on the upper ocean. The data from the following 24 hours indicates a warming trend.

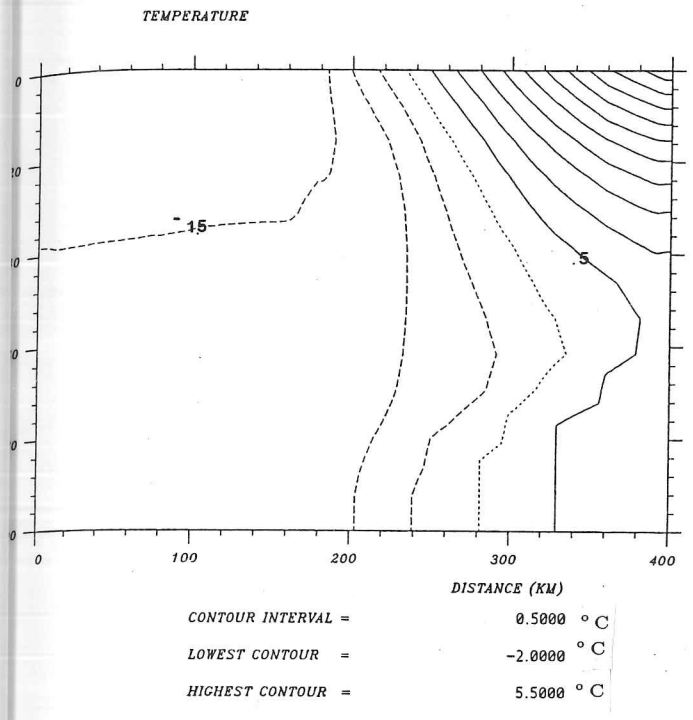

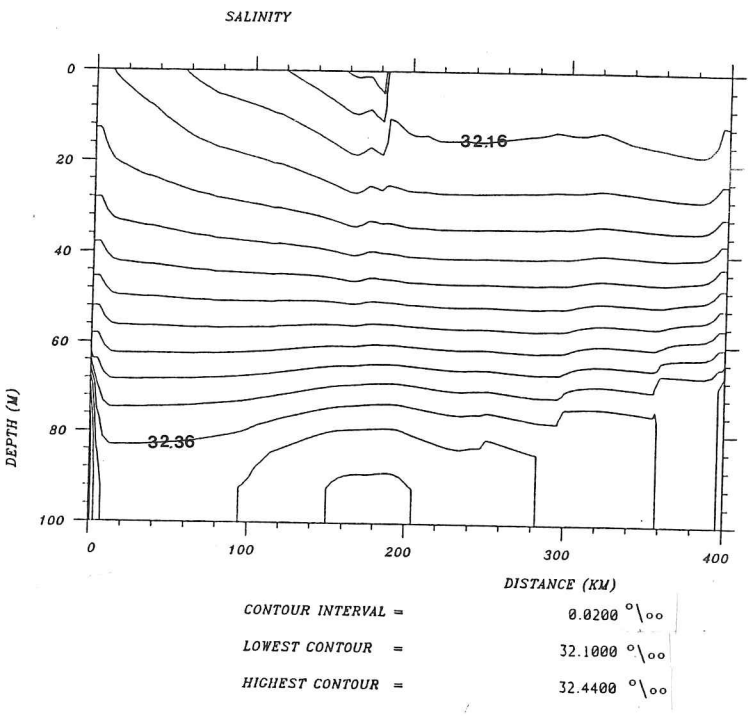

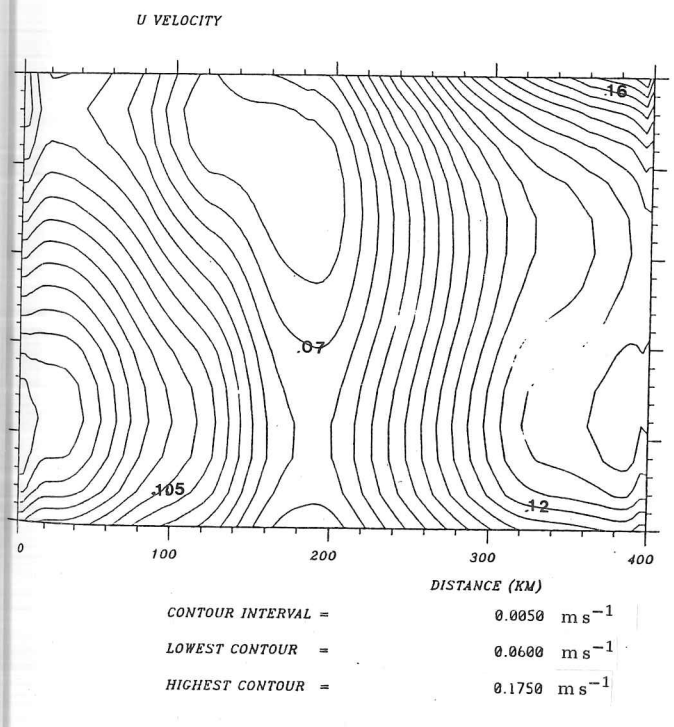

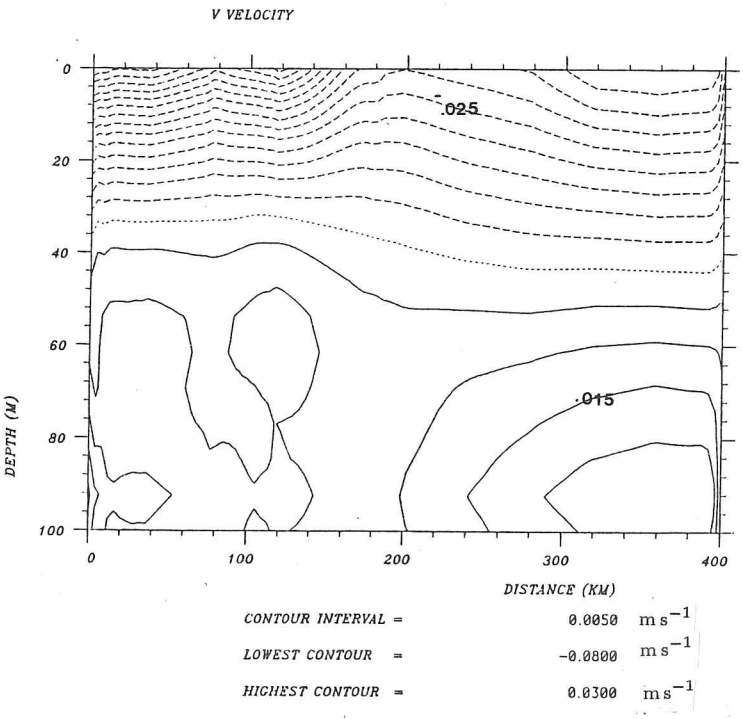

FIGURE 5.10: Temperature, salinity, u and v velocity cross-sections 48 hours into the Bering Sea simulation, with no ice rheology, forced by data from JD35-37 period.

distribution is the result of conservation of flow within the water column as imposed by the rigid lid condition. Although the use of an Orlanski condition within model levels as an open boundary condition is not correct, there are only some small gradient marks on the contours close to the boundary. The use of this scheme does not introduce significant errors more than 20 km from the boundary (equivalent to 5 model grid points).

The velocity fields at the end of day 41 in the JD40-42 simulation (Figure 5.11) are dominated by the effect of strong surface winds ($15 - 18\,\mathrm{m\,s^{-1}}$) . In the 30 outermost grid points all along-edge velocities are greater than $20\,\mathrm{cm\,s^{-1}}$ with a maximum velocity of $75\,\mathrm{cm\,s^{-1}}$ being recorded. The wide contour interval of $5\,\mathrm{cm\,s^{-1}}$ used in this plot gives poor detail in the ice edge velocity regime, and 2 days into the simulation ice edge velocity had not yet been affected by the stronger winds. However, there is some upwelling of a single isoline in the along-edge velocity field which is confirmed by the cross-edge velocity field and which again shows a sharp horizontal gradient at the ice edge.

At the edge of the strong wind forcing regime there was a decrease of $6\,\mathrm{m\,s^{-1}}$ within the spacing of 10 grid points in the data set for JD41 am. This gradient instigated an upwelling of over 40 m in the salinity contours close to the ice edge (Figure 5.11). Alongside is a smaller upwelling signature coincident with the lull of $4\,\mathrm{m\,s^{-1}}$ seen in the forcing data for JD41 pm. These features also appeared in the base of mixed layer salinity plots generated along with the main time series displayed in Figure 5.2 but they are not as strong in the case when the ice model was solved along the characteristics.

The velocity, temperature and salinity cross-sections after 2 days simulation of the JD59-61 (Figure 5.12) show similar patterns to the earlier cases. However, in this run the temperature distribution also displays the upwelling signature observed in the salinity distribution with three patches of significant cooling associated with strong wind gradients superimposed upon the warming trend instigated by the open water heat flux values. These features are again not present when the ice model is solved along characteristics for the same external forcing period.

The along-edge velocity field (Figure 5.12) represents a geostrophic balance with the density contours, and although there are some closed contours there is no obvious jet-like feature. The cross edge velocities are again a maximum beneath the ice with upwelling of isolines at the ice edge. There is also a signature in the v velocity field which is coincident with the upwelling disturbance seen in the temperature and salinity distributions.

Overall, despite the fact that the model does not contain the tidal mixing process seen on the

distribution is the result of conservation of flow within the water column as imposed by the rigid lid condition. Although the use of an Orlanski condition within model levels as an open boundary condition is not correct, there are only some small gradient marks on the contours close to the boundary. The use of this scheme does not introduce significant errors more than 20 km from the boundary (equivalent to 5 model grid points).

The velocity fields at the end of day 41 in the JD40-42 simulation (Figure 5.11) are dominated by the effect of strong surface winds ($15 - 18\,\mathrm{m\,s^{-1}}$). In the 30 outermost grid points all along-edge velocities are greater than $20\,\mathrm{cm\,s^{-1}}$ with a maximum velocity of $75\,\mathrm{cm\,s^{-1}}$ being recorded. The wide contour interval of $5\,\mathrm{cm\,s^{-1}}$ used in this plot gives poor detail in the ice edge velocity regime, and 2 days into the simulation ice edge velocity had not yet been affected by the stronger winds. However, there is some upwelling of a single isoline in the along-edge velocity field which is confirmed by the cross-edge velocity field and which again shows a sharp horizontal gradient at the ice edge.

At the edge of the strong wind forcing regime there was a decrease of $6\,\mathrm{m\,s^{-1}}$ within the spacing of 10 grid points in the data set for JD41 am. This gradient instigated an upwelling of over 40 m in the salinity contours close to the ice edge (Figure 5.11). Alongside is a smaller upwelling signature coincident with the lull of $4\,\mathrm{m\,s^{-1}}$ seen in the forcing data for JD41 pm. These features also appeared in the base of mixed layer salinity plots generated along with the main time series displayed in Figure 5.2 but they are not as strong in the case when the ice model was solved along the characteristics.

The velocity, temperature and salinity cross-sections after 2 days simulation of the JD59-61 (Figure 5.12) show similar patterns to the earlier cases. However, in this run the temperature distribution also displays the upwelling signature observed in the salinity distribution with three patches of significant cooling associated with strong wind gradients superimposed upon the warming trend instigated by the open water heat flux values. These features are again not present when the ice model is solved along characteristics for the same external forcing period.

The along-edge velocity field (Figure 5.12) represents a geostrophic balance with the density contours, and although there are some closed contours there is no obvious jet-like feature. The cross edge velocities are again a maximum beneath the ice with upwelling of isolines at the ice edge. There is also a signature in the v velocity field which is coincident with the upwelling disturbance seen in the temperature and salinity distributions.

Overall, despite the fact that the model does not contain the tidal mixing process seen on the

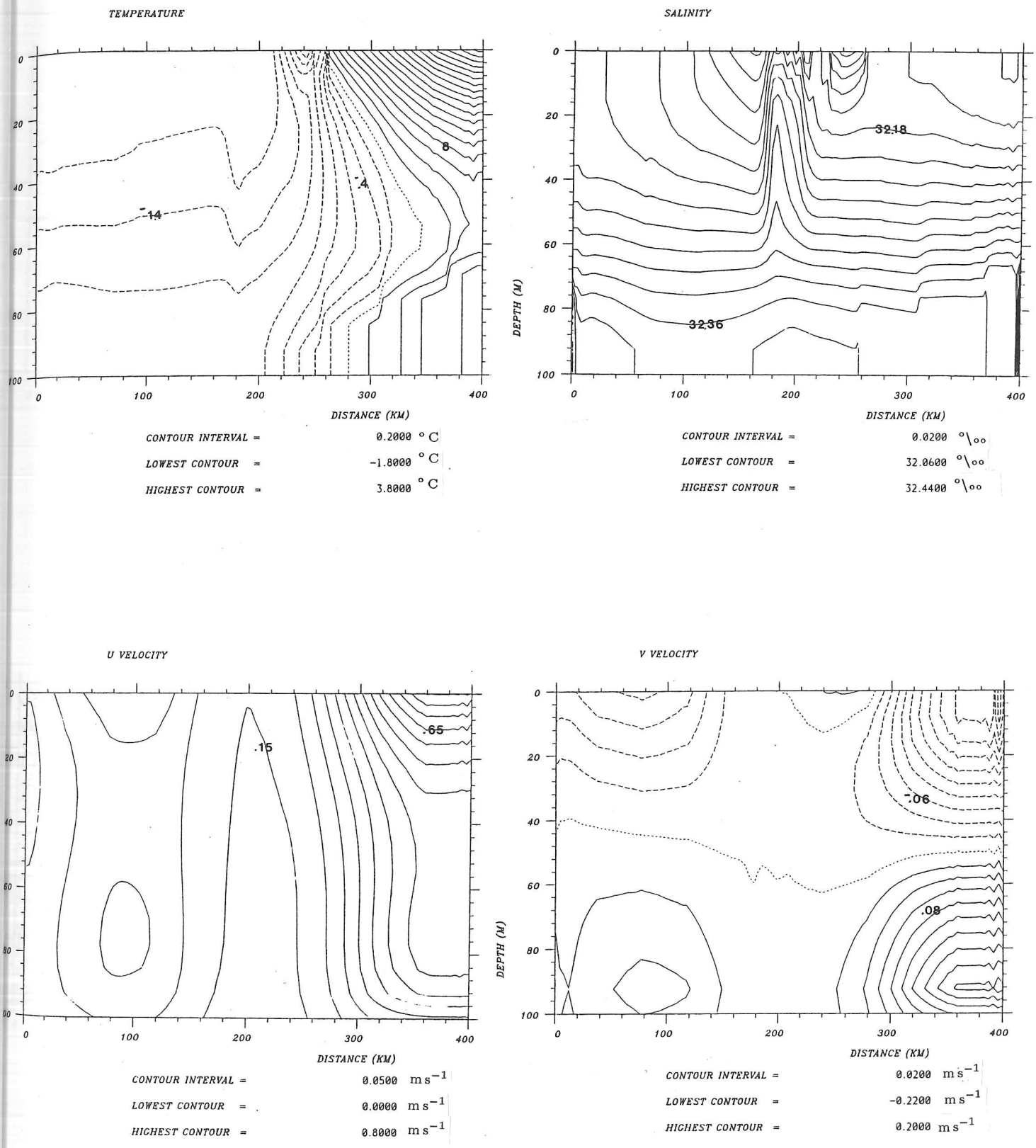

FIGURE 5.11: Temperature, salinity, u and v velocity cross-sections 48 hours into the Bering Sea simulation, with no ice rheology, forced by data from JD40-42 period.

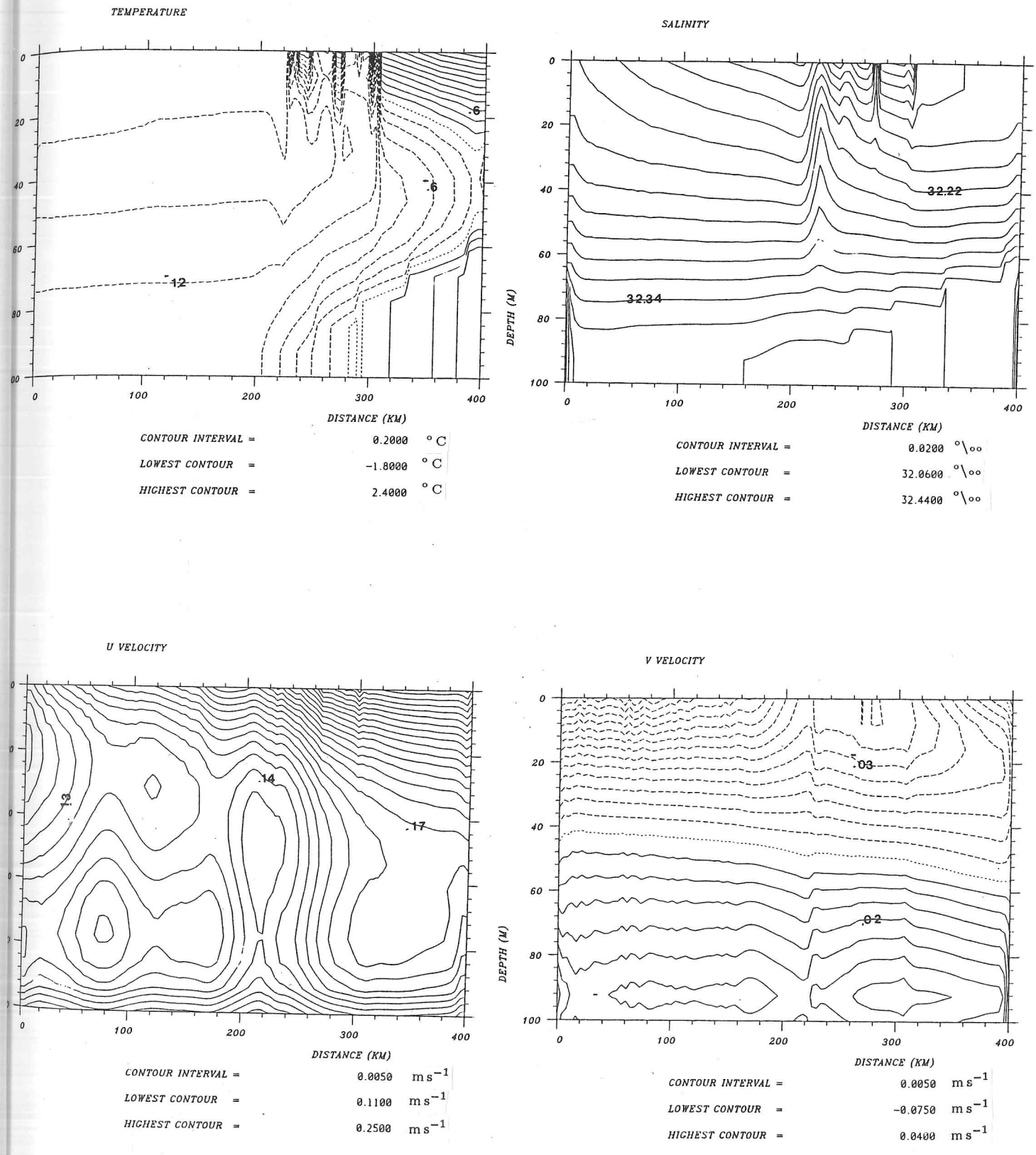

FIGURE 5.12: Temperature, salinity, u and v velocity cross-sections 48 hours into the Bering Sea simulation, with no ice rheology, forced by data from JD59-61 period.

Bering Sea shelf and the wind mixing is dependent on the stability as well as the velocity shear in the water column, the model does produce reasonable temperature and salinity cross sections which can be compared with those in Chapter 3. Sections for 6-9 th February are reproduced here as Figure 5.8. We recognize that there is still a problem with the open water surface condition, and that the bottom mixed layer is produced by a flux mechanism rather than tidal mixing.

5.2 Conclusions and Future Work

In this thesis we have attempted to understand the processes in the Bering Sea ice edge frontal regime using data from the physical environment and numerical models with some degree of success. Although the environment of leads formed in the East Greenland Sea marginal ice zone in summer, where we used our Mini-CTD instrument, is different from that of the mid-winter Bering Sea, there were a number of similarities.

In the Greenland Sea the melt rate of the sea ice is dominated by local processes, principally direct insolation and heat entrapment in the open water area. The flux from the warmer Atlantic layer present at about 100m from the surface and the ice position relative to the Polar front are secondary factors in defining the melt regime.

In the Bering Sea case a thermodynamic balance is maintained between the ocean heat stored seaward of the edge, and the wind driven advection of the ice from the north. Additionally, there are disparities between the wind mixing regimes in the two cases; Greenland sea summer conditions typically had slack winds ($< 5\,\mathrm{m\,s^{-1}}$), while the winter Bering Sea was dominated by strong North Easterlies ($> 10\,\mathrm{m\,s^{-1}}$).

The data obtained with our portable CTD device (appendix A) showed little evidence of significant small scale fronts in the surface waters of summer leads. However, this may not be entirely surprising as there is only slight horizontal variability in the pycnocline regions beneath the area sampled by the CTD. Unfortunately, there is also still some uncertainty in the results generated due to problems in the instrumentation. Extra robustness has now been added to the package so that on future deployments small scale gradients should be accurately measured.

Of the three types of model investigated only the coupled ice-ocean finite difference multi-level scheme produced anything approaching a realistic picture of the ice cover and ocean dynamics on the Bering Sea shelf. The model was capable of reproducing many of the processes expected in

ice edge regimes, such as, brine rejection, meltwater front formation and ice divergence under suitable external forcing. Problems arose, however, when all the possible dynamic and thermodynamic processes were incorporated into one simulation. This is partially due to unrealistic initial conditions for the ocean density structure, and secondly, to there being several processes involved which can cause instabilities. Moreover, any disturbances which arise will be amplified as the different mechanisms act to reinforce each other.

The thermodynamics growth rates used in the ice model conservation equations were derived from schemes used in climate models (Semtner, 1976b). These schemes did not work successfully on short time scales; in particular the algorithm under-estimated the rapid ice growth that can occur in open water when suitable conditions prevail. Parameterization of open water new ice growth and thermodynamic changes when leads develop within the ice pack is not specifically included in the model except by the use of two 'ice thickness' levels (Hibler, 1979). This is a major shortcoming of the model when used over 2-3 day time scales.

The salt and heat flux algorithms, which are dependent on both ice concentration levels and external forcing terms can result in neighbouring grid points having considerably different fluxes. This leads to unrealistically strong horizontal gradients in the upper ocean if insufficient diffusion is present in the model.

Several simulations of the model were undertaken to examine a range of ice rheologies, the aim being to find the most suitable parameterization for the internal ice stress for use in the marginal ice zone. Rheologies in forms similar to those used in large scale models (Hibler, 1979) became unstable. This is because the amplitude of the ice strength function is close to the stability limit for the size of the model grid. It is difficult to discretize the sharp drop in ice strength which occurs at the ice edge within the finite difference grid, and moving to a finer grid requires an even lower magnitude for the ice strength.

The most successful scheme we implemented in the ice model utilized the method of characteristics also employed by Røed and O'Brien (1983). Although this scheme involved using a simplified rheology where the internal stress was represented only by a pressure gradient, term it offered an adequate representation of the decrease in ice-ice interaction and hence of ice coherence in the MIZ.

The next stage in following up the results of our ice-ocean coupled model would be an improved representation of the thermodynamics, particularly in the ice edge zone—with respect to new ice

growth—and within leads and polynyas within the main pack. This would involve moving away from the zero-level climate model of Semtner (1976b) to concentrate more closely on the time scale of new ice growth in the open water region.

The addition of topography to the ocean model would allow a better representation the ocean dynamics off-shelf, but for the currents generated to be realistic we would require the use of a second horizontal dimension. This, however, moves us away from a small scale modelling project studying local physical processes, into the realm of general circulation ice-ocean models (Hibler and Bryan, 1984; Semtner, 1987).

As a final point, parameterization of the physics of the ice-ocean interaction process is fundamental to our understanding of MIZ dynamics. The processes involved in both heat and momentum transfer are complex (both physically and mathematically), but if we are to advance our knowledge of the polar oceans and hence of our climate, it is at the level of sub-grid scale physics that the greatest improvements will be found. It is hoped that such improvements are attained, and can be configured simply enough for inclusion in the next generation of general circulation ocean models (such as FRAM, Fine Resolution Antarctic Model) which include polar latitudes.

5.3 Summary

1. The dynamics of the ice edge frontal region in the Bering sea is controlled by a balance between the buoyant meltwater input from the ice advected from the north of the region and the heat flux from the on-shelf barotropic slope current.

2. One-dimensional and two layer geostrophic models were not adequate to explain all the ocean processes occurring at the ice margin; the full three dimensional picture is required. However, due to limited computer resources only a two dimensional model of the cross-section of the ice edge front could be employed, though it did include both dynamic and thermodynamic coupling to an active ice model.

3. The coupled model was able to demonstrate the development of a frontal regime when realistically forced. Under strong wind gradients, however, the model had a tendency to become unstable. By including an internal stress term in the form of an ice pressure gradient which decayed rapidly at the ice edge, the model responded more smoothly to external forcing conditions. However, this pressure gradient term generated jet structures in the ice cover which

changed the velocity gradients in such a way that the ice cover was no longer advected in the expected direction.

4. Our comparison with the meltwater density regime in leads within the Greenland Sea pack was not entirely successful as our portable CTD instrument was not operating reliably, and we did not encounter suitable conditions.

Appendix A

Instrumentation and experimental deployment

A.1 Aims of experiment on Marginal Ice Zone Boundary Layer Dynamics

An important part of the MIZEX-84 oceanography programme was to study the ocean boundary layer formed under the marginal ice zone. The dynamics of this boundary layer need to be considered when discussing the velocity structure of the upper ocean, for it is through this layer that the ice-water stress is transmitted (McPhee, 1982). Boundary layer depth and other characteristics are modified by the stabilizing effect of input of melt water from the ice as a counterbalance to energy from summer storms which acts to re-establish a mixed layer.

At the MIZEX-84 interior drifting station, boundary layer studies were conducted from a vertical array of conductivity, temperature and velocity sensors by M. McPhee. Also at this inner station measurements of heat transfer and other ice properties were collected with the purpose of calculating a mass balance for the summer marginal ice zone.

The level of buoyancy input at the interior station was considerably lower than that observed at the ice edge. In the active outer regions the ratio of ice loss from lateral/bottom melting increased (Perovich, 1983). Experiments in this outer region were undertaken during MIZEX-84 from the M/S Kvitbjørn, which made numerous sections across the ice margin and also from M S Lance in Fram Strait in August 1984. These experiments included ice ablation measurements collected by

E.G. Josberger of the USGS (United States Geological Survey). SPRI undertook a complementary programme, studying the effect of meltwater input into the upper ocean at the ice edge. This latter study was designed to encompass both the immediate impact of fresh water input on the ocean boundary layer, and to follow the development of the newly formed layer when this buoyant water is mixed to the depth of the thermocline. On a local scale the lateral density front formed at the ice margin, marking the boundary between the melt influenced Polar water and the Greenland Sea water is analogous to the Bering Sea front. We aimed to study these fronts and in particular to examine the effect on the upper ocean as floes drifted across the front into warmer water.

A.2 Instrument specifications and design

A.2.1 Instrument requirements

To carry out a programme of ocean profiles at the extreme edge of the marginal ice zone the instrumentation had to meet 3 main criteria:

1) it had to be sensitive enough to measure the small temperature and conductivity gradients in the near isothermal layer.

2) it had to be robust enough to be used in leads in the ice, where loose ice could damage the instrument.

3) it had to be portable enough to operate away from the ship, either at the edge of ice floes or from small boats (no helicopters available).

As no portable CTD (conductivity, temperature, depth) instrument with these requirements was available commercially at that time, a unit was designed and built at the University of Cambridge (Scott Polar Research Institute and Department of Earth Sciences) by S.C. Moore and T.R.E. Owen to a specification provided by the author.

A.2.2 Instrument configuration

The instrument (Figure A.1) is manufactured from aluminium; the main section being a cylinder 375 mm long with interior diameter 89 mm and 110 mm exterior diameter. The head of the instrument is a solid paraboloid which was streamlined so as not to disturb the density field measured by the sensors. In the constant diameter part of the head section there are two inlets providing access

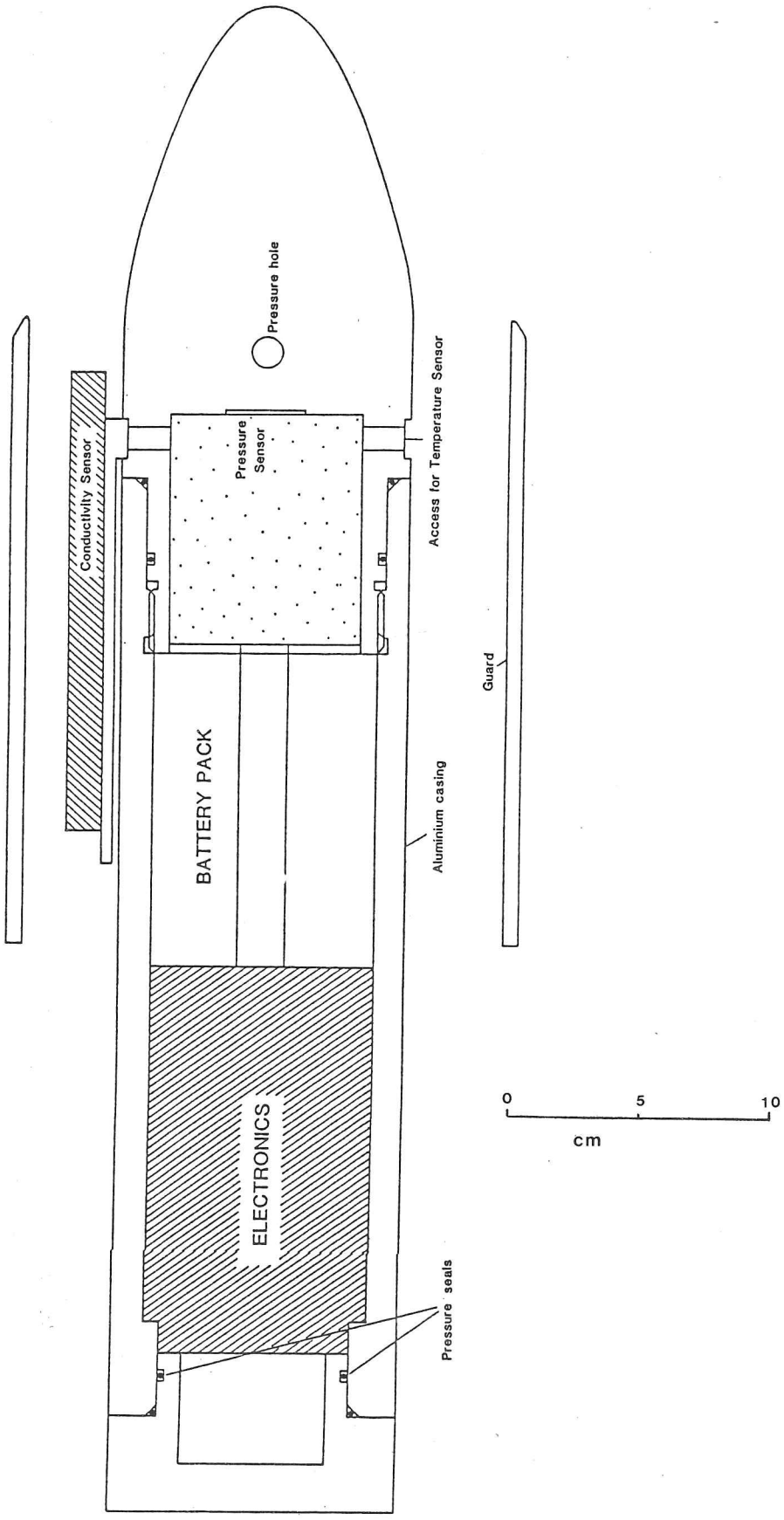

FIGURE A.1: Diagram indicating major components of the SPRI portable CTD instrument package.

to the pressure sensor. Perpendicular to these inlets are brackets for the conductivity and temperature probes. The system is powered by a block of ten 1.5 V Ni-cad, C-cells which are rechargeable through the waterproof connector when the instrument is at the surface. The battery block was placed just above the sensor's internal connections in order to weight the instrument. Additionally, the parabaloid head was made of solid aluminium so that sufficient mass was available within the package itself and the use of extra weights which might disturb the water column in advance of the sensors, could be avoided. It was decided that the data should be recorded at the surface so that the instrument package could be compact as no internal logging was required. Also, with the signals being recorded at the surface they could be scanned in real-time by a microcomputer (section A.4).

The sensor signal is passed up the centre of the battery block to the sensor electronics for conditioning and coding as frequency signals (Figure A.2). Three electronics boards, one for each sensor, are arranged in a triangle on a circular plate and bolted on to the battery block. The whole central section is tightly pressure sealed at the base of the cylinder. A pressure release knob is fitted to the seal joining the end cap to the main cylinder. A 10-way connector positioned at the top of the electronics section links to the interior part of the seawater connector (manufactured by SeaCon no. RMSJ5). A 3-core co-axial cable is attached through a hookend connector to the winch and is moulded onto the outer part of the seawater connector. The central portion of the instrument from a point just above the sensor probes, is protected by an aluminium guard of diameter 202 mm, length 254 mm and thickness 5 mm. The guard was drilled to lighten overall weight of the instrument (Figure A.3).

A.2.3 Sensors incorporated into instrument package

The pressure sensor is located just behind the parabolic head in the base of the instrument. It is positioned centrally beneath the battery package and electronics section. Access to the outside pressure field is made through two 13 mm diameter holes (Figure A.4). The sensor was a commercially-built pressure transducer manufactured by Druck UK Ltd., part type PDCR 110/W, with an operating range above 10 bar. The transducer was separated from the fluid media by a stainless steel isolating diaphragm. The output signal from the transducer had a full-scale deflection of 100 mv with a d.c. offset of 3 mV. The sensor operates on a voltage of 10 V d.c. at a current of 15 mA. Problems arising in the manufacturing of the transducer and the urgency of our assembly deadline, led to the pressure sensor installed in the CTD being outside the manufacturer's calibration and linearity

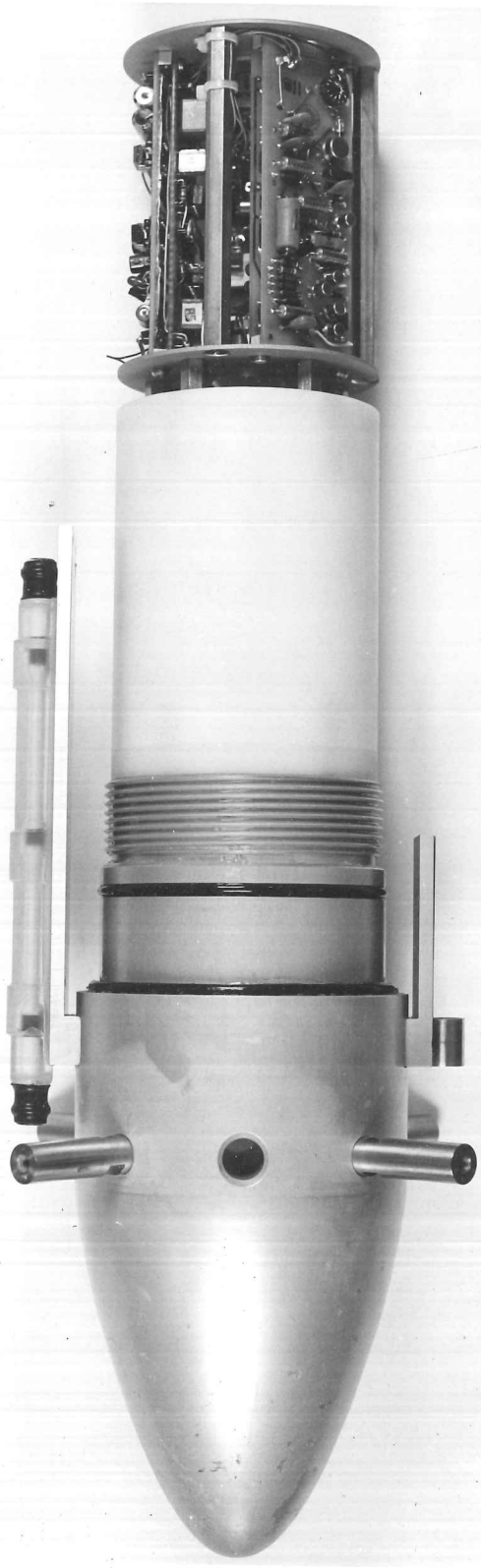

FIGURE A.2: Internal structure of CTD instrument showing conductivity cell and the thermistor package attached to the side of the casing. The photograph also shows the location of the electronic boards, mounted above the battery pack.

FIGURE A.3: Photograph of complete CTD package showing external SEACON connector at the base and a guard protecting the sensors close to the head.

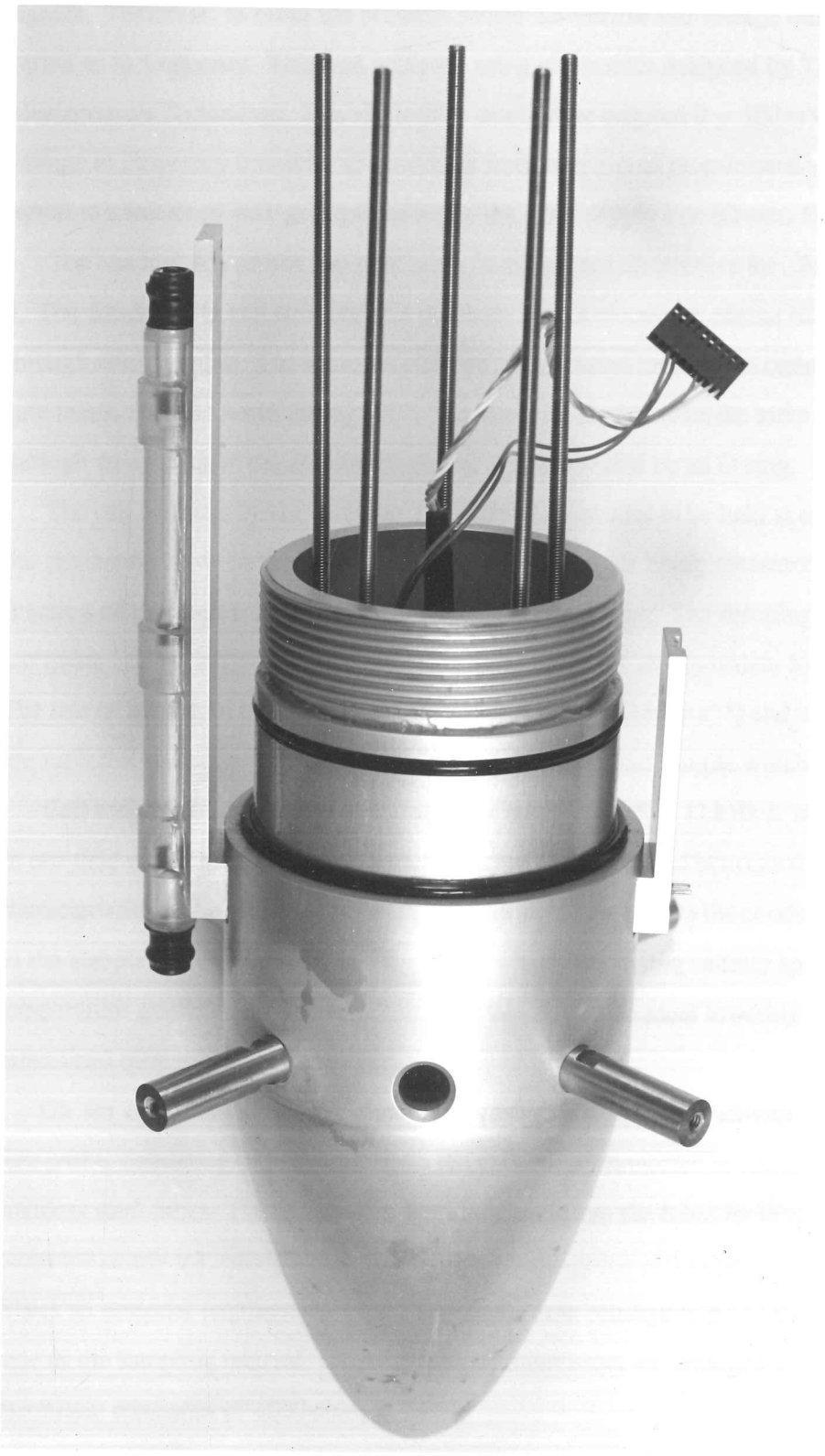

FIGURE A.4: Close up of the conductivity cell, access hole to the pressure sensor and the steel tubes guarding the thermistors.

specifications. The electronics for the conductivity and temperature probes was purchased along with the sensors (figure A.5). Output from these electronic boards was in the form of frequency signals. Therefore, to make the pressure sensor compatible the voltage output needed to be converted to to frequency. This was achieved using electronics designed by T.R.E Owen of Carrack Measurement Technology. The electronics amplify the original $0 - 100\,\mathrm{mV}$ signal before using a voltage to frequency converter to produce a frequency signal proportional to the ratio of the input signal to a reference voltage, represented by the $-5\,\mathrm{V}$ supply line (Owen, 1984).

The conductivity sensor was purchased from SeaBird Electronics Inc. WA. USA, type no SBE-4. The conductivity cell consists of 3 platinum coated electrodes placed 62.5 mm apart in a flow-through configuration. The sensor is attached via a bracket to the main casing just behind the pressure inlets, though rotated through 90°. The electrode signal enters the main body of the instrument through an opening in the aluminium casing which is sealed by an O-ring.

The cell operates by allowing the outer pair of electrodes to be held at the same potential, with the resistance between the centre electrode and outer pair being measured. This resistance is a function of the fluid's conductivity and the cell dimensions. The resulting measurement may be interpreted as an integration of the conductivity value for an equivalent length of water column. The rate of descent of the cell through the water column ($0.166\,\mathrm{m\,s^{-1}}$) and the sampling rate (0.5 s) are sufficient to obtain several records for the volume of fluid sample which fills the cell.

Cell resistance is converted to a frequency in the range $5 - 11\,\mathrm{kHz}$ at an rms voltage of 0.7 V. In our field experience in the Arctic the frequency output ranged between $6.5 - 7.5\,\mathrm{kHz}$. Flushing characteristics of the cell, viz., the ability to determine how rapidly the conductivity sensor responds to the sample flowing through, are important when interpreting salinity spiking caused by strong temperature gradients in the thermocline. However, with manual lowering speeds this problem is minimized (Gregg and Hess, 1985).

On the opposite side of the aluminium casing from the conductivity sensor is the temperature probe, consisting of two thermistors (STC U23US) connected in series and encased in narrow stainless steel tubes. The thermistors were insulated from the tubes by lacquered resin. These unprotected nearly microscopic thermistors were advantageous as they possessed a fast response time. It was an essential requirement for the thermistor time constant to be of the same order of magnitude as the sampling interval. When the pair of thermistors are arranged in series they gave a total thermistor resistance of 4000 ohms at 20° C.

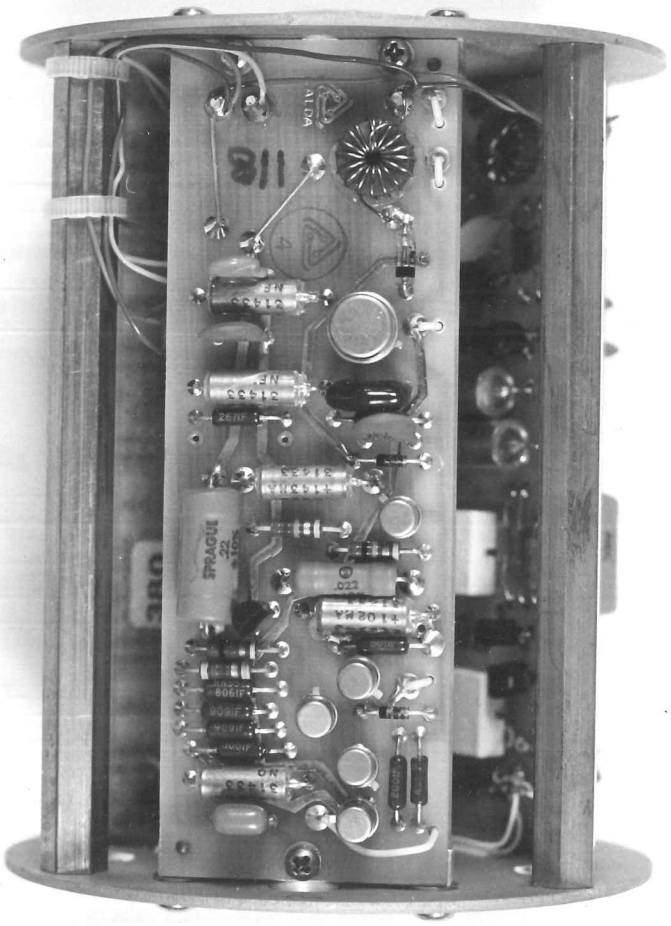

FIGURE A.5: Close up of the 3 sets of electronics, one for each sensor, mounted triaxially on a metal plate.

TABLE A.1: Sensor precision

	Pressure dbar	Salinity ‰	Temperature °C	Conductivity mmho cm^{-1}
Range	0.0-100.0	28-36	-1.8-5.0	22-38
Proposed Resolution	0.10	0.002	0.001	0.002
Least count Resolution	$2.5 - 10 \times 10^{-3}$	3.0×10^{-3}	0.5×10^{-3}	$1.5 - 2.5 \times 10^{-3}$

A.2.4 Sensor precision

The sensor precision and resolution characteristics for the SPRI CTD are given in Table A.1. The quoted least count resolution is not constant for individual sensors as the scale of measurement often exceeds the upper value of the electronic counter and moves onto a separate range (Section A.2.6).

A.2.5 Winch and Slip-ring assembly

As the Mini-CTD instrument was in the first instance only required for shallow (< 100 m) profiles, and since our budget was limited, a manual winch was purchased (Braystroke Gauge Winch SK78L, supplied by Valeport Developments). The winch, manufactured from steel, was supplied with approximately 100 m of 3-core coaxial cable ending in a hookend connector for attachment to the instrument package. The winch was fitted with a payout counter, though this often jammed during use. A combination of a ratchet stop and an adjustable brake were used to secure the load at a given cable extension. The total weight of the winch was 31 kg and it had a load capacity of 100 kg. The winch was fitted with instrument grade, three-way slip rings. The stainless steel armouring on the cable was utilized as signal ground.

A.2.6 Electronic counter

An electronic counter used to analyse the frequency signals from the CTD instrument, was located in the logging box on the surface. All the parts of the logging electronics were designed and built by T.R.E. Owen of Carrack Measurement Technology. The logger was controlled by an RCA CMOS 1800 series processor with timing provided by a 153.4375 kHz high frequency clock pulse. The logger had data capacity for 48K bytes in the form of hard core random access memory (RAM),

enough for approximately 68 minutes of data. Each data point represents the number of clock pulses occurring during 2048 cycles of the input signal (Owen, 1984).

The resolution of the electronic counter was increased using period counting methods in preference to a direct binary count of the frequency signal. The counter produces a 16 bit number which can be interpreted on several range settings which are not known *a priori*. A new range setting is invoked when the counter exceeds the maximum 16 bit number for a given range. The first 2 bits of the data 'word' represent channel coded information, whilst the remaining 14 bits are the last 14 bits of the original 'word'. All the data is coded in hex with two hexadecimal characters representing 1 byte. Hence, by coding the first two bits according to the channel, data in the range 4000-7FFF represents pressures, from 8000-BFFF represents temperature and from C000 to FFFF represents conductivity. Words less than '4000' represent time, date or end-of-file marks.

A.3 Deployment and Field Operations

The CTD instrumentation was mounted within an aluminium frame in order to facilitate its suspension over the side of the floe (Fig. A.6). The winch was positioned at the back of the frame counter balancing the instrument's weight. The signal cable passes over a pulley to the CTD fish. The complete apparatus was hauled across the floes on an aluminium sledge. The chosen floe was usually of multiyear type, had more than 20 cm freeboard, and had a diameter between 30 and 200 m. The floe was examined both on approach and after anchoring for a safe edge where the wave field had not eroded away the ice wall at, and below water level. The snow cover on most of the floes used was light and the ice concentration in the area ranged from 3/10 near the ice margin to about 9/10 in the interior, i.e., the limit to which Kvitbjørn would normally enter the ice.

Once the site was chosen and the instrument frame secured by tethering it to a stake, the CTD fish could then be attached and the whole apparatus suspended over the side of the floe. The cable between the logging box and slip ring assembly was connected and the key turned in the logging box. If this was the first profile of the series the internal clock of the logger had to be set through the Epson HX-20 computer. A spot reading was taken to check if all counters were functioning (only the temperature and pressure readings will give sensible readings in air). The instrument was then set into logging mode if automatic logging was being utilized, or the logging was conducted under the control of the Epson HX-20 computer (Section A.4.2).

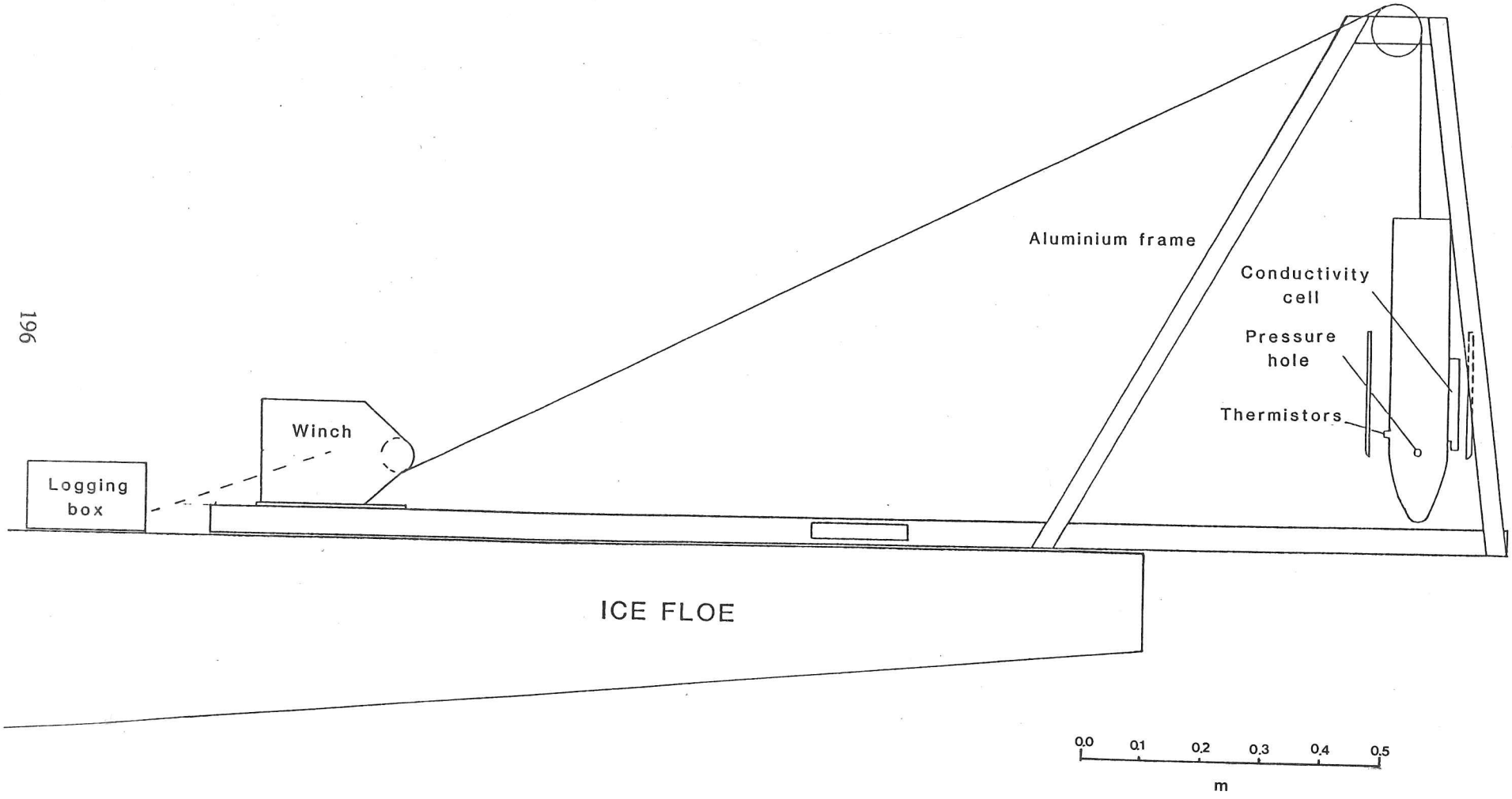

FIGURE A.6: Diagram showing the instrument frame and winch configuration used in normal deployment over the side of an ice floe.

Most field deployments involved obtaining a few CTD casts from a single drifting station. On some occasions data were also recorded during the upcast. During short ship stops (1.5-2 hours), 2 stations to depths of 70 m or 3 stations to 40 m were normally obtained. The time for lowering at each station was about 5 minutes, whilst hauling the instrument to the surface normally took at least twice as long. On several occasions a time series of short casts was maintained over periods of a day, during the ice drift phases undertaken by both Kvitbjørn and Lance. The CTD fish was also left in the pycnocline to obtain a time series for periods of up to 45 minutes. This time was limited by the size of the data buffer and the 2 Hz sampling rate. During these data time series, the floe drifted and a continuous gradient in temperature and conductivity was seen in the records. This may be similar to the drift which occurs during winch stops, as no flushing of the flow-through conductivity cell occurs (Bauer *et al*, 1977).

The instrument was also deployed from small boats, enabling variations in the upper boundary layer of leads to be studied. During Lance's section across the East Greenland pack ice in Fram strait, maximum ice concentration was rarely above 6/10, and work in the open water around the floes was often carried out as an alternative to work from the floes themselves, especially when the floe edges were badly eroded or awash with waves. This method of deployment was also easier and quicker, since the instrumentation could be set up in the boat between stations. The frame was mounted either in the stern (Lance) or the bow (Kvitbjørn) of the small boat and the engine was normally off during profiling operations. On some occasions the boat was anchored to a small floe while obtaining measurements. In some of the open water sequences there are regular spikes in the data due to the movement of the boat under the action of incoming swell, its own bow wave, or the bow wave of other 'Zodiac' inflatables deployed simultaneously from the ship.

Table A.2 is a summary of all the CTD operations which produced data profiles stored on floppy disc (see section A.4). (Some of the early data records were lost in the intermediate micro-cassette stage). The geographical position of Kvitbjørn was found by interpolation from a tape of SatNav positions which were logged every minute. These data were collected and made available by R. Mickle, Atmospheric Environmental Services, Canada.

TABLE A.2 Summary of CTD Stations

Station	Time	Position	Depth (m)	Remarks
6 July PA	1840	80° 04.01′ N 0° 38.34′ E	70+	Far side of large floe used as base in second Mini-drift, Bergen thermistor position, heavy snow cover, melt pools.
6 July PB	1910	80° 03.68′ N 0° 36.70′ E	70+	Second lowering at the same site, note increase in wind driven surface current from change in wire angle.
6 July PC	1945	80° 03.28′ N 0° 34.73′ E	70+	As experiment, fish allowed to fall under gravity for upper 30 m, continuous jerking of wire.
9 July P1	1626	78° 37.44′ N 2° 12.69′ E	70+	Toroid and USGS Ablation site on eddy tongue, rapid rotation of floe, both visually and from pitch and tilt records (SPRI).
9 July P2	1633	78° 37.50′ N 2° 12.51′ E	70+	Upcast, data record never broken when at base, pressure sensor reversed so may have reached minimum.
9 July P3	1658	78° 37.71′ N 2° 11.87′ E	70+	A further downcast at same station.
9 July P4	1706	78° 37.64′ N 2° 11.78′ E	70+	Upcast of P3.
12 July P1	1402	78° 49.85′ N 2° 33.59′ W	70+	First station of transect. Pressure sensor reversed, still poor signal.
12 July P2	1453	78° 49.40′ N 2° 34.11′ W	70+	Repeat of P1, to check pressure sensor again.
12 July P3	1822	78° 50.60′ N 2° 24.79′ W	70+	Second station of transect. 100 – 200 m floe, light snow. Full test of electronics carried out on ice.
17 July PA	0402	79° 09.32′ N 0° 08.18′ E	64	Station carried out at Mini-drift and Toroid site B. Profile obtained in narrow lead with crushed ice.
17 July PB	0434	79° 09.2′ N 0° 08.11′ E	64	Repeat of Station PA
17 July PC	2059	79° 11.92′ N 0° 12.04′ E	62	First station at central site for SPRI 3rd mini-drift. Series not continued due to oil slicks. Adjacent to USGS current meter mooring.

TABLE A.2 Summary of CTD Stations

Station	Time	Position	Depth (m)	Remarks
18 July P1	1000	79° 09.95′ N 0° 10.74′ E	40	Time series of profiles at far side of mini drift floe, strong opposing surface current. Light winds $1-2\,m\,s^{-1}$.
18 July P2	1012	79° 09.90′ N 0° 10.85′ E	40	
18 July P3	1026	79° 09.80′ N 0° 11.03′ E	25	After this profile instrument left at depth in centre of Pycnocline for 45 minute time series.
18 July P4	1421	79° 08.12′ N 0° 10.86′ E	40	Afternoon time series, at same site on floe, visibility improved, hence larger insolation, wide tidal polynya opening up.
18 July P5	1436	79° 08.05′ N 0° 10.36′ E	40	
18 July P6	1453	79° 07.96′ N 0° 10.25′ E	40	
18 July P7	1507	79° 07.88′ N 0° 11.00′ E	25	Instrument left at 25 m depth for 30 minutes.
18 July P8	2012	79° 07.07′ N 0° 12.59′ E	40	Evening station at same site, short outing as tidal polynya had re-closed and the tight pack did not allow redeployment.
18 July P9	2018	79° 07.06′ N 0° 12.69′ E	40	Data recorded on upcast of P8. Spikes from winch stops.
18 July P10	2023	79° 07.05′ N 0° 12.77′ E	20	
18 July P11	2025	79° 07.05′ N 0° 12.80′ E	20	Upcast of P10.
19 July P1	1019	79° 04.32′ N 0° 20.74′ E	30	Cast on far side of closing tidal polynya station taken alongside large kilometre floe from ships boat.
19 July P2	1023	79° 04.32′ N 0° 20.78′ E	50	Continuation of P1 after boat manoeuvring, some overlap.
19 July P3	1029	79° 04.31′ N 0° 20.88′ E	50	Upcast of P1/P2.
19 July P4	1043	79° 04.29′ N 0° 21.19′ E	32	Station among crushed floe pieces at far end of polynya, upwind of ship.
19 July P5	1102	79° 04.26′ N 0° 21.87′ E	32	Profile in narrow lead between floes.
19 July P6	1106	79° 04.25′ N 0° 22.20′ E	32	Upcast stopped in mid-depth due to oil slick.
19 July P7	1116	79° 04.20′ N 0° 22.26′ E	33	Station in loose broken floes.
19 July P8	1120	79° 04.17′ N 0° 22.30′ E	33	Upcast stopped when loose ice piece jammed on wire.

TABLE A.2 Summary of CTD Stations

Station	Time	Position	Depth (m)	Remarks
19 July P9	1542	79° 02.29′ N 0° 26.80′ E	32	Stations in widening polynya. First profile near floes at 70 m from ship.
19 July P10	1547	79° 02.21′ N 0° 26.53′ E	32	Upcast of P9.
19 July P11	1556	79° 02.16′ N 0° 26.57′ E	33	Cast beside 10 m berg in centre of polynya.
19 July P12	1601	79° 02.12′ N 0° 26.60′ E	33	Upcast
19 July p13	1610	79° 02.06′ N 0° 26.67′ E	34	Far side of polynya, 600 m alongside same large floe as in the morning.
19 July P14	1622	79° 01.98′ N 0 ° 26.75′ E	34	Station in open water, 300 m from ship, strong tidal currents.
19 July P15	1627	79° 01.89′ N 0° 26.38′ E	34	Upcast.
19 July P16	1633	79° 01.89′ N 0° 26.18′ E	34	Data gap 20 – 25 m. Open water, 150m from ship, polynya diverging rapidly and hence, boat drifted during profile.
19 July P17	1638	79° 01.85′ N 0° 26.09′ E	34	Upcast.
19 July P18	1644	79° 01.82′ N 0° 26.10′ E	34	Cast ahead of ship alongside pressure ridges on main work floe.
19 July P19	1650	79° 01.77′ N 0° 26.09′ E	34	Upcast
22 July PDA	0314	78° 41.00′ N 1° 21.50′ W	40	Calibration of instrument with Bergen Group Neil Brown CTD Station 326.
22 July PUA	0320	78° 41.00′ N 1° 21.50′ W	40	
22 July PDB	0350	78° 41.00′ N 1° 32.80′ W	36	Calibration with CTD station 327.
22 July PUB	0355	78° 41.00′ N 1° 32.80′ W	36	
20 Aug P1	1711	81° 44.50′ N 18° 52.00′ E	50	Polynya experiment in open water adjacent to ship 4/10 cover, ice too rotten to use as base.
20 Aug P2	1729		50	Downcast.
20 Aug P3	1743		50	Downcast, centre of polynya, boat rotated during profile.
20 Aug P4	1757		50	Occasional manoeuvre, to avoid drifting ice.
20 Aug P5	1812		50	Again manoeuvring to avoid ice
20 Aug P6	1817		50	Upcast, false start. Large movement when fish at 30 m.
20 Aug P7	1826		50	30° upwind of ship.
20 Aug P8	1839		50	Again close alignment with ship.

TABLE A.2 Summary of CTD Stations

Station	Time	Position	Depth (m)	Remarks
20 Aug P9	1853		50	Close to ice at far end of polynya.
20 Aug P10	1923		70	Next polynya just inside connecting channel.
20 Aug P11	1928		70	Returned close to ship, Light fog, Adjacent to very melted crystalline floe.
22 Aug P1	0603	81° 21.08′ N 15° 27.12′ E	70	A series of casts taken from floe. alongside ship. Same position as NP cast 224.
22 Aug P2	0615		70	Upcast halted due to winch spring jam, restarted at 0617
22 Aug P3	0651		70	Down only, air temperature below freezing, heavy snow
22 Aug P4	0714		70	Downcast.
22 Aug P5	1638	80° 47.90′ N 12° 54.00′ E	80+	2 profiles full extent of cable
22 Aug P6	1704		80+	Ship knock against floe jerking wire. Rocking of frame due to uneven surface. Data reasonable despite pulling on connector.
23 Aug P1	0732	80° 36.52′ N 4° 10.95′ E	70	Cloudy, 200 m floe all meltwater refrozen, 5 Down casts At site on far side of floe from ship.
23 Aug P2	0807		70	
23 Aug P3	0841		70	
23 Aug P4	0905		70	
23 Aug P5	0936		70	
23 Aug P6	1627	80° 22.60′ N 1° 30.00′ E	70	1 station in open water before CTD battery dropped below operating freshhold. Connector broke during upcast.
24 Aug P1	1956	80° 49.20′ N 7° 21.00′ W	70	Cross calibration with NP cast 242.
24 Aug P2	2006		70	Upcast.
24 Aug P3	2105	80° 52.60′ N 7° 40.00′ W	70	Second cross-calibration, NP cast 243. Larger wire angle (currents) on this cast.

TABLE A.2 Summary of CTD Stations

Station	Time	Position	Depth (m)	Remarks
25 Aug P1	1156	80° 49.90′ N 8° 47.00′ W	50	2 shallow casts in water of < 90 m. Floe with recently fractured edge and ridge system. Meltwater pools refrozen. Wind 5 m s^{-1}
25 Aug P2	1206		50	Upcast.
25 Aug P3	1215		60	Start delayed by ice pieces near frame.
25 Aug P4	1224		50	Upcast.
26 Aug P1	0702	78° 55.70′ N 5° 30.00′ W	85	6 downcasts. 5 m piece of broken floe often moving threateningly. Ice knocked wire when fish at 70 m.
26 Aug P2	0731		75	Strong wave field, wind 7 m s^{-1}.
26 Aug P3	0758		75	
26 Aug P4	0822		75	Cast stopped for 2 minutes when at 35 m depth, loose ice.
26 Aug P5	0845		70	
26 Aug P6	0916		70	
26 Aug P7	1433	78° 51.00′ N 4° 09.00′ W	70	Far side of floe from ship Interruption due to ship knocking floe, after mooring broke.
26 Aug P8	1505		70	Brash ice interrupted upcast.
26 Aug P9	1805	78° 51.20′ N 3° 27.30′ W	80	Frame unsteady positioned on firn so some jerking of wire. Base weighted to prevent to much harm but this reduced lowering rate
26 Aug P10	1839		80	Ice pieces frequently being broken off floe close to site.
26 Aug P11	1916		80	Cast temporarily halted at 40 m
26 Aug P12	2218	78° 54.60′ N 2° 38.00′ W	50	Floe practically in open water. Warm water intrusion at 16 m.
26 Aug P13	2226		50	Upcast.
26 Aug P14	2233		30	Short cast as wave field breaking over floe beach close to site.
26 Aug P15	2238		30	

TABLE A.2 Summary of CTD Stations

Station	Time	Position	Depth (m)	Remarks
27 Aug P1	0659	79° 07.50′ N 1° 34.20′ W	70	Start of 24 hour station.
27 Aug P2	0751		70	Floe 3 – 4 m thick when observed on approach. Ridges increase this to 6 m.
27 Aug P3	0812		65	
27 Aug P4	0901		65	
27 Aug P5	1331	79° 06.40′ N 1° 38.00′ W	70	8 downcasts to various depths.
27 Aug P6	1358		65	Air temperature below freezing, snow.
27 Aug P7	1506		70	
27 Aug P8	1655	79° 06.20′ N 1° 39.00′ W	70	
27 Aug P9	1731		50	
27 Aug P10	1752		40	
27 Aug P11	1815		50	
27 Aug P12	1840		70	

On Lance, the SatNav information was not logged but a graph plotter recorded details of the ship's track and drift. The positions used in Table A.2 for the station locations were derived principally from the ship's CTD log which is a relatively accurate guide as most ice based stations were either preceded or accompanied by a CTD cast. This position information was normally added to the file header on creation of the Epson HX-20 cassette file. Any gaps in these data were interpolated from the log and drift tracks given in Vinje (1984). All times in the table are GMT, which was the ship operating time zone on Kvitbjørn. Whilst on board Lance, local time was GMT plus 2 hours.

A.4 Microcomputers involved in field processing

The microcomputers/processors used in the field for processing the CTD data, comprised a CDP 1805 processor on the logging electronics board, and an Epson HX-20 microcomputer. The latter served as the control computer and on-ice data processing unit. The Epson micro-cassette system was used as an intermediate storage medium for the data. On board ship, data were transferred from micro-cassette to floppy disc on a 'Torch' microcomputer, where all stages of processing from HEX input data files to graphical output of the CTD profile could be accomplished.

A.4.1 The Logging microprocessor

Only two direct actions can be taken by the operator with respect to the logging electronics. Firstly, the use of the reset switch and secondly, enabling the LOG/REM switch which controls automatic logging. The automatic logging mode was introduced to cover the possibility of Epson internal battery failure at low temperatures. In the event, the automatic logging was a useful addition as it enabled profiles to be stored circumventing the Epson buffering problems which will be described in Section A.4.2. Pausing during automatic logging was achieved by switching into REM mode and depressing the reset switch. The logging of CTD data is controlled by the Epson HX-20 computer through the RS232C interface when the logging switch is in the REM position. Instructions are sent to the processor as single ASCII characters which invoke modules and subroutines in the micro-processor program. The modules which made up this program were written by D. White (Dept. of Earth Sciences) and included facilities for reading, writing, searching and unloading the data buffer at specific locations. The main controlling program for the CTD monitor was composed from a combination of these subroutines in ADVOCET systems 1805 cross assembler. The program was written by T. R. E. Owen and was implemented on the logger electronics board on an EPROM chip (Owen, 1984).

Each individual profile of HEX data records is started with a data and time mark, and ended with a file mark. The data record is interspersed with time marks written at the start of every minute. A pointer is maintained by the monitor which contains the memory location of the next position to which data is to be written (Owen, 1984).

A.4.2 The Epson HX-20 microcomputer

The Epson Hx-20 is a compact microcomputer with 16K RAM internal store. Its portability meant that it was well suited to the task of controlling the logger; additionally it was able to provide an initial scan of the data in the field. It contains a micro-cassette drive, to which data from the logger can be downloaded via the RS232C port. Later transfer to the 'Torch' microcomputer was facilitated by a further program. The time for unloading the data buffer to cassette is governed by the speed of the tape drives and in general takes twice as long as the original recording operation. The heavy power consumption for the transfer operation dictated that it should normally be carried out on-board ship to save battery power.

The main purpose of the Epson logging program was to average data counts as they are received

at the buffer, simultaneously to the data being stored in RAM core. After logging has been completed, the Epson calculates conductivity temperature and depth values and displays the averaged profile. However, in the field this did not work satisfactorily as the Epson RS232 buffer overflowed causing major problems in the logging operation. This event normally occurred after the system had been functioning for several minutes because the rate of removal of the data from the buffer was fractionally slower than the sampling rate. Many attempts were made to solve the problem, involving closure of the port with subsequent data loss as the amount of data in the buffer neared its 256 byte limit. Reductions were also made in the number of operations within the main receiving loop. The solution still proved difficult, possibly due to the fact that the timing of the clocks contained within the two processors were not synchronous. The time available to solve the buffer problem was limited by other 'teething' problems with the whole CTD system, arising during early field operations. Automatic logging once used, proved satisfactory, provided that the HEX data was scanned after every profile.

A.4.3 Torch Microcomputer

The Torch microcomputer was used to convert raw HEX data into frequency values. These data were further processed via calibration algorithms to produce values of conductivity, temperature and depth for each data record. Subsequently, these data were used to derive salinity and density for the profile. Programs also existed on the Torch for plotting data on the screen and dumping it to an Epson FX-80 printer to produce hard copy output. Also several utility programs were available on the microcomputer for calculating calibration curves and density algorithms.

The main problems with handling the data at this stage arose during HEX to frequency conversion. Occurrences when the range setting limits were accidentally crossed, were often misinterpreted by the microcomputer conversion program. No foolproof criterion could be established to eradicate such erroneous points. These errors occurred when there was occasional loss of significant bits in the upper part of the data 'word' during its allocation to the data buffer. These errors are easy to trace and remove in clean data records but in noisy records (section A.6.3), considerable effort is required to edit the hex files to produce a meaningful time series. Occasionally, the data records 'slipped' and data values appeared under incorrect channel headings. Incidences of the above errors occurred in less than 10-15% of the data records.

A.5 Calibration

A formal calibration of the CTD instrument has never been carried out for a number of reasons, viz. urgency of assembly and shipment in the pre-field stage, and instrumental failure and sensor drift by the time the CTD package had returned to Cambridge. The instrument was originally tested in the laboratory to check if it was operating sensibly, though at this stage the instrument was not complete so it could not be totally immersed in seawater. The seawater samples used in the bath ranged in salinity from 22-38 ‰ and in temperature from 5 – 15 ° C. The salinity samples were bottled and the salinities were evaluated using the AutoSal at the Enviromental Science Department, University of East Anglia (courtesy of Prof. P. Liss). Preliminary though inaccurate calibration curves, for use in the field were extrapolated from the data, though sensor drift impaired their longterm service.

The temperature measurements during this pre-field calibration were not made to the same degree of accuracy as those for conductivity samples. Hence, extrapolated values for the temperature calibration curves were less reliable. Also, no tests were made using temperatures close to or below zero at this stage. This is doubly important for the triple point of water (0.01 ° C) is used as the reference temperature in the conversion algorithms, and the range in which field observations of temperature occurred was concentrated about 0 ° C.

Also, at this preparation stage only one trial measurement was conducted at a conductivity within the range experienced in the field (for conductivity is also a function of temperature). This same sample gave a low conductivity ratio measurement in the AutoSal compared to the reference value provided by standard sea water. Hence, it was likely to be a less accurate measurement, and besides was subject to fluctuations. The associated uncertainty in the temperature value for this sample could lead to substantial errors in the pivotal data for this part of the conductivity scale (Section A.6.1). Some of the differences observed between pre-field, shipboard calibration and post-field laboratory results may be explained by the accidental removal of anti-foulant and platinum paint from the electrodes.

In the field, cross-calibrations were carried out between the SPRI CTD and shipboard Neil Brown Mk III CTDs. These calibrations were typically undertaken during the hourly CTD cast, whilst the small boat was sampling alongside or close to the vessel. On two occasions, one on each ship, the instrument platform was set up alongside the main CTD and the two instrument fishes were in the water simultaneously.

Post-calibration of the instrument was not possible due to the breakage of the insulation on one of the thermistors. This led to faulty readings as the probe self-earthed. A large amount of drift in all temperature ranges occurred as a result of the altered resistance of the thermistor combination. Without this temperature sensor operating, a full calibration of the conductivity to obtain salinity was pointless. However, the cell was filled with a standard sea water sample at low (near freezing) temperature to cross check the field calibration measurements, and to see if further drift in the conductivity cell resistance had occurred. Moreover, a reasonable match was found when compared to data from the field period, and to a lesser degree with the earlier samples measured in the laboratory

A.6 Data processing

Stages in the CTD data processing, undertaken first in the field and later in the laboratory, are summarized in the schematic in Figure A.7. Algorithms were formulated to convert each of the data channels from frequency to their dependent variables. These were implemented on all the available data sets (exceptions, Section A.6.5), and the resulting temperatures and conductivities were used to derive salinity and density values using 'practical salinity' algorithms (Fofonoff and Millard, 1983).

Even after the data had passed through the calibration algorithms a considerable amount of processing and de-spiking was necessary to produce a reasonable final set. Segments of data representing either upward movements or temporary halts of the sensors in the water column have to be removed; frequently winch stops will cause spiking and sensor drift. Upward moving sections can often be removed directly (Pingree, 1971), though care must be taken if large sensor mismatch is present. Correction for the time response of the sensors should precede any data removal.

A.6.1 Algorithms

The algorithms were derived from known data points obtained from cross-calibration profiles, and from data values derived from ship-board and land-based laboratory work. The form of the relationship was based on the physics governing the sensor operation. The method involves selecting combinations of points covering the range of field operations and beyond if possible, followed by polynomial fitting. Other data combinations from the set were calculated from these algorithms, and the errors minimized to produce the best algorithm. The higher the order of polynomial expression

FIGURE A.7: Summary diagram indicating the stages involved in the data processing.

used, the greater the number of points of inflexion generated within the range of interest. Therefore, polynomial expressions of order greater than four were discarded as unsuitable for consideration.

1) Pressure

The pressure sensor was supplied from the manufacturer as being 87.5% linear. After electronic conversion of the pressure diaphragm signal to frequency values, the system did not operate in a linear fashion over its entire range. Small quadratic corrections to the pressure algorithm were attempted unsuccessfully. The pressure was calculated using the surface frequency (a function of atmospheric pressure) as a reference. Hence, depth D is given by

$$D = a_1(f_m - f_s) \tag{A.1}$$

where f_m is frequency at depth, f_s is surface frequency and a_1 is a calibration coefficient set at

$$a_1 = 1.7879 \times 10^{-2}\,\mathrm{m\,s} \tag{A.2}$$

2) Temperature

The temperature measured by the thermistors is exponentially related to probe resistance. Calibration equations are normally defined with reference to a given resistance, chosen here to be the triple point of water. The relationship between resistance and frequency output is assumed to be linear. Some controversy exists over the number of terms that should be used in the polynomial expression to convert from resistance to temperature (Bennett, 1972; Steinhart and Hart, 1968;). We have tested all combinations on our data and have found that in this case a second order polynomial provides the most consistent fit (a third order polynomial on occasions produced an additional turning point in the usable range). Hence, the relationship between frequency and absolute temperature (T) is given by

$$1/T - 1/273.15 = a_1 \ln(f_m/f_o) + a_2 \ln^2(f_m/f_o) \tag{A.3}$$

where f_m is the measured frequency and f_o is the frequency at a temperature of 273.15 K. The calibration coefficients a_1 and a_2 are given as

$$\begin{aligned} a_1 &= -7.2971 \times 10^{-4}\,\mathrm{K^{-1}} \\ a_2 &= 2.7640 \times 10^{-3}\,\mathrm{K^{-1}} \end{aligned} \tag{A.4}$$

3) Conductivity

Pederson and Gregg (1979) derived an algorithm to fit the SeaBird sensor based on the assumption that the resistance of the cell is inversely proportional to the square of the measured frequency. Extra terms were added to compensate for the impedanceof the circuitry and temperature effects. Hence, the formula they used for the conductivity (C) (inverse of resistance) was

$$C = \frac{f_m^2}{(a - bf_m^n)^2} + cT^2 \tag{A.5}$$

where f_m is measured frequency, a, b and n are coefficients associated with the circuit impedence, and c is a calibration coefficient to correct for temperature.

In our case, this approach failed due to the amount of leeway available in the choice of the power value n in the denominator. The least squares direct power law fit to the data gave an exponent for the frequency term of 1.8, close to the square law proposed by Pederson and Gregg (1979). Hence, we chose to use a polynomial function of only the frequency value. Both third and fourth order equations produced reasonable values with no inflexion points for the required range of the sensor. Thus the chosen formula for Conductivity C is given by

$$C = a_1 f_m + a_2 f_m^2 + a_3 f_m^3 \tag{A.6}$$

where f_m is measured frequency, and a_1, a_2 and a_3 are calibration coefficients given as

$$\begin{aligned} a_1 &= 3.2315 \times 10^{-2}\,\text{mmho s} \\ a_2 &= -8.5532 \times 10^{-6}\,\text{mmho s}^2 \\ a_3 &= 6.3995 \times 10^{-10}\,\text{mmho s}^3 \end{aligned} \tag{A.7}$$

A.6.2 Sensor mismatch

Sensor mismatch is frequently indicated by spikes in the salinity profile in regions of strong temperature/conductivity gradients. This mismatch is principally related to the effective time lag of the temperature sensor. Most correction formulae absorb the smaller conductivity lag into the temperature adjustment. The time lag is often expressed in exponential form and can be calculated from the temperature gradients using a subjective method (Scarlet, 1975).

Horne and Toole (1980) approached the problem of sensor mismatch by examining the frequency response function of the temperature sensor. Filtering data to correct for mismatch using a

transfer function had previously been undertaken using filter coefficients derived from the differential equation governing the sensor response (Lueck *et al*, 1977). In Horne and Toole's more direct method the frequency response function is used as the correction filter. Moreover, the inclusion of phase terms in the filtering process produced greater improvement when correcting for mismatch in the profile.

Despite the improvement in data quality after correction for temperature lag, both the above methods are dependent on a steady descent rate of the sensor package. In practice the CTD fish descent rate is never constant, especially with our manual winch, and averaging data over depth intervals after ignoring reversed points may be necessary (Horne and Toole, 1980).

A.6.3 Noise

Calculations of the noise level of the instrument sensors can only be attempted in steady operating conditions. Such conditions can be generated in a calibration tank, or at considerable depths in the water column where near constant water properties prevail. As no such suitable data set was available for this purpose an attempt to quantify the instrument noise was made using the time series measured in the pycnocline on the 18th July. This data record was superimposed on a background drift of the temperature and conductivity sensors.

The long term trend could either be removed from the power spectra by filtering the record or alternatively, by leaving the signal to act as a reference amplitude for the significant signal variations. The choice of the cut off point for the spectra is subjective and depends on knowing all the interactive physics in the system. The aim here is to provide some estimate of the tolerance in the data, even after all processing and lag corrections have been included. The noise was determined from the power spectra shown in Figure A.8. The numbers quoted below are defined over a bandwidth of 4.6512×10^{-3} Hz and represent the upper limit of the 95% confidence level for each sensor:-

$$\begin{aligned} \text{Temperature} \quad & 7.665 \times 10^{-6} \,^{\circ}\mathrm{C}^2\,\mathrm{Hz}^{-1} \\ \text{Conductivity} \quad & 2.2 \times 10^{-6} (\mathrm{mmho\,cm}^{-1})^2\,\mathrm{Hz}^{-1} \\ \text{Depth} \quad & 1.752 \times 10^{-3}\,\mathrm{m}^2\mathrm{Hz}^{-1}. \end{aligned} \tag{A.8}$$

The instrument noise level calculated above is an order of magnitude greater than that introduced in the signal by the digitizing process. This least count noise (LCN) is defined for period counting

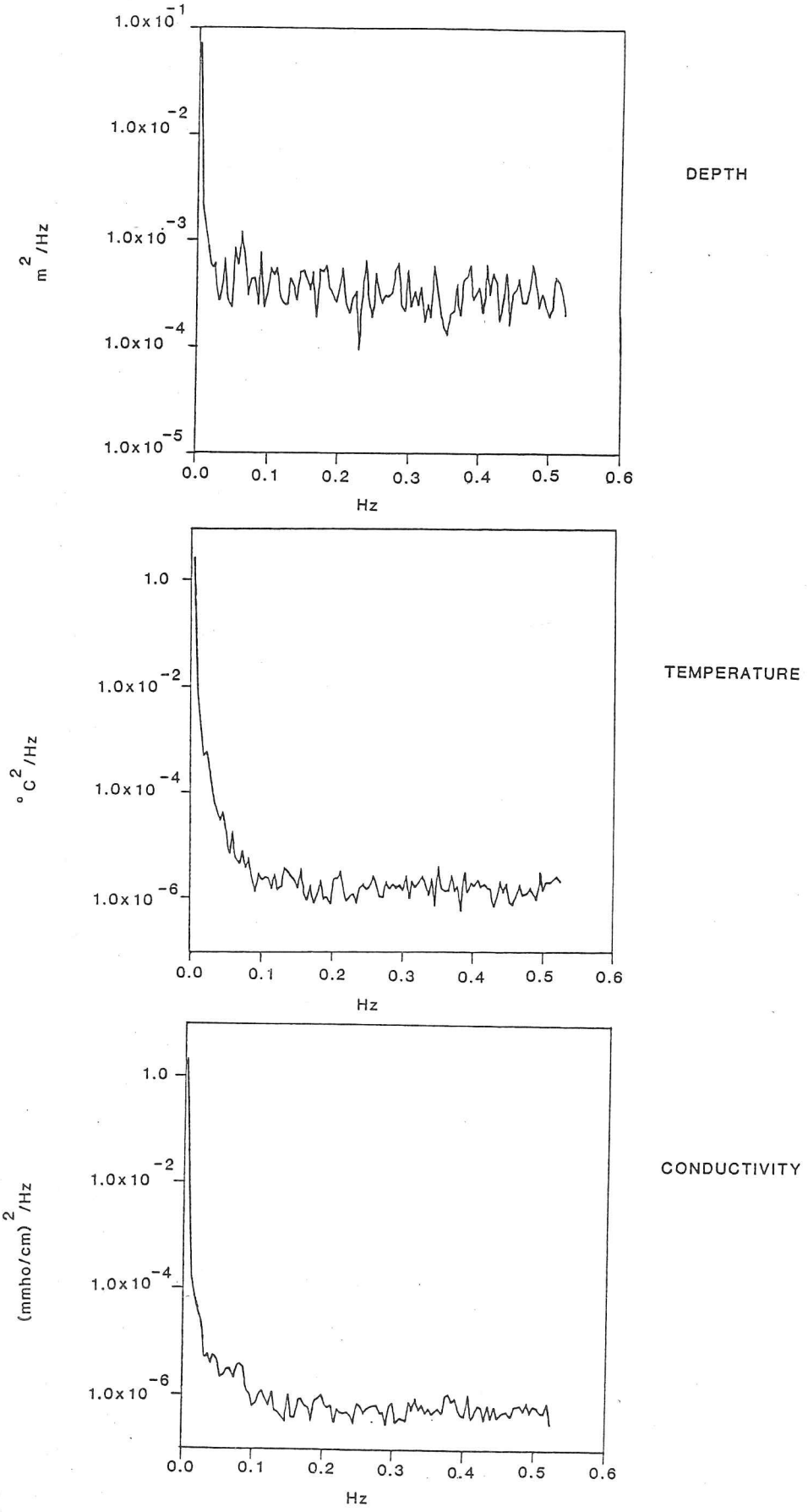

FIGURE A.8: Logarithmic spectra used to determine noise levels of sensors calculated from a time series obtained when the instrument was stationary in the water column.

techniques as

$$LCN = \tau_s \frac{\Delta^2}{6} \tag{A.9}$$

where τ_s is the sampling interval and Δ is the least count resolution (Irish and Levine, 1978). For example, the least count noise for the temperature sensor is $2.1 \times 10^{-9} \circ C^2 Hz^{-1}$.

A.6.4 Filtering

In early stages of the data processing a simple running average filter was used, but as more elaborate techniques were employed to correct for mismatch and despiking it was considered that filtering should be done at a later stage. Spikes can be removed either by assuming that no two consecutive data points are more than a specific distance apart or by the application of a median filter (Sy, 1985). Examination of the density profile after subsequent processing through the algorithms shows that further small scale smoothing may be necessary, but it is arguable at which stage of the processing it is best to carry this out when the highly non-linear calibration algorithms involved are considered.

It may also be necessary to average the data over depth intervals (see Section A.6.2) to produce a better record, removing problems caused by an unsteady lowering rate. Data from later stations were extremely noisy due to self-earthing of the thermistor probe. A large amount of filtering was necessary to extract any useful information from these data, and even then profiles were not smooth, leading to a high degree of uncertainty in the derived quantities.

A.6.5 Data rejection

For a number of reasons a large number of the profiles were of degraded quality, and data had to be rejected from the overall analysis. Problems arose in three main areas

1) In the early stages of the field programme the polarity of the pressure sensor was reversed. This oversight was corrected on 12th July. However, even then the pressure did not span the depth range over which the fish was lowered. Attempts to reverse the algorithms have not been successful in overcoming the problem as the pressure signal itself is noisy. These data may eventually only be utilized by invoking a constant lowering rate. The quality of the remaining channels during this early stage was not high with noise levels an order of magnitude above those measured later in the field season.

2) The sea water connector had to be rewired necessitating the removal of the moulded rubber

protection for the connector. When it was repaired it was not sufficiently robust to withstand the pressures imposed at depth and seawater entered the connector. This initially caused noisy signals, eventually forcing the frequency signals to mix and confusing the logging electronics into counting the signal from the wrong channel. The connector was rebuilt on a number of occasions but never successfully on a longterm basis. Some of the profiles are only affected in this way when the instrument is at depth. Seawater corrosion also affected the battery recharging pin in the connector, reducing the amount of charge stored in the instrument and curtailing some of the outings to the ice to obtain data.

3) The insulation separating the thermistor from the protective steel tubing broke. This caused the sensor to earth in the sea water, and the signal to oscillate around its true value. Table A.3 groups all the profiles taken during the field season and details of any problems associated with any of the data channels.

A.7 Data obtained from instrumental package

All the raw data obtained from the CTD sensors during the two field periods were processed from Hexadecimal period counts to frequencies. Table A.3 indicates that a number of profiles contained errors and these data had to be discarded at this stage. Only profiles which displayed correct pressure signals, contained no evidence of mixing of data channels, or records indicating self-earthing by noisy and intermittent signals will be considered. This data subset was derived principally from stations obtained between the 17th - 22nd July, and 22nd - 23rd August. These data were processed through the algorithms and filtering programs described in Section A.6.

When sufficient stations were undertaken to represent a time series we were able to construct a two-dimensional spatial picture of the upper ocean. Consequently, data from a single profile or say, repeat profiles undertaken for verification will not be included in this group, nor will profiles taken away from the ice edge. On some stations, data were recorded during the upcast of the sensor package in an attempt to expand the data sets in time/position. These data also gave information on how successful the streamlining of the instrument shape was in practice. Inclusion of upcast information adjacent to downcast within a contoured cross-section produced discrepancies in the

TABLE A.3: State of data channels for each profile

Cast Identification	Depth	Temperature	Conductivity	Remarks
6-9 July	Reversed	Jerks,Noisy	Jerks, Noisy	Unexplained changes on all channels.
12 July	Corrected	Noisy	Noisy	Pressure signal still odd. Signals mixing, Seawater in connector.
17-19 July	Good signal	Good signal	Good signal	
22 July	Good signal	Good signal	Inconsistent signal	May have been some contaminant in cell, improved during course of 2 casts.
20 Aug	Good signal	No signal	Good signal	Temperature followed conductivity, seawater in connector.
22 Aug	Good signal	Good signal	Good signal	
23 Aug	Good signal	Good signal	Good signal	
24 Aug	Good signal	Self-earthing	Good signal	Insulation on thermistor broken, probe earthing in sea water.
25 Aug	Good signal	Self-earthing	Good signal	Temperature follows pressure signal when fish is at depth.
26 Aug	Good signal	Self-earthing	Good signal	
27 Aug	Good signal	Self-earthing	Good signal	

vertical position of the density interfaces of the order of 3 m. Such differences were particularly noticeable in the boat stations, with less variability present in the upcast from the more stable ice floe platform. This variability was encountered both on the conductivity and temperature records, creating inverted shifts in the isohalines at several depths. As all data sets demonstrated variation between up and downcast, we will only include the latter in the contoured sections. (Fig A.10-A.14). All sections consist of a minimum of 3 downcast profiles. In addition for comparison we have contoured the data set obtained from 500 m casts utilizing the Neil Brown system on Kvitbjørn (Fig A.9). Note, some of the calibration points for the SPRI CTD were obtained from this data set. (Note, in the text that we refer to stations by numbers whilst in the plots we have used station times in an attempt to allow the contoured sections to better represent the spatial picture. This is based on the assumption that the ice is drifting at constant speed, $25 - 50\,\mathrm{cm\,s^{-1}}$.)

Kvitbjørn

The data set obtained on the 18th of July was taken in three separate sessions at a station located on the edge of a large (1 km) ice floe to which the ship was anchored for the 3 day mini-drift experiment. The first two data gathering periods occurred at the same site located at the furthest point from the ship to prevent possible fouling of the surface water. During the third period, data were collected closer to the vessel as the original site was now surrounded by closely packed ice.

Hourly shipboard sampling with Kvitbjørn's Neil Brown sensor indicated that the isohalines were almost horizontal over a 10 hour period, particularly those below 20 m depth, (equivalent to the 33.0 ‰ surface) (Figure A.9). Although at these temperatures the stratification of the water column is dominated by the salinity value, there is some evidence from the temperature distribution of dynamical changes. Examination of the data indicates slightly warmer surface water upto the station occurring at 1608. Also, in the early evening stations an intrusion of warm Atlantic water (> 2.0) was found below 70 m depth.

In order to obtain greater spatial and temporal coverage we did not operate the SPRI CTD to the full extent of the 90 m+ wire. Therefore, we did not detect this warm water intrusion (Figure A.10). However, a warm water tongue present in stations NB 271-274 (NB indicates a Neil Brown cast), with a core at $35 - 40$ m is seen in the Mini-CTD profiles at the same depth, and with an anomaly of equal magnitude for stations (S1, S2) obtained in the morning. During the early part of the afternoon session a weakened signal of this intrusion was detected. Overriding this warm

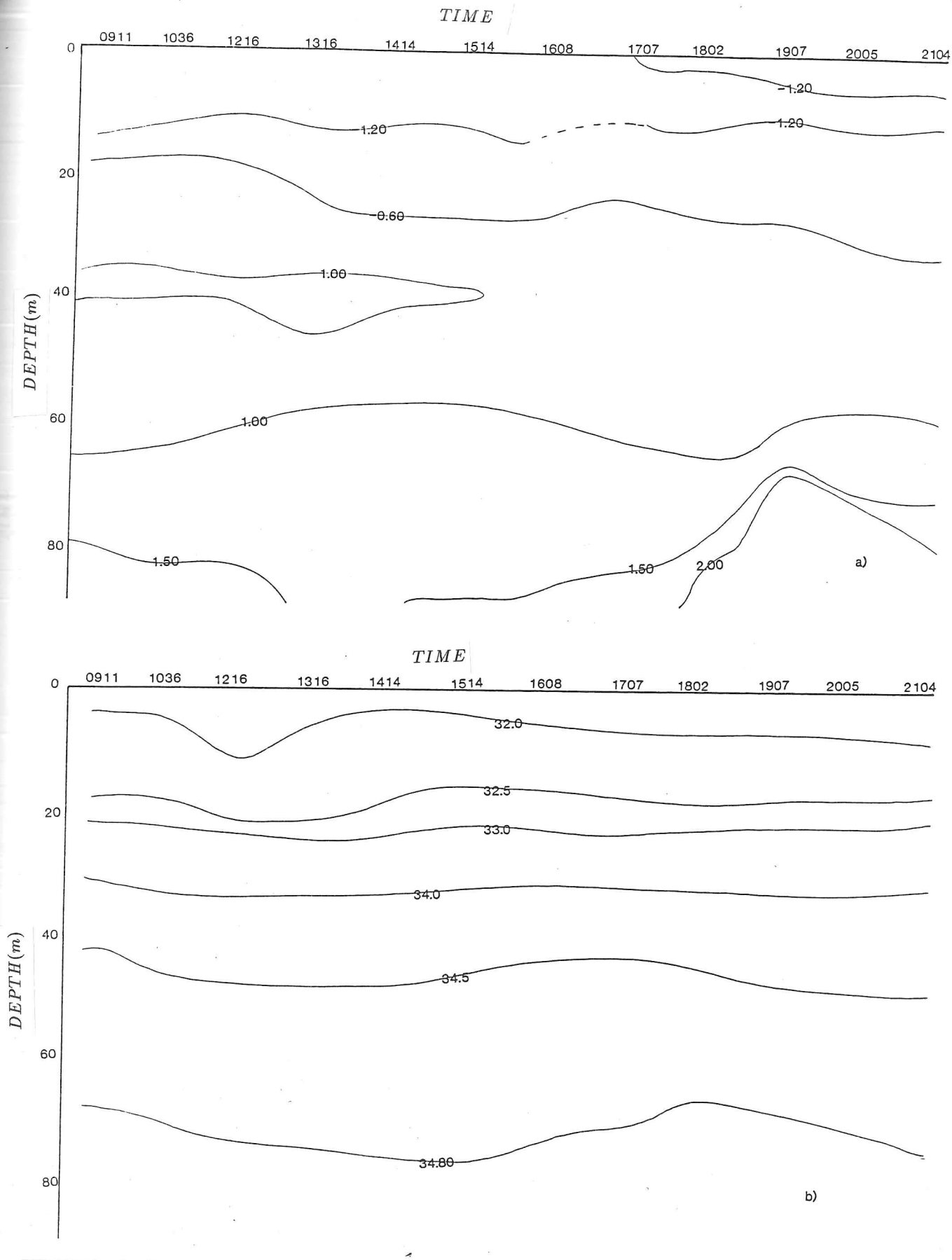

Figure A.9: a) Temperature, b) Salinity time series measured with Neil Brown CTD from Kvitbjørn on 18th July 1984.

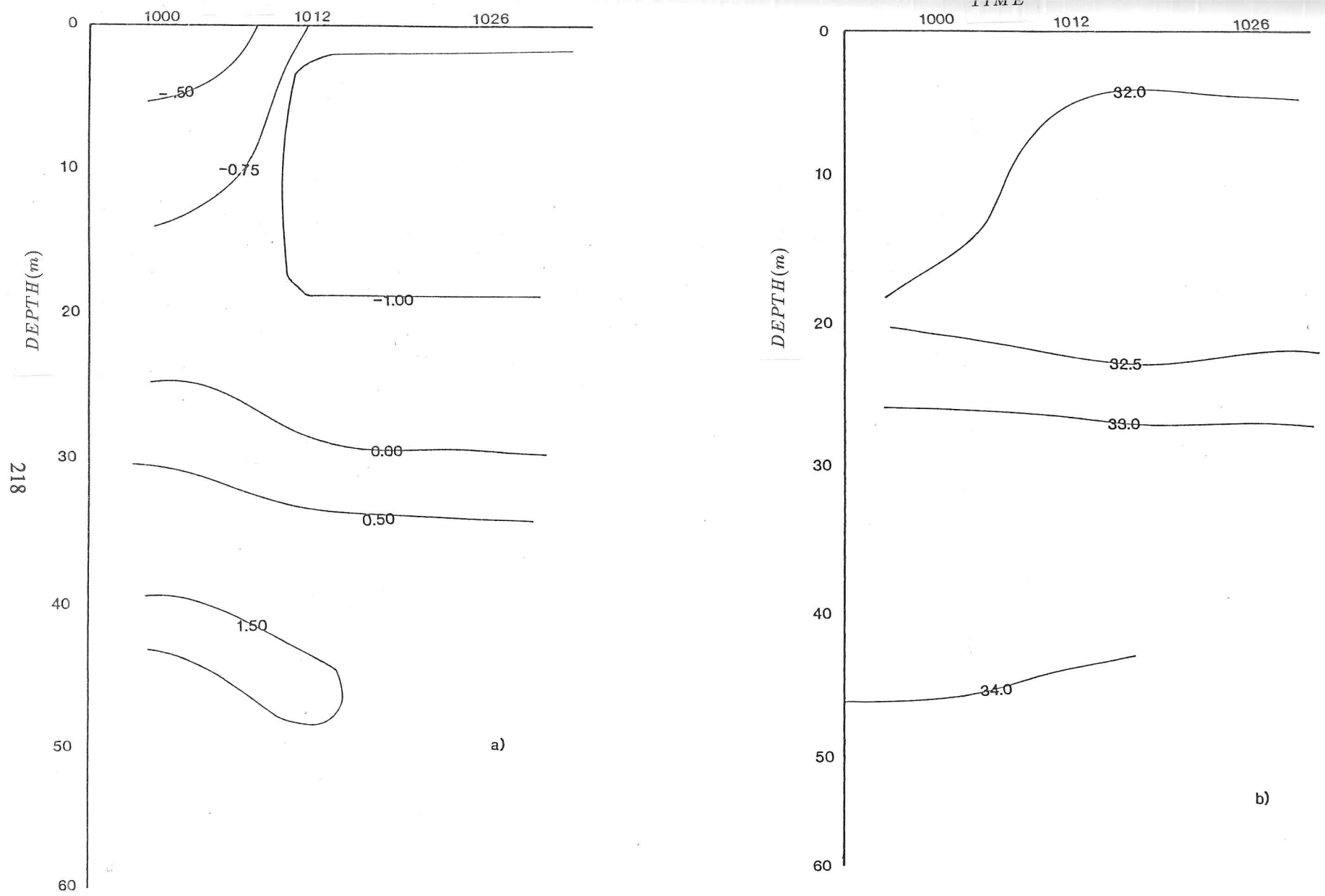

Figure A.10: a) Temperature, b) salinity sections derived from SPRI CTD measurements (stations S1-S3) obtained from the side of an ice floe on 18th July 1984 at 79° 09′ N 0° 11′ E.

tongue was a cooler water mass located at stations S4 and S5 between 20 – 30 m depth (Figure A.11). On this occasion, however, the values given by the two CTDs for the minimum temperature in this water mass disagreed by 0.4 ° C.

This discrepency is attributed to calibration error. Unfortunately, small shifts in the frequency allocated to the triple point of water about which the temperature algorithm is pivoted (equation A.3) produce significant changes when temperature values are close to 0 ° C, i.e., the range in which we are focussing. In particular, no non-physical value less than the sea-water freezing point (−1.8 ° C) can be assigned through errors in the algorithm. Moreover, the minimum temperature region of the profile was prone to considerable noise levels and frequent spiking of the record. Numerous isolated data spikes were removed from such records by single point methods before filtering (sec A.6.4). However, some influence of extreme values may still be present in the final profiles. Grouping the data over 0.5 m depth intervals could lead to gaps in the data about the temperature minimum region of the profile. As a point of interest, the temperature minimum region was not normally coincident with the strongest temperature gradient so the cause of prominent spikes, some representing changes in frequency of 1 kHz, is uncertain. However, there is no indication of the spikes being derived from the sensor electronics.

Turning now to the salinity measurements below 15 m, we were able to confirm with the Mini-CTD the near horizontal isohaline distribution measured by the Neil Brown time series. Maximum variations encountered in the contoured surfaces ranged from 5 – 10 m. The possibility of some upwelling in the region was raised by observing the doming of the surface isohalines obtained in the section of stations S4-S7 during the afternoon of the 18th July. Some confirmation of this effect is present in the Neil Brown station obtained at approximately the same time (NB275).

A noted feature of the temperature/salinity sections is the difference between adjacent profiles of the Mini-CTD with anomalous warm temperatures encountered when the sensors first entered the sea water. As salinity is a function of temperature and conductivity, anomalously low salinity measurements also occur on the first cast of each series. This observation suggests that the thermistor assembly took some time to adjust to new surroundings. This time interval was considerably more that the manufacturers quoted time response, and was also longer than the response used when correcting for sensor mismatch. In between stations the package was not removed the water, but left with the conductivity sensors partially emersed and the thermistors totally emersed. The signal for the start of the new profile was the first intelligible signal from the conductivity sensor

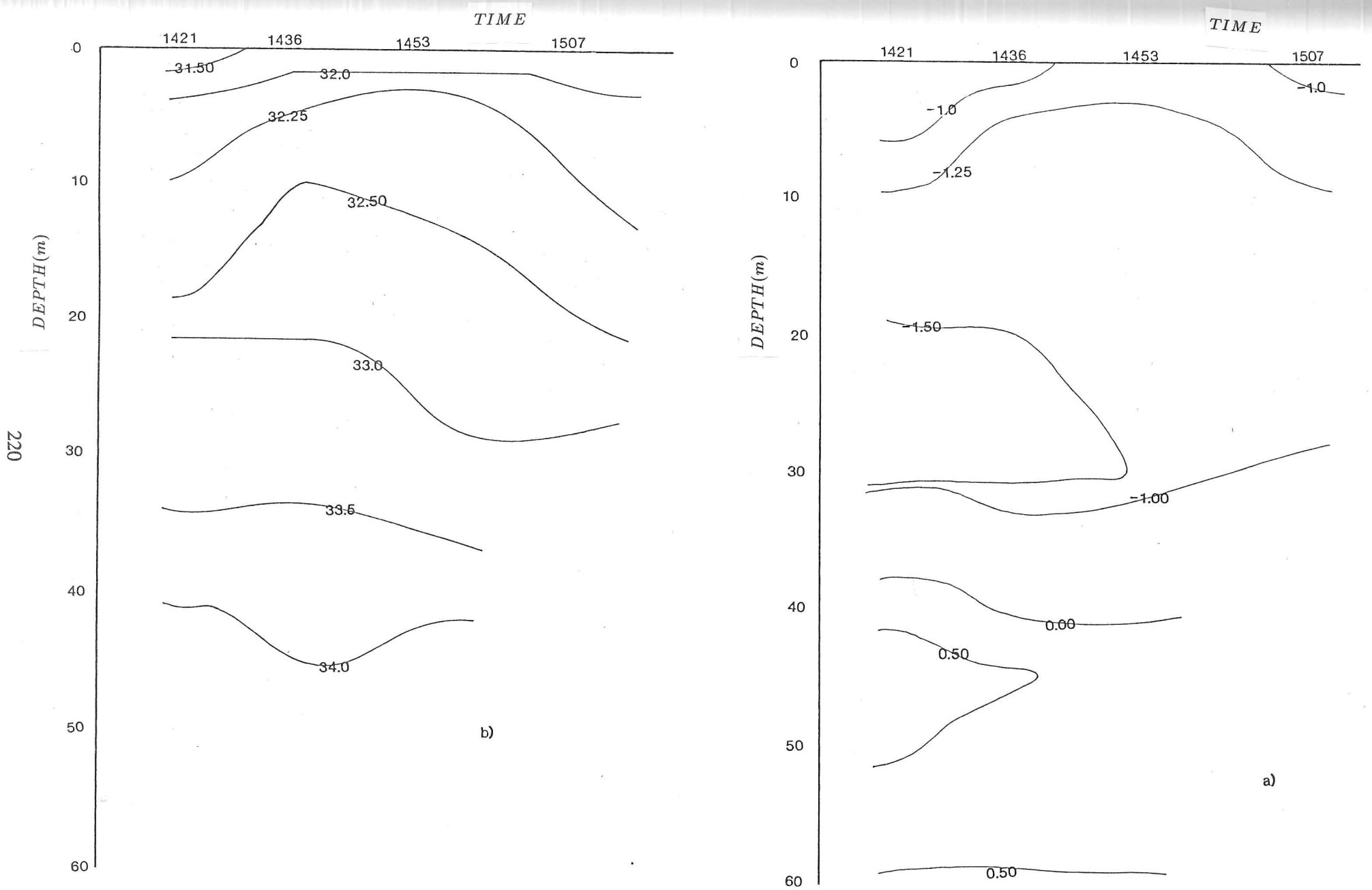

Figure A.11: a) Temperature, b) salinity sections derived from SPRI CTD measurements (stations S4-S7) obtained from the side of an ice floe on 18th July 1984 at 79° 08′N 0° 10′E.

after complete emersion. Little improvement in the anomalous low salinities was observed when a pre-selected pressure value was chosen to mark the surface position.

At the end of each group of profiles the CTD fish was left in the pycnocline allowing the remaining 30-45 minutes of data storage to be used to collect time series at a given depth. These records were disappointing, showing little evidence of any significant pycnocline disturbance. Despite drift in the values recorded for temperature and salinity, the calculated density time series remained almost constant at $26.94 \pm 0.03\ \sigma_t$.

Data obtained on the 19th July were collected using the ships boat from stations in an opening in the pack ice caused by tidal currents. In order to undertake this section the instrument package and frame were mounted in the stern of the boat. During profiling operations the boat was either tethered to a floe or left with motor switched off in the tidal stream ($0.5 - 1.0\,\mathrm{m\,s^{-1}}$). During transportation by boat between stations the sensor package was removed from the water. Hence, we would expect the adjustment of the thermistor package discussed above to occur at every station, but oddly the strongest anomaly still occurred on the first cast. The stability of the ships boat as a sensor platform is poor so we would expect a significant increase in data spiking. On this occasion this was not a serious problem as any spikes that occurred could be removed by single point techniques. However, the disparity in values calculated between up and down casts increased. The Neil Brown CTD indicated that there was no strong frontal regime present at any significant depth which compared well with our data (Figure A.12). Isolated low salinity data values recorded by the instrument could be due to the slowness of thermistor response or to a failure to correctly mark total emersion of the conductivity cell. However, examination of Neil Brown station NB299 suggests that the isohalines do approach the surface, so some of the localized measurements of low salinities may represent a recently mixed melt water input.

Lance

Though several attempts to obtain data in lead areas were undertaken from Lance most of the data which are of sufficient quality to be included in this section were obtained from stations when the instrumentation was located on ice floes. Early on in the cruise, two days in particular produced successful casts (22nd and 23rd August). Temperatures measured in the upper ocean during this period were considerably higher than in July, principally due to the presence of a warm core of Atlantic water. On one occasion, this water mass was detected by the ship's CTD to be as close

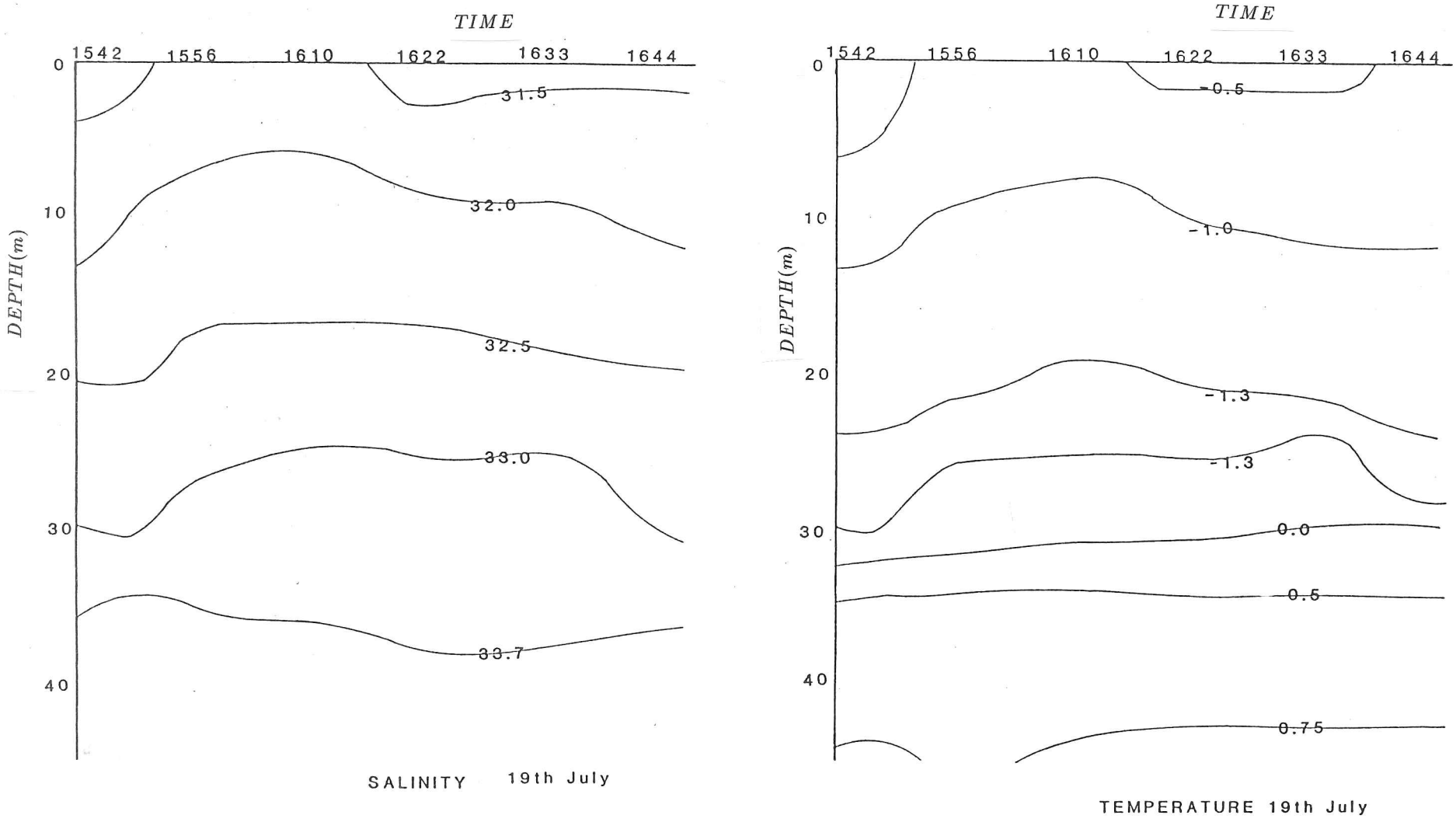

Figure A.12: a) Temperature, b) salinity sections derived from SPRI CTD measurements (stations S9-S19) obtained from a lead using the ships boat on 19th July 1984 at 79° 04′N 0° 22′ E.

as 16 m to the surface. During the cruise, the ice pack was much more dispersed than observed in Fram Strait during the MIZEX experiment. Hence, the Lance was allowed an easy passage across the East Greenland current to the coast including the completion of a long section at 82.0 ° N. Little evidence of sea water freezing was evident during this section with most floes in a late stage of summer melt.

Despite the 4 week gap between gathering data sections, the same calibration algorithms used on Kvitbjørn have had to be invoked. Unfortunately, cross-calibration of instruments occurred immediately after a major problem developed within the instrument causing the self-earthing of the thermistor probes. Hence, it did not provide a useful guide as to how the instrument had drifted over the intervening period. Spot measurements in the laboratory when no self-earthing of the thermistors occurred were made with air temperatures ranging between 6 – 14 ° C. These measurements proved consistent with the earlier algorithms and with earlier room temperature measurements made on board Kvitbjørn.

Five downcast stations were recorded from a single floe on the morning of 23rd August. The instrument package was mounted on the far side of the floe from the ship to minimize frequent data jerks which occurred when the ship knocked against the floe. The third station in the series shows evidence of isopycnal disturbance both near the surface and in the Atlantic layer. A small front appeared to be developing in the surface 5 m. Atlantic water (> 3.0 ° C, 34.85 ‰) was present below 40 m and obviously has a strong influence on the thermal properties of the overriding water mass due to entrainment processes (Figure A.13).

The above data suggest that the dominant influence on the upper ocean structure at this time was the proximity of the Atlantic water mass. There are, however, examples where the density structure of the surface waters was still dependent on local ice concentration and atmospheric heat transfer. On the morning of the 22nd August three downcasts were obtained from a floe where all the surface meltwater had refrozen (Figure A.14). During the casts the air temperature was below freezing and there was driving snow. Hence, this density section was similar to that observed by Kvitbjørn with minimum surface salinities of 31.5 ‰ measured in a temperature range of -0.5 to 1.0 ° C. Beneath this layer was a cold tongue with a minimum temperature of −1.64 ° C measured at 27 m depth. The water beneath is virtually isohaline. However, there is a continuous gradient of temperature with depth until the boundary of the Atlantic core is measured at 75 m.

In similar manner to the Kvitbjørn stations we find that the first cast in each section (Figure

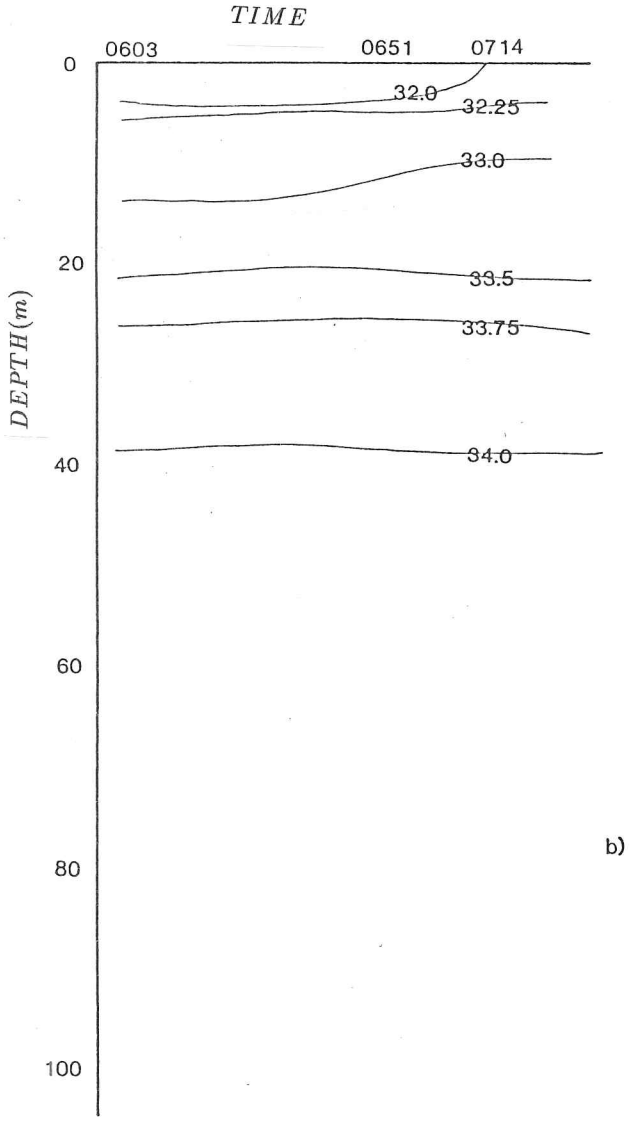

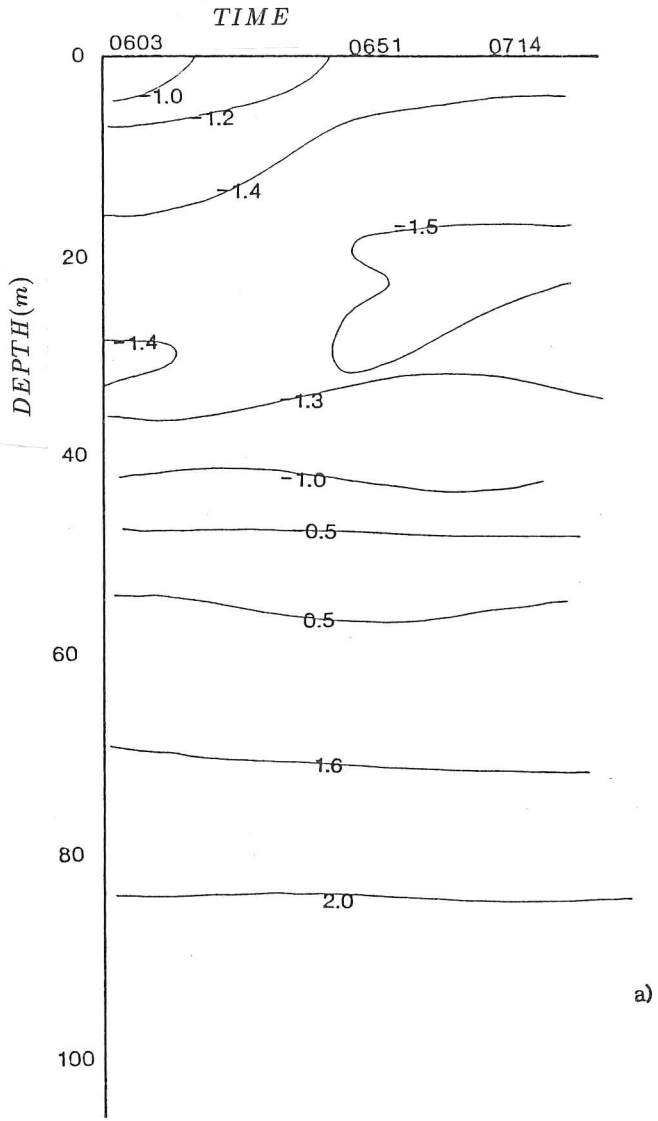

Figure A.13: a) Temperature, b) salinity sections derived from SPRI CTD measurements (stations S1-S5) obtained from the side of an ice floe on 22nd August 1984 at 81° 21′N 15° 27′ E.

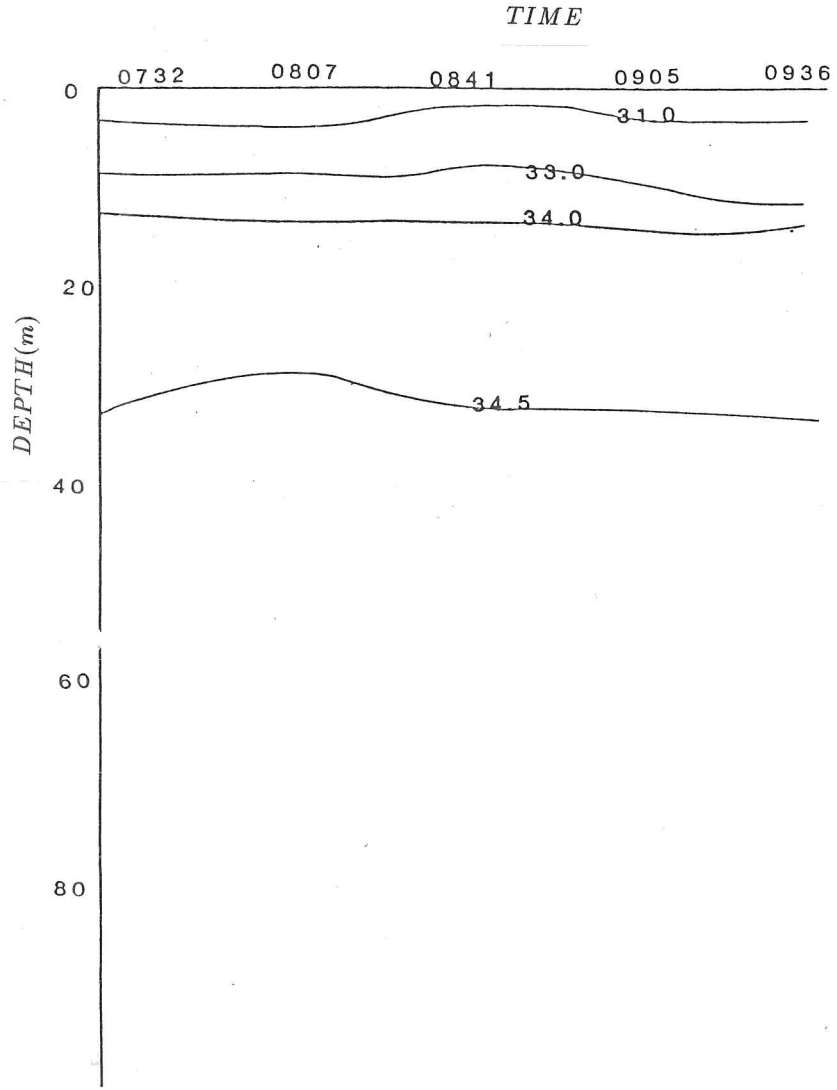

SALINITY

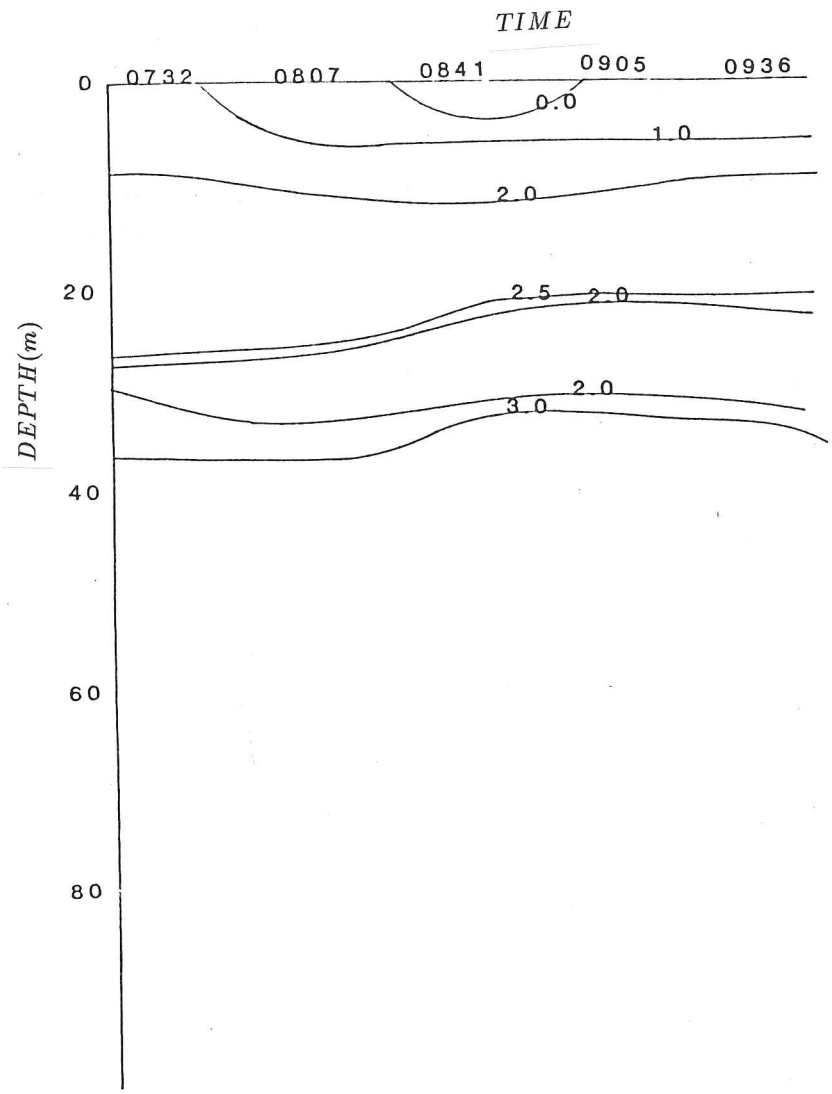

TEMPERATURE 23rd August

Figure A.14: a) Temperature, b) salinity sections derived from SPRI CTD measurements (stations S1, S3, S4) obtained from the side of an ice floe on 23rd August 1984 at 80° 22′N 01° 30′ E.

A.13-A.14) displays water temperatures several 10ths of a degree warmer than the adjacent casts. After disregarding this artefact, there is still some evidence of a frontal zone between stations S4 and S5 obtained on the 22nd August. The 32.00 ‰ isohaline breaks surface between these two stations and there is a sub-surface signature of a cool tongue beneath this feature.

Summary

Despite the numerous problems with the instrument package and sea-water connector we were able to collect some useful data. However, these data did not enable us to meet our objectives, partly because we did not meet either ideal boundary layer or surface melt water fronts in the conditions of summer 1984. We also had no control over the length and position of stations within the larger scale cruise plans. Despite teething troubles, we have proved the ability of the instrument to measure to reasonably high resolution away from ship/helicopter. Recent advances in micro-technology would influence the design of a second generation instrument, both as far as data storage and processing in real time were concerned.

References

AAGAARD, K. and L. K. COACHMAN, 1975, Toward an ice free Arctic ocean. *EOS*, 56, 484-486.

AAGAARD, K. and P. GRIESMAN, 1975, Towards new mass and heat budgets for the Arctic ocean. *J. Geophys. Res.*, 80, 3821-3827.

AAGAARD, K., L. K. COACHMAN and E. CARMACK, 1981, On the halocline of the Arctic ocean. *Deep Sea Res.*, 28(6) 529-545.

ACKLEY, S. J. and S. J. SMITH, 1983, Report of the US-USSR Weddell polynya expedition, October-November, 1981. Vol 5 : sea ice. CRREL Special Report 83-2 Hanover, N.H.

ADAMEC, D., R. L. ELSBERRY, R. W. GARWOOD Jr., and R. L. HANEY, 1981, An embedded mixed layer ocean circulation model. *Dyn. Atmos. Oceans.*, 3, 69-96.

ALEXANDER, R. C. and J. W. KIM, 1976, Diagnostic model study of mixed layer depths in the summer North Pacific. *J. Phys. Oceanogr.*, 6, 293-8.

ALEXANDER, V. and H. J. NIEBAUER, 1981, Oceanography of the eastern Bering sea ice edge zone in spring. *Liminol. Oceanogr.*, 26, 1111-1125.

AUGSTEIN, E., 1987, The winter expedition of RV Polarstern to the Antarctic. *Reports on Polar Res.*, Alfred Wegner Institute for Marine and Polar Research, 71-114.

BAUER, E., K. HUNKINS and A. AMOS, 1977, STDs in AIDJEX: Simultaneous daily CTD casts at four ice stations over one year. Proc 4th Plessey CTD Conf., 1977, San Diego, Calif.

BAUER, J. and S. MARTIN, 1980, Field observations of the Bering sea ice edge properties during March 1979. *Mon. Wea. Rev.*, 108, 2045-2056.

BENNETT, A. J., 1972, The calibration of thermistors over the range 0 – 30 °C. *Deep Sea Res.*, 19, 157-163.

BERSCH, M. and G. A. BECKER, 1984, Upper layer thermal structure in the Atlantic sector of the Southern ocean. *Dt. Hydrogr. Z.*, 37, 71-86.

BOOK, D. L., J. P. BORIS and K. HAIN, 1975, Flux corrected transport II. Generalization of the method. *J. Comput. Phys.*, 18, 248-283.

BRATCHIE, I. L., 1984, Modelling sea ice floe fields. Phd. Thesis, University of Cambridge.

BROWER, W. A., H. F. DIAZ and A. S. PRECHTEL, 1977, Climatic atlas of the outer continental shelf waters and coastal regions of Alaska. Vol. 2 Bering Sea. NOAA.

BRYAN, K. and M. D. COX, 1968, A non-linear model of an ocean driven by wind and differential heating. Part 1 : Description of the three dimensional velocity and density fields. *J. of Atmos. Sci.*, 25, 945-967.

BRYAN, K., 1969, A numerical method for the study of the circulation of the world ocean. *J. of Comp. Phys.*, 4, 347-376.

BRYDEN, H. L., 1979, Poleward heat flux and conversion of available potential energy in Drake Passage. *J. Mar. Res.*, 37, 1-22.

BRYDEN, H. L., D. HALPERN and R. D. PILLSBURY, 1980, Importance of eddy heat flux in a heat budget for Oregon coastal waters. *J. Geophys. Res.*, 85, 6649-6653.

BUCKLEY, J. R., T. GAMMELSRØD, J. A. JOHANNESSEN, O. M. JOHANNESSEN and L. P. RØED, 1979, Upwelling: Oceanic structure at the ice edge of the Arctic pack ice in winter. *Science*, 203, 165-167.

BUDYKO, M. I., 1969, The effect of solar radiation variation on the climate of the earth. *Tellus*, 21, 611-619.

CAMERLENGO, A, L, and J. J. O'BRIEN, 1980, Open boundary conditions in Rotating fluids. *J. Comput. Phys.*, 35, 12-35.

CAMPBELL, W., 1965, The wind driven circulation of ice in a polar ocean. *J. Geophys. Res.*, 70, 3279-3301.

CARMACK, E. C. and K. AAGAARD, 1973, On the deep water of the Greenland Sea. *Deep Sea Res.*, 20, 687-715.

CARSEY, F. D., B. HOLT, S. MARTIN, L. MCNUTT, D. A. ROTHROCK, V. A. SQUIRE and W. F. WEEKS, 1986, Weddell-Scotia Sea marginal ice zone observations from Space, October 1984. *J. Geophys. Res.*, 91(C3), 3920-3924.

CHAPMAN, D. C., 1985, Numerical treatment of cross-shelf open boundaries in a barotropic coastal ocean model. *J. Phys. Oceanogr.*, 15, 1060-1075.

CLARKE, A. J., 1978, On wind driven quasi-geostrophic water movement near fast ice edges. *Deep Sea Res.*, 25, 41-51.

CLIMATOLOGICAL DATA ALASKA, 1983, Vol 69. National Oceanic and Atmospheric Administration.

COACHMAN, L. K., 1982, Flow convergence over a broad flat continental shelf. *Cont. Shelf Res.*, 1, 1-14.

COACHMAN, L. K. and C. A. BARNES, 1963, The movement of Atlantic water in the Arctic ocean. *Arctic*, 16, 8-16.

COACHMAN, L. K. and K. AAGAARD, 1974, Physical oceanography of Arctic and sub-Arctic seas: *in* Marine Geology and Oceanography of Arctic Seas. ed. Y. Herman. Springer-Verlag, New York, pp 1-72.

COACHMAN, L. K. and J. J. WALSH, 1981, A diffusion model of cross-shelf exchange of nutrients in the southeast Bering Sea. *Deep Sea Res.*, 28, 819-846.

COWAN, A. M. and K. A. ULBRICHT, 1984, Observations and study of ice edge eddy dynamics in the East Greenland as seen from satellite. 18th International symposium on remote sensing of Environment. Paris, October 1984.

CSNADY, G. T., 1978, Wind effects on surface to bottom fronts. *J. Geophys. Res.*, 83(C9), 4633-4640.

CSNADY, G. T., 1984, The influence of wind stress and river runoff on a shelf sea front. *J. Phys. Oceanogr.*, 14, 1383-1392.

DEFANT, A., 1961, Physical Oceanography. Vol 1, Pergamon, 727pp.

DENMAN, K. L. and M. MIYAKE, 1973, Upper layer modification at ocean station Papa: observations and simulations. *J. Phys. Oceanogr.*, 3, 185-196.

EKMAN, V. W., 1905, On dead-water in Norwegian North-Polar Expedition 1893-6, Scientific results vol 5, ed. F. Nansen, 152pp, Longman.

FARMER, D. M., 1975, Penetrative convection in the absence of mean shear. *Quart. J. R. Met. Soc.*, 101, 869-91.

FLAGG, C. N. and R. C. BEARDSLEY, 1978, On the stability of the shelf water/slope water front south of New England. *J. Geophys. Res.*, 83, 4623-4631.

FOFONOFF, N. P., and R. C. MILLARD Jr., 1983, Algorithms for computation of fundamental properties of seawater. UNESCO Tech. papers in Mar. Sci. 44, UNESCO, Paris.

GAMMELSRØD, T., M. MORK and L. P. RØED, 1975, Upwelling possibilities at an ice edge, homogeneous model. *Mar. Sci. Comm.*, 1, 115-145.

GARRISON, G. R. and E. A. PENCE, 1973, Studies in the marginal ice zone of the Chukchi and Beaufort seas. A report on project MIZPAC-71B, Applied Physics Laboratory, University of Washington.

GARVINE, R. W., 1974, Dynamics of small scale oceanic fronts. *J. Phys. Oceanogr.*, 4, 557-569.

GARVINE, R. W., 1979, An integral hydrodynamic model of the upper ocean frontal dynamics. Part I Development and analysis. *J. Phys. Oceanogr.*, 9, 1-18.

GASKILL, H. G., R. J. LOPEZ and G. E. SWATERS, 1980, Free drift of sea ice: A comparison of models. C-CORE Technical report. 80-16. 132pp.

GEORGI, D. T. and A. R. PIOLA, 1981, Winter hydrographic observations from the south-western Atlantic, the northwestern Scotia sea and the Drake Passage. *Antarctic Journal of the U.S.*, 16, 103-5

GILL, A. E. and J. S. TURNER, 1975, A comparison of seasonal thermocline models with observation. *Deep Sea Res.*, 23, 391-401.

GRAHAM, G. P., 1978, Fine structure, fronts and currents in the Pacific marginal ice zone. MIZPAC 77 Tech. Rep. NPS. 68-78000, Naval Postgrad. School. Monterey.

GREGG, M. C. and W. C. HESS, 1985, Dynamic response calibration of Sea-Bird temperature and conductivity probes. *J. Atmos. Ocean. Tech.*, 2, 304-313.

GRIFFITHS, R. W. and P. F. LINDEN, 1981, The stability of buoyancy-driven coastal currents. *Dyn. Atmos. Oceans*, 5, 281-306.

HACHMEISTER, L. E. and R. D. MUENCH, 1981, Interactions between internal waves and ice bands in the marginal ice zone. *EOS*, 62, 895.

HAKKINEN, S., 1984, Dynamics of the coupled ice-ocean system in the marginal ice zone: Study of the mesoscale process and of constitutive equations for sea ice. Mesoscale Air-Sea Interaction group. Florida State University, Tech rep., 95pp.

HAKKINEN, S., 1986, Ice banding as a response of the coupled ice ocean system to temporarally varying winds. *J. Geophys. Res.*, 91(C4), 5047-5053.

HAMILTON, P. and M. RATTRAY, Jr., 1978, A numerical model of the depth dependant wind driven upwelling circulation on a continental shelf. *J. Phys. Oceanogr.*, 8, 437-457.

HARTREE, D. R., 1952, Numerical analysis. Oxford University Press.

HASSELMAN, K., 1979, Linear statistical models. *Dyn. Atmos. Ocean*, 3, 501-521.

HASTINGS, J. R., 1976, A single layer hydrodynamic numerical model of the eastern Bering Sea shelf. *Mar. Sci. Comm.*, 2, 335-356.

HASTENRATH, S., 1982, On meridional heat transport in the world ocean. *J. Phys. Oceanogr.*, 12, 922-927.

HENDRICKS, P. J., R. D. MUENCH and G. R. STEGAN, 1985, A heat balance for the Bering Sea ice edge. *J. Phys. Oceanogr.*, 15, 1747-1758.

HERMAN, G. F., 1984, The interaction of sea ice and climate as inferred from global circulation models. In Report of the meeting of experts on sea ice and climate modelling. WMO. Joint planning staff for WCRP, Geneva. Appendix C, 24pp.

HIBLER, W. D. III, 1979 A dynamic thermodynamic sea ice model. *J. Phys. Oceanogr.*, 9, 815-846.

HIBLER, W. D. III, 1980, Modelling a variable thickness sea ice cover. *Mon. Wea. Rev.*, 108(12), 1943-1973.

HIBLER, W. D. III, 1984a, The role of sea ice dynamics in modelling CO_2 increases. *in* Climate processes and climate sensitivity, ed. J.E HANSEN and T. TAKAHASHI, American Geophysical Union, Washington D. C., pp 238-253.

HIBLER, W. D. III, 1984b, Ice dynamics, Cold Regions Research and Engineering Laboratory, Monograph 84-3.

HIBLER, W. D. III and K. BRYAN, 1984, Ocean circulation: its effect on seasonal sea ice simulations. *Science*, 224, 489-492.

HORNE, E. P. W., and J. M. TOOLE, 1980, Sensor response mismatch and lag corrections techniques for temperature-salinity profilers. *J. Phys. Oceanogr.*, 10, 1122-1130.

HSUEH, Y and B. CUSHMAN ROISIN, 1983, On the formation of surface to bottom fronts over steep topography. *J. Geophys. Res.*, 88(C1) 743-750.

HUNKINS, K., 1980, Review of the AIDJEX oceanographic program. *in* Sea ice processes and models, ed. R. S. Pritchard. University of Washington Press.

HUPPERT, H. E. and E. G. JOSBERGER, 1980, The melting of ice in cold stratified water. *J. Phys. Oceanogr.*, 10, 953-960.

IKEDA, M., 1985, A coupled ice-ocean model of a wind driven coastal flow. *J. Geophys. Res.*, 90(C5), 9115-9128.

IKEDA, M., 1986, A mixed layer beneath melting sea ice in the Marginal ice zone using a one-dimensional turbulence closure model *J. of Geophys. Res.*, 91(C4), 5054-5060.

IRISH, J. D. and M. D. LEVINE, 1978, Digitizing error from period and frequency counting techniques. *Deep Sea Res.*, 25, 211-219.

IVANOV, V. V., 1975, Water balance and water resources of Arctic lands. *Tr. Arkt. Antarkt. Naucho. Issled. Inst.*, 323, 4-25.

IVERSON, R. L., T. E. WHITLEDGE and J. J. GOERING, 1979, Chlorophyll and nitrate finestructure in the south eastern Bering sea shelf break front. *Nature* Lond., 281, 664-660.

JACOBS, S. S., 1984, Oceanographic evidence for land ice/ocean interactions in the southern oceans. *in* GLaciers, Ice sheets and sea-level: Effect of a CO_2 induced climatic change, p 116-128. Report of Workshop Seattle Sept. 1984.

JAMES, I. D., 1984, Three dimensional numerical shelf sea model with variable eddy viscosity and diffusivity. *Cont. Shelf Res.* 3(1), 1984, 69-98.

JOHANNESSEN, O. M. and L. A. FOSTER, 1978, A note on the topographically controlled oceanic polar front in the Barents sea. *J. Geophys. Res.*, 83, 4567-4571.

JOHANNESSEN, O. M., J. A. JOHANNESSEN, J. MORRISON, B. A. FARRELLY and E. A. S. SVENDSON, 1983, Oceanographic conditions in the marginal ice zone north of Svalbard in early fall 1979 with an emphasis on mesoscale processes. *J. Geophys. Res.*, 88, 2755-2769.

JOHANNESSEN, J. A., O. M. JOHANNESSEN, E. SVENDSON, R. SCHUCHMAN, T. MANLEY, W. J. CAMPBELL, E. G. JOSBERGER, S. SANDVEN, J. C. GASCARD, T. OLAUSSEN, K. DAVIDSON, and J. VAN LEER., 1987, Mesoscale eddies in the Fram Strait Marginal ice zone during the 1983 and 1984 Marginal Ice Zone Experiments, *J. Geophys. Res.*, 92, 6754-6772.

JOSBERGER, E. G. and S. MARTIN, 1981, A laboratory and theoretical study of the boundary layer adjacent to a vertical melting ice wall in salt water. *J. Fluid Mech.*, 111, 439-473.

JOSBERGER, E. G., 1983, Sea ice melting in the marginal ice zone. *J. Geophys. Res.*, 88(C5), 2827-2835.

JOSBERGER, E. G., 1984, Reply to 'Comment on Sea Ice Melting in the Marginal Ice Zone'. *J. Geophys. Res.*, 89, 761-2.

JOSBERGER, E. G. and D. MELDRUM, 1985, Bottom Ablation measurements and heat transfer coefficients from MIZEX-West, February 1983. *MIZEX Bull.*, VI, Cold Regions Research and Engineering Laboratory, Special Report 85-6, 68-72.

JOYCE, T. M., W. ZENK and J. M. TOOLE, 1978, The anatomy of the Antarctic Polar Front in Drake Passage. *J. Geophys. Res.*, 83, 6093-6113.

KAO, T. W., 1981, The dynamics of oceanic fronts. Part II. Shelf water structure due to freshwater discharge. *J. Phys. Oceanogr.*, 11, 1215-1223.

KELLOGG, W. W., 1975, Climatic feedback mechanisms involving the polar regions: *in* Climate of

the Arctic, G. Weller and S. A. Bowling (Eds.) Geophysical Institute. University of Alaska. pp 111-116.

KILLWORTH, P. D., 1983, Deep convection in the world ocean. *Rev. of Geophys. and Space Phys.*, 21, 1-26.

KILLWORTH, P. D. and N. PALDOR, 1985, A model of sea ice front instabilities. *J. Geophys. Res.*, 90, 883-888.

KIM, J. W., 1976, A generalized bulk model of the oceanic mixed layer. *J. phys. Oceanogr.*, 6, 686-695.

KINDER, T. H. and L. K. COACHMAN, 1978, The front overlying the continental shelf in the Eastern Bering sea. *J. Geophys. Res.*, 83, 4551-4559.

KINDER, T. H. and J. D. SCHUMACHER, 1981a, Hydrographic structure over the continental shelf of the south eastern Bering sea. *in* The Eastern Bering sea shelf: Oceanography and Resources ed. D. W. Hood and J. A. Calder pp 31-52. University of Washington press.

KINDER, T. H. and J. D. SCHUMACHER, 1981b, Circulation over the continental shelf of the south eastern Bering sea. *in* The Eastern Bering sea shelf: Oceanography and Resources. ed. D. W. Hood and J. A. Calder, pp 53-75. University of Washington press.

KOZO, T. L., 1983, Initial model results for Arctic mixed layer circulation under a refreezing lead. *J. Geophys. Res.*, 88(C5), 2926-2934.

KRAUS, E. B. and J. S. TURNER, 1967, A one dimensional model of the seasonal thermocline. II. The general theory and its consequences. *Tellus*, 19, 98-106.

LeBLOND, P. H., 1982, Satellite observations of Labrador current undulations. *Atmos. Ocean*, 20, 129-142.

LEMKE, P., 1979, A model for the seasonal variation of the mixed layer in the Arctic ocean. GFD summer school WHOI.

LEMKE, P., E. W. TRINKL and K. HASSELMAN, 1980, Stochastic dynamic analysis of polar sea ice variability. *J. Phys. Oceanogr.*, 10, 2100-2120.

LEMKE, P., and T. O. MANLEY, 1984, The seasonal variation of the mixed layer and pycnocline under polar sea ice. *J. Geophys. Res.*, 89(C4), 6494-6505.

LEMKE, P., 1986, Stochastic description of Atmospheric-sea ice-ocean interaction. *in* The Geophysics of Sea Ice, Proc of NATO Institute, Maratea 1981, ed. N. UNTERSTEINER, Plenum. Chapter 13. (in press).

LEPPARANTA, M. and W. D. HIBLER III, 1985, The role of plastic ice interaction in Marginal Ice Zone dynamics. *J. Geophys. Res.*, 90(C6), 11,899-11,909.

LEPPARANTA, M. and W. D. HIBLER III and O. JOHANNESSEN, 1986, On estimating ice stress from MIZEX 83 Ice deformation and Current Measurements. *MIZEX Bull* VI, USA Cold Regions Research and Engineering Laboratory, Special Report 86-3, 17-19.

LINDSAY, R. W., 1976, Wind and Temperature profiles taken during Arctic lead experiment. *AIDJEX Bulletin*, 33, 102-104.

LIU, S. K. and J. J. LEENDERTSE, 1978, Three-dimensional sub-grid scale energy model for the Eastern Bering Sea. *Proc. SVI Coast Eng. Conf. Amer. Soc. Civil.*

LUECK, R. G., D. HARTZMAN and T. R. OSBORN, 1977, The spectral response of thermistors. *Deep Sea Res.*, 24, 951-970.

LUTJEHARMS, J. R. E. and L. H. MCQUAID, 1986, Changes in the structure of thermal fronts south of Africa over a three-month period. *S. Afr. J. of Science*, 82, 470-476.

LUTJEHARMS, J. R. E. and A. FOLDVIK, 1986, the thermal structure of the upper ocean layers between Africa and Antarctica during the period December 1978 to March 1979. *S. Afr. J. Antarct. Res.*, 16 13-20.

MACAYEAL, D. R., 1984, Thermohaline circulation below the Ross Ice Shelf: A consequence of tidally induced vertical mixing and basal melting. *J. Geophys. Res.*, 89(C1), 597-606.

MANABE, S., K. BRYAN and M. J. SPELMAN, 1975, A global ocean-atmosphere climate model. Part 2. The oceanic circulation. *J. Phys. Oceanogr.*, 5, 30-46.

MANLEY, T. O., K. HUNKINS and W. TIEMAM, 1980, AIDJEX 1975-1976, Physical oceanography data reports, Vols 1-4, Lamont-Doherty Geological Observatory, Columbia University, New York.

MARKHAM, D. G., 1983, Ocean mixing and circulation response in the marginal ice zone. Masters Thesis. U. S. Naval Postgraduate School, Monterey.

MARTIN, S., 1985 Introduction to MIZEX-West. *MIZEX Bull.* VI, Cold Regions Research and Engineering LAboratory, Spec. Report 85-6. 11-12.

MARTIN, S., P. KAUFFMAN and C. PARKINSON, 1983, The movement and decay of ice edge bands in the Winter Bering Sea. *J. Geophys. Res.*, 88, 2803-2812.

MAYKUT, G. A., 1978, Energy exchange over young sea ice in the central Arctic. *J. Geophys. Res.*, 83, 3646-3658.

MAYKUT, G. A., 1982, Large scale heat exchange and Ice production in the central Arctic. *J. Geophys. Res.*, 87, 7971-7984.

MAYKUT, G. A., 1987, Surface heat and mass balance. *in* The Geophysics of sea ice. Proc. of NATO Institute Maratea 1981, ed. N. UNTERSTEINER, Plenum (in press).

MAYKUT, G. A. and N. UNTERSTEINER, 1971, Some results from a time dependant thermodynamic model of sea ice. *J. Geophys. Res.*, 76(6), 1550-1575.

MCNUTT, S. L., 1981, Remote sensing analysis of ice growth and distribution in the Eastern Bering Sea. The Eastern Bering Sea shelf: Oceanography and Resources. ed D. W. Hood and J. A. Calder, p141-166, University of Washington Press.

MCPHEE, M. G. and J. D. SMITH, 1976, Measurements of the turbulent boundary layer under pack ice. *J. Phys. Oceanogr.*, 6, 696-711.

MCPHEE, M. G., 1982, Sea ice drag laws and simple boundary layer concepts including application to rapid melting. CRREL Report 82-4, U. S. Army Cold Regions Research and Engineering Laboratory, Hanover, NH.

MCPHEE, M. G., 1983, Turbulent heat and momentum transfer in the oceanic boundary layer under melting pack ice. *J. Geophys. Res.*, 88, 2822-2835.

MCPHEE, M. G., 1984a, Turbulence frame Experiments. *MIZEX Bull.*, V Cold Regions Research and Engineering, Special Report. 84-29, 35-37.

MCPHEE, M. G., 1984b, Comment on 'Sea ice modelling in the Marginal Ice Zone' by E. G. Josberger. *J. Geophys. Res.*, 89, 759-760.

MELLOR, G. L. and T. YAMADA, 1974, A hierarchy of turbulent closure models for planatry boundary layers. *J. Atmos. Sci.*, 31, 1791-1806.

MESINGER, F. and A. ARAKAWA, 1976, Numerical methods used in Atmosphere models. *GARP Publication Series*, 17(1), WMO-ICSU.

MICKLIN, P. P., 1981, A preliminary analysis of impacts of proposed Soviet river diversions on Arctic sea ice. *EOS*, 62, 489-493.

MIZEX-West Study Group. 1983, MIZEX-West Bering Sea marginal ice zone experiment. *EOS*, 64. 578-579.

MOFJELD, H. O., 1986, Observed tides in the northeastern Bering Sea shelf. *J. Geophys. Res.*, 91(C2), 2593-2606.

MOFJELD, H. O., J. D. SCHUMACHER and D. J. PASHINSKI, 1984, Theoretical and observed profiles of tidal currents at two sites on the south eastern Bering Sea shelf. NOAA Tech. Memo. ERL,

PMEL-62.
MOLER, C. B. and G. W. STEWART, 1973, An algorithm for generalized matrix eigen value problems. *SIAM J. Numer. Anal.*, 10(2) 241-256.
MUENCH, R. D. and R. L. CHARNELL, 1977, Observations of medium-scale features along the seasonal sea ice edge in the Bering sea. *J. Phys. Oceanogr.*, 7, 602-606.
MUENCH, R. D., 1983, Mesoscale oceanographic features associated with the Central Bering sea ice edge: February - March 1981. *J. Geophys. Res.*, 88, 2715-2722.
MUENCH, R. D., P. H. Leblond, and L. E. HACHMEISTER, 1983, On some possible interactions between internal waves and sea ice in the Marginal ice zone. *J. Geophys. Res.*, 88, 2819-2826.
MUENCH, R. D. and J. D. SCHUMACHER, 1985, On the Bering Sea ice edge front. *J. Geophys. Res.*, 90, 3185-3198.
MUENCH, R. D., J. L. NEWTON and R. L. RICE, 1985, Temperature and salinity observations in the Bering sea winter MIZ. *MIZEX Bull.*, VI, Cold Regions Research and Engineering Laboratory, Special Report, 85-6 11-12.
MUENCH, R. D. and J. T. GUNN, 1985, Near-inertial currents on the eastern Bering sea shelf. *EOS*, 66, 916.
MUENCH, R. D. and H. O. MOFJELD, 1985, Seasonal variations in tidal constituents on the Eastern Bering sea shelf. *EOS*, 66(52), 1362.
MUNK, W. H. and E. R. ANDERSON, 1948, Note on the theory of the thermocline. *J. Mar. Res.*, 7, 276-295.
NERELLA, V. R. and S. W. LIU, 1979, A simple model to calculate the compaction of ice floes. *J. Glac.*, 24(90), 407-414.
NEWTON, J. L., 1982, Temperature-Salinity structure of the wintertime Bering Sea. Science Applications Inc. Rep. SAI-085-82-082-LJ, La Jolla, California.
NIEBAUER, H. J., 1981, Recent fluctuations in sea ice distribution in the Eastern Bering sea, The Eastern Bering sea shelf: Oceanography and Resources, ed D. W. Hood and J. A. Calder, p133-140. University of Washington press.
NIEBAUER, H. J., 1982, Wind and melt driven ocean circulation in a marginal sea ice edge frontal system: A numerical model. *Cont. Shelf Res.*, 1, 49-98.
NIEBAUER, H. J. and V. ALEXANDER, 1985, Oceanographic frontal structure and biological productivity at an ice edge. *Cont. Shelf Res.*, 4, 367-388.
NIILER, P. P., 1977, One-dimensional models of the seasonal thermocline. *in* The Sea. Vol 6. chapter3. pp 97-115.
NIILER, P. P., and E. B. KRAUS, 1977, One dimensional models of the upper ocean. *in* Modelling and prediction of the upper layers of the ocean. ed. E. B. Kraus. Pergamon Press.
NORSEX GROUP, 1980, A CTD report from the NORSEX marginal ice zone program north of Svalbard in Sept.-Oct. 1979. University of Bergen Report.
O'BRIEN J. J. and R. O. REID, 1967, The non-linear response of a two-layer baroclinic ocean to a stationary, axially symmetric hurricane: Part 1. Upwelling induced by momentum transfer. *J. Atmos. Sci.*, 24, 197-207.
ORHEIM, O., 1984, Iceberg discharge and mass balance of Antarctica. in, Glaciers, ice sheets and sea level: Effect of a CO_2 induced climatic change. p 210-215. Rep of Workshop, Seattle, Sept. 1984.
ORLANSKI, I., 1976, A simple boundary condition for unbounded hyperbolic flows. *J. Comp. Phys.*, 21, 251-269.
OU, H. W., 1983, Some two-layer models of the shelf slope front: Geostrophic adjustment and its maintenance. *J. Phys. Oceanogr.*, 13, 1798-1808.

OU, H. W., 1984a, Geostrophic adjustment a mechanism for frontogenesis. *J. Phys. Oceanogr.*, 14, 994-1000.

OU, H. W., 1984b, Wind driven motion near a shelf slope front. *J. Phys. Oceanogr.*, 14, 985-993.

OVERLAND, J. E. and C. H. PEASE, 1982, Cyclone Climatology of the Bering Sea and its relation to sea ice extent. *Mon. Wea. Rev.*, 110, 5-13.

OVERLAND, J. E., H. MOFJELD and C. H. PEASE, 1984, Wind driven ice drift in a shallow sea. *J. Geophys. Res.*, 89(4), 6525-6531.

OVERLAND, J. E., and B. A. WALTER, 1985, Further aircraft measurements of air-ice drag coefficients. *MIZEX Bull.*, Cold Regions Research and Engineering Lab. Spec. Report. 85-6, 79-84.

OWEN, T. R. E., 1984, Conductivity, depth and temperature profiler. CTD 484. Tech. Rep. Carrack Measurement Technology, Cambridge.

PALUSZKIEWICZ, T. and H. J. NIEBAUER, 1984, Satellite observations of circulation in the Eastern Bering sea. *J. Geophys. Res.*, 89, 3663-3678.

PAQUETTE, R. G. and R. H. BOURKE, 1981, Ocean circulation and fronts as related to ice melt-back in the Chukchi Sea. *J. Geophys. Res.*, 86(C5), 4215-4230.

PARKINSON, C. L. and W. M. WASHINGTON, 1979, A large scale numerical model of sea ice. *J. Geophys. Res.*, 84(C1), 311-337.

PARKINSON, C. L. and W. W. KELLOGG, 1979, Arctic sea ice decay simulated for a CO_2 induced temperature rise. *Climatic change*, 2, 149-162.

PEARSON, C. A., MOFJELD, H. O. and R. B. TRIPP, 1981, Tides of Eastern Bering sea shelf. in The Eastern Bering Sea Shelf Oceanographic and Resources, Vol 1, ed D. W. Hood and J. A. Calder, University of Washington Press.

PEASE, C. H., 1980, Eastern Bering sea ice processes. *Mon. Wea. Rev.*, 108 2015-2023.

PEASE, C. H., M. REYNOLDS, G. A. GALASSO, V. L. LONG, S. A. SALO and B. D. WEBSTER, 1985, Sea ice dynamics and regional meteorology for the Arctic polynya experiment (APEX) Bering sea 1985, NOAA Tech. Memo. ERL PMEL-64.

PEASE, C. H., 1985, Theory of wind driven coastal polynyas. *MIZEX Bull.* VI, Cold Regions Research and Engineering Laboratory, Spec. Report 85-6, p 112-119.

PEDERSON, A. M., and M. C. GREGG, 1979, Development of a small in-situ conductivity instrument. IEEE *J. of Ocean Eng.*, 4, 69-75.

PEROVICH, D. K., 1983, On the summer decay of a sea ice cover. PhD. Thesis, University of Washington.

PINGREE, R. D., 1971, Regularly spaced instrumental temperature and salinity structures. *Deep Sea Res.*, 18, 841-844.

POLLARD, D., M. L. BATTEEN and Y. J. HAN, 1983, Development of a simple upper ocean and sea ice model. *J. Phys. Oceanogr.*, 13, 754-768.

REYNOLDS, M., 1984, On the local meteorology of the marginal ice zone of the Bering sea. *J. Geophys. Res.*, 89, 6515-6524.

REYNOLDS, M. R. and PEASE, C. H., 1984, Drift characteristics of northeastern Bering Sea ice during 1982. NOAA Tech Memo ERL PMEL-55, 135pp.

REYNOLDS, M., C. H. PEASE and J. E. OVERLAND, 1985, Ice drift and regional meteorology in the southern Bering Sea. Results from MIZEX West. *J. Geophys. Res.*, 90(C6), 11967-11981.

RØED, L. P. and J. J. O'BRIEN, 1981, Geostrophic adjustment of highly dispersive media: An application to the marginal ice zone. *J. Geophys. Astrophys. Fluid Dyn.*, 18, 263-278.

RØED, L. P., 1983, Sensitivity studies with a coupled ice-ocean model of the marginal ice zone. *J. Geophys. Res.*, 88, 6039-6042.

RØED, L. P. and J. J. O'BRIEN, 1983, A coupled ice-ocean model of upwelling in the marginal ice zone. *J. Geophys. Res.*, 88, 2863-2872.

RØED, L. P., 1984, A thermodynamic coupled ice-ocean model of the marginal ice zone. *J. Phys. Oceanogr.*, 14, 1921-1929.

RØED, L. P. and O. M. SMEDSTAD, 1984, Open boundary conditions for forced waves in a rotating fluid. *SIAM J. Sci. Stat. Comput.*, 5, 414-426.

SALO, S. A., J. D. SCHUMACHER and L. K. COACHMAN, 1983, Winter currents on the Eastern Bering shelf. NOAA Technical Memo, ERL-PMEL 45, 53pp.

SCARLET, R. I., 1975, A data processing method for temperature and depth profiles. *Deep Sea Res.*, 22, 509-515.

SCHAUS, R. H. and J. A. GALT, 1973, A thermodynamic model of an Arctic lead. *Arctic*, 26, 208-221.

SCOR, 1979, The Arctic ocean heat budget. Report from working group 58, Scientific Committee on Oceanic Research, Rep. 52, Geophys. Inst., Univ. of Bergen,. Norway.

SCHNEIDER, S. H., 1975, Surface temperature-albedo coupling: Implications for climate stability. *in* Climate of the Arctic, G. Weller and S. A. Bowling (Eds.) Geophysical Institute. University of Alaska. 166-171.

SCHUMACHER, J. D. K. AAGAARD, C. H. PEASE and R. B. TRIPP, 1983, Effects of a shelf polynya on flow and water properties in the Northern Bering Sea. *J. Geophys. Res.*, 88(C5), 2723-2732.

SEMTNER, A. J. Jr., 1973, A numerical investigation of Arctic ocean circulation. Phd. Thesis, Princetown University, 251pp.

SEMTNER, A. J. Jr., 1976a, Numerical simulation of Arctic ocean circulation. *J. Phys. Oceanogr.*, 6, 409-425.

SEMTNER, A. J. Jr., 1976b, A model for the thermodynamic growth of sea ice in numerical investigations of Climate. *J. Phys. Oceanogr.*, 6, 379-389.

SEMTNER, A. J. Jr., 1984a, On modelling the seasonal thermodynamic cycle of sea ice studies of climatic change. *Climatic change*, 6, 27-37.

SEMTNER, A. J. Jr., 1984b, The climatic response of the Arctic ocean to Soviet river diversions. *Climatic change*, 6, 109-130.

SEMTNER, A. J. Jr., 1987, A numerical study of sea ice and ocean circulation in the Arctic *J. Phys. Oceanogr.*, 17, 1077-1099.

SIELECKI, A., 1968, An energy conserving difference scheme for the storm surge equations. *Mon. Wea. Rev.*, 96, 150-156.

SIMMONS, T. J., 1980, Circulation models of lakes and inland seas. *Can. Bull. of Fish and Aquatic Sciences*, no203.

SIMPSON, J. H., C. M. ALLEN and N. C. G. MORRIS, 1978, Fronts on the continental shelf. *J. Geophys. Res.*, 83, 4615-4622.

SJØBERG, B. and M. MORK, 1985, Wind induced stratified ocean response in the ice edge region: An analytic approach. *J. Geophys. Res.*, 90, 7273-7285.

SMITH, D. C., J. H. MORRISON, J. A. JOHANNESSEN and N. UNTERSTEINER, 1984, Topographic generation of an eddy at the ice edge of the East Greenland current. *J. Geophys. Res.*, 89, 8205-8208.

SMITH, G. D., 1978, Numerical solution of partial differential equation: Finite difference methods. Oxford University Press.

SMITH, S. D., 1981, Coefficients for sea surface wind stress and heat exchange. Rep. BI-R-81-19. Bedford Institute of Oceanography, Dartmouth, N. S. Canada.

SMEDSTAD, O. M. and L. P. RØED, 1985, A coupled ice-ocean model of ice break up and banding in the marginal ice zone. *J. Geophys. Res.*, 90, 876-882.

SQUIRE, V. A. and S. C. MOORE, 1980, Direct measurement of the attenuation of ocean waves by pack ice. *Nature* Lond., 253, 365-368.

SQUIRE, V. A., P. WADHAMS, A. M. COWAN, S. O'FARRELL and R. WEINTRAUB, 1983, MIZEX-83 Data summary. Sea ice Group Rep 83-1, Scott Polar Research Institute.

SQUIRE, V. A., and P. WADHAMS, 1985, Some wave attenuation results from MIZEX-WEST. *MIZEX Bull.* VI, Cold Regions Research and Engineering Laboratory Special Report, 85-6, p73-78.

STEIGBRANT, A., 1981, A model for the thickness and salinity of the upper layer in the Arctic ocean and the relationship between ice thickness and some external parameters. *J. Phys. Oceanogr.*, 11, 1407-1422.

STEINHART, J. S. and S. R. HART, 1968, Calibration curves for thermistors. *Deep Sea Res.*, 15, 497-503.

STEVENSON, J. W., 1979, On the effect of dissipation in seasonal thermocline models. *J. Phys. Oceanog.*, 9, 57-64.

STOMMEL, H. and G. VERONIS, 1980, Barotropic response to cooling. *J. Geophys. Res.*, 85(C11), 6661-6666.

SY, A., 1985, An alternative editing technique for oceanographic data. *Deep Sea Res.*, 32 1591-1599.

TURNER, J. S., 1973, Buoyancy effects in fluids. Cambridge University Press.

UNTERSTEINER, N and A. S. THORNDIKE, 1982, Arctic data buoy program. *Polar Record*, 21, 127-135.

VINJE, T., 1977, Sea ice studies in the Spitzbergen-Greenland area. Landsat Rep. E77-10206. U. S. Dept of Commerce.

VINJE, T., 1984, The Fram Strait cruise with M/S Lance, 17-31 August 1984. *Rapp. Norsk Polarinstitutt*, Nr. 18, 34pp.

WADHAMS, P., 1973, Attenuation of swell by sea ice. *J. Geophys. Res.* 78, 3552-3563.

WADHAMS, P., A. E. GILL and P. F. LINDEN, 1979, Transects by submarine of the East Greenland polar front. *Deep Sea Res.*, 26, 1311-1328.

WADHAMS, P., 1981, The ice cover in the Greenland and Norwegian seas. *Rev. of Geophys. and Space Physics*, 19(3), 345-393.

WADHAMS, P., 1983, A mechanism for the formation of ice edge bands. *J. Geophys. Res.*, 88, 2813-2818.

WADHAMS, P. and V. A. SQUIRE, 1983, An ice water vortex at the edge of the East Greenland Sea. *J. Geophys. Res.*, 88, 2770-2781.

WADHAMS, P., and S. P. O'FARRELL, 1985, The motion of ice edge radar transponders during MIZEX-West. *MIZEX Bull.* VI, Cold Regions Research and Engineering Laboratory, Spec. Report 85-6. 50-67.

WALSH, J. E., 1987, Diagnostic studies of large scale air-sea-ice interactions. In The Geophysics of sea ice. Proc. of NATO Institute, Maratea 1981, ed N. UNTERSTEINER. Plenum. (in press).

WALSH, J. E. and C. M. JOHNSON, 1979, Interannual atmospheric variability and associated fluctuations in Arctic sea ice extent. *J. Geophys. Res.*, 6915-6928.

WANG, D. P., 1984, Mutual intrusion of a gravity current and density front formation. *J. Phys. Oceanogr.*, 14, 1191-1199.

WCP-108, 1985, General Circulation of the Southern Ocean: Status and recommendations for research. A report by SCOR WG-74. October 1985.

WILSON, J. G., A. L. COMISKEY, R. W. LINDSAY and V. L. LONG, 1984, Regional Meteorology of the Bering Sea during MIZEX-West. February and March, 1983, NOAA Spec Report. Pacific Marine Enviromental Laboratory, Seattle, 115p.

ZWALLY, H. J. and P. GLOERSEN, 1977, Passive microwave images of the polar regions and research applications. *Polar Record*, 18, 431-450.

ZWALLY, H. J., J. C. COMISO, C. L. PARKINSON, W. J. CAMPBELL, F. D. CARSEY, P. GLOERSON, 1983, Antarctic sea ice 1973-1976: Satellite Passive microwave observations. NASA Washington DC.